Sören Vogel

Kalman Filtering with State Constraints Applied to Multi-sensor Systems and Georeferencing

München 2020

Kalman Filtering with State Constraints Applied to Multi-sensor Systems and Georeferencing

Von der Fakultät für Bauingenieurwesen und Geodäsie

der Gottfried Wilhelm Leibniz Universität Hannover

zur Erlangung des Grades

Doktor-Ingenieur (Dr.-Ing.)

genehmigte Dissertation

Vorgelegt von

Sören Vogel, M.Sc.

Geboren am 07.04.1988 in Leimen

München 2020

Adresse der DGK:

Prüfungskommission:

Vorsitzender: Prof. Dr. Philipp Otto

Referent: Prof. Dr.-Ing. Ingo Neumann

Korreferenten: Prof. Dr.-Ing. Hans-Berndt Neuner (TU Wien)
Prof. Dr.-Ing. Steffen Schön

Tag der mündlichen Prüfung: 05.08.2020

Abstract

Active research on the development of autonomous vehicles has been carried out for several years now. However, some significant challenges still need to be solved in this context. Particularly relevant is the constant guarantee and assurance of the integrity of such autonomous systems. In order to ensure safe manoeuvring in the direct environment of humans, an accurate, precise, reliable and continuous determination of the vehicle's position and orientation is mandatory. In geodesy, this process is also referred to as georeferencing with respect to a superordinate earth-fixed coordinate system. Especially for complex inner-city areas, there are no fully reliable methods available so far. The otherwise suitable and therefore common Global Navigation Satellite System (GNSS) observations can fail in urban canyons. However, this fact does not only apply exclusively to autonomous vehicles but can generally also be transferred to any kinematic Multi-Sensor System (MSS) operating within challenging environments.

Especially in geodesy, there are many MSSs, which require accurate and reliable georeferencing regardless of the environment. This is indispensable for derived subsequent products, such as highly accurate three-dimensional point clouds for 3D city models or Building Information Modelling (BIM) applications. The demand for new georeferencing methods under aspects of integrity also involves the applicability of big data. Modern sensors for capturing the environment, e.g. laser scanners or cameras, are becoming increasingly cheaper and also offer higher information density and accuracy. For many kinematic MSSs, this change leads to a steady increase in the amount of acquired observation data. Many of the currently methods used are not suitable for processing such amounts of data, and instead, they only use a random subset. Besides, big data also influences potential requirements with regard to possible real-time applications.

If there is no excessive computing power available to take into account the vast amounts of observation data, recursive methods are usually recommended. In this case, an iterative estimation of the requested quantities is performed, whereby the comprehensive total data set is divided into several individual epochs. If the most recent observations are successively available for each epoch, a filtering algorithm can be applied. Thus, an efficient estimation is carried out and, with respect to a comprehensive overall adjustment, generally larger observation sets can be considered. However, such filtering algorithms exist so far almost exclusively for explicit relations between the available observations and the requested estimation quantities. If this mathematical relationship is implicit, which is certainly the case for several practical issues, only a few methods exist or, in the case of recursive parameter estimation, none at all. This circumstance is accompanied by the fact that the combination of implicit relationships with constraints regarding the parameters to be estimated has not yet been investigated at all.

In this thesis, a versatile filter algorithm is presented, which is valid for explicit and for implicit mathematical relations as well. For the first time, methods for the consideration of constraints are given, especially for implicit relations. The developed methodology will be comprehensively validated and evaluated by simulations and real-world application examples of practical relevance. The usage of real data is directly related to kinematic MSSs and the related tasks of calibration and georeferencing. The latter especially with regard to complex inner-city environments. In such challenging environments, the requirements for georeferencing under integrity aspects are of special importance. Therefore, the simultaneous use of independent and complementary information sources is applied in this thesis. This enables a reliable georeferencing solution to be achieved and a prompt notification to be issued in case of integrity violations.

Keywords: Recursive State-Space Filtering, State Constraints, Implicit Functions, Georeferencing, Integrity

Kurzfassung

Bereits seit einigen Jahren wird aktiv an der Entwicklung von autonomen Fahrzeugen geforscht. Allerdings gilt es in diesem Zusammenhang noch einige signifikante Herausforderungen zu lösen. Besonders relevant ist dabei die ständige Gewährleistung und Sicherstellung der Integrität solcher autonomen Systeme. Um ein sicheres Manövrieren in der direkten Umgebung von Menschen gewährleisten zu können, ist eine genaue, präzise, zuverlässige und kontinuierliche Positions- und Orientierungsbestimmung des Fahrzeuges zwingend erforderlich. Im Bezug zu einem übergeordneten erdfesten Koordinatensystem wird dieser Vorgang in der Geodäsie auch als Georeferenzierung bezeichnet. Besonders für komplexe innerstädtische Gebiete existieren jedoch noch keine vollumfänglich zuverlässigen Lösungsmethoden. Die ansonsten geeigneten und daher auch gebräuchlichen Beobachtungen eines Global Navigation Satellite Systems (GNSS) können in dieser Hinsicht in engen Häuserschluchten versagen. Diese Tatsache gilt jedoch nicht nur ausschließlich für autonome Fahrzeuge, sondern lässt sich im Allgemeinen auf jedes kinematische Multisensorsystem (MSS) übertragen.

Gerade auch in der Geodäsie existieren eine Vielzahl solcher MSS, welche eine stets genaue und zuverlässige Georeferenzierung unabhängig von der jeweiligen Umgebung erfordern. Für daraus abgeleitete Folgeprodukte, wie z.B. hochgenaue dreidimensionale Punktwolken für Anwendungen im Rahmen von 3D Stadtmodellen oder Building Information Modelling (BIM), ist dies unverzichtbar. Mit dem Bedarf an neuen Methoden für eine Georeferenzierung unter Aspekten der Integrität, geht zeitgleich auch die Anwendbarkeit von Massendaten einher. Moderne Sensoren zur Erfassung der Umgebung, wie z.B. Laserscanner oder Kameras, werden immer preiswerter und weisen zudem in Relation dazu eine immer höhere Informationsdichte und Genauigkeit auf. Dies führt bei zahlreichen kinematischen MSS zu einem stetigen Anstieg der erfassten Beobachtungsdaten. Viele derzeitige Methoden sind dafür nicht ausgelegt beziehungsweise verwenden stattdessen nur eine zufällige Untermenge der eigentlich verfügbaren Informationen. Zusätzlich beeinflusst dies auch potentielle Ansprüche hinsichtlich möglicher Echtzeitanwendungen.

Steht keine überdurchschnittliche Rechenleistung zur Berücksichtigung der großen Datenmengen zur Verfügung, bieten sich in der Regel rekursive Verfahren an. Dabei wird eine iterative Schätzung der gesuchten Größen durchgeführt, wobei die umfassende Gesamtmenge an Beobachtungsdaten in mehrere einzelne Epochen aufgeteilt wird. Liegen aktuellste Beobachtungen sukzessive pro Epoche vor, kann ein Filteralgorithmus angewendet werden. So wird ebenfalls eine effiziente Schätzung durchgeführt und es können in Relation zu einer umfassenden Gesamtauswertung im Allgemeinen größere Beobachtungsmengen berücksichtigt werden. Solche Filterverfahren existieren bislang jedoch fast ausschließlich für explizite Beziehungen zwischen den verfügbaren Beobachtungen und den gesuchten Schätzgrößen. Ist dieser mathematische Zusammenhang implizit, was durchaus bei vielen praktischen Fragestellungen der Fall ist, existieren nur sehr wenige Methoden beziehungsweise im Falle der rekursiven Parameterschätzung gar keine. Dieser Umstand geht mit der Gegebenheit einher, dass das Zusammenwirken von impliziten Zusammenhängen mit Restriktionen hinsichtlich der zu schätzenden Parameter bislang noch überhaupt nicht untersucht wurde.

Im Rahmen dieser Arbeit wird daher ein vielseitig einsetzbarer Filteralgorithmus präsentiert, welcher sowohl für explizite als auch für implizite mathematische Zusammenhänge gilt. Zusätzlich werden erstmalig Möglichkeiten zur Berücksichtigung von Restriktionen auch und insbesondere für implizite Beziehungen gegeben. Die entwickelte Methodik wird anschließend umfassend anhand von Simulationen und praxisrelevanten realen Anwendungsbeispielen validiert und kritisch beurteilt. Die Verwendung von Echtdaten steht dabei in direktem Zusammenhang zu kinematischen MSS und den damit verbundenen Aufgaben der Kalibrierung und Georeferenzierung. Letztere insbesondere im Bezug auf komplexe innerstädtische Umgebungen. In einem derart anspruchsvollen Umfeld sind die Anforderungen an die Georeferenzierung unter Integritätsaspekten von besonderer Bedeutung. Dies wird in dieser Arbeit durch die gleichzeitige Nutzung unabhängiger und komplementärer Informationsquellen realisiert. Dadurch kann eine zuverlässige Georeferenzierung erreicht werden und eine zeitnahe Benachrichtigung bei Integritätsverletzungen erfolgen.

Schlagwörter: Rekursive Zustandsschätzung, Restriktionen, Implizite Funktionen, Georeferenzierung, Integrität

Contents

List of Figures

List of Tables

Acronyms

1

Introduction

1.1 Motivation

The use of domestic robots (e.g. robotic vacuum cleaners) has increased steadily in recent years. As a result, it has become a widespread routine that such mainly autonomously acting systems are moving in the immediate environment of humans (Bogue, 2017). The risk potential for these small robots to injure humans is, in this context, quite low. However, the situation will be completely different, if in the upcoming years more and more fully autonomous cars will be involved in public road traffic. Already today, local public transport buses and taxis operate autonomously in defined areas, with a growing trend (Fagnant and Kockelman, 2015; Mallozzi et al., 2019; Boudette, 2019). At present, the presence of a trained operator is still mandatory to ensure safety. Unexpected collisions can have serious consequences in this context, which must be prevented. For this reason, vehicles are already equipped with a variety of different sensors. In addition to vehicle-specific sensors, these are mainly those that are used for positioning and orientation of the vehicle to its environment (e.g. Global Navigation Satellite System (GNSS) antennas or Inertial Measurement Units (IMUs)). Furthermore, there exist sensors that are increasingly used for environmental perception, such as laser scanners and cameras. In combination, they ensure the *integrity*[1] of the vehicle. The accurate, precise, reliable and complete pose[2] estimation of such a system is of great importance. Its exact determination must be known continuously at all points in time. This must be ensured independently of the environment.

However, these requirements are of great importance not only for autonomous vehicles. In general, these demands can also be applied to any *kinematic Multi-Sensor System (MSS)*. After all, a modern vehicle with all its sensors is nothing else than such a kinematic MSS. Therefore, accurate information about the current position and orientation is not only necessary to ensure the integrity of a vehicle, but it is also essential for other purposes. In this context, it can generally also refer to the *georeferencing* of an MSS with respect to a superordinate coordinate system. For example, accurate and precise pose estimation is also indispensable when using Mobile Mapping Systems (MMSs) on the ground and in the air. These MMSs are mobile platforms containing several of the above-mentioned sensors in order to acquire spatial data of the environment (Wang et al., 2019). Such systems usually do not operate autonomously, but even in case of, i.e. an Unmanned Aerial Vehicle (UAV), their pose to a fixed coordinate system must be precisely known at all times (Colomina and Molina, 2014). Only under these conditions, it is possible to derive highly accurate maps and three-dimensional models of the reality from the acquired data (Glennie, 2007). This, in turn, is the basis for obtaining, for example, an up-to-date Building Information Modeling (BIM) system (Borrmann et al., 2018) or 3D city models (Vosselman and Dijkman, 2001).

Although numerous approaches and methods already exist, independence with respect to the environment is still a major challenge. Urban areas, in particular, cause difficulties. So-called urban canyons lead to the fact that the otherwise frequently used pose information based on GNSS and IMU observations is

---

[1] *Integrity*, in this context, means that the complete, safe and accurate operability of the vehicle within certain predefined thresholds can be guaranteed at all times, and that information is provided in a timely manner if these thresholds are exceeded (Hegarty et al., 2017).
[2] combination of position and orientation in the relevant dimension

often too inaccurate (Zhu et al., 2018). Shadowing as well as multipath and drift effects are the reasons for this. Such unreliable georeferencing is risky, especially in highly frequented urban environments. This circumstance has led to the fact that other sensors for georeferencing, such as laser scanners and cameras, as well as additional map information, are already being considered more intensively in the systems mentioned. Thus, the acquired data cannot only be used to map the environment but also to actively contribute to the improvement of georeferencing. However, this leads simultaneously to new challenges. Especially the increased use of laser scanners in such kinematic MSSs leads to an enormous increase in the amount of data collected. Besides, automotive laser scanners (such as solid-state scanners), for example, have recently become less expensive, which makes them even more suitable for more frequent use in cars for the future (Randall, 2019). There are already multiple automotive laser scanners available that have a small and lightweight design and a remarkable level of accuracy (Velodyne LiDAR, 2018b; Ibeo Automotive Systems, 2020; Robosense, 2020). At the same time, the resolution, range and density of these three-dimensional sensors are increasing. The availability of at least $500\,000$ points per second is already common. Slightly larger sensors than such automotive laser scanners already capture about 2.2 million points per second (Velodyne LiDAR, 2018a). For this reason, the terminology of *big data* is quite appropriate in this context. Big data requires the need for efficient algorithms to realise potentially real-time capable systems. To process these vast amounts of point cloud data at all, usually, only a random subset of the total collected data is currently used (Elseberg et al., 2013b). Although there are approaches that perform spatial or temporal subsampling, there is no specific assessment of the individual observed quantities with regard to their contribution to an improved estimation. Thus, a more structured reduction of the entire data set is achieved, but important observations might be lost. Since this identification of relevant observations is quite challenging, depending on the application, it is advisable to use as much information as possible. Batch processing, where the data is used within an overall adjustment, is often applied for this purpose, but reaches its limitations with such increasing amounts of 3D points. Although such batch methods provide excellent results, they usually have to be performed in post-processing on powerful computers. Otherwise, enormous mobile computing power is required or, for example, the use of Graphics Processing Units (GPUs). However, this is in contradiction to the demands for online approaches, such as those needed for autonomous driving. Current applications of this kind require recursive approaches.

Especially suitable for such tasks is the use of *recursive state-space filtering*. This methodology covers decades of development and deals with the estimation of arbitrary and not directly measurable states, by the fusion of arbitrary observation data via a suitable mathematical model (Kalman, 1960). Applications of such filters are extensive. However, these are primarily based on explicit[3] mathematical relationships between the observations and the parameters to be estimated. This mathematical limitation is in contrast to a multitude of issues in various fields of expertise (Heuel, 2001; Perwass et al., 2005), and especially in geodesy (Steffen and Beder, 2007; Dang, 2007; Ning et al., 2017). Often, when dealing with geometrical issues, mathematically implicit[4] relationships occur. Although there are approaches but they are rare. This becomes evident, for example, from the fact that the use of constraints regarding the state parameters in connection with implicit relationships has not yet been investigated. However, the presence of appropriate additional information when using constraints is always recommended and generally has a beneficial impact on the estimation results (Simon, 2010). For example, the integration of various (geometric) constraints regarding the previously mentioned challenging urban setting for autonomous driving might be useful. In addition, there is still a need to develop and assess these methods with regard to compliance with integrity aspects (Wörner et al., 2016; Reid et al., 2019). Therefore, possible solutions should consider the inclusion of new independent and complementary sources of information. This will further improve redundancy, and any loss of integrity can be identified and reported in a timely manner.

In summary, due to the availability of inexpensive modern sensor technologies, the amount of data for various current topics is constantly increasing. Consequently, there is a demand to develop new recursive methods for the reliable georeferencing of kinematic MSSs in challenging urban environments. This allows ensuring the integrity of, e.g. autonomous vehicles or to accurately map environments when using MMSs. Solutions are based on applications from the field of recursive state-space filtering in combination with appropriate constraints and additional information from object space.

---

[3]The observations result directly from the parameters under consideration of a functional relationship
[4]The observations and parameters cannot be separated from each other to either side of the equation.

1.2 Objective and Outline

The main focus of this thesis is on the development of a versatile Kalman filter. This filter should consider non-linear explicit and implicit mathematical relationships between available observations and requested state parameters. In addition, existing methods for the consideration of arbitrary non-linear state constraints have to be applied and validated for the implicit relationships. The main focus here lies on the distinction between hard and soft constraints, and their application to prior information which is affected by a specific degree of uncertainty. It is also necessary to analyse the impact of wrong prior information with regard to the different methods for taking constraints into account. The application of the methodology in this thesis is directly related to kinematic MSSs and associated tasks, like their efficient calibration and georeferencing. In particular, this addresses current challenges in complex urban environments, as well as the development of methods for georeferencing with integrity aspects even under such difficult conditions. For this purpose, independent and complementary sources of information should be used, providing at least long-term support. However, basic applicability to any other issues should also be possible. For this reason, it is also necessary to investigate the extent to which the newly developed methods within this thesis perform with vast amounts of data compared to the existing approaches. This is directly related to current and future big data applications. According to these objectives, this thesis is structured as follows.

Chapter 2 gives an overview of the methods and models applied in this thesis. Firstly, this includes the fundamentals of parameter estimation and associated models. Secondly, the idea of recursive state-space filtering is presented. The corresponding methodology is provided for both explicit and implicit relationships. Thirdly, a comprehensive overview of different possibilities for the consideration of linear and non-linear state constraints is given.

The own methodological contributions of this thesis are presented in chapter 3. This includes the introduction of the versatile recursive state-space filter and mainly the possibilities to consider different state constraints in the context of implicit measurement equations. Furthermore, a realisation of a recursive Gauss-Helmert Model (GHM) is presented from these studies. Also, a geometric application example is presented, which serves as the validation base for the described methods.

Chapter 4 contains a detailed application of the proposed methods concerning the calibration of a kinematic MSS. A general definition of such a system is given at the beginning, and the primary tasks involved are described. This is followed by the motivation and description of the specific calibration task. The results based on the new methods are presented and discussed concerning existing standard approaches.

A second application related to the georeferencing of kinematic MSSs is described in chapter 5. In addition to a motivation and a description of the experimental setup used, current methods of solving the problem are discussed together with their weaknesses. Subsequently, the newly developed approach and the respective results are presented and evaluated.

The thesis concludes with a summary of the most relevant results and findings in chapter 6. At last, an outlook is given in which remaining questions are formulated, and ideas for further research are presented.

2

Fundamentals of Recursive State-space Filtering

This chapter is dedicated to the basic principles of recursive state-space filtering. As part of the parameter estimation in section 2.1, two well-known adjustment models for overdetermined equation systems are generally introduced. These models are then extended by the consideration of constraints. Based on this, the differences to the recursive state-space filtering in section 2.2 are presented. These filters are generally applied to non-linear relationships, which must be exclusively explicit in a first method and implicit in a further method. Subsequently, section 2.3 gives a detailed overview of the various possibilities for considering state constraints in Kalman filtering.

2.1 Parameter Estimation

Adjustment theory provides a fundamental structure for solving overdetermined systems of equations. Such problems are omnipresent in many scientific communities. During a measurement process, arbitrary types of observations l_i are carried out to determine the unknown parameters x_j. Corresponding parameters and observations can be arbitrarily suitable physical or mathematical quantities (e.g., coordinates, angles, distances). The relationship between these observations and parameters can be formulated by any suitable mathematical real-valued functions[1] $\boldsymbol{h}\left(\cdot\right)$, depending on the respective application. This becomes reasonable if the unknown parameters are not directly observable (e.g., coordinates of a new point by observed distances and angles from known points). Furthermore, a set of overdetermined equation systems can increase reliability (e.g., detection of outliers) and improve quality measures (e.g., accuracy, precision). By contrast, overdetermined equation systems can have multiple solutions. For this reason, the optimal solution of such an equation system must be found by parameter estimation.

Different adjustment models can realise such an estimation. The correct choice of the model depends on the independent functional relationships between the observations available and the parameters requested. A careful derivation of such functions by physical or mathematical laws is essential. However, strictly speaking, functional relations are only valid for the true observations $\tilde{l}_i$ and parameters $\tilde{x}_j$. To overcome inconsistencies, unknown expected values $\mathbb{E}\left(\cdot\right)$ are included when using the real values. Furthermore, residuals are introduced to use the real observations and parameters to the respective model (Niemeier, 2008, pp. 120 ff.). This procedure will lead to the best estimates of the values requested.

A stochastic model is used to account for the random behaviour of the observations. In a simplified approach, independent and identically distributed random variables are usually applied. It is assumed that the observed values result from additive deviations — which are random — from the true values. The uncertain observations are therefore modelled by any distribution, e.g. by the Gaussian distribution. An expected value and a Variance-Covariance Matrix (VCM) can give the distribution. This stochastic model will influence the estimation of the unknown parameters as well as their quality measures.

Furthermore, the respective adjustment model is applied with an arbitrary estimator. The most common estimator is Least-Squares (LS). Underlying concept of the optimisation criterion is to minimise the sum

---

[1]Also referred to as *functional model*

of the squared residuals between real observations l_i and their related expected values $\mathbb{E}(l_i) = h_i(\boldsymbol{x})$ by the unknown parameters $\boldsymbol{x}$ (Koch, 1999, pp. 152). If the functional model $\boldsymbol{h}(\cdot)$ is linear, the estimation is referred to as Best Linear Unbiased Estimate (BLUE) in the context of the optimality properties. The strict solution of the LS estimator is independent from the underlying distribution of the observations (Förstner and Wrobel, 2016, pp. 80 ff.). Also other (robust) estimators (e.g. Huber, Hampel) can be applied, which are based on maximum likelihood methods. Nevertheless, only the LS estimator is used in the following.

The general case of adjustment, also known as GHM, forms the basis for such adjustment models. The special case, also known as Gauss-Markov Model (GMM) and the transformation of a GHM into an equivalent GMM are presented subsequently. Such standard methods are commonly used in the geodetic community and are described in detail by (Koch, 1999; Lenzmann and Lenzmann, 2004; Jäger et al., 2005; Wichmann, 2007; Niemeier, 2008). Furthermore, consideration of additional constraints to the requested parameters is given at least for the GMM by the authors mentioned. However, constraints in the sense of a GHM are rather an exception and are mentioned by only a few authors, such as (Rietdorf, 2005; Lösler and Nitschke, 2010; Steffen, 2013; Heiker, 2013; Roese-Koerner, 2015).

There are two basic possibilities for realisation of LS adjustment. The particular preference depends on the existing application. Measurements can be carried out as a whole, which will result in a post-processing approach for all available observations acquired. This will be referred to as *overall adjustment* or *batch approach*. In contrast to such a batch approach, new observations can be considered epochwise as soon as they are acquired. This will result in a recursive parameter estimation[2] approach. This means the parameters requested are updated step-by-step by latest observations available. However, recursive parameter estimation for a GHM does not exist at all.

In general, it is assumed to receive only a well-posed normal equation system to obtain a unique inverse of a regular matrix. Singular entities, e.g., due to datum defects or linear dependencies, are not considered and would require additional special attention.

It should be noted that the different adjustment models partly use the same denominations for the non-linear functions as well as individual vectors and matrices. This multiple use is intended to ensure clarity. However, — if not mentioned otherwise — new variables can be assumed when a new adjustment model is introduced.

2.1.1 Gauss-Markov Model

Unconstrained Gauss-Markov Model

The GMM, also referred to as *adjustment of observations*, represent an *explicit* relation between stochastic observations and unknown deterministic parameters. In general, the non-linear GMM is defined by the $n \times 1$ observation vector $\boldsymbol{l}$ and the $u \times 1$ parameter vector $\boldsymbol{x}$ as

$$\mathbb{E}(\boldsymbol{l}) = \boldsymbol{h}(\boldsymbol{x}), \tag{2.1}$$

or without expected values of the observations and more detailed

$$l_i + v_i = h_i(x_1, x_2, \ldots, x_u). \tag{2.2}$$

The residuals within the vector $\boldsymbol{v}$ are assumed to be Gaussian with expected value $\mathbb{E}(\boldsymbol{v}) = \boldsymbol{0}$

$$\boldsymbol{v} \sim N(\boldsymbol{0}, \boldsymbol{\Sigma}_{ll}) \quad \text{with} \quad \boldsymbol{\Sigma}_{ll} = \sigma_0^2 \cdot \mathbf{Q}_{ll} = \sigma_0^2 \cdot \boldsymbol{P}^{-1}, \tag{2.3}$$

where $\boldsymbol{\Sigma}_{ll}$ is the known positive-definite VCM of the observations, $\mathbf{Q}_{ll}$ the related cofactor matrix, σ_0^2 the a priori variance factor and $\boldsymbol{P}$ the weight matrix. Altogether they describe the weighting of the observations among each other and are referred to as stochastic model. A linear functional model $\boldsymbol{h}(\cdot)$ is required for

---

[2]Also referred to as *sequential parameter estimation* (Niemeier, 2008, pp. 314 ff.)

the adjustment. Linearisation of Equation (2.2) can be performed for non-linear models by Taylor series expansion up to the linear segment, which leads to the matrix form

$$l + v = \underbrace{h(x_0)}_{l_0} + A \cdot \underbrace{(x - x_0)}_{\Delta x} \quad \text{with} \quad A = \nabla_x\, h(x)\Big|_{x=x_0} \tag{2.4a}$$

$$= l_0 + A \cdot \Delta x \qquad\qquad \text{with} \quad \Delta l = l - l_0. \tag{2.4b}$$

The design matrix A is assumed to be of full rank and the partial derivatives are evaluated at the initial parameters x_0. It should be noted that in the following process only the parameter vector x is used instead of the reduced parameter vector Δx. Therefore, the necessary updating must still be taken into account. The same applies to the reduced observation vector Δl and the initial observations l_0. In addition, the estimated values of the individual quantities are only given from the level of the normal equations. Up to this stage, the unknown true values are given. Regardless of this, the linearisation should also apply to the estimated values. To obtain an optimal estimation of the parameters, the residuals of the objective function $L_{\text{GMM}}(x)$ are minimised according to LS estimation (cf. section 2.1). The Gauss-Newton method is used for this purpose, hence

$$L_{\text{GMM}}(x) = v^T \cdot P \cdot v \tag{2.5a}$$

$$= (A \cdot x - l)^T \cdot P \cdot (A \cdot x - l) \tag{2.5b}$$

$$= x^T \cdot A^T \cdot P \cdot A \cdot x - 2 \cdot x^T \cdot A^T \cdot P \cdot l + l^T \cdot P \cdot l \to \min. \tag{2.5c}$$

This is done by setting the partial derivative of the objective function with respect to the optimisation variable x equal to zero (Wichmann, 2007, pp. 106)

$$\nabla_x\, L_{\text{GMM}}(x) = 2 \cdot A^T \cdot P \cdot A \cdot x - 2 \cdot A^T \cdot P \cdot l \stackrel{!}{=} 0. \tag{2.6}$$

This leads to the optimal estimation of the parameters by using LS adjustment (Koch, 1999, pp. 158)

$$\hat{x} = \underbrace{\left(A^T \cdot P \cdot A\right)^{-1}}_{N_{\text{GMM}}} \cdot A^T \cdot P \cdot l, \tag{2.7}$$

where N_{GMM} is the normal equation matrix. The estimated residuals $\hat{v}$ can be obtained by

$$\hat{v} = A \cdot \hat{x} - l \tag{2.8}$$

to receive the adjusted observations $\hat{l}$

$$\hat{l} = l + \hat{v}. \tag{2.9}$$

The cofactor matrix $\mathbf{Q}_{\hat{x}\hat{x}}$ with the co-/variances of the estimated parameters $\hat{x}$ can be obtained by the inverse of the regular normal equation matrix N_{GMM}

$$\mathbf{Q}_{\hat{x}\hat{x}} = N_{\text{GMM}}^{-1} = \left(A^T \cdot P \cdot A\right)^{-1}. \tag{2.10}$$

Taking into account the a posteriori variance factor

$$\hat{\sigma}_0^2 = \frac{\hat{v}^T \cdot P \cdot \hat{v}}{n - u}, \tag{2.11}$$

the estimated VCM $\hat{\Sigma}_{\hat{x}\hat{x}}$ for the estimated parameters results in

$$\hat{\Sigma}_{\hat{x}\hat{x}} = \hat{\sigma}_0^2 \cdot \mathbf{Q}_{\hat{x}\hat{x}}. \tag{2.12}$$

In addition, the following also applies

$$\boldsymbol{\Sigma}_{\hat{\boldsymbol{x}}\hat{\boldsymbol{x}}} = \sigma_0^2 \cdot \mathbf{Q}_{\hat{\boldsymbol{x}}\hat{\boldsymbol{x}}}, \tag{2.13}$$

where the VCM $\boldsymbol{\Sigma}_{\hat{\boldsymbol{x}}\hat{\boldsymbol{x}}}$ refers to the a priori variance factor. This VCM is of interest if the Degrees of Freedom (DoF) of the adjustment task are low or if the estimation cannot be trusted for other reasons. Strict recommendations on when to prefer which VCM do not exist. This depends on the specific task and the present (measurement) configuration. In the context of this thesis appropriate conditions are assumed. For this reason, $\boldsymbol{\Sigma}_{\hat{\boldsymbol{x}}\hat{\boldsymbol{x}}}$ will not be given in the following.

Constrained Gauss-Markov Model

The parameters $\boldsymbol{x}$ might be restricted by s independent non-linear equality constraints

$$\boldsymbol{g}(\boldsymbol{x}) = \boldsymbol{b}, \tag{2.14}$$

with independent real-valued non-linear functional relations $\boldsymbol{g}(\cdot)$ and the related constant $s \times 1$ vector $\boldsymbol{b}$. Similar to the non-linear functional model in Equation (2.2), the non-linear constraint function $\boldsymbol{g}(\cdot)$ needs to be linearised by Taylor expansion. A truncation of the Taylor expansion after the linear term leads to the following substitution

$$\boldsymbol{C} \cdot \boldsymbol{x} = \boldsymbol{d} \quad \text{with} \quad \boldsymbol{C} = \nabla_{\boldsymbol{x}} \boldsymbol{g}(\boldsymbol{x})\Big|_{\boldsymbol{x}=\boldsymbol{x}_0}, \tag{2.15a}$$

$$\boldsymbol{d} = \boldsymbol{b} - \boldsymbol{g}(\boldsymbol{x}_0) + \boldsymbol{C} \cdot \boldsymbol{x}_0, \tag{2.15b}$$

where $\boldsymbol{C}$ is the $u \times s$ matrix of equality constraints and $\boldsymbol{d}$ is the related constant $s \times 1$ vector. Such an extension by constraints can be reasonable in case of suitable prior information regarding mathematical relationships between specific parameters. A common example of using equality constraints is to ensure a normalised normal vector of a plane. To apply such additional information, the objective function in Equation (2.5c) must be extended

$$L_{\text{C-GMM}}(\boldsymbol{x}, \boldsymbol{\lambda}) = L_{\text{GMM}}(\boldsymbol{x}) + 2 \cdot \boldsymbol{\lambda}^T (\boldsymbol{C} \cdot \boldsymbol{x} - \boldsymbol{d}) \to \min \tag{2.16a}$$

$$= \boldsymbol{x}^T \cdot \boldsymbol{A}^T \cdot \boldsymbol{P} \cdot \boldsymbol{A} \cdot \boldsymbol{x} - 2 \cdot \boldsymbol{x}^T \cdot \boldsymbol{A}^T \cdot \boldsymbol{P} \cdot \boldsymbol{l} + \boldsymbol{l}^T \cdot \boldsymbol{P} \cdot \boldsymbol{l}$$
$$+ 2 \cdot \boldsymbol{\lambda}^T (\boldsymbol{C} \cdot \boldsymbol{x} - \boldsymbol{d}) \to \min, \tag{2.16b}$$

with the $s \times 1$ vector $\boldsymbol{\lambda}$ of Lagrangian multipliers. The solution is again achieved through the related partial derivatives of the Lagrangian according to the Gauss-Newton method. These derivatives are set equal to zero with respect to $\boldsymbol{x}$ and $\boldsymbol{\lambda}$ (Koch, 1999, pp. 170 ff.)

$$\nabla_{\boldsymbol{x}} L_{\text{C-GMM}}(\boldsymbol{x}, \boldsymbol{\lambda}) = 2 \cdot \boldsymbol{A}^T \cdot \boldsymbol{P} \cdot \boldsymbol{A} \cdot \boldsymbol{x} - 2 \cdot \boldsymbol{A}^T \cdot \boldsymbol{P} \cdot \boldsymbol{l} + 2 \cdot \boldsymbol{C}^T \cdot \boldsymbol{\lambda} \overset{!}{=} \boldsymbol{0}, \tag{2.17}$$

$$\nabla_{\boldsymbol{\lambda}} L_{\text{C-GMM}}(\boldsymbol{x}, \boldsymbol{\lambda}) = 2 \cdot (\boldsymbol{C} \cdot \boldsymbol{x} - \boldsymbol{d}) \overset{!}{=} \boldsymbol{0}. \tag{2.18}$$

On this basis, Equation (2.7) need to be extended into a block structure

$$\underbrace{\begin{bmatrix} \boldsymbol{A}^T \cdot \boldsymbol{P} \cdot \boldsymbol{A} & \boldsymbol{C}^T \\ \boldsymbol{C} & \boldsymbol{0} \end{bmatrix}}_{N_{\text{C-GMM}}} \begin{bmatrix} \hat{\boldsymbol{x}} \\ \hat{\boldsymbol{\lambda}} \end{bmatrix} = \begin{bmatrix} \boldsymbol{A}^T \cdot \boldsymbol{P} \cdot \boldsymbol{l} \\ \boldsymbol{d} \end{bmatrix}, \tag{2.19}$$

where $N_{\text{C-GMM}}$ is the extended normal equation matrix. As Roese-Koerner (2015, pp. 16) mentioned, Lagrange multipliers do not have a physical unit and often a multiple is used to ensure convenient equations. The linear system of Equation (2.19) has an unique solution if the bordered normal equation matrix $N_{\text{C-GMM}}$ is regular ($N_{\text{C-GMM}}$ need to be of full rank) (Wichmann, 2007, pp. 113). The cofactor matrix $\mathbf{Q}_{\hat{\boldsymbol{x}}\hat{\boldsymbol{x}}}$

with the co-/variances of the estimated parameters $\hat{x}$ can be obtained by the inverse of the normal equation matrix $N_{\text{C-GMM}}$.

The extension with regard to the VCM $\hat{\Sigma}_{\hat{x}\hat{x}}$ results from Equation (2.12), whereby $\hat{\sigma}_0^2$ results under consideration of the s constraints as follows

$$\hat{\sigma}_0^2 = \frac{\hat{v}^T \cdot P \cdot \hat{v}}{s + n - u}. \tag{2.20}$$

Finally, it should be noted that within this Constrained Gauss-Markov Model (C-GMM) only equality and no inequality constraints can be taken into account.

2.1.2 Gauss-Helmert Model

Unconstrained Gauss-Helmert Model

The general case of adjustment becomes applicable, as soon as $n \times 1$ stochastic observations and $u \times 1$ unknown deterministic parameters are strictly interconnected by an arbitrary real-valued function $h(\cdot)$. Such a non-linear *implicit* relation can be formulated by equality constraints

$$h\left(\mathbb{E}(l), x\right) \overset{!}{=} 0, \tag{2.21}$$

or by using residuals instead of the expected values of the observations

$$h_i\left(l_1 + v_1, l_2 + v_2, \ldots, l_n + v_n, x_1, x_2, \ldots, x_u\right) \overset{!}{=} 0, \tag{2.22}$$

To obtain a linear functional model approximate values l_0 and x_0 to both observations and parameters need to be selected carefully for Taylor series expansion (Lenzmann and Lenzmann, 2004). The following applies

$$h(l + v, x) = h(l_0 + \Delta l + v, x_0 + \Delta x) \quad \text{with} \quad \Delta l = l - l_0 \tag{2.23a}$$

$$\approx \underbrace{h(l, x)\big|_{l,x}}_{w_0} + \underbrace{\nabla_l h(l, x)\big|_{l,x}}_{B} \cdot (\Delta l + v) + \underbrace{\nabla_x h(l, x)\big|_{l,x}}_{A} \cdot \Delta x \tag{2.23b}$$

$$= w_0 + B \cdot (\Delta l + v) + A \cdot \Delta x \tag{2.23c}$$

$$= \underbrace{w_0 + B \cdot \Delta l}_{w} + B \cdot v + A \cdot \Delta x \tag{2.23d}$$

$$= B \cdot v + A \cdot \Delta x + w \overset{!}{=} 0, \tag{2.23e}$$

where B is the $q \times n$ condition matrix with partial derivatives of the q condition equations with respect to the observation vector l, and w refers to the $q \times 1$ vector of contradictions. According to Lenzmann and Lenzmann (2004), note that the partial derivatives are evaluated at the location[3] of

$$l = l_0 + v, \tag{2.24}$$

$$x = x_0 + \Delta x, \tag{2.25}$$

where the residuals v and the reduced parameter vector Δx will continuously change during the estimation. To obtain an estimate for l, v, x and Δl minimising of the objective function $L_{\text{GHM}}(v, \Delta x, \lambda)$ with respect to LS estimation (cf. section 2.1) can be performed by Lagrangian multipliers

$$L_{\text{GHM}}(v, \Delta x, \lambda) = v^T \cdot P \cdot v - 2 \cdot \lambda^T (B \cdot v + A \cdot \Delta x + w) \to \min. \tag{2.26}$$

---

[3]Also referred to as *development point*

Setting the related partial derivatives with respect to v, Δx and λ equal to zero

$$\nabla_v \, L_{\mathrm{GHM}} \left(v, \Delta x, \lambda \right) = 2 \cdot P \cdot v - 2 \cdot B^T \cdot \lambda \overset{!}{=} 0 \qquad \Leftrightarrow \qquad v = P^{-1} B^T \cdot \lambda, \tag{2.27}$$

$$\nabla_{\Delta x} \, L_{\mathrm{GHM}} \left(v, \Delta x, \lambda \right) = -2 \cdot A^T \cdot \lambda \overset{!}{=} 0 \qquad \Leftrightarrow \qquad A^T \cdot \lambda = 0, \tag{2.28}$$

$$\nabla_\lambda \, L_{\mathrm{GHM}} \left(v, \Delta x, \lambda \right) = -2 \cdot \left(B \cdot v + A \cdot \Delta x + w \right) \overset{!}{=} 0 \quad \Leftrightarrow \quad B \cdot v + A \cdot \Delta x + w = 0, \tag{2.29}$$

leads to the solution of the restricted minimisation problem by the linear normal equation system in block structure

$$\underbrace{\begin{bmatrix} B \cdot P^{-1} \cdot B^T & A \\ A^T & 0 \end{bmatrix}}_{N_{\mathrm{GHM}}} \begin{bmatrix} \hat{\lambda} \\ \Delta \hat{x} \end{bmatrix} = \begin{bmatrix} -w \\ 0 \end{bmatrix}. \tag{2.30}$$

Depending on the selection of reasonable approximate values for l_0 and x_0, several iterations for repeated linearisation are required to obtain accurate estimates for the unknown parameters. Assuming that the inverse of N_{GHM} exist, the estimates for each iteration are

$$Q_{bb} = B \cdot P^{-1} \cdot B^T, \tag{2.31}$$

$$\hat{k} = Q_{bb}^{-1} \left(\mathbf{I} - A \cdot \left(A^T \cdot Q_{bb}^{-1} \cdot A \right)^{-1} \cdot A^T \cdot Q_{bb}^{-1} \right) \cdot \left(-w \right), \tag{2.32}$$

$$\hat{v} = Q_{ll} \cdot B^T \cdot \hat{k}, \tag{2.33}$$

$$\hat{l} = l_0 + \hat{v}, \tag{2.34}$$

as well as

$$\Delta \hat{x} = \left(A^T \cdot Q_{bb}^{-1} \cdot A \right)^{-1} \cdot A^T \cdot Q_{bb}^{-1} \cdot \left(-w \right), \tag{2.35a}$$

$$\hat{x} = x_0 + \Delta \hat{x}. \tag{2.35b}$$

The cofactor matrix $\mathbf{Q}_{\hat{x}\hat{x}}$ with the co-/variances of the estimated parameters $\hat{x}$ can be derived either by inverting the entire regular normal equation matrix N_{GHM}

$$N_{\mathrm{GHM}}^{-1} = \begin{bmatrix} \mathbf{Q}_{\hat{k}\hat{k}} & \mathbf{Q}_{\hat{k}\hat{x}} \\ \mathbf{Q}_{\hat{k}\hat{x}}^T & -\mathbf{Q}_{\hat{x}\hat{x}} \end{bmatrix}, \tag{2.36}$$

or by applying the law of error propagation[4] to the estimated parameters in Equation (2.35a), which leads to

$$\mathbf{Q}_{\hat{x}\hat{x}} = \left(A^T \cdot Q_{bb}^{-1} \cdot A \right)^{-1}. \tag{2.37}$$

Also here the extension results to the a posteriori VCM $\hat{\Sigma}_{\hat{x}\hat{x}}$ according to Equations (2.11) and (2.12). Again, the a priori VCM $\Sigma_{\hat{x}\hat{x}}$ can be obtained according to Equation (2.13), whereby the same applies with regard to its use as for GMM.

Constrained Gauss-Helmert Model

Similar to the C-GMM, the parameters x of the GHM might be also restricted by s independent non-linear equality constraints

$$g \left(x \right) = b, \tag{2.38}$$

---

[4]Also referred to as *propagation of uncertainty*

which can be transformed according to Equation (2.15) into linear constraints

$$C \cdot x = d. \tag{2.39}$$

According to (Roese-Koerner, 2015, pp. 19 ff.) the parameter vector x needs to be divided into the approximation value x_0 and the reduced parameter vector Δx, which leads to

$$C\,(x_0 + \Delta x) = d^* \tag{2.40a}$$
$$C \cdot \Delta x = d^* - C \cdot x_0 =: d. \tag{2.40b}$$

The consideration of suitable prior information for a Constrained Gauss-Helmert Model (C-GHM) makes it necessary to extend the objective function in Equation (2.26) to

$$L_{\text{C-GHM}}\,(v, \Delta x, \lambda_1, \lambda_2) = L_{\text{GHM}}\,(v, \Delta x, \lambda) - 2 \cdot \lambda_2^T\,(C \cdot \Delta x - d) \to \min \tag{2.41a}$$

$$\begin{aligned} &= v^T \cdot P \cdot v - 2 \cdot \lambda_1^T\,(B \cdot v + A \cdot \Delta x + w) \\ &\quad - 2 \cdot \lambda_2^T\,(C \cdot \Delta x - d) \to \min. \end{aligned} \tag{2.41b}$$

As in the unconstrained GHM, the related partial derivatives with respect to $v, \Delta x, \lambda_1$ and λ_2 of the Lagrangian are set equal to zero

$$\nabla_v\,L_{\text{C-GHM}}\,(v, \Delta x, \lambda_1, \lambda_2) = 2 \cdot P \cdot v - 2 \cdot B^T \cdot \lambda_1 \overset{!}{=} 0$$
$$\Leftrightarrow \quad v = P^{-1} B^T \cdot \lambda_1, \tag{2.42}$$

$$\nabla_{\Delta x}\,L_{\text{C-GHM}}\,(v, \Delta x, \lambda_1, \lambda_2) = -2 \cdot A^T \cdot \lambda_1 - 2 \cdot C^T \cdot \lambda_2 \overset{!}{=} 0$$
$$\Leftrightarrow \quad A^T \cdot \lambda_1 + C^T \cdot \lambda_2 = 0, \tag{2.43}$$

$$\nabla_{\lambda_1}\,L_{\text{C-GHM}}\,(v, \Delta x, \lambda_1, \lambda_2) = -2 \cdot (B \cdot v + A \cdot \Delta x + w) \overset{!}{=} 0$$
$$\Leftrightarrow \quad B \cdot v + A \cdot \Delta x + w = 0, \tag{2.44}$$

$$\nabla_{\lambda_2}\,L_{\text{C-GHM}}\,(v, \Delta x, \lambda_1, \lambda_2) = -\,(C \cdot \Delta x - d) \overset{!}{=} 0$$
$$\Leftrightarrow \quad C \cdot \Delta x = d, \tag{2.45}$$

leads to the solution of the constrained minimisation problem by the linear normal equation system in block structure

$$\underbrace{\begin{bmatrix} B \cdot P^{-1} \cdot B^T & A & 0 \\ A^T & 0 & C^T \\ 0 & C & 0 \end{bmatrix}}_{N_{\text{C-GHM}}} \begin{bmatrix} \hat{\lambda}_1 \\ \Delta\hat{x} \\ \hat{\lambda}_2 \end{bmatrix} = \begin{bmatrix} -w \\ 0 \\ d \end{bmatrix}. \tag{2.46}$$

Again, several iterations for repeated linearisation are required and the cofactor matrix $\mathbf{Q}_{\hat{x}\hat{x}}$ can be derived by inverting the regular normal equation matrix $N_{\text{C-GHM}}$

$$N_{\text{C-GHM}}^{-1} = \begin{bmatrix} \mathbf{Q}_{\hat{k}_1\hat{k}_1} & \mathbf{Q}_{\hat{k}_1\hat{x}} & \mathbf{Q}_{\hat{k}_1\hat{k}_2} \\ \mathbf{Q}_{\hat{k}_1\hat{x}}^T & -\mathbf{Q}_{\hat{x}\hat{x}} & \mathbf{Q}_{\hat{x}\hat{k}_2} \\ \mathbf{Q}_{\hat{k}_1\hat{k}_2}^T & \mathbf{Q}_{\hat{x}\hat{k}_2}^T & -\mathbf{Q}_{\hat{k}_2\hat{k}_2} \end{bmatrix}. \tag{2.47}$$

By substitution and transformation of Equations (2.42) and (2.43) the corresponding residuals read

$$\hat{v} = -P^{-1} \cdot B^T\,\left(B \cdot P^{-1} \cdot B^T\right)^{-1} \cdot (A \cdot \Delta\hat{x} + w)\,, \tag{2.48}$$

with which the estimated VCM $\hat{\Sigma}_{\hat{x}\hat{x}}$ for the estimated parameters $\hat{x}$ can be obtained according to Equations (2.12) and (2.20).

Again, as for the C-GMM, only equality constraints and not inequalities can be considered. Arbitrary inequality constraints would lead to a more complex optimisation problem. A solution to this problem was introduced in Roese-Koerner (2015, pp. 77 ff.). Since inequalities are very helpful and occur in several applications, this is a useful, albeit more complex, possibility to consider them.

Transformation of a Gauss-Helmert Model into a Gauss-Markov Model

Note that the estimation of the parameters requested of a GHM in Equation (2.35) has a similar structure to the GMM in Equation (2.7) (Jäger et al., 2005, pp. 163 ff.; Dang, 2007, pp. 69). This can be utilized to transform a non-linear GHM into an equivalent GMM. This transformation is required if recursive parameter estimation is to be applied and leads to

$$\tilde{l} + \tilde{v} = \tilde{A} \cdot \tilde{x} \quad \text{with} \quad \tilde{v} \sim N\left(\mathbf{0}, \Sigma_{\tilde{l}\tilde{l}}\right), \tag{2.49}$$

taking into consideration the substitutions

$$\tilde{l} := -w_0 - B \cdot \Delta l = -w, \tag{2.50}$$
$$\tilde{v} := -B \cdot v, \tag{2.51}$$
$$\tilde{A} := \nabla_x\, h\,(l,x)\big|_{l=l_0+v,x=x_0+\Delta x}, \tag{2.52}$$
$$\tilde{x} := \Delta x, \tag{2.53}$$
$$\Sigma_{\tilde{l}\tilde{l}} := B \cdot \Sigma_{ll} \cdot B^T. \tag{2.54}$$

Note that the tilde symbol indicates the transformed quantities. Furthermore, this transformation is also used for the Kalman filter approach with implicit measurement equations (cf. section 2.2.2).

2.1.3 Recursive Parameter Estimation

In case of vast quantities of observations and self-contained epochs, a batch algorithm might be computationally expensive. For this reason, recursive estimation on an epochwise basis can be a suitable option and has already been studied by Plackett (1950); Kalman and Bucy (1961). Therefore, the parameters requested are updated continuously when a new measurement epoch is available. This offers the advantage to just consider new observations for the parameter update, instead of re-adjustment of the whole data set.

Consideration of the additional observation vector l_e with n_e new observations requires an extension of the initial GMM given by Equations (2.3) and (2.4b) (Niemeier, 2008, pp. 314 ff.)

$$\Sigma_{ll,e} = \sigma_0^2 \cdot \mathbf{Q}_{ll,e} = \sigma_0^2 \cdot \begin{bmatrix} \mathbf{Q}_{ll} & \mathbf{0} \\ \mathbf{0} & \mathbf{Q}_{ee} \end{bmatrix} = \sigma_0^2 \cdot \begin{bmatrix} P^{-1} & \mathbf{0} \\ \mathbf{0} & P_{ee}^{-1} \end{bmatrix}, \tag{2.55}$$

$$\begin{bmatrix} l \\ l_e \end{bmatrix} + \begin{bmatrix} v \\ v_e \end{bmatrix} = \begin{bmatrix} A \\ A_e \end{bmatrix} \cdot x_e. \tag{2.56}$$

As a result the normal equation matrix N_e and the related parameter vector $\hat{x}_e$ are given recursively by

$$N_e = \underbrace{A^T \cdot P \cdot A}_{N_{\text{GMM}}} + A_e^T \cdot P_{ee} \cdot A_e, \tag{2.57}$$

$$\hat{x}_e = N_e^{-1} \cdot \left(A^T \cdot P \cdot l + A_e^T \cdot P_{ee} \cdot l_e\right). \tag{2.58}$$

Again, the cofactor matrix $\mathbf{Q}_{\hat{x}\hat{x},e}$ can be obtained by the inverse of the regular normal equation matrix N_e.

However, this recursive parameter estimation is usually only used if the parameters requested have already been estimated by a pre-existing dataset of observations (e.g., cyclic measurements for a geodetic monitoring network). Consideration of multiple new epochs is usually not within the scope of this approach. Moreover, such a recursive procedure does not exist for a GHM.

2.2 Recursive State-space Filtering

Parameter estimation is a useful method to receive an optimal estimate for freely definable parameters which have a unique relationship to arbitrary observations. In general, the parameters requested are obtained by a batch approach as a whole or by recursive estimation as soon as epochs of new observations are available (cf. section 2.1). However, those approaches are suitable as long as the true parameters are temporally constant during data acquisition. Changes (e.g., the position parameters of a moving vehicle) are not intended and would cause several problems.

In contrast, recursive state-space filters are meant for such changeable applications. The difference to parameter estimation consists in the fact that besides already used measuring information, additional system information is considered. Furthermore, the parameter vector is no longer deterministic but becomes probabilistic. This enables the possibility to take into account suitable physical models which describe the temporal and spatial dynamics of the state parameters requested mathematically. Thus, both measurements and physical properties are considered within a recursive estimation approach. The linear Kalman Filter (KF) provides the optimal estimation for this problem and was proposed by Kalman (1960). In this context, an optimal estimate implies that it is unbiased and has a minimal variance (Simon, 2006, pp. 84 ff.). However, these optimality properties only apply as long as Gaussian noise — for both the measurements and for the physical system — and linear relationships exist.

The time-discrete KF is a recursive two-step procedure. For a theoretically unlimited number of $k = 1 \dots K$ epochs the state parameters are predicted by a suitable process model $\boldsymbol{f}(\cdot)$ and updated by an appropriate measurement model $\boldsymbol{h}(\cdot)$ subsequently. Both are arbitrary real-valued functions. To be also applicable for non-linear relationships (for both system model and measurement model), Taylor series expansion within the so-called Extended Kalman Filter (EKF) is possible. Since non-linearities comprise the majority of applications, only this more complex case is referred to. However, the linearisation causes the KF to lose its optimality. Instead, an approximation is carried out. These KFs are also of importance in geodesy and are used, for example, to estimate the position and orientation of various multi-sensor systems (Sternberg, 2000; Vennegeerts, 2011; Paffenholz, 2012; Schlichting, 2018; Zwiener, 2019).

During the prediction step, selected physical relationships (e.g., motion models) are applied to the previous state parameters $\boldsymbol{x}_{k-1}$ from the last past epoch. Further influencing factors like zero-mean process noise $\boldsymbol{w}_k$ with VCM $\Sigma_{ww,k}$ and controls $\boldsymbol{u}_k$ are also taken into account at this stage. During the subsequent update step, the forecasted state parameters are corrected by the latest set of sensor observations $\boldsymbol{l}_k$. Known zero-mean measurement noise $\boldsymbol{v}_k$ with VCM $\Sigma_{ll,k}$ must also be taken into account here. Thus, this non-linear discrete model can be assumed according to Simon (2006, pp. 407) as follows

$$\boldsymbol{x}_k = \boldsymbol{f}\left(\boldsymbol{x}_{k-1}, \boldsymbol{u}_{k-1}, \boldsymbol{w}_{k-1}\right), \tag{2.59}$$

$$\boldsymbol{l}_k + \boldsymbol{v}_k = \boldsymbol{h}\left(\boldsymbol{x}_k\right), \tag{2.60}$$

$$\boldsymbol{w}_k \sim N\left(\boldsymbol{0}, \Sigma_{ww,k}\right), \tag{2.61}$$

$$\boldsymbol{v}_k \sim N\left(\boldsymbol{0}, \Sigma_{ll,k}\right). \tag{2.62}$$

To distinguish between the predicted and updated state parameters, $\boldsymbol{x}_k^-$ denotes the a priori estimate and $\boldsymbol{x}_k^+$ the a posteriori estimate of the state vector. The same applies to related VCMs for the predicted states $\Sigma_{xx,k}^-$ and for the updated states $\Sigma_{xx,k}^+$, respectively.

In general, the process noise is Gaussian and describe the uncertainty and imperfections of the physical model. The same applies to the measurement noise concerning the related measurement model. Furthermore, there are also possibilities to consider noise with non-Gaussian distributions (e.g., by a probabilistic Particle Filter (PF)). Beyond that, there is a multitude of several linear and non-linear filters (e.g., Unscented Kalman Filter (UKF), Ensemble Kalman Filter (EnKF)). For a detailed compilation with full derivations the reader is referred to, e.g., Kalman (1960); Jazwinski (1970); Gelb (1974); Bar-Shalom et al. (2001); Thrun et al. (2005); Simon (2006).

In principle, all these different realisations of filters can be described with Bayesian sequential estimation. It is assumed that, taking into account all available observations $\boldsymbol{L}_k = \{\boldsymbol{l}_1, \dots, \boldsymbol{l}_k\}$ up to epoch k, the

a posteriori Probability Density Function (PDF) $p(\boldsymbol{x}_k|\boldsymbol{L}_k)$ of the system state $\boldsymbol{x}_k$ can be approximated. According to Thrun et al. (2005, pp. 31 ff.) and Simon (2006, pp. 462 ff.), this conditional density can be determined by using the Bayes' theorem. This generally represents the update step introduced above and the following applies:

$$p(\boldsymbol{x}_k|\boldsymbol{L}_k) = \frac{p(\boldsymbol{l}_k|\boldsymbol{x}_k)\, p(\boldsymbol{x}_k|\boldsymbol{L}_{k-1})}{p(\boldsymbol{l}_k|\boldsymbol{L}_{k-1})}, \tag{2.63}$$

where the a posteriori PDF $p(\boldsymbol{x}_k|\boldsymbol{L}_k)$ is obtained by convolution of the likelihood PDF $p(\boldsymbol{l}_k|\boldsymbol{x}_k)$ and the a priori PDF $p(\boldsymbol{x}_k|\boldsymbol{L}_{k-1})$. Furthermore, the evidence PDF $p(\boldsymbol{l}_k|\boldsymbol{L}_{k-1})$ is used for normalisation, but is usually neglected. The a priori density corresponds to the classical prediction step and can be obtained by the solution of the Chapman-Kolmogorov integral

$$p(\boldsymbol{x}_k|\boldsymbol{L}_{k-1}) = \int p(\boldsymbol{x}_k|\boldsymbol{x}_{k-1})\, p(\boldsymbol{x}_{k-1}|\boldsymbol{L}_{k-1})\, d\boldsymbol{x}_{k-1}. \tag{2.64}$$

Here, $p(\boldsymbol{x}_{k-1}|\boldsymbol{L}_{k-1})$ describes the a posteriori PDF from the last past epoch $k-1$. For the first prediction step, an assumption for this PDF is made by $p(\boldsymbol{x}_0)$ as part of the initialisation. Furthermore, the transition PDF $p(\boldsymbol{x}_k|\boldsymbol{x}_{k-1})$ results from the non-linear system model (cf. Equation (2.59)) and the PDF of the corresponding process noise $\boldsymbol{w}_k$ (cf. Equation (2.61)). It thus describes the system model and indicates the transition probability from the last known state to the current state. This is also how the likelihood PDF $p(\boldsymbol{l}_k|\boldsymbol{x}_k)$ from Equation (2.63) is defined. The non-linear measurement model (cf. Equation (2.60)) and the associated measurement noise (cf. Equation (2.62)) are used for this purpose. In this way the current observations $\boldsymbol{l}_k$ are considered in the update step (cf. Equation (2.63)) and the a priori PDF $p(\boldsymbol{x}_k|\boldsymbol{L}_{k-1})$ is corrected. Based on the knowledge of the a posteriori PDF, an estimate of the state vector can be done. Different estimators can be selected for this (Candy, 2016, pp. 38 ff.). The mean value of the a posteriori PDF is typically determined by an estimate of the Minimum Mean Square Error (MMSE) according to

$$\hat{\boldsymbol{x}}_k^{\mathrm{MMSE}} = \mathbb{E}\left(\boldsymbol{x}_k|\boldsymbol{L}_k\right) = \int \boldsymbol{x}_k \cdot p(\boldsymbol{x}_k|\boldsymbol{L}_k)\, d\boldsymbol{x}_k. \tag{2.65}$$

Another estimate can be obtained by the Maximum a Posteriori Probability (MAP) approach, where

$$\hat{\boldsymbol{x}}_k^{\mathrm{MAP}} = \arg\max_{\boldsymbol{x}_k} p(\boldsymbol{x}_k|\boldsymbol{L}_k). \tag{2.66}$$

For other estimates, see Koch (2000). Similarly, the variance over the second central moment can also be determined. In general, this recursive estimate, which is also referred to as a Bayesian filter, represents an optimal solution. However, the Chapman-Kolmogorov integral in Equation (2.64) can only be solved numerically if linear models with Gaussian noise are available[5]. In addition, the consideration of all previous observations leads to numerical problems (Candy, 2016, pp. 39 ff.). The latter challenge can be countered by applying a first-order Markov chain. As a result, not all available observations $\boldsymbol{L}_k$ are taken into account, instead only the observations of the last past epoch[6] $\boldsymbol{L}_k = \{\boldsymbol{l}_{k-1}, \boldsymbol{l}_k\}$. To address non-linear models with non-Gaussian noise, approximative filter techniques must be applied (Simon, 2006, pp. 465 ff.). If at least Gaussian noise is present, the already mentioned EKF can be applied.

However, the literature has so far dealt almost exclusively with explicit relationships between measurements and states (cf. Equation (2.60)) in the context of the filters mentioned. Such a model can be referred to as a GMM from section 2.1.1. Implicit relations (related to a GHM from section 2.1.2) are only mentioned by a few researchers (Soatto et al., 1994; Steffen and Beder, 2007; Dang, 2007, 2008; Petersen and Koch, 2010; Ettlinger et al., 2018; Vogel et al., 2018, 2019; Garcia-Fernandez et al., 2019). This situation is in contrast to a multitude of applications that are based on implicit relationships. These are mainly geometric entities (Heuel, 2001; Perwass et al., 2005). While, for example, an UKF can also deal with non-linear equations by approximating the PDF, only in Ning et al. (2017) an approach is shown which considers implicit measurement equations. So far, this is based exclusively on simulated data. The

---

[5]This special case describes the time-discrete linear KF.
[6]Also referred to as Markov assumption

presented general Bayesian filter is not analytically solvable if implicit measurement equations are to be considered and therefore does not yet exist in this form. For this reason, the framework of explicit and implicit models is introduced in detail by an Iterated Extended Kalman Filter (IEKF) subsequently.

2.2.1 Iterated Extended Kalman Filter for Gauss-Markov Models

The IEKF is an additional advancement of the EKF for non-linear equations and was initially proposed by Denham and Pines (1966). The only difference between the two approaches is a repeated linearisation during the update step. Here, the IEKF execute several additional iterations to correct the development point of the first-order linearisation within each iteration. This is less computationally complex than performing Taylor series expansion of higher orders Simon (2006, pp. 417 ff.). Highly non-linear equations are therefore controllable. In the IEKF algorithm described below, the equations are not derived. A detailed derivation can be found in Simon (2006, pp. 407 ff.).

Initialisation

As with all filters in general, the IEKF requires initialisation. Therefore the initialised $u \times 1$ state vector estimate $\hat{x}_{k=0}^{+}$ and corresponding $u \times u$ VCM $\Sigma_{\hat{x}\hat{x},k=0}^{+}$ is given by

$$\hat{x}_{k=0}^{+} = x_0, \tag{2.67}$$

$$\Sigma_{\hat{x}\hat{x},k=0}^{+} = \Sigma_{xx,0}. \tag{2.68}$$

Prediction Step

By first-order Taylor series expansion of the system model (cf. Equation (2.59)), the Jacobian matrices for the state transition Φ_{k-1} and the noise matrix G_{k-1} can be obtained

$$\Phi_{k-1} = \nabla_x f(x)\Big|_{\hat{x}_{k-1}^{+}, u_{k-1}, w_{k-1}}, \tag{2.69}$$

$$G_{k-1} = \nabla_w f(x)\Big|_{\hat{x}_{k-1}^{+}, u_{k-1}, w_{k-1}}. \tag{2.70}$$

Quite often, however, the noise matrix G_{k-1} can be omitted. In general, the following applies for the predicted state vector estimate $\hat{x}_k^{-}$ with associated VCM matrix $\Sigma_{\hat{x}\hat{x},k}^{-}$

$$\hat{x}_k^{-} = f\left(\hat{x}_{k-1}^{+}, u_{k-1}, 0\right), \tag{2.71}$$

$$\Sigma_{\hat{x}\hat{x},k}^{-} = \Phi_{k-1} \cdot \Sigma_{\hat{x}\hat{x},k-1}^{+} \cdot \Phi_{k-1}^{T} + G_{k-1} \cdot \Sigma_{ww,k-1} \cdot G_{k-1}^{T}. \tag{2.72}$$

Update Step

The explicit relationship between observations and states is given by the measurement model (cf. Equation (2.60)), where l_k is the $n \times 1$ observation vector. Since non-linearities can usually occur here as well, the linearisation should also be carried out here by a first-order Taylor series expansion. As already mentioned, it is the special characteristic of the IEKF to perform additional iterations during the update step. For this reason, in addition to the epoch-index k, an additional index m is introduced with regard to the current iteration run.

After initialisation for the iterative parameters and observations by

$$\hat{x}_{k,m=0}^+ = \hat{x}_k^-, \tag{2.73}$$

$$l_{k,m=0} = l_k, \tag{2.74}$$

$$v_{k,m=0} = v_k \tag{2.75}$$

it follows for $m = 0, \ldots, M - 1$ with the maximum number of iterations M

$$\mathbf{A}_{k,m} = \nabla_x \, h \left(\hat{x}_{k,m}^+ \right) \Big|_{\hat{x}_{k,m}^+, l_{k,m}, v_{k,m}}, \tag{2.76}$$

$$\mathbf{M}_{k,m} = \nabla_v \, h \left(\hat{x}_{k,m}^+ \right) \Big|_{\hat{x}_{k,m}^+, l_{k,m}, v_{k,m}}, \tag{2.77}$$

$$\mathbf{K}_{k,m} = \Sigma_{\hat{x}\hat{x},k}^- \cdot \mathbf{A}_{k,m}^T \cdot \left(\mathbf{A}_{k,m} \cdot \Sigma_{\hat{x}\hat{x},k}^- \cdot \mathbf{A}_{k,m}^T + \mathbf{M}_{k,m} \cdot \Sigma_{ll,k} \cdot \mathbf{M}_{k,m}^T \right)^{-1}, \tag{2.78}$$

$$\hat{x}_{k,m+1}^+ = \hat{x}_k^- + \mathbf{K}_{k,m} \cdot \left(l_k - h \left(\hat{x}_{k,m}^+ \right) - \mathbf{A}_{k,m} \cdot \left(\hat{x}_k^- - \hat{x}_{k,m}^+ \right) \right), \tag{2.79}$$

$$\Sigma_{\hat{x}\hat{x},k,m+1}^+ = \left(\mathbf{I} - \mathbf{K}_{k,m} \cdot \mathbf{A}_{k,m} \right) \cdot \Sigma_{\hat{x}\hat{x},k}^-. \tag{2.80}$$

Here, $\hat{x}_{k,m}^+$ is the stepwise updated state vector and $\Sigma_{\hat{x}\hat{x},k,m}^+$ the associated VCM. The estimation of the updated states is influenced by the so-called Kalman matrix $\mathbf{K}_{k,m}$. This matrix provides for the weighting between predicted states $\hat{x}_k^-$ and current observations l_k at each epoch. Again, quite often, the Jacobian matrix $\mathbf{M}_{k,m}$ related to the residuals $v_{k,m}$ is usually not taken into account. The final a-posteriori state estimate and associated VCM are than

$$\hat{x}_k^+ = \hat{x}_{k,M}^+, \tag{2.81}$$

$$\Sigma_{\hat{x}\hat{x},k}^+ = \Sigma_{\hat{x}\hat{x},k,M}^+. \tag{2.82}$$

The general process of the individual filter steps is shown in Figure 2.1 with its relevant estimates. Note that for $M = 0$ the IEKF reduces to the standard EKF without additional iterations. There is theoretically no limit to the maximum number of iterations M within the IEKF. In practice, a maximum number of iterations is usually specified. Alternatively, this can also be provided with an abort criterion. A possible threshold value, which must be reached below, can be for example the absolute change between two consecutive epochs. Studies show, however, that in practice, often already one or two additional iterations are sufficient (Krebs, 1980, pp. 194). Further iterations, therefore, do not necessarily lead to further improvements. Regardless of this, a larger number of iterations would also be inefficient from a computational point of view.

In principle, it is also possible to perform an improved linearisation during the prediction step[7] (cf. Equation (2.71)). In practice, however, this is rarely used and only required for highly non-linear system (Krebs, 1980, pp. 188). In addition, the focus will be on the measurement model in the further chapters, which is why more details can be found directly in Jazwinski (1970, pp. 279 ff.).
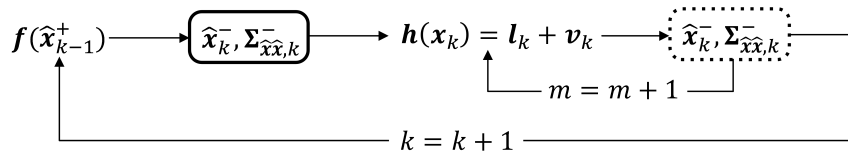
Figure 2.1: *Flowchart of the IEKF for explicit measurement equations with predicted (solid box) and updated states (dotted box)*

---

[7]In Jazwinski (1970, pp. 280) this is called the *Iterated Linear Filter-Smoother*

2.2.2 Iterated Extended Kalman Filter for Gauss-Helmert Models

The basic principle of the IEKF was already introduced in the previous section 2.2.1. However, it is limited exclusively to explicit relationships between state parameters and observations within the measurement model $h(\cdot)$ (cf. Equation (2.60)). In this section, therefore, a possibility is presented that allows implicit relationships to be taken into account. Thus greater flexibility can be guaranteed regarding different applications. The main idea of the transfer towards implicit measurement models is based on Dang (2007, 2008). His approach is again based on the transformation of a linear GHM into a linear GMM according to transformation rule from Equations (2.50) – (2.54).

Compared to the IEKF for GMM, the basic procedure regarding prediction step and update step remains the same. Therefore, only the update step is affected by the introduction of an implicit model. The measurement model from Equation (2.60) therefore results in

$$h\left(l_k + v_k, x_k\right) = 0, \tag{2.83}$$

where the states and observations are inseparable. However, the other assumptions of Equations (2.59), (2.61) and (2.62) remain. At this point, note that in addition to the filtered states x_k^+, filtered observations l_k^+ are now also estimated. Here, Equation (2.83) is an auxiliary condition of the LS problem definition

$$\begin{pmatrix} l_k^+ - l_k \\ x_k^+ - x_k^- \end{pmatrix}^T \begin{bmatrix} \Sigma_{ll,k} & 0 \\ 0 & \Sigma_{xx,k}^- \end{bmatrix}^{-1} \begin{pmatrix} l_k^+ - l_k \\ x_k^+ - x_k^- \end{pmatrix} \to \min. \tag{2.84}$$

To perform linearisation of Equation (2.83) the Taylor series expansion according to Equation (2.23) leads to

$$h\left(l_k + v_k, x_k\right) \approx \underbrace{-\nabla_x h\left(\cdot\right)\big|_{\check{l},\check{x}}}_{A_k} \left(x_k^+ - \check{x}_k\right) + \underbrace{\nabla_l h\left(\cdot\right)\big|_{\check{l},\check{x}}}_{B_k} \left(l_k^+ - \check{l}_k\right) + h\left(\check{l}_k, \check{x}_k\right) \tag{2.85a}$$

$$= A_k \cdot x_k^+ + B_k \cdot l_k^+ + \underbrace{h\left(\check{l}_k, \check{x}_k\right) - A_k \cdot \check{x}_k - B_k \cdot \check{l}_k}_{w_k} \tag{2.85b}$$

$$= A_k \cdot x_k^+ + B_k \cdot l_k^+ + w_k \overset{!}{=} 0, \tag{2.85c}$$

where $\check{x}_k$ and $\check{l}_k$ are corresponding development points of the first-order linearisation. Similar to Equation (2.26), an objective function can also be set up here by using Lagrangian multipliers. This must be minimised. The objective function L_{IEKF} can be set up by LS (cf. Equation (2.84)) and the auxiliary condition in Equation (2.85) which leads to

$$\begin{aligned} L_{\text{IEKF}} = &\begin{pmatrix} l_k^+ - l_k \\ x_k^+ - x_k^- \end{pmatrix}^T \begin{bmatrix} \Sigma_{ll,k} & 0 \\ 0 & \Sigma_{xx,k}^- \end{bmatrix}^{-1} \begin{pmatrix} l_k^+ - l_k \\ x_k^+ - x_k^- \end{pmatrix} \\ &- 2 \cdot \lambda_k^T \cdot \left(A_k \cdot x_k^+ + B_k \cdot l_k^+ + w_k\right) \to \min, \end{aligned} \tag{2.86}$$

where λ is the Lagrangian multiplier. Setting the related partial derivatives with respect to x_k^+, l_k^+ and λ_k of the Lagrangian equal to zero

$$\begin{aligned} \nabla_{x_k^+} L_{\text{IEKF}} &= 2 \cdot \left(x_k^+ - x_k^-\right)^T \cdot \left(\Sigma_{xx,k}^-\right)^{-1} - 2 \cdot \lambda_k^T \cdot A_k \overset{!}{=} 0 \\ &\Leftrightarrow x_k^+ = x_k^- + \Sigma_{xx,k}^- \cdot A_k^T \cdot \lambda_k, \end{aligned} \tag{2.87}$$

$$\begin{aligned} \nabla_{l_k^+} L_{\text{IEKF}} &= 2 \cdot \left(l_k^+ - l_k\right)^T \cdot \left(\Sigma_{ll,k}\right)^{-1} - 2 \cdot \lambda_k^T \cdot B_k \overset{!}{=} 0 \\ &\Leftrightarrow l_k^+ = l_k + \Sigma_{ll,k} \cdot B_k^T \cdot \lambda_k, \end{aligned} \tag{2.88}$$

$$\nabla_\lambda L_{\text{IEKF}} = A_k \cdot x_k^+ + B_k \cdot l_k^+ + w_k \overset{!}{=} 0, \tag{2.89}$$

leads to the linear normal equation system N_{IEKF} in block structure

$$
\underbrace{\begin{bmatrix} -\mathbf{I} & \mathbf{0} & \Sigma_{\hat{x}\hat{x},k}^{-} \cdot A_k^T \\ \mathbf{0} & -\mathbf{I} & \Sigma_{ll,k} \cdot B_k^T \\ A_k & B_k & \mathbf{0} \end{bmatrix}}_{N_{\text{IEKF}}} \begin{bmatrix} \hat{x}_k^+ \\ \hat{l}_k^+ \\ \hat{\lambda}_k \end{bmatrix} = \begin{bmatrix} -\hat{x}_k^- \\ -l_k \\ -w_k \end{bmatrix}. \tag{2.90}
$$

Comparable with the solution of GHM in batch processing (cf. Equation (2.30)), the filtered states $\hat{x}_k^+$ and observations $\hat{l}_k^+$ can be obtained by the inverse of the normal equation system N_{IEKF}. For the first iteration run $m = 0$ of the update step, the development points $\check{x}_{k,m=0}$ and $\check{l}_{k,m=0}$ should be selected by the predicted state estimates $\hat{x}_k^-$ and currently available observations l_k

$$
\check{x}_{k,m=0} = \hat{x}_k^-, \tag{2.91}
$$

$$
\check{l}_{k,m=0} = l_k. \tag{2.92}
$$

After initialisation of the first update step the development points change continuously. For the subsequent iterations $m = 0, \ldots, M - 1$, the development points are replaced by the current filtered state estimate $\hat{x}_{k,m}^+$ and filtered observations $\hat{l}_{k,m}^+$. This corresponds to a similar linearisation procedure as for the GHM (cf. section 2.1.2). As with the IEKF for GMM (cf. section 2.2.1), the iterations of the update step terminate after a specific number of runs, unless an abort criterion has already been reached. The related VCM of the filtered states $\Sigma_{\hat{x}\hat{x},k}^+$ is determined once at the end of the update step for $m = M - 1$ and reads

$$
\Sigma_{\hat{x}\hat{x},k}^+ = (\mathbf{I} - K_k \cdot A_k) \cdot \Sigma_{\hat{x}\hat{x},k}^- \cdot (\mathbf{I} - K_k \cdot A_k)^T + K_k \cdot \left(B_k \cdot \Sigma_{ll,k} \cdot B_k^T \right) \cdot K_k^T, \tag{2.93}
$$

where K_k is the Kalman gain

$$
K_k = \Sigma_{\hat{x}\hat{x},k}^- \cdot A_k^T \cdot \left(\left(A_k \cdot \Sigma_{\hat{x}\hat{x},k}^- \cdot A_k^T \right) + \left(B_k \cdot \Sigma_{ll,k} \cdot B_k^T \right) \right)^{-1}. \tag{2.94}
$$

Afterwards the state vector and related VCM are predicted again for the next epoch $k + 1$ (cf. Equations (2.71) and (2.72)). The general process of the individual filter steps is shown in Figure 2.2 with its relevant estimates. Note that the Kalman gain in Equation (2.94) results from the application of the transformation rule from Equations (2.50) – (2.54) in combination with the solutions of the IEKF for GMM (cf. section 2.2.1). This also results in the detailed filter equation for the iteratively updated state vector below $\hat{x}_{k,m+1}^+$

$$
\hat{x}_{k,m+1}^+ = \hat{x}_k^- - K_{k,m} \cdot \left(h \left(\check{l}_{k,m}, \check{x}_{k,m} \right) + B_{k,m} \cdot \left(l_k - \check{l}_{k,m} \right) + A_{k,m} \cdot \left(\hat{x}_k^- - \check{x}_{k,m} \right) \right). \tag{2.95}
$$

In addition, the iteratively updated observation vector $\hat{l}_{k,m+1}^+$ result as follows

$$
\begin{aligned}
\hat{l}_{k,m+1}^+ = l_k - &\left(\Sigma_{ll,k} \cdot B_{k,m}^T \cdot \left(\left(A_{k,m} \cdot \Sigma_{\hat{x}\hat{x},k}^- \cdot A_{k,m}^T \right) + \left(B_{k,m} \cdot \Sigma_{ll,k} \cdot B_{k,m}^T \right) \right)^{-1} \right) \\
&\cdot \left(h \left(\check{l}_{k,m}, \check{x}_{k,m} \right) + B_{k,m} \cdot \left(l_k - \check{l}_{k,m} \right) + A_{k,m} \cdot \left(\hat{x}_k^- - \check{x}_{k,m} \right) \right).
\end{aligned} \tag{2.96}
$$

As mentioned before, only a few other researchers besides Dang (2007, 2008) have so far dealt with implicit measurement equations within a KF. In Ettlinger et al. (2018), the approach is to realise a decomposed system equation by two sets of equations. The first set consists of the predicted state parameters and the second set consists of condition equations according to the GHM. The fusion of both sets of equations leads to a system model of a KF. The solution then results from the usual formulas of the GHM. However, no iterations according to an IEKF or state constraints according to section 2.3 can yet be realised. Furthermore, the approaches from Petersen and Koch (2010); Steffen and Beder (2007) are based on a similar approach to that of Dang (2007, 2008), but only Steffen and Beder (2007) uses an IEKF.
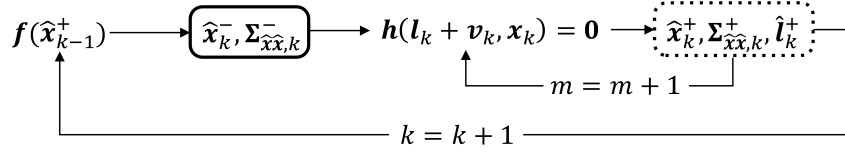
Figure 2.2: *Flowchart of the IEKF for implicit measurement equations with predicted states (solid box) and updated states & observations (dotted box)*

2.3 State Constraints

The IEKF, and in general also the KF, provide a suitable framework for estimating precise state parameters, taking into account suitable physical or mathematical system models and measurement models (cf. section 2.2). In addition to the models, additional prior information regarding the states to be estimated is often also known. These can be mathematical definitions, physical laws, geometric restrictions or other practical or logical specifications. Possible specific examples could be the attention to orthonormal rows of a rotation matrix, maximum upper limits of a motion velocity or a given intersection angle. Simplified, this additional information is generally referred to as constraints or restrictions. Although such constraints would theoretically exist for many applications, they are not always applied (Simon and Chia, 2002). However, the consideration of suitable, reliable and applicable constraints can theoretically only lead to an improvement of the estimation results. Especially for non-linear systems, in which the IEKF does not provide optimal estimation results in the sense of minimum variance, the integration of constraints to the states provides a significant gain in accuracy (Chiang et al., 2002; Simon, 2010). For this reason, many different methods have been developed for constrained KFs. A comprehensive overview can be found in Simon (2006, pp. 212 ff.); Gupta and Hauser (2007); Simon (2010).

State constraints can be defined by a linear or non-linear functional context. However, any non-linear state constraint can be transformed into a linear state constraint by Taylor series expansion. This linearisation is regarded as a sufficiently accurate approximation, as long as the uncertainties are small compared to the quantities that occur. Further details on linearisation and related inaccuracies are given in section 2.3.3. Thus, all existing approaches for linear state constraints are also applicable for non-linear state constraints. Therefore, the methods are described below in terms of linear relationships. Furthermore, a distinction between hard constraints[8] and Soft Constraints (SCs)[9] is done. Hard constraints are used if the exact permissible value is known. They are non-negotiable and must be fulfilled exactly. This ensures strict compliance with the state constraints. In contrast, SCs only have to be fulfilled approximately. A certain tolerance is allowed, and the exact value is not required. This type is mainly used if a certain uncertainty in the functional context of the state constraint is already known. If several constraints are applied simultaneously, linear independence between them is assumed. This will avoid any numerical instabilities due to rank deficiency (Wichmann, 2007, pp. 113).

All methods have in common that finally an improved estimation of the state vector x_k^c with associated VCM $\Sigma_{xx,k}^c$ based on the applied constraints is available. As long as truthful state constraints are considered, this leads to a solution that is generally closer to the true value compared to the filtered state x_k^+ without considering constraints. At least a deterioration is not possible under these assumptions (Simon, 2010). The state constraints described here only apply to the update step. However, there are also a few methods that can be taken into account in the prediction step. Nevertheless, this affects the required computational effort and does not represent a relevant gain in accuracy (Gupta and Hauser, 2007).

Due to the diversity of existing state of the art methods, only the most widely used methods required for this thesis are discussed here. In addition, note that those methods described below for considering state constraints refer exclusively to the use of KFs with explicit measurement equations (cf. section 2.2.1).

---

[8]Also referred to as *strong* constraints
[9]Also referred to as *weak* constraints

The application of state constraints to KFs with implicit measurement equations (cf. section 2.2.2) has several special requirements and does not yet exist. Methods for this are described in detail in chapter 3.

2.3.1 Hard Constraints

Hard constraints can be subdivided into equality state constraints

$$\boldsymbol{D} \cdot \boldsymbol{x}_k \;=\; \boldsymbol{d}, \tag{2.97}$$

and inequality state constraints

$$\boldsymbol{D} \cdot \boldsymbol{x}_k \;\leq\; \boldsymbol{d}, \tag{2.98}$$

where $\boldsymbol{D}$ is a known $s \times u$ constraint matrix and $\boldsymbol{d}$ is a known $s \times 1$ constraint vector. The variable s refers to the number of attached constraints and is less than or equal to the number of states u. In general, $\boldsymbol{D}$ and $\boldsymbol{d}$ are time-variable and can vary for different epochs k. Subscription of $\boldsymbol{D}$ and $\boldsymbol{d}$ is not done to simplify notation. In principle, both quantities are also time-dependent and can be different in their dimensions and values per epoch k. The mathematical consideration of such constraints within a KF depends on the respective method.

Equality Constraints

The ***Perfect Measurements (PMs)*** method converts state constraints of Equation type (2.97) into fictitious observations[10] and treats them as additional observations (Porrill, 1988). In contrast to conventional observations, these fictitious observations are not subject to any uncertainties. For this reason we can extend Equation (2.97) by adding zero measurement noise $\boldsymbol{v}_{d,k}$ from which follows

$$\boldsymbol{d} = \boldsymbol{D} \cdot \boldsymbol{x}_k + \boldsymbol{v}_{d,k}, \quad \boldsymbol{v}_{d,k} \sim N\left(\boldsymbol{0}, \boldsymbol{\Sigma}_{l_d l_d, k}\right), \tag{2.99}$$

where the related VCM $\boldsymbol{\Sigma}_{l_d l_d, k}$ is the zero matrix. By adding such a PM equation for each constraint requested, the total number of measurement equations increases to $n + s$. The implementation is done via extension of the observation vector $\boldsymbol{l}_k$ and related VCM $\boldsymbol{\Sigma}_{ll,k}$ in Equation (2.60). The basic process of the IEKF with its relevant estimates is shown in Figure 2.3. Note that this modification leads to a singular VCM of the measurement noise $\boldsymbol{\Sigma}_{ll,k}$. However, this is not necessarily a problem but can lead to numerical instabilities (de Geeter et al., 1997). Furthermore, an extension of the measurement functions obviously leads to generally higher dimensions of related matrices, which can result in a higher computational effort (Simon and Chia, 2002).

Figure 2.3: *Flowchart of the IEKF for explicit measurement equations with predicted (solid box) and constrained states (dashed box) under consideration of additional PMs (red)*

---

[10] Also referred to as *pseudo* observations

In contrast to the PMs method, the ***Projection (PRO)*** method is based on the unconstrained filtered state estimate $\hat{x}_k^+$. So the regular update step of the general KF remains identical. According to Simon and Chia (2002), the filtered state estimate $\hat{x}_k^+$ is projected onto the constraint surface by minimising

$$\hat{x}_k^c = \arg\min_{x_k}\left\{ \left(x_k - \hat{x}_k^+\right)^T \cdot W \cdot \left(x_k - \hat{x}_k^+\right) \;\middle|\; D \cdot x_k = d \right\}, \tag{2.100}$$

where the $u \times u$ weight matrix W can be selected as $W = I$. This will result in a constrained solution closer to the true state than an unconstrained estimation. Alternatively, it can also be selected as $W = \left(\Sigma_{\hat{x}\hat{x},k}^+\right)^{-1}$ which will end in a minimum variance filter (Simon and Chia, 2002). However, this only applies to linear systems (Simon and Chia, 2002). The effect of selecting W is well illustrated by Figure 2.4.

The solution of Equation (2.100) results in the constrained state estimate $\hat{x}_k^c$ and corresponding VCM $\Sigma_{\hat{x}\hat{x},k}^c$

$$\hat{x}_k^c = \hat{x}_k^+ - W^{-1} \cdot D^T \left(D \cdot W^{-1} \cdot D^T\right)^{-1} \left(D \cdot \hat{x}_k^+ - d\right), \tag{2.101a}$$

$$\Sigma_{\hat{x}\hat{x},k}^c = \Sigma_{\hat{x}\hat{x},k}^+ - \Sigma_{\hat{x}\hat{x},k}^+ \cdot D^T \left(D \cdot \Sigma_{\hat{x}\hat{x},k}^+ \cdot D^T\right)^{-1} D \cdot \Sigma_{\hat{x}\hat{x},k}^+. \tag{2.101b}$$

For the implementation, the constraints after the update step are applied, and its results are used for the prediction step in the subsequent epoch $k + 1$. The basic process of the IEKF with its relevant estimates is shown in Figure 2.5. In addition, there are also other methods to consider equality state constraints in Kalman filtering. For example, the so-called ***model reduction*** method reduces the complexity on the level of the system model parametrization, but generally, the physical interpretability of the states is lost (Simon, 2006, pp. 212 ff.). Furthermore, an extension of the model reduction method to inequalities is not possible. However, this is possible with the other methods described below.

Inequality Constraints

In contrast to equality, inequality constraints can be used to exclude entire impermissible or infeasible value ranges of the states. A common method to consider such state constraints of Equation type (2.98) for Kalman filtering is given by ***PDF truncation*** method. Within this framework, the PDF of the unconstrained filtered state estimate $\hat{x}_k^+$ (which is assumed to be Gaussian) is truncated by using the s state constraints requested. The constrained state estimate $\hat{x}_k^c$ then results from the mean of the truncated PDF (Shimada et al., 1998). This truncation is performed for every single constraint $i = 1, \dots, s$ successively. Therefore s truncations are necessary in total. If the constraints are not decoupled from each other, the order in which they are considered affects the result (Simon and Simon, 2010). There are several individual
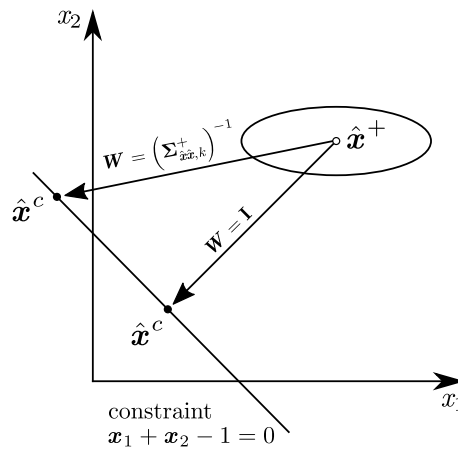
Figure 2.4: *Impact of selecting the weight matrix in the context of the consideration of state constraints by the PRO method. Modified according to Simon (2006, pp. 218).*
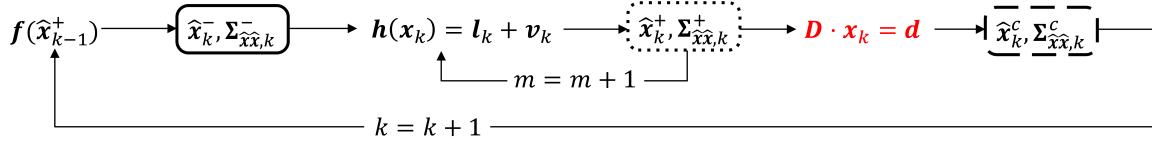
Figure 2.5: *Flowchart of the IEKF for explicit measurement equations with predicted (solid box), updated (dotted box) and constrained states (dashed box) when using the PRO method (red)*

steps needed to perform this method. A detailed overview is given in Simon (2006); Simon and Simon (2010); Vogel et al. (2019). In general, this PDF truncation method can also be used for two-sided inequality state constraints of the form

$$\boldsymbol{d}_{\text{lower}} \quad \leq \quad \boldsymbol{D} \cdot \boldsymbol{x}_k \quad \leq \quad \boldsymbol{d}_{\text{upper}}, \tag{2.102}$$

where $\boldsymbol{d}_{\text{lower}}$ relates to the lower and $\boldsymbol{d}_{\text{upper}}$ to the upper boundary of the constraint (cf. Figure 2.6). For this reason, inequality constraints can be considered as the general case in terms of state constraints. If the lower and upper boundaries are identical, a two-sided inequality conforms to an equality state constraint. To handle one-sided inequality constraints, $\boldsymbol{d}_{\text{lower}} = -\infty$ or $\boldsymbol{d}_{\text{upper}} = +\infty$ could be used. In addition, this PDF truncation method can also be applied for equality constraints. Also, combinations of equality and inequalities state constraints are possible, making this method very versatile. The basic process of the IEKF with its relevant estimates using the PDF truncation method is shown in Figure 2.7. Simon and Simon (2010) further recommend an independent execution of the unconstrained Kalman filtering and PDF truncation process. Instead of using the constrained state for prediction for the subsequent epoch $k + 1$, the unconstrained state should be used. This is to prevent that the multiple use of the information in the constraint results in a supposed normal distribution. Otherwise, this can lead to a monotonously increasing mean value or monotonously decreasing variance.

The already introduced PRO method can also be extended with regard to inequality state constraints. However, only with respect to one-sided formulation according to Equation (2.98). The minimisation problem in Equation (2.100) need to be modified and leads to

$$\hat{\boldsymbol{x}}_k^c = \arg\min_{\boldsymbol{x}_k}\left\{ \left(\boldsymbol{x}_k - \hat{\boldsymbol{x}}_k^+\right)^T \cdot \boldsymbol{W} \cdot \left(\boldsymbol{x}_k - \hat{\boldsymbol{x}}_k^+\right) \;\middle|\; \boldsymbol{D} \cdot \boldsymbol{x}_k \leq \boldsymbol{d}\right\}. \tag{2.103}$$

However, this results in a quadratic programming problem (Simon, 2006, pp. 216 ff.). A so-called ***active-set method*** is a suitable approach to solve this problem (Fletcher, 2008). A subset (active set) of the inequality constraints are treated as equality constraints and the optimisation problem is solved. This subset comprises all constraints which are active at the solution of the problem. If the solution satisfy
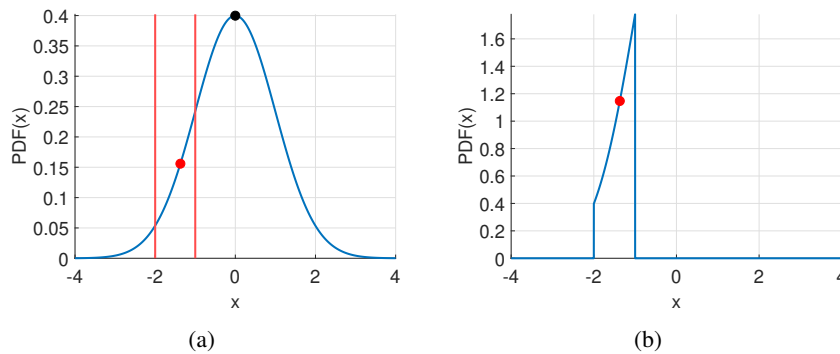
Figure 2.6: *Basic principle of the PDF truncation method (unconstrained PDF (a) and constrained PDF (b)) according to Simon and Simon (2010). The lower and upper boundaries are marked with red lines. The unconstrained state is highlighted by a black circle and the constrained state by a red circle. The constrained state refers to the centroid of the truncated PDF and can be obtained, for example, from the MMSE estimator (cf. Equation (2.65)).*
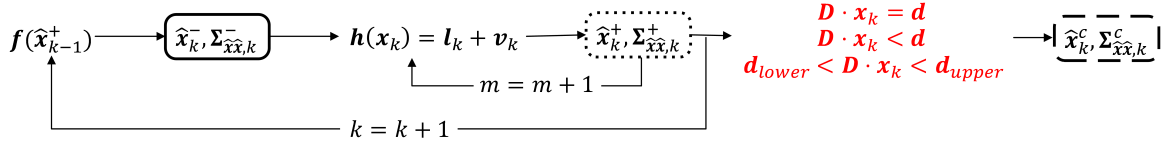
Figure 2.7: *Flowchart of the IEKF for explicit measurement equations with predicted (solid box), updated (dotted box) and constrained states (dashed box) when using the PDF truncation method (red)*

the initial inequality constraints subsequently, the problem is solved. Otherwise an iterative process is necessary. However, it is unfavourable, since the necessary computational effort of the active-set method increases exponentially with the number of constraints (Simon, 2010).

2.3.2 Soft Constraints

As already shown, a feasible range of values can be specified with two-sided inequality constraints (cf. Equation (2.98)). A similar possibility exists through the use of SCs according to

$$\boldsymbol{D} \cdot \boldsymbol{x}_k \;\approx\; \boldsymbol{d}, \tag{2.104}$$

where the constraints are only required to be approximately fulfilled. Realisation is identical to the PMs method for equality state constraints (cf. Equation (2.99)) (Simon, 2010). The additional pseudo observations are considered by a small nonzero measurement noise $\boldsymbol{v}_{d,k}$. Thus, the VCM $\boldsymbol{\Sigma}_{l_d l_d, k}$ is also a nonzero matrix. The basic process of the IEKF with its relevant estimates is shown in Figure 2.8. In contrast to the other methods, it is difficult to define an explicit feasible range of values with this method. One-sided constraints cannot be realised with this either. In addition, there are other methods to apply SCs. For example, in Simon and Simon (2006) an additional regularisation term was used in the general KF.

2.3.3 Non-linear Constraints

So far, only linear state constraints have been considered. In general, state constraints can be formulated by non-linear functions

$$\boldsymbol{g}\left(\boldsymbol{x}_k\right) = \boldsymbol{b}, \tag{2.105}$$

where $\boldsymbol{g}\left(\cdot\right)$ is an arbitrary non-linear function and $\boldsymbol{b}$ is a known $s \times 1$ constraint vector. Note that this can also be transferred one-to-one to inequality constraints of Equation type (2.98). The simplest possibility is to linearise $\boldsymbol{g}\left(\boldsymbol{x}_k\right)$ so that the methods from sections 2.3.1 and 2.3.2 can be applied. However, de Geeter et al. (1997) mentions that applying the PM method (cf. Equation (2.99)) to non-linear state constraints can lead to convergence problems. Regardless of this, the linearisation is basically identical to Equation (2.15) and is based on ***first-order Taylor expansion*** (Porrill, 1988; Simon and Chia, 2002)

$$\boldsymbol{D} = \nabla_{\boldsymbol{x}} \, \boldsymbol{g}\left(\hat{\boldsymbol{x}}_k^-\right)\Big|_{\boldsymbol{x}=\hat{\boldsymbol{x}}_k^-}, \tag{2.106a}$$

$$\boldsymbol{d} = \boldsymbol{b} - \boldsymbol{g}\left(\hat{\boldsymbol{x}}_k^-\right) + \boldsymbol{D} \cdot \hat{\boldsymbol{x}}_k^-. \tag{2.106b}$$

Here, it should be noted that the derivations and evaluations of the non-linear function $\boldsymbol{g}\left(\cdot\right)$ must be carried out on the basis of the state prediction estimate $\hat{\boldsymbol{x}}_k^-$. At least this procedure is indicated by default in the literature above. In addition, it is also possible to select other suitable development points for linearisation. For IEKF, for example, the current estimated value within the iterative update step can be used. Whenever non-linear constraints occur in this thesis, they are approximated by linear constraints based on this method. In addition, one should be aware that linearisation can also lead to linearisation errors, as shown in Figure 2.9.

$$f(\widehat{x}_{k-1}^+) \longrightarrow \boxed{\widehat{x}_k^-, \Sigma_{\widehat{x}\widehat{x},k}^-} \longrightarrow \begin{array}{c} h(x_k) = l_k + v_k \\ \textcolor{red}{D \cdot x_k \approx d} \end{array} \longrightarrow \overline{\boxed{\widehat{x}_k^c, \Sigma_{\widehat{x}\widehat{x},k}^c}}$$
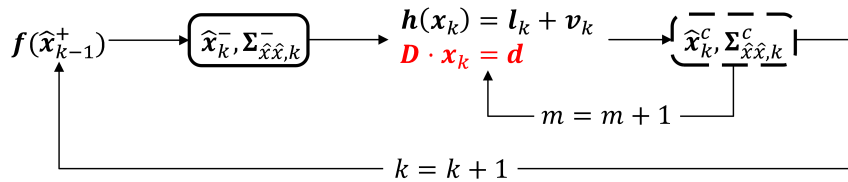
$$m = m + 1$$

$$k = k + 1$$
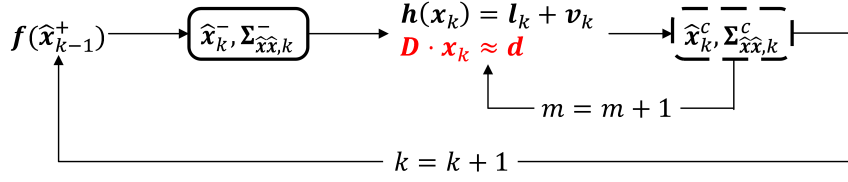
Figure 2.8: *Flowchart of the IEKF for explicit measurement equations with predicted (solid box) and constrained states (dashed box) under consideration of SCs (red)*
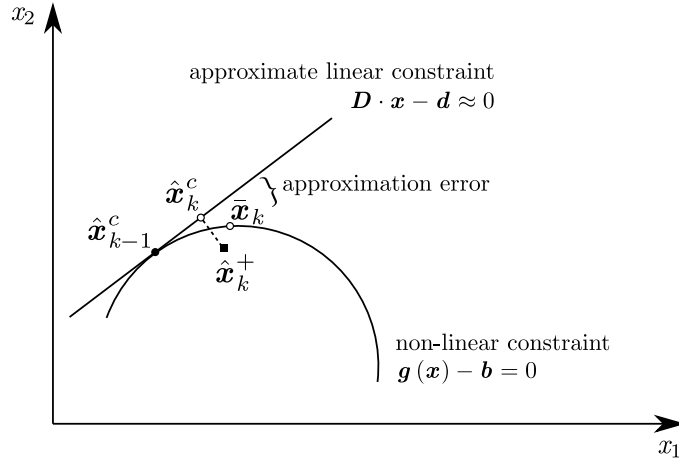
Figure 2.9: *Linearisation errors in case of non-linear state constraints. Modified according to Yang and Blasch (2009).*

Nevertheless, there are further possibilities to consider such non-linear state constraints directly. The termination of Taylor linearisation after the first order represents a weak point depending on the strength of the non-linearity. A possible alternative is therefore to include the ***second-order-expansion*** derivation (Yang and Blasch, 2009; Simon, 2010). However, the resulting optimisation problem can only be solved numerically. Sircoulomb et al. (2008) proposes an iterative process to successively improve the development point for linearisation of the non-linear constraints. Furthermore, non-linear equality state constraints can be integrated directly within a ***Smoothly Constrained Kalman Filter (SCKF)***. This approach is also based on the linearisation of the constraints and then considers them as an additional PM. This is done iteratively, and the uncertainty of the constraints is increased in each repetition (de Geeter et al., 1997). However, both methods have so far not been applied for implicit measurement equations according to section 2.2.2. The same applies to the consideration of non-linear state constraints in the context of UKFs (Teixeira et al., 2008) and PFs (Prakash et al., 2008). In Ebinger et al. (2015), for example, an arbitrary state constraint is applied to the conditional mean estimate of a posterior density. In addition, ***Moving Horizon Estimation (MHE)*** should be mentioned, which is a general approach for solving non-linear equality and inequality constraints (Robertson et al., 1996). This also leads to a non-linear optimisation problem that has not been investigated for implicit relationships between states and observations. Simultaneously, the required run time is considerably higher than that of the other methods described above (Ungarala et al., 2007; Simon, 2010). In general, methods for the consideration of non-linear constraints can also be applied to linear constraints.

In conclusion, it can be summarised that there is an extensive range of different methods for considering state constraints. They depend on the type of constraints and have different advantages and disadvantages. In the case of non-linear systems and constraints, in general, all approaches lead to slightly different results (Simon, 2010). Moreover, the application of non-linear inequalities represents the most significant challenge (Sircoulomb et al., 2008). Not all techniques are suitable for the direct adaptation of the described methods regarding implicit relationships. In the context of this work, therefore, only the methods described in detail will be considered. An overview of these methods depending on the type of constraint is given in Figure 2.10.
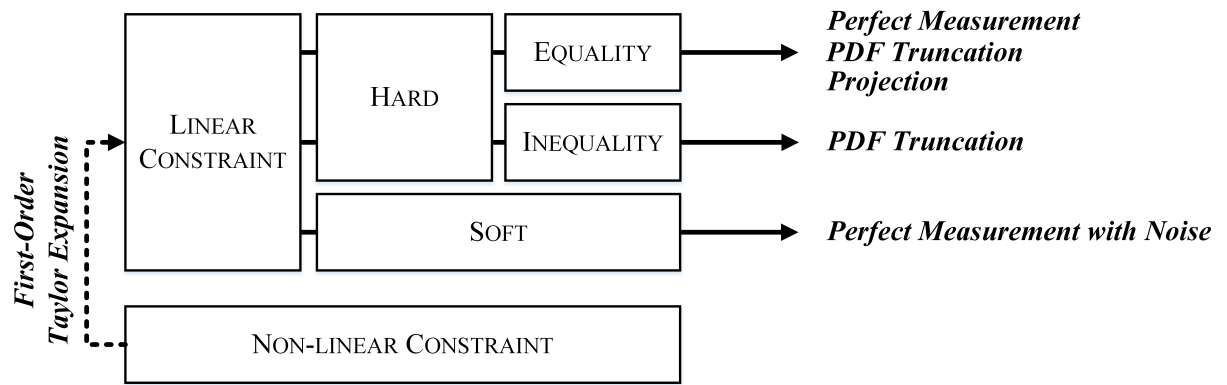
Figure 2.10: *Overview of different methods (bold font) for considering state constraints regarding explicit relations, depending on the type of constraint (boxes). The selection is based on the appropriate techniques used in this thesis.*

3

Methodological Contributions

This chapter presents new methods for the consideration of arbitrary state constraints in the context of implicit measurement equations for IEKFs. In section 3.1 the basic idea of a versatile recursive state-space filter approach is introduced. The new possibilities to consider different types of state constraints are presented in section 3.2. The main differences compared to usual filter methods with explicit measurement equations are discussed, and different possible solutions are shown. Subsequently in section 3.3, an adaptation of the IEKF to enable a recursive GHM with the possibility of including constraints is presented. Finally, the own methodological contributions are applied and validated within the framework of a Monte-Carlo (MC) simulation in section 3.4. With its theoretical aspects, this chapter thus comprises the main part of the own methodological contributions of this thesis.

3.1 Versatile Recursive State-space Filter

The IEKF, initially introduced in Dang (2007), is a practical method to use implicit measurement equations for recursive state estimation. This method was already adopted in Vogel et al. (2018) and significantly extended with regard to two aspects. This contains previously unstated uncertainty information about the updated observation estimates $\hat{l}_k^+$ in the form of VCM $\Sigma_{\hat{l}\hat{l},k}^+$ by propagation of uncertainty. In addition, more fundamentally the consideration of equality state constraints in combination with implicit relations was described in this contribution. This consideration of state constraints within the IEKF with implicit measurement equations is described in detail in the following section 3.2. The derivation of uncertainty information about the estimated observation estimates $\hat{l}_k^+$ is directly stated below. This VCM $\Sigma_{\hat{l}\hat{l},k}^+$ is essential to make quantitative statements about the uncertainty of the estimated observations. In addition, this information might also be necessary for subsequent calculations, such as further propagation of uncertainty. The VCM $\Sigma_{\hat{l}\hat{l},k}^+$ is based on the equation for calculating the updated observation estimates $\hat{l}_k^+$ (cf. Equation (2.96)) which has to be transformed and substituted. Based on

$$\hat{l}_k^+ = l_k - \Sigma_{ll,k} \cdot B_k^T \cdot \left(A_k \cdot \Sigma_{\hat{x}\hat{x},k}^- \cdot A_k^T + \underbrace{B_k \cdot \Sigma_{ll,k} \cdot B_k^T}_{\Sigma_{ll,k}^*} \right)^{-1}$$

$$\cdot \left(h\left(\check{l}_k, \check{x}_k \right) + B_k \cdot \left(l_k - \check{l}_k \right) + A_k \cdot \left(\hat{x}_k^- - \check{x}_k \right) \right) \tag{3.1a}$$

$$= l_k - \underbrace{\Sigma_{ll,k} \cdot B_k^T \cdot \left(A_k \cdot \Sigma_{\hat{x}\hat{x},k}^- \cdot A_k^T + \Sigma_{ll,k}^* \right)^{-1}}_{F_k}$$

$$\cdot \underbrace{\left(h\left(\check{l}_k, \check{x}_k \right) - B_k \cdot \check{l}_k - A_k \cdot \check{x}_k + B_k \cdot l_k + A_k \cdot \hat{x}_k^- \right)}_{w_k}, \tag{3.1b}$$

the following results

$$\hat{l}_k^+ = l_k + F_k \cdot \Big(\underbrace{w_k - B_k \cdot l_k}_{l_k^*} - A_k \cdot \hat{x}_k^- \Big) \tag{3.2a}$$

$$= l_k + F_k \cdot l_k^* - \underbrace{F_k \cdot A_k}_{H_k} \cdot \hat{x}_k^-. \tag{3.2b}$$

Subsequently, the law for propagation of uncertainty can be applied to Equation (3.2b), from which follows

$$\Sigma_{\hat{l}\hat{l},k}^+ = \underbrace{\mathbf{I} \cdot \Sigma_{ll,k} \cdot \mathbf{I}^T}_{\Sigma_{ll,k}} + F_k \cdot \Sigma_{ll,k}^* \cdot F_k^T - H_k \cdot \Sigma_{\hat{x}\hat{x},k}^- \cdot H_k^T. \tag{3.3}$$

Equation (3.3) must be determined for each epoch k. The estimation is performed concurrently with the VCM $\Sigma_{\hat{x}\hat{x},k}^+$ of the updated state estimate $\hat{x}_k^+$ at the end of the respective update step.

In Vogel et al. (2019), the approach of Dang (2007) is adopted again. In addition to the consideration of inequality state constraints, the possibilities of the IEKF for versatility are also discussed. This is mainly based on the possibility to consider explicit measurement equations within the IEKF for implicit relations. This fact is decisive when it comes to a versatile method that can handle as many different mathematical functions as possible. So far, there is no reference to the possibility that the IEKF for implicit relations can be used completely independent of the type of measurement equation (i.e. whether implicit or explicit). Because every explicit equation (cf. Equation (2.60)) can be transformed into an implicit equation (cf. Equation (2.83)) according to

$$l_k + v_k - h(x_k) = 0. \tag{3.4}$$

This transformation is possible in principle, since the explicit model (GMM) can generally be regarded as a special case of the implicit model (GHM). According to this, the following applies after linearisation of Equation (3.4)

$$A_k \cdot x_k + \underbrace{\mathbf{I}}_{B_k} \cdot l_k + \underbrace{v_k - h(\check{x}_k) - A_k \cdot \check{x}_k}_{w_k} = 0 \tag{3.5}$$

From this the definition as in Equation (2.85) can then be represented again

$$A_k \cdot x_k + B_k \cdot l_k + w_k = 0. \tag{3.6}$$

Taking all these aspects together regarding the type of measurement equation and the use of different additional prior information as state constraints, a concept of a versatile recursive state estimator can be established. For this reason, the IEKF for implicit relations represents a broadly based foundation which can flexibly consider different measurement equations and constraints. This overall concept is illustrated in Figure 3.1. Here the focus is on the connection of the different steps of the IEKF to the state parameters requested, the available observations, as well as appropriate prior information. The coloured arrows show different possibilities of how the filter can be applied optimally depending on the application. The extent to which the different types of constraints can be taken into account in this context is described in the following section 3.2. Moreover, this flexibility and versatility of the approach is also highlighted in Bureick et al. (2019b) and adapted for a specific application. The full algorithm is given in Appendix A.1.

3.2 Kalman Filtering with State Constraints for Gauss-Helmert Models

As already mentioned in section 2.3, the consideration of suitable constraints can lead to an additional improvement of the estimation results within the framework of Kalman filtering. Although this is already used by default in combination with explicit measurement equations (cf. section 2.2.1), there is currently no experience with this (apart from own work) for the implicit case (cf. section 2.2.2). A direct transfer of
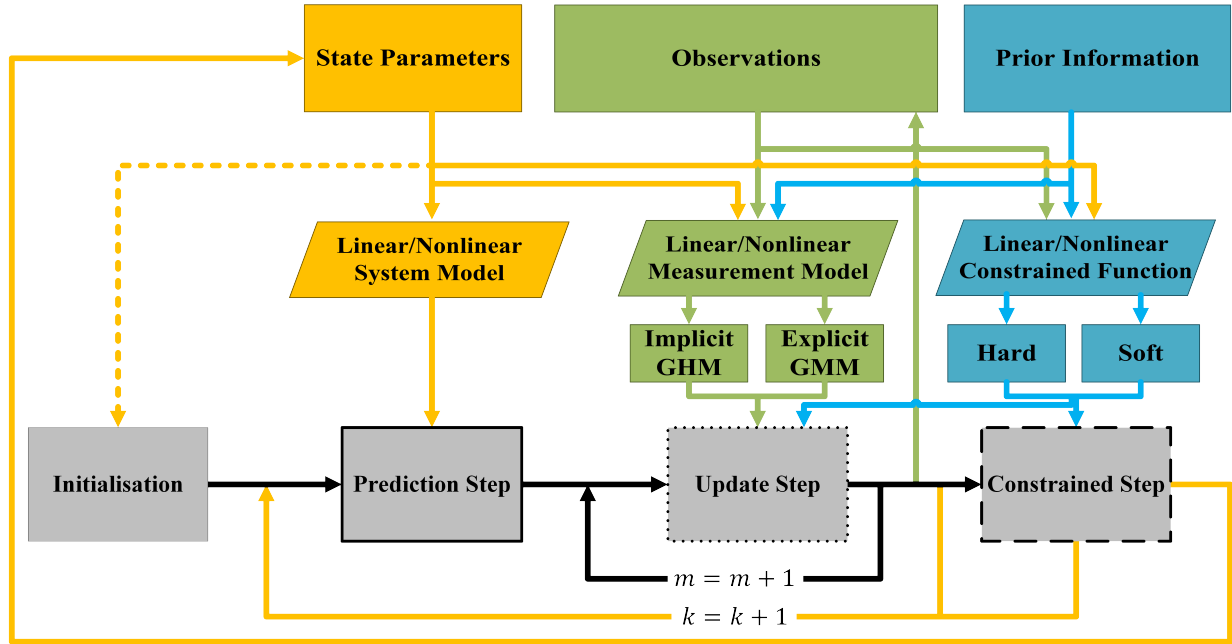
Figure 3.1: *Schematic overview and flow diagram of the versatile recursive state-space filter based on an IEKF according to Vogel et al. (2019). It shows the individual steps of the filter (grey) and the associated state parameters (yellow), observations (green) and additional prior information (blue).*

the methods presented in section 2.3 is generally not possible without additional adjustments and considerations. The reason for this is the direct dependence of the measurement equations on the observations (cf. Equation (2.83)). This in turn leads to an extended LS problem (cf. Equation (2.86)) in which filtered observations are estimated in addition to the state parameters. First approaches have already been described in Vogel et al. (2018, 2019); Bureick et al. (2019b); Moftizadeh (2019). However, not all different types of state constraints (cf. section 2.3) can be considered with the methods described there. Furthermore, there were some inconsistencies, which are referred to and remedied below.

As the term itself implies, state constraints apply exclusively to corresponding elements of the state vector. The observations are therefore not affected by the restrictions. This is applicable for explicit contexts. If implicit relations exist, this usually leads to a conflict. The application of state constraints leads to a change of the state parameters (from $\boldsymbol{x}_k^+$ towards $\boldsymbol{x}_k^c$) in the sense that the specified constraints are fulfilled. At the same time, however, it must also be ensured that the measurement equations are fulfilled as an auxiliary condition (cf. Equation (2.83)), i.e. that the contradictions are close to zero. However, this is generally not guaranteed in implicit relationships (Vogel et al., 2019). This can be clearly compared in Table 3.1, for example, by applying the PRO method (the same also applies to the PDF truncation method) according to section 2.3.

The consideration of constraints within the framework of the perfect measurement method, where the constraints are included directly in the update step, is also not directly applicable. For this reason, three different approaches are shown in the following, with which the methods presented in section 2.3 can also be applied for implicit relationships under consideration of modifications. First, an extension to ***implicit pseudo observations*** is introduced in section 3.2.1. With this, equality constraints, as well as SCs for implicit relations, can be considered. The second approach in section 3.2.2 describes a ***Constrained Objective Function (COF)*** and is based in its principles on the use of constraints in the GHM according to section 2.1.2. This enables the direct consideration of equality constraints within the update step. In a third approach, a procedure is presented which allows using the PRO and PDF truncation method in combination with implicit equations. This procedure (referred to as ***improvement of implicit contradictions***) is capable of resolving the problems listed in Table 3.1 and is described in detail in section 3.2.3. This can then be used to solve equality and inequality constraints.

Table 3.1: *Compliance ($\checkmark$) and non-compliance ($\nleq$) with the measurement equation and constraint equation for implicit relationships. Exemplary for the PRO method in which the constraints are considered separately after the update step.*

	unconstrained estimates x_k^+, l_k^+		constrained estimates x_k^c, l_k^+	
measurement equation	$h\left(l_k^+ + v_k, x_k^+\right) = \mathbf{0}$	$\checkmark$	$h\left(l_k^+ + v_k, x_k^c\right) = \mathbf{0}$	$\nleq$
constraint equation	$g\left(x_k^+\right) = b$	$\nleq$	$g\left(x_k^c\right) = b$	$\checkmark$

3.2.1 Implicit Pseudo Observations

The basic principle is still based on the idea of PMs (cf. section 2.3.1) or SCs (cf. section 2.3.2) applied to explicit contexts. The general implicit measurement equations (cf. Equation (2.83)) are extended by s arbitrary constraint equations. Every single constraint is treated as an additional pseudo observation with corresponding measurement noise. In the case of hard constraints, the measurement noise is specified as zero. A noise greater than zero, on the other hand, leads to SCs. Accordingly, for the s constraints the respective additional measurement equations follow

$$d = D \cdot x_k + v_{d,k}, \quad v_{d,k} \sim N\left(\mathbf{0}, \Sigma_{l_d l_d, k}\right), \tag{3.7}$$

where the measurement noise $v_{d,k}$ of the constraint must be selected appropriately. However, the impact of the actual observations within the measurement equation must now be taken into account. After extending the linearised measurement equations (cf. Equation (2.85)), the following applies

$$\begin{bmatrix} \mathbf{0} \\ d \end{bmatrix} = \underbrace{\begin{bmatrix} A_k \\ D \end{bmatrix}}_{A_k^\dagger} x_k + \underbrace{\begin{bmatrix} B_k \\ \mathbf{0} \end{bmatrix}}_{B_k^\dagger} l_k + \underbrace{\begin{bmatrix} w_k \\ v_{d,k} \end{bmatrix}}_{w_k^\dagger}, \quad \text{where} \tag{3.8}$$

$$l_k^\dagger = \begin{bmatrix} l_k \\ d \end{bmatrix}, \quad \Sigma_{ll,k}^\dagger = \begin{bmatrix} \Sigma_{ll,k} & \mathbf{0} \\ \mathbf{0} & \Sigma_{l_d l_d, k} \end{bmatrix}. \tag{3.9}$$

This extension leads to additional rows in the extended design matrix $A_k^\dagger$ and condition matrix $B_k^\dagger$. In addition, the number of columns in $B_k^\dagger$ increases due to the additional pseudo observations in the extended vector $l_k^\dagger$. The same applies to the extended VCM of the observations $\Sigma_{ll,k}^\dagger$ which must be extended analogously by corresponding rows and columns. The selection of the $\Sigma_{l_d l_d, k}$ entries alone decides whether the additional information should be considered as hard constraints or SCs. The process within the IEKF for implicit measurement equations remains basically the same and is shown in Figure 3.2.

Where the incorporation of additional pseudo observations could already lead to singularities in the explicit case (Simon, 2010), the risk is even higher in the implicit case. At least several sparsely filled rows and columns are added to some matrices, which can encourage singularities. The extent to which the

Figure 3.2: *Flowchart of the IEKF for implicit measurement equations with predicted states (solid box) as well as updated observations and constrained states (dashed box) under consideration of additional PMs or SCs (red)*

normal equation matrix is ill-posed depends on the particular application. Although this is not necessarily a problem, numerical instabilities can occur for this reason when calculating the inverse of the normal equation matrix. In this case, the use of the Moore-Penrose inverse[1] can help (Koch, 1999, pp. 53 ff.). Besides, it is also possible to regularise the normal equation matrix. Different possibilities for this are, for example, given in Tikhonov and Arsenin (1977, pp. 45 ff.), Björck (1996, pp. 99 ff.) and Hansen (2007). However, those were not applied in the present thesis but should be considered in the future. Instead, if ill-posed normal equation matrices occur, an adapted estimation of the VCM $\Sigma^c_{\hat{x}\hat{x},k}$ of the constrained state estimates $\hat{x}^c_k$ (according to Equation (2.93)) is proposed here, which has a regularising effect. For this adaptation the following applies, if the normal equation matrix N_{IEKF} from Equation (2.90) is well-posed

$$\Sigma^c_{\hat{x}\hat{x},k} = \left(I - K_k \cdot A^\dagger_k\right) \cdot \Sigma^-_{\hat{x}\hat{x},k} \cdot \left(I - K_k \cdot A^\dagger_k\right)^T + K_k \cdot \left(B^\dagger_k \cdot \Sigma^\dagger_{ll,k} \cdot \left(B^\dagger_k\right)^T\right) \cdot K^T_k, \tag{3.10}$$

with the following dimensions

$$dim\left(A^\dagger_k\right) = r + s \times u, \tag{3.11a}$$

$$dim\left(K_k\right) = u \times r + s, \tag{3.11b}$$

$$dim\left(B^\dagger_k \cdot \Sigma^\dagger_{ll,k} \cdot \left(B^\dagger_k\right)^T\right) = r + s \times r + s, \tag{3.11c}$$

where r indicates the number of condition equations, u the number of state parameters and s the number of state constraints. If N_{IEKF} is ill-posed, the dimensions of the mentioned matrices are adjusted accordingly, as if there were no additional pseudo observations. Thus Equation (3.10) remains, but the following expressions are truncated to the extent that the subsequent dimensions apply

$$dim\left(A^\dagger_k\right) = r \times u \qquad \text{where} \qquad A^\dagger_k = A_k, \tag{3.12a}$$

$$dim\left(K_k\right) = u \times r, \tag{3.12b}$$

$$dim\left(B^\dagger_k \cdot \Sigma^\dagger_{ll,k} \cdot \left(B^\dagger_k\right)^T\right) = r \times r. \tag{3.12c}$$

Apart from that, the calculation process stays the same. When using this method of implicit pseudo observations for SCs, the question still arises in which order of magnitude the measurement noise $v_{d,k}$ of the pseudo observations must be chosen. Since no numerical methods exist for this purpose, experimental testing is recommended in the first instance. The smaller the value, the more the SC changes into a hard constraint.

3.2.2 Constrained Objective Function

As already mentioned, the application of the implicit pseudo observations method can lead to numerical instabilities. Another possibility to consider state constraints in the context of implicit relationships (without the risk of numerical instabilities) is to extend the associated objective function in Equation (2.86). In the actual state, it refers only to the connection of implicit measurement equations with respect to the estimation principle of the IEKF. The inclusion of equality constraints can be done in a similar manner to section 2.1.2 of the C-GHM (cf. Equation (2.41b)). If Equation (2.86) is extended by Equation (2.97), the following applies for the COF $L_{\text{C-IEKF}}$

$$\begin{aligned} L_{\text{C-IEKF}} = &\begin{pmatrix} l^+_k - l_k \\ x^+_k - x^-_k \end{pmatrix}^T \begin{bmatrix} \Sigma_{ll,k} & 0 \\ 0 & \Sigma^-_{xx,k} \end{bmatrix}^{-1} \begin{pmatrix} l^+_k - l_k \\ x^+_k - x^-_k \end{pmatrix} \\ &- 2 \cdot \lambda^T_{1,k} \cdot \left(A_k \cdot x^+_k + B_k \cdot l^+_k + w_k\right) \\ &- 2 \cdot \lambda^T_{2,k} \cdot \left(D_k \cdot x^+_k - d_k\right) \rightarrow \min, \end{aligned} \tag{3.13}$$

---

[1]Also referred to as *pseudo inverse* or *generalised inverse*

where $\boldsymbol{\lambda}_1$ and $\boldsymbol{\lambda}_2$ are the Lagrangian multipliers. The parameter w_k is already defined by Equation (2.85b). Setting the related partial derivatives with respect to $\boldsymbol{x}_k^+, \boldsymbol{l}_k^+, \boldsymbol{\lambda}_{1,k}$ and $\boldsymbol{\lambda}_{2,k}$ of the Lagrangian equal to zero

$$
\begin{aligned}
\nabla_{\boldsymbol{x}_k^+} L_{\text{C-IEKF}} &= 2 \cdot \left(\boldsymbol{x}_k^+ - \boldsymbol{x}_k^- \right)^T \cdot \left(\boldsymbol{\Sigma}_{\boldsymbol{xx},k}^- \right)^{-1} - 2 \cdot \boldsymbol{\lambda}_{1,k}^T \cdot \boldsymbol{A}_k - 2 \cdot \boldsymbol{\lambda}_{2,k}^T \cdot \boldsymbol{D}_k \overset{!}{=} \boldsymbol{0} \\
&\Leftrightarrow \boldsymbol{x}_k^+ = \boldsymbol{x}_k^- + \boldsymbol{\Sigma}_{\boldsymbol{xx},k}^- \cdot \boldsymbol{A}_k^T \cdot \boldsymbol{\lambda}_{1,k} + \boldsymbol{\Sigma}_{\boldsymbol{xx},k}^- \cdot \boldsymbol{D}_k^T \cdot \boldsymbol{\lambda}_{2,k},
\end{aligned}
\tag{3.14}
$$

$$
\begin{aligned}
\nabla_{\boldsymbol{l}_k^+} L_{\text{C-IEKF}} &= 2 \cdot \left(\boldsymbol{l}_k^+ - \boldsymbol{l}_k \right)^T \cdot \left(\boldsymbol{\Sigma}_{\boldsymbol{ll},k} \right)^{-1} - 2 \cdot \boldsymbol{\lambda}_{1,k}^T \cdot \boldsymbol{B}_k \overset{!}{=} \boldsymbol{0} \\
&\Leftrightarrow \boldsymbol{l}_k^+ = \boldsymbol{l}_k + \boldsymbol{\Sigma}_{\boldsymbol{ll},k} \cdot \boldsymbol{B}_k^T \cdot \boldsymbol{\lambda}_{1,k},
\end{aligned}
\tag{3.15}
$$

$$
\nabla_{\boldsymbol{\lambda}_{1,k}} L_{\text{C-IEKF}} = \boldsymbol{A}_k \cdot \boldsymbol{x}_k^+ + \boldsymbol{B}_k \cdot \boldsymbol{l}_k^+ + w_k \overset{!}{=} \boldsymbol{0},
\tag{3.16}
$$

$$
\nabla_{\boldsymbol{\lambda}_{2,k}} L_{\text{C-IEKF}} = \boldsymbol{D}_k \cdot \boldsymbol{x}_k^+ - \boldsymbol{d}_k \overset{!}{=} \boldsymbol{0},
\tag{3.17}
$$

results in the linear normal equation system $N_{\text{C-IEKF}}$ in block structure

$$
\underbrace{\begin{bmatrix}
-\mathbf{I} & \boldsymbol{0} & \boldsymbol{\Sigma}_{\hat{\boldsymbol{x}}\hat{\boldsymbol{x}},k}^- \cdot \boldsymbol{A}_k^T & \boldsymbol{\Sigma}_{\hat{\boldsymbol{x}}\hat{\boldsymbol{x}},k}^- \cdot \boldsymbol{D}_k^T \\
\boldsymbol{0} & -\mathbf{I} & \boldsymbol{\Sigma}_{\boldsymbol{ll},k} \cdot \boldsymbol{B}_k^T & \boldsymbol{0} \\
\boldsymbol{A}_k & \boldsymbol{B}_k & \boldsymbol{0} & \boldsymbol{0} \\
\boldsymbol{D}_k & \boldsymbol{0} & \boldsymbol{0} & \boldsymbol{0}
\end{bmatrix}}_{N_{\text{C-IEKF}}}
\begin{bmatrix}
\hat{\boldsymbol{x}}_k^+ \\
\hat{\boldsymbol{l}}_k^+ \\
\hat{\boldsymbol{\lambda}}_{1,k} \\
\hat{\boldsymbol{\lambda}}_{2,k}
\end{bmatrix}
=
\begin{bmatrix}
-\hat{\boldsymbol{x}}_k^- \\
-\boldsymbol{l}_k \\
-\boldsymbol{w}_k \\
\boldsymbol{d}_k
\end{bmatrix}.
\tag{3.18}
$$

Its form is similar to the normal equation system N_{IEKF} in Equation (2.90). However, the rows and columns of $N_{\text{C-IEKF}}$ have been extended to take constraints into account. Other changes compared to the unconstrained IEKF procedure (cf. Equations (2.93) – (2.94)) are not necessary. This also applies to the computation of the design matrix $\boldsymbol{A}_k$ and the condition matrix $\boldsymbol{B}_k$, which, in contrast to the implicit pseudo observation method, do not have to be extended. However, in order to obtain the corresponding VCM $\boldsymbol{\Sigma}_{\hat{\boldsymbol{x}}\hat{\boldsymbol{x}},k}^c$ with respect to constrained states, the VCM of the filtered states $\boldsymbol{\Sigma}_{\hat{\boldsymbol{x}}\hat{\boldsymbol{x}},k}^+$ must be determined analogously to the PRO method according to Equation (2.101b). This results in the basic process shown in Figure 3.3. The general applicability presupposes that $N_{\text{C-IEKF}}$ can be inverted. As already mentioned at the beginning of section 2.3, this requires linear independence of the constraints to be considered.

The extension regarding inequalities is identical to the situation described for the C-GHM in section 2.1.2. In principle, the approach of an inequality C-GHM from Roese-Koerner (2015, pp. 77 ff.) is also transferable to an IEKF with inequality state constraints. However, this leads to a much more complex optimization problem, which does not yet exist for this particular constellation of IEKF, implicit measurement equations and inequality state constraints.

3.2.3 Improvement of Implicit Contradictions

Adding pseudo observations or constraining the objective function are methods that directly consider state constraints during the update step. Thus, the measurement equation and constraint condition are fulfilled simultaneously. If this is not done simultaneously but successively, problems arise, as described in Table 3.1. The constraint conditions are fulfilled, but the combination of filtered observation estimates
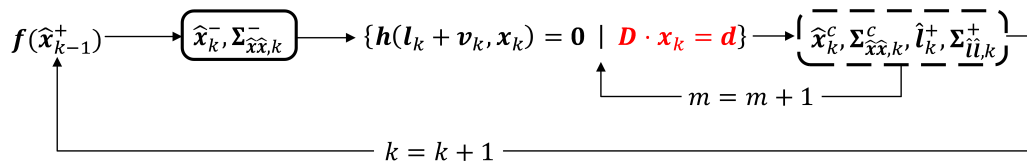
Figure 3.3: *Flowchart of the IEKF for implicit measurement equations with predicted states (solid box) as well as updated observations and constrained states (dashed box) under consideration of a COF (red)*

$\hat{l}_k^+$ and constrained state estimates $\hat{x}_k^c$ leads to significant contradictions in the measurement equations (cf. Equation (2.83)). This is because the state constraints do not affect the observations. Instead of being close to zero, the contradictions can vary or even increase over time.

The linearisation error of the EKF can be used as a relatively comparable problem. With the IEKF, this is eliminated by introducing an iterative process by successively improving the development point. The approach from Sircoulomb et al. (2008), which also suggests an iterative process for an improved linearisation of a non-linear constraint, is also based on this procedure. Such an iterative process can also be used to reduce the contradictions mentioned above. By iterative repetition, the contradictions of the implicit measuring equations must be allowed to approach zero, and at the same time, the states must be permitted to satisfy the constraints. In particular, this means to realise an iterative loop around the update and constrained step, where the constrained states are used as initial values for the update step in the next iteration. Once the constraints are applied to the state estimation and the initial measurement equations are most likely to be violated, a re-estimation of both steps is carried out. In the following, this additional iterative process is referred to as a *contradiction loop*. The maximum number of iterations is indicated by $j = 1, \ldots, J$, but should be applied together with a threshold value. The maximum absolute contradiction is suitable for this. Furthermore, it has to be considered that within the update step, the iterative linearisation still takes place as well. This general principle is simplified with all relevant loops in Figure 3.4. The transition parameters between iteration run j and $j+1$ are important for the implementation of this procedure. This refers to the choice of revised start values for the iterative part of the update step.

This contradiction loop can be used to apply the PRO and PDF truncation method also to implicit relationships in the framework of IEKF. The basic process is shown in Figure 3.5 for the PRO method and in Figure 3.6 for the PDF truncation method. It turns out that there are no fundamental changes apart from the additional contradiction loop. However, this is sufficient to satisfy both the implicit measurement equation and the state constraints.
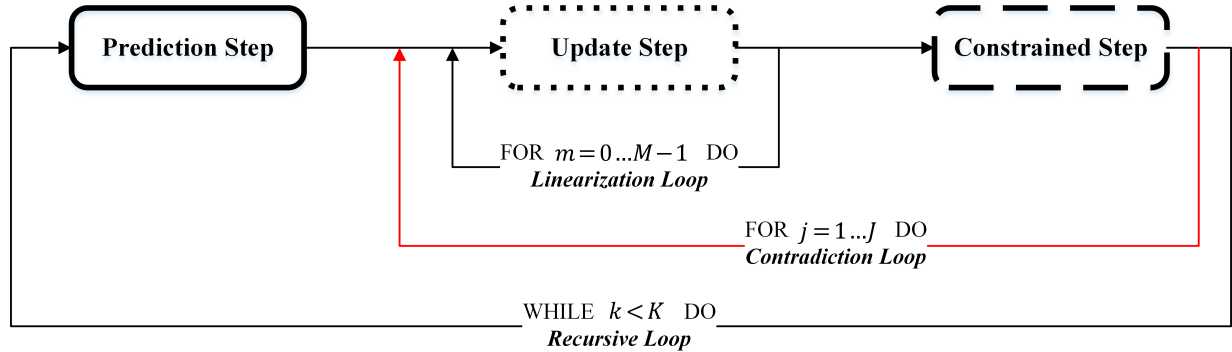
Figure 3.4: *Simplified representation of iterative loops (whereas the contradiction loop is highlighted in red) for improved linearisation and compliance with near-zero contradictions and state constraint equations. This refers only to the usage of implicit measurement equations in IEKF with state constraints, which are applied in a separate constrained step (e.g., PRO method).*
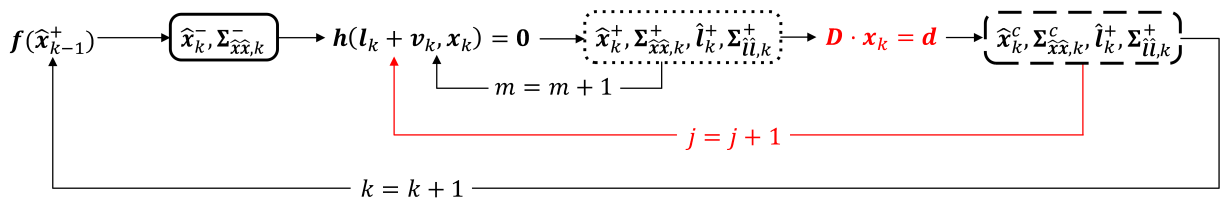
Figure 3.5: *Flowchart of the IEKF for implicit measurement equations with predicted states (solid box), updated observations & states (dotted box) and constrained states (dashed box) when using the PRO method together with the contradiction loop (red)*

$$f(\widehat{x}_{k-1}^+) \longrightarrow \boxed{\widehat{x}_k^-, \Sigma_{\widehat{x}\widehat{x},k}^-} \longrightarrow h(l_k + v_k, x_k) = 0 \longrightarrow \vdots\widehat{x}_k^+, \Sigma_{\widehat{x}\widehat{x},k}^+, \widehat{l}_k^+, \Sigma_{\widehat{l}\widehat{l},k}^+\vdots$$
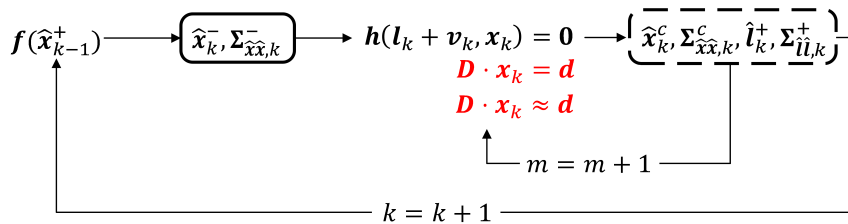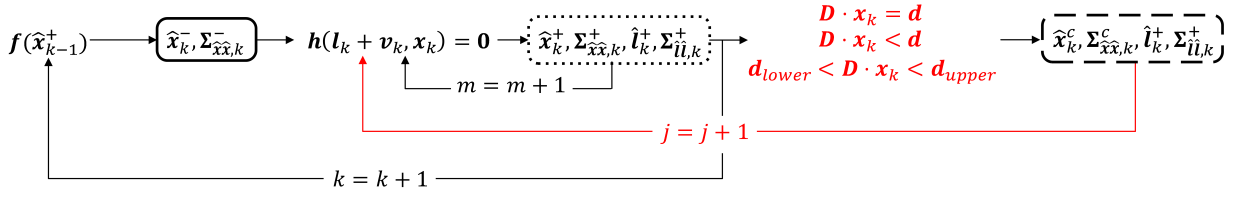

Figure 3.6: *Flowchart of the IEKF for implicit measurement equations with predicted states (solid box), updated observations & states (dotted box) and constrained states (dashed box) when using the PDF truncation method together with the contradiction loop (red)*

3.3 Recursive Gauss-Helmert Model

As mentioned earlier, the IEKF for implicit measurement equations, initially introduced by Dang (2007, 2008), is a recursive state estimation approach. Its application is particularly beneficial in the case of continuously arising measurement epochs, where a certain physical regularity can be assigned to the temporal characteristic of the parameters to be estimated. This is the usual field of application for a filter approach. In addition, this general procedure can be used for another application — a ***recursive GHM***.

The relevance of recursive parameter estimation is, among other aspects, mainly related to the use of big data (e.g. geodetic networks with a large number of point coordinates or dense 3D point clouds) within a batch approach. Large amounts of data usually lead to higher-dimensional matrices, which in turn leads to a significant increase in the required computing time. The synthetic partitioning of an overall adjustment into individual, per se artificial, epochs and the application of recursive parameter estimation can result in a significant improvement of the computing time. With a recursive method, subsampling of the data set can be avoided, and all available information can be used instead. However, it must be ensured that partitioning of the data logically makes sense and is possible at all. As a typical application example, where such large amounts of data occur, the three-dimensional acquisition of the environment with a static 3D laser scanner can be mentioned. Depending on the laser scanner, several thousand measured 3D points of the surroundings can be available. The efficient estimation of relevant parameters (e.g. geometric or calibration parameters) can then be done either by subsampling the existing point cloud or by partitioning it into separate sub-epochs. While point observations are lost through subsampling, all information can be used by dividing the point cloud into individual epochs. Therefore, recursive estimation offers immense advantages, especially in applications where only limited computing capacities are available (e.g. low-power on-board computers in a UAV).

Section 2.1.3 introduces recursive parameter estimation for explicit relationships as part of the fundamentals. It is expected that the parameters will change only slightly in a limited number of epochs. The main problem is that so far, there is no possibility of recursive parameter estimation in the implicit GHM. This circumstance can be remedied by a small modification of the IEKF for implicit relationships from section 2.2.2. In addition, this can also be linked directly with the methods from section 3.2 for the consideration of constraints and thus be extended by an additional option. Due to the IEKF's flexibility towards explicit and implicit measurement equations, a generally valid method for recursive parameter estimation in GMM and GHM can be presented.

The essential difference between recursive state estimation and recursive parameter estimation consists in the consideration or disregard of a functional dynamic model with which the temporal and spatial behaviour of the parameters to be estimated can be predicted. For the KF, this corresponds exactly to the prediction step. Furthermore, the difference between deterministic and probabilistic parameters already mentioned in section 2.2 still exists. Neglecting this prediction within a KF thus provides the basis for applying a recursive state estimator as a recursive parameter estimation. In the case of KFs with explicit relationships, this procedure is also referred to as *random walk-based model* (Mulquiney et al., 1995).

Applied specifically to the IEKF prediction step from section 2.2.2, this means the following for the original Equations (2.71) and (2.72) in each epoch k:

$$x_k^- = x_{k-1}^+, \tag{3.19}$$

$$\Sigma_{xx,k}^- = \Sigma_{xx,k-1}^+ + \Sigma_{ww,k}. \tag{3.20}$$

This means that the predicted state vector x_k^- of epoch k is identical to the updated state vector x_{k-1}^+ of epoch $k-1$. The same applies to the corresponding VCM $\Sigma_{xx,k}^-$, which can still be extended by a suitable process noise $\Sigma_{ww,k}$. In specific terms, suitable means that numerical instabilities are avoided, but still no too strong influence results from its choice. An investigation in this matter can be found in Appendix A.2 with regard to the subsequent example of application in section 3.4. In theory, the process noise should be zero for a recursive GHM. Since the realisation here is based on an IEKF, which requires a sufficiently accurate initialisation, the consideration of a non-zero process noise has a regularising effect. The respective order of magnitude and physical interpretation should be considered depending on the specific application. The complete update step remains unchanged from this modification. Since there is no impact from a system model anymore, the state parameters are only affected by the availability of new observations for each epoch. However, there are some minor differences towards the estimation of a GHM in batch processing. The decisive difference is that the GHM in batch processing computes improvements to the observations. With recursive GHM, on the other hand, directly adjusted observations are estimated. In addition, the underlying principle is different. The overall adjustment iterates and linearises several times, but always directly for the entire data set. In the recursive approach, linearisation is much more frequent because of the partition into artificial epochs. This leads to linearisation at different development points, which affects the result. In the course of the MC simulation, this topic is addressed again in the following section 3.4.

It should be noted that it is not always useful to take all observations into account. Depending on the application, a variety of redundant information is usually available, which does not represent a significant added value. To avoid this, an appropriate selection of the essential and helpful observation quantities is required. Currently, this is done by spatial or temporal subsampling. However, this does not necessarily apply to all observation data. Instead, there is a need for new methods to assess the contribution of a single observation to the overall estimation result. In the context of this thesis, this question will not be analysed in detail. Instead, the advantages are regarded in the recursive consideration of as many observations as possible. Thus, the loss of important information is avoided. This is contrary to the simple subsampling to make batch methods applicable to mass data.

3.4 Example of Application

A two-dimensional ellipse is a well suited geometrical object which can be described by an implicit equation (Lösler and Nitschke, 2010). If the centre is assumed to be identical with the origin of a Cartesian coordinate system and the semi-major axis a as well as the semi-minor axis b are axially parallel, the non-linear implicit equation for an ellipse is given by

$$\left(\frac{x}{a}\right)^2 + \left(\frac{y}{b}\right)^2 - 1 = 0 \quad \text{with} \quad a, b > 0. \tag{3.21}$$

Here, x and y are arbitrary 2D Cartesian coordinates which fulfil this equation. If there are $j = 1, \ldots, J$ sets of 2D coordinates available, the parameters a and b can be determined based on a GHM in batch processing (cf. section 2.1.2) by using the measurement model

$$h_j(l_j, x) = \left(\frac{x_j}{a}\right)^2 + \left(\frac{y_j}{b}\right)^2 - 1 = 0, \tag{3.22}$$

where the observation vector $\boldsymbol{l}$ and the parameter vector $\boldsymbol{x}$ are given by

$$\boldsymbol{l} = [x_1, y_1, \ldots, x_J, y_J]^T, \tag{3.23}$$

$$\boldsymbol{x} = [a, b]^T. \tag{3.24}$$

In order to apply a recursive GHM (cf. section 3.3), the observation vector $\boldsymbol{l}$ can be subdivided into $k = 1, \ldots, K$ individual epochs with $n = 1, \ldots, N$ 2D coordinates, respectively. If N equals J, the recursive approach is identical to a batch approach. As a consequence, the parameters will be estimated for each individual epoch k and gathered in the state parameter vector $\boldsymbol{x}_k$

$$\boldsymbol{l}_k = [x_{k,1}, y_{k,1}, \ldots, x_{k,N}, y_{k,N}]^T \quad \text{with} \quad N \leq J, \tag{3.25}$$

$$\boldsymbol{x}_k = [a_k, b_k]^T. \tag{3.26}$$

An equality constraint can be applied by the eccentricity e (defined by the distance between the two focal points $F1$ and $F2$ and the origin of the ellipse), which implies the a priori ratio between both semi-axes by the non-linear function

$$g(\boldsymbol{x}_k) = \sqrt{a_k^2 - b_k^2} = e. \tag{3.27}$$

This constraint can also be used for batch processing. In this case, the epoch index k in Equation (3.27) is negligible. To consider this non-linear equality constraint, a linearisation of $g(\boldsymbol{x}_k)$ by Taylor series expansion needs to be performed (cf. Equation (2.106)). A schematic sketch of such an ellipse is given in Figure 3.7. The methods presented in section 2.1.2 and 3.3 are applied to the following ellipse parameters. The true state $\bar{\boldsymbol{x}}$ is given by

$$\bar{\boldsymbol{x}} = [\bar{a}, \bar{b}]^T = [5, 3]^T, \tag{3.28}$$

where both semi-axes are given without any specific metric unit. Based on these parameters, the corresponding true eccentricity $\bar{e}$ for the equality constraint (cf. Equation (3.27)) can be determined

$$\bar{e} = \sqrt{a^2 - b^2} = 4. \tag{3.29}$$

Based on these ellipse parameters, $J = 2500$ sets of faultless 2D coordinates $\check{x}$ and $\check{y}$ are generated by means of $K = 100$ individual epochs with each $N = 25$ random 2D coordinates of the total quantity

$$\check{\boldsymbol{l}} = [\check{x}_1, \check{y}_1, \ldots, \check{x}_{2500}, \check{y}_{2500}]^T. \tag{3.30}$$
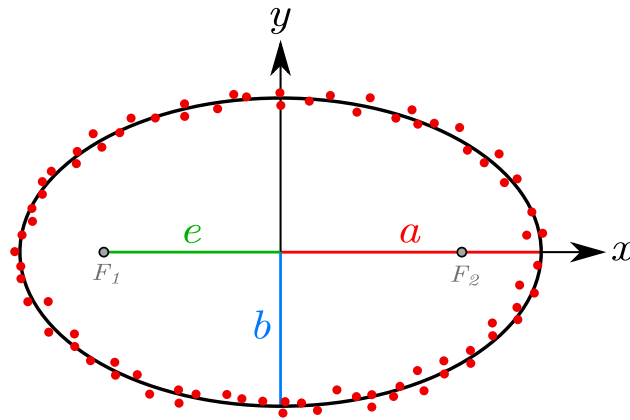
Figure 3.7: *Ellipse with semi-major axis a, semi-minor axis b, focal points F1 and F2 as well as the eccentricity e. Noisy 2D coordinates of the ellipse are depicted by red dots. It should be noted that the illustration is only schematic and not representative of the following numerical values.*

Attention has to be paid to a suitable spatial distribution of all these individual subsets to avoid un-favourable geometric configurations when describing the ellipse. For the specific case here, it must be ensured that each quadrant of the coordinate system contains at least one of the N 2D coordinates. To obtain non-perfect observations, specific random Gaussian noise v_x and v_y with respect to the length of the semi-axes is added to each 2D coordinates $\check{x}_j$ and $\check{y}_j$ for $j = 1 : 2500$. For $j = 1, \ldots, J$ applies

$$x_j = \check{x}_j + v_{x_j}, \quad v_{x_j} \sim N\left(0, \sigma_x^2\right),$$ (3.31a)

$$y_j = \check{y}_j + v_{y_j}, \quad v_{y_j} \sim N\left(0, \sigma_y^2\right),$$ (3.31b)

$$l = [x_1, y_1, \ldots, x_{2500}, y_{2500}]^T$$ (3.31c)

Here, the measurement noises σ_x and σ_y are chosen to consider suitable noise values by $\eta = 1.5\,\%$ of the length of the semi-axes. This leads to a noise of the observed quantities of different order of magnitude. In addition, these standard deviations are applied for the uncorrelated VCM of the measurement noise $\Sigma_{ll_j,k}$

$$\sigma_x = a \cdot \eta = 0.075,$$ (3.32a)

$$\sigma_y = b \cdot \eta = 0.045,$$ (3.32b)

$$\Sigma_{ll_j,k} = \begin{bmatrix} \sigma_x^2 & 0 \\ 0 & \sigma_y^2 \end{bmatrix}.$$ (3.32c)

Furthermore, the process noise σ_w and the initial VCM of the state parameters $\Sigma_{xx,0}$ are selected as follows

$$\sigma_w = 1 \cdot 10^{-3},$$ (3.33)

$$\Sigma_{xx,0} = \begin{bmatrix} 1 \cdot 10^{-1} & 0 \\ 0 & 1 \cdot 10^{-1} \end{bmatrix}.$$ (3.34)

The selection of the used measurement and process noise was investigated in advance and is based on its findings. A verification of this can be found in Appendix A.2. The initial state parameter vector x_0 is given by the true states $\bar{x}$. This is important due to different processes of linearisation between classical batch processing of the GHM and the recursive GHM approach introduced. Results based on nine different methods are presented. The corresponding properties of the respective methods are summarised in Table 3.2. If the state constraint is considered as SC, the measurement noise $\bar{v}_{d,k} = 0.25$ is applied. The inequality constraint used for PDF truncation has limits of $\bar{d}_{lower} = \bar{e} - \bar{e} \cdot 2\,\%$ and $\bar{d}_{upper} = \bar{e} + \bar{e} \cdot 2\,\%$.

Table 3.2: *Overview of the investigated methods with regard to their respective properties. In this study, the application of PDF truncation by using equality constraints is abbreviated as 'PT equ.' and by using inequality constraints as 'PT inequ.'.*

Method	Batch Approach	Recursive Approach	Equality Constraint	Inequality Constraint	Soft Constraint
batch GHM	✓				
batch C-GHM	✓		✓		
recursive GHM		✓			
recursive C-GHM (PM)		✓	✓		
recursive C-GHM (SC)		✓			✓
recursive C-GHM (PRO)		✓	✓		
recursive C-GHM (COF)		✓	✓		
recursive C-GHM (PT equ.)		✓	✓		
recursive C-GHM (PT inequ.)		✓		✓	

3.4.1 Monte-Carlo Simulation and Consistency

In order to analyse not only individual estimation results but also entire methods, the consistency of the different filter approaches is analysed. In general, a state estimator of a filter is consistent, if the estimates converge to the true value. Possible reasons why this is not the case are modelling, numerical or programming errors (Bar-Shalom et al., 2001, pp. 232). A statistical test to verify the filter consistency is introduced in Bar-Shalom et al. (2001, pp. 234 ff.). For this, the Normalised (State) Estimation Error Squared (NEES) e_k is defined as a quality measure according to

$$e_k = (\bar{\boldsymbol{x}}_k - \hat{\boldsymbol{x}}_k)^T \cdot \left(\boldsymbol{\Sigma}_{\hat{\boldsymbol{x}}\hat{\boldsymbol{x}},k}\right)^{-1} \cdot (\bar{\boldsymbol{x}}_k - \hat{\boldsymbol{x}}_k), \tag{3.35}$$

where the differences between true state $\bar{\boldsymbol{x}}_k$ and estimated state $\hat{\boldsymbol{x}}_k$ are considered for each epoch k. Furthermore, a weighting is applied via the VCM $\boldsymbol{\Sigma}_{\hat{\boldsymbol{x}}\hat{\boldsymbol{x}},k}$ of the states estimated. Based on this quadratic quantity, the null hypothesis H_0 can be tested within the framework of a MC simulation to what extent the filter is consistent. The average NEES $\tilde{e}_k$ of the random variable e_k can be obtained by

$$\tilde{e}_k = \frac{1}{S} \sum_{i=1}^{S} e_{i,k}, \tag{3.36}$$

where S is the total number of independent MC runs. It is assumed that the average NEES follows a χ^2 distribution with $S \cdot u_{\boldsymbol{x}}$ degrees of freedom, where $u_{\boldsymbol{x}}$ is the number of states. This χ^2 test is accepted if the null hypothesis

$$P\left\{\tilde{\mathbf{e}}_k \in [r_1, r_2] \,|\, H_0\right\} = 1 - \alpha \tag{3.37}$$

is fulfilled. Here α indicates the so-called significance level and is usually set to $5\,\%$. The two critical values r_1 and r_2 result from

$$r_1 = \chi^2\left(\alpha/2, u_{\boldsymbol{x}} \cdot S\right) \cdot \frac{1}{S}, \tag{3.38a}$$

$$r_2 = \chi^2\left(1 - \alpha/2, u_{\boldsymbol{x}} \cdot S\right) \cdot \frac{1}{S}. \tag{3.38b}$$

Since the true state is never known in practice and a large number of MC simulations have to be carried out for this quality measure, NEES can only be applied to simulated data (de Geeter et al., 1997). However, this NEES is based on the assumption of a χ^2 distribution. If there are any doubts about this assumption, so-called MC *bootstrap* approaches have to be considered. These are described in detail in (Efron and Tibshirani, 1993, pp. 45 ff.) and (Efron and Hastie, 2016, pp. 159 ff.), for example. They enable the analytical solution of test statistics in case of approximated probability distributions (Alkhatib et al., 2019).

To achieve meaningful conclusions, the presented results are based on the mean value for $S = 5000$ repetitions of a MC simulation. The individual realisations differ with regard to the random Gaussian noises v_x and v_y respectively. In contrast to the execution of a single realisation, statistically verifiable statements can be obtained in addition to the consistency check. Moreover, without this simplified form of bootstrapping, no information on the estimated results expected would be available. This procedure is of essential importance with regard to the non-linearity of the problem at hand (and the associated inaccuracies in the linearisation of the respective methods) and the non-existent optimality of the recursive GHM. The additional use of constraints reinforces this even more. Also Zwiener (2019, pp. 138 ff.) mentioned that the limitation of a solution set by considering a constraint represents a non-linear transformation. This is in contradiction to the previously assumed normal distribution, which is thereby violated. In addition, the MC simulation allows statements on precision and shifting with respect to the selected true value. Thus, the accuracy information can be validated based on the estimated VCM of the recursive estimate. For this purpose, the specification of confidence intervals and ellipses is useful. These visualise the area around the estimated state in which the true state is located with a certain probability of $1 - \alpha$. According to

Niemeier (2008, pp. 276), the two semi-axes a_{conf} and b_{conf} of the confidence ellipse result from the χ^2 distribution as follows

$$a_{\text{conf}} = \sqrt{\lambda_1 \cdot \chi^2_{2,1-\alpha}}, \tag{3.39a}$$

$$b_{\text{conf}} = \sqrt{\lambda_2 \cdot \chi^2_{2,1-\alpha}}, \tag{3.39b}$$

where λ_1 and λ_2 are the eigenvalues of the respective VCM sorted by size. The orientation θ_{conf} of the confidence ellipse results from the corresponding elements of the eigenvector s_1 of the VCM according to

$$tan^{-1}\left(\theta_{\text{conf}}\right) = \frac{s_1(1)}{s_1(2)}. \tag{3.40}$$

3.4.2 Results

Run Time Analysis

Due to the underlying method, there is a fundamental distinction between batch processing and recursive estimation of the required run time. The limiting factor is the inversion of an arbitrary $(m \times m)$-matrix. Based on the standard Gauss-Jordan elimination, this requires a complexity of $\mathcal{O}(m^3)$. Even if more efficient methods (e.g., Strassen algorithm with a complexity of $\mathcal{O}(m^{2.807})$) are applied, this is still the limiting factor (Strassen, 1969). For this reason, the required run time in this example also depends strongly on the length of the observation vector l and is given in Table 3.3 as mean values of the $S = 5000$ replications. It should be noted that only relative run times are given since the absolute values depend on the computing capacities used. Therefore, the run times are given as multiples with respect to the fastest solution (recursive C-GHM (COF)). Furthermore, the corresponding standard deviations over the $S = 5000$ replications are given with respect to two different units. Apart from the indication in absolute seconds, the percentage relation to the absolute run times is indicated in an additional column. This allows a better comparison with the relative run times. The disadvantage assumed on the basis of the complexity estimation regarding the necessary run time can be proven with the results presented here. While the GHM uses 2×2500 2D coordinates in batch processing, the recursive GHM contains only 2×25 2D coordinates within each of the 100 epochs k. The relative run time shows that the difference in the number of observations is more decisive than the number of epochs. In this example, it takes much longer to carry out an overall adjustment. The consideration of constraints in batch processing only leads to a

Table 3.3: *Mean relative run times with related standard deviations by means of $S = 5000$ replications for batch processing and different recursive approaches with respect to the fastest solution (recursive C-GHM (COF)). The absolute standard deviations (specified in seconds) are also specified in percent with respect to the absolute run times.*

Method	Run Time $[-]$	$\sigma[s]$	$\sigma[\%]$
batch GHM	44.1	14.8	43.8
batch C-GHM	38.1	11.6	39.7
recursive GHM	1.2	0.2	25.3
recursive C-GHM (PM)	1.2	0.2	20.0
recursive C-GHM (SC)	1.0	0.3	33.9
recursive C-GHM (PRO)	6.2	1.0	20.6
recursive C-GHM (COF)	1.0	0.2	39.7
recursive C-GHM (PT equ.)	7.6	1.4	23.4
recursive C-GHM (PT inequ.)	5.6	1.3	30.0

slight reduction in the run time. Furthermore, there is also a significant variation in the required run times compared to recursive estimation, measured by the standard deviation over all replications. Only minor differences exist within the various options for considering constraints in recursive estimation. Only the methods in which the contradictions are reduced by an additional loop show slightly increased run times. However, these are still significantly lower than with batch processing. The same can also be observed by the respective standard deviations. The general consideration of constraints in the recursive approach, therefore, does not necessarily have to result in a reduction of the run time.

Accuracy Analysis

Since efficiency with regard to the required run time is only one aspect, the estimated parameters $\hat{\boldsymbol{x}}$ (in case of the recursive GHM after the 100-th epoch $\hat{\boldsymbol{x}}_{k=100}$) together with corresponding standard deviations are given in Table 3.4 for both semi-axes a and b together. There are deviations from the true values from the third decimal place onwards. Moreover, the averaged estimates are all greater than the true ones, regardless of the method chosen. The deviations are in the order of magnitude of $0.3 \cdot 10^{-3}$ to $1.6 \cdot 10^{-3}$. While equality constraints improve the estimate of semi-major axis a, they do not improve semi-minor axis b. However, both parameters are highly correlated with each other (described by the eccentricity e (cf. Equation (3.27))). The occurring standard deviations are only slightly higher than the deviations themselves. They show an improvement again if equality constraints are taken into account. If recursive estimation does not take constraints into account at all, the results will be identical to those if soft or inequality constraints are used. The other methods for the consideration of equality constraints provide nearly identical results. However, the most accurate overall results can be achieved with batch processing (especially taking constraints into account). This can be explained by the different process of estimation between batch processing and recursive estimation. While the former takes all observations into account simultaneously, the latter only takes partial quantities within several epochs into account. This epochwise estimation also leads to repeated linearisation (and therefore also more frequent linearisation errors) at different positions. The same conclusions can also be made in the analysis of the Root-Mean-Square Error (RMSE) with respect to the true parameters within Figure 3.8. For the recursive methods, the results thus include the average deviations overall $K = 100$ epochs. In addition, the confidence intervals with a significance level of $\alpha = 5\%$ are also shown here. They also provide a suitable indication of the distribution of the respective methods across the $S = 5000$ replications. These are larger overall for recursive methods, especially if no equality constraints are applied.

Table 3.4: *Mean of the estimated semi-major axis $\bar{a} = 5$ and semi-minor axis $\bar{b} = 3$ together with corresponding standard deviations $\sigma_{\hat{a}}$ and $\sigma_{\hat{b}}$ by means of $S = 5000$ replications batch processing and different recursive approaches with respect to last epoch $k = 100$ in case of recursive estimation*

Method	$\hat{a}$	$\sigma_{\hat{a}}$	$\hat{b}$	$\sigma_{\hat{b}}$
batch GHM	5.0005	$2.6 \cdot 10^{-3}$	3.0004	$1.6 \cdot 10^{-3}$
batch C-GHM	5.0003	$0.8 \cdot 10^{-3}$	3.0005	$1.3 \cdot 10^{-3}$
recursive GHM	5.0016	$3.6 \cdot 10^{-3}$	3.0011	$2.8 \cdot 10^{-3}$
recursive C-GHM (PM)	5.0008	$1.4 \cdot 10^{-3}$	3.0014	$2.4 \cdot 10^{-3}$
recursive C-GHM (SC)	5.0016	$3.5 \cdot 10^{-3}$	3.0011	$2.8 \cdot 10^{-3}$
recursive C-GHM (PRO)	5.0008	$1.4 \cdot 10^{-3}$	3.0014	$2.4 \cdot 10^{-3}$
recursive C-GHM (COF)	5.0008	$1.4 \cdot 10^{-3}$	3.0014	$2.4 \cdot 10^{-3}$
recursive C-GHM (PT equ.)	5.0009	$1.4 \cdot 10^{-3}$	3.0014	$2.4 \cdot 10^{-3}$
recursive C-GHM (PT inequ.)	5.0016	$3.6 \cdot 10^{-3}$	3.0011	$2.8 \cdot 10^{-3}$

Figure 3.8: *Mean of the RMSE by means of S = 5000 replications and the related confidence intervals with a significance level of α = 5 % for the semi-major axis a (blue) and semi-minor axis b (red) for batch processing and different recursive approaches. In case of the recursive approaches, only the results of the last epoch k = 100 are taken into consideration.*

Strictly speaking, the discussed deviations and differences (both between the different methods and with respect to the true values) have to be analysed for significance by using a statistical test. However, the use of a squared test size (which follows the χ^2 distribution) is not applicable here. According to the current state of research, there is simply no probability distribution for parameters estimated in a GHM. Another difficulty is that in the methods presented here, the parameters are additionally affected by non-linear equality and inequality constraints. Thus, a normal distribution can no longer be assumed at the parameter level. To make statistically verified conclusions even in the case of unknown probability distributions, so-called *bootstrap hypothesis testing* according to Efron and Tibshirani (1993, pp. 220 ff.) and MacKinnon (2007) can be applied.

To evaluate the temporal behaviour of the recursive GHM over all $k = 1, \ldots, 100$ epochs, the temporal progression of the RMSE can be analysed. Figures 3.9 and 3.10 also show the corresponding confidence intervals with $\alpha = 5\%$. In the former, the comparison between the GHM without constraints in batch processing and the recursive GHM without constraints is shown separately for both semi-axes. In the second, the difference in consideration of constraints (with respect to the solution with constrained objective function in the recursive case) is shown. As expected, the RMSE is lower if constraints are taken into account, so the solution is more accurate. Overall, the RMSE (and the associated confidence intervals) for all methods decrease significantly within the first epochs and then decrease continuously, apparently against a certain threshold. However, the RMSE of all recursive approaches is greater than that of the batch processing approaches (also taking into account the confidence interval). For a few areas, only the confidence intervals overlap. The confidence interval is larger if no constraints are used and is always larger with the recursive approach compared to the batch approach.

In the following, the corresponding standard deviations of the estimated parameters are shown in Figure 3.11. These are based both on classical error propagation (already given in Table 3.4) and on the application of MC simulation. The comparison between these two methods shows that classical error propagation is too pessimistic for all recursive methods. Thus, the actual standard deviations based on MC simulation (cf. section 3.4.1) are a factor between 0.5 to 0.7 smaller. The cause of these deviations might lie in the propagation of possible linearisation errors or in the implicit filter model, which is based on a transformation of a GHM into a GMM. Moreover, the additional constraints can be another possible cause of this effect. After all, the combination of implicit equations and constraints within a KF has not been investigated before this thesis. The largest deviations occur in methods where no, soft or inequality constraints are applied. As expected, the batch processing approaches are realistic and show negligible differences compared to the MC simulation results.

(a)   (b)
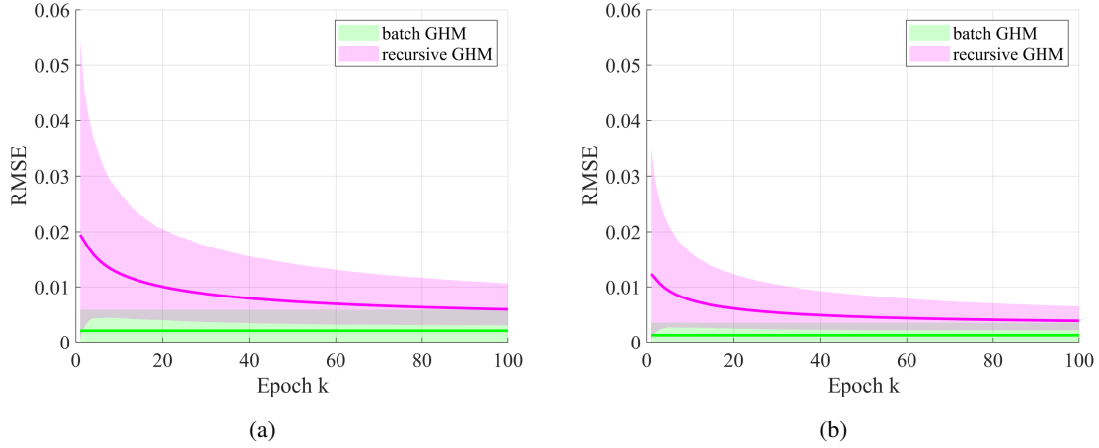
Figure 3.9: *Temporal progression of the mean RMSE (solid lines) and related confidence intervals (coloured areas) with a significance level of $\alpha = 5\,\%$ by means of $S = 5000$ replications. The results for the semi-major axis a are given in (a) and for the semi-minor axis b in (b). Green refers to the solution of the GHM by means of batch processing and magenta refers to the recursive solution of the GHM. The solution of batch processing (green) is represented constantly for all epochs. Constraints are not considered.*

(a)   (b)
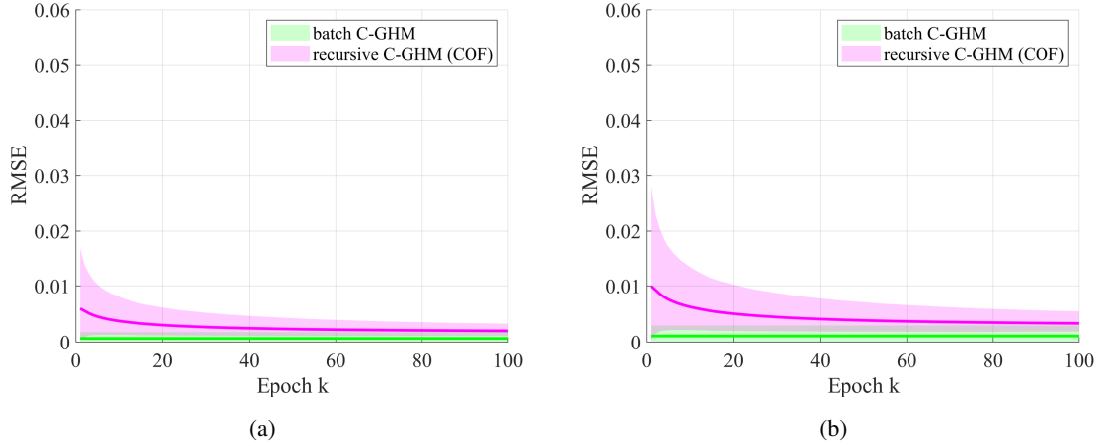
Figure 3.10: *Temporal progression of the mean RMSE (solid lines) and related confidence interval (coloured areas) with a significance level of $\alpha = 5\,\%$ by means of $S = 5000$ replications. The results for the semi-major axis a are given in (a) and for the semi-minor axis b in (b). Green refers to the solution of the C-GHM by means of batch processing and magenta refers to the recursive solution of the C-GHM with COF. The solution of batch processing (green) is represented constantly for all epochs.*

Consistency Check by NEES

Since the recursive methods mentioned here are all based on a recursive filter approach, their consistency must be checked based on the NEES (cf. section 3.4.1). It should be noted that the NEES is defined for explicit measurement equations within the update step of the filter. Besides, the impact of state constraints can also affect the consistency check. Results of this check are given in Figure 3.12. There are different behaviours depending on the method used to consider the constraint. Within the permissible limits, which indicate the consistency of the respective filter depending on the sample size (here: $S = 5000$), there is only the approach without the consideration of constraints, as well as when they are considered as SCs. However, their NEES values are only within the specified limits between epoch 3 to 17 (recursive GHM) and epoch 5 to 14 (recursive C-GHM (SC)) and then fall below the permissible range. The course of both solutions is identical, the use of SCs is only constantly shifted negatively by a small offset of 0.02. If the measurement noise of the SC $\boldsymbol{v}_{d,k}$ is close to zero — which corresponds to PMs — the basic behaviour is comparable to the solutions described above, but clearly shifted by about 0.8 in negative direction. This
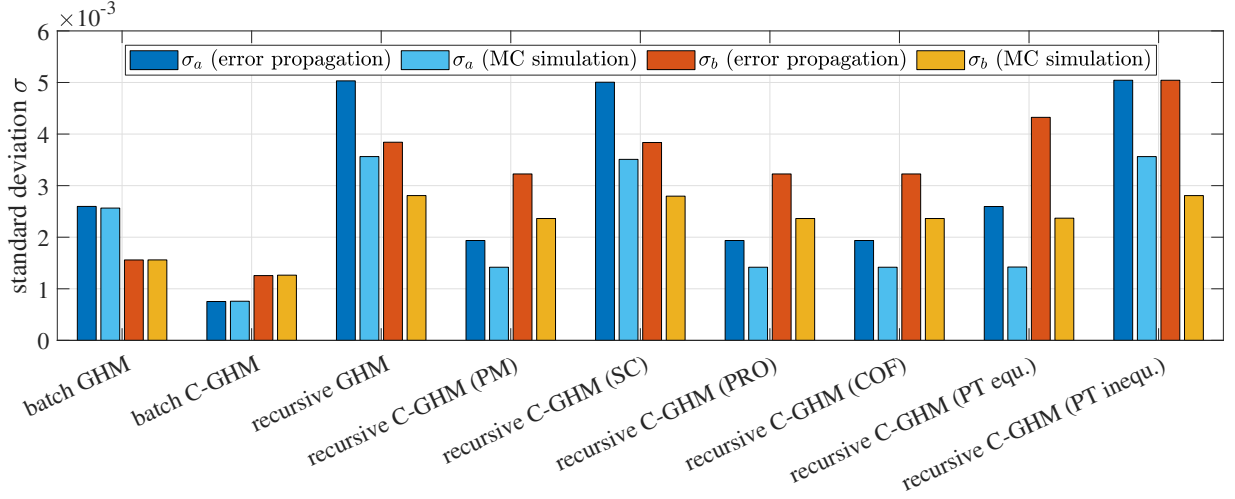
Figure 3.11: *Standard deviations of the semi-major axis a and the semi-minor axis b for batch processing and different recursive approaches. Results are given with respect to classical error propagation (blue and orange) and by means of MC simulation (light blue and yellow).*
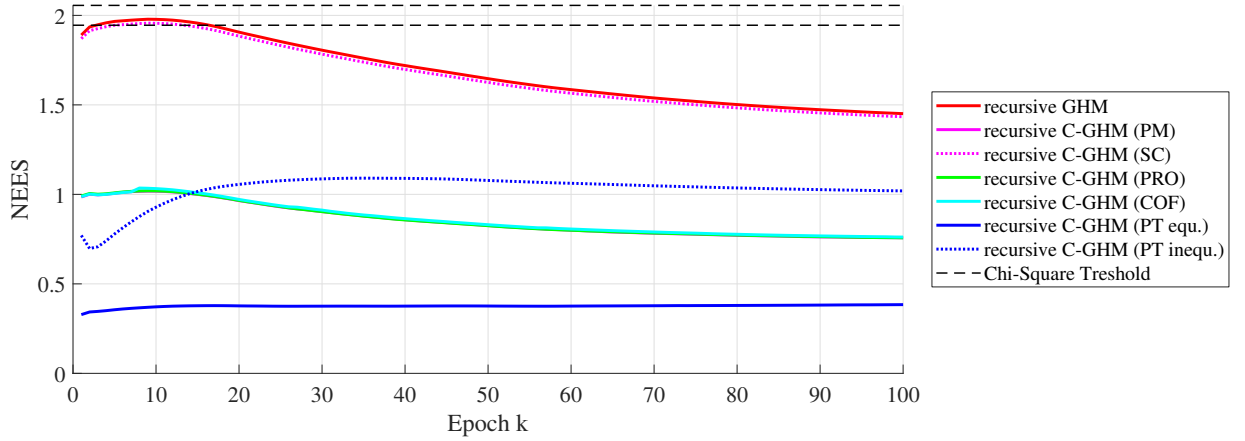
Figure 3.12: *NEES by means of $S = 5000$ replications for different recursive approaches. Thresholds by means of the χ^2 distribution are given by the two black dashed lines*

solution is then almost identical with the PRO method and the approach of the COF (all methods take equality constraints into account). Both approaches for truncation of the PDF show a slightly different progression. While the consideration of equalities within this method leads to the largest deviation from the expected range, the application of inequalities over all epochs K is closer to the boundary than the three other methods for equality constraints. Based on these results, an inconsistent estimation of the recursive filters presented here can be considered. The causes for this cannot be fully clarified at this point. A clear impact of the consideration of constraints on consistency can be recognised. However, the impact of the implicit measurement model is unknown. Model errors can be excluded because of the simple example. Effects caused by linearisation errors cannot be excluded.

Contradiction Analysis

For the sake of completeness, the maximum contradictions over all epochs are shown in Figure 3.13 for the different methods. While most methods have contradictions close to zero, applying the PRO method and applying equality constraints by using the PDF truncation method leads to significantly higher contradictions (cf. Figure 3.13(a)). The reason for this has already been given in section 3.2.3. The
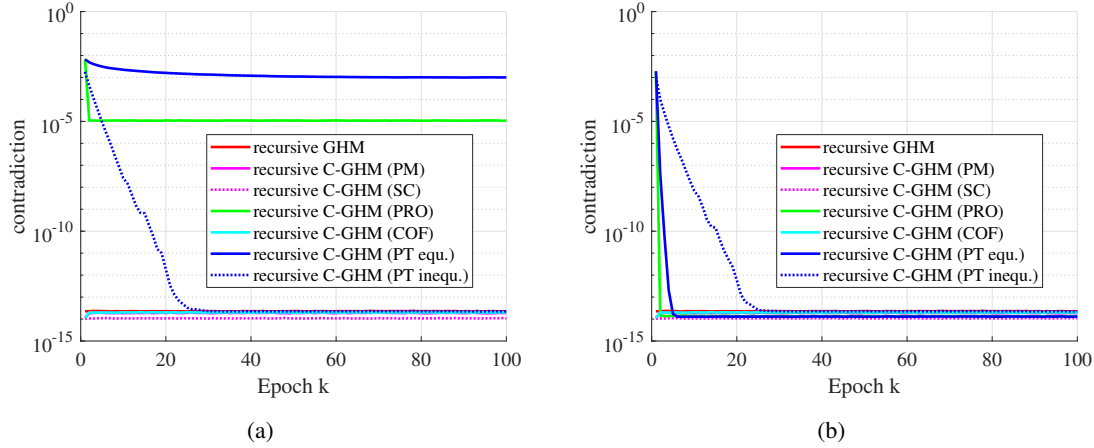
Figure 3.13: *Mean of the maximum contradictions within each epoch k by means of S = 5000 replications for different recursive approaches. The additional contradiction loop described in section 3.2.3 is disregarded in (a) and applied in (b). Note the logarithmic representation of the vertical axis.*

contradictions which are present by PDF truncation with inequality constraints start for the first epoch in the same order of magnitude, but then fall within 25 epochs to the otherwise typical value close to zero. By using the contradiction loop described in section 3.2.3, contradictions in the same range as the other methods (close to zero) can be achieved for the PRO method as well as for the PDF truncation method (cf. Figure 3.13(b)). Here, the number of additional passes of the contradiction loop to reach the targeted order of magnitude varies depending on the respective method and current epoch. The upper limit was set by 20 iterations, which were rarely necessary. In the case of inequality constraints, it is not possible to achieve the typical order of magnitude earlier. Effects on the estimated states and their standard deviations could not be observed. For this reason, it must be taken into account that the fulfilment of the contradictions by the additional contradiction loop has an increase in the run time by a factor of 4 to 5 compared to the non-consideration.

Impact of Wrong Prior Information

The results shown above are based on the assumption that the prior information regarding the constraint applied is valid. In the following, it shall be assumed that the prior information regarding the known eccentricity e between the two semi-axes a and b (cf. Equation (3.27)) is wrong. This results in an inadvertently wrong constraint on the parameters. For this reason, it is necessary to analyse, in accordance with the magnitude of the wrong prior information, the extent, to which the methods presented here for the consideration of state constraints deal with such misinformation. This is a rather important question because it is possible in real applications that prior information is affected by a specific uncertainty and is still available as a possible constraint. To analyse this, the true eccentricity $\bar{e}$ is modified by the percentage factor ϵ according to

$$e = \bar{e} + \bar{e} \cdot \epsilon. \tag{3.41}$$

When the value $\epsilon = 0\,\%$, valid prior information is therefore available. If invalid prior information is taken into account when using equality constraints, this has an immediate negative effect on the estimated values. Based on their mathematical definition, no inaccuracies are allowed, and the corresponding constraint value is assumed to be completely error-free. This has the consequence that the estimation results are strongly influenced by the wrong information, and it leads to wrong results. The magnitude of the deviation depends directly on ϵ. Figure 3.14 shows the deviations from the true values (by means of the RMSE) for the individual methods when $\epsilon = 0.5\,\%$ is selected. In comparison to Figure 3.8, where $\epsilon = 0\,\%$ is valid, the large increase in the methods that take equality constraints into account is obvious. The two methods, which do not take any restrictions into account (batch and recursive GHM), are
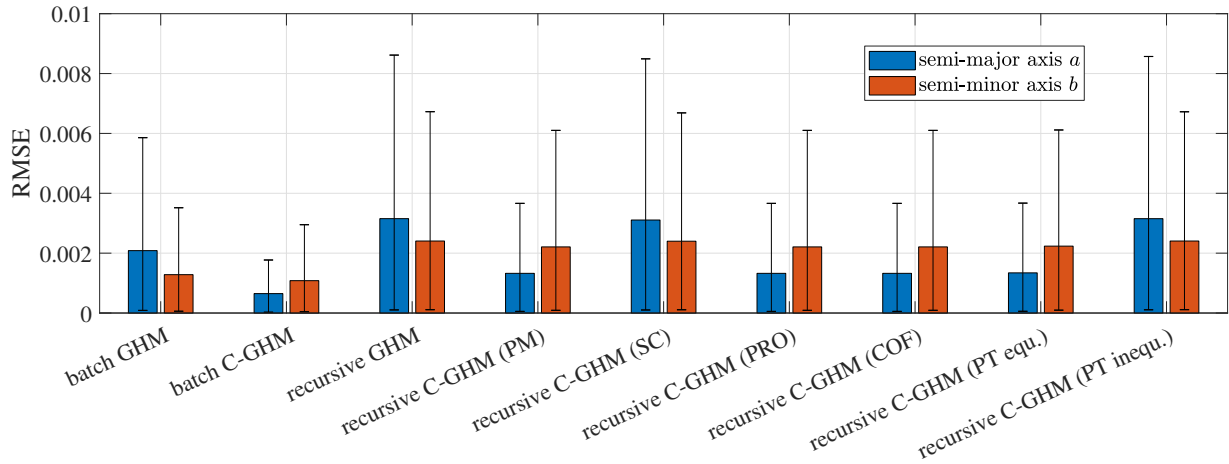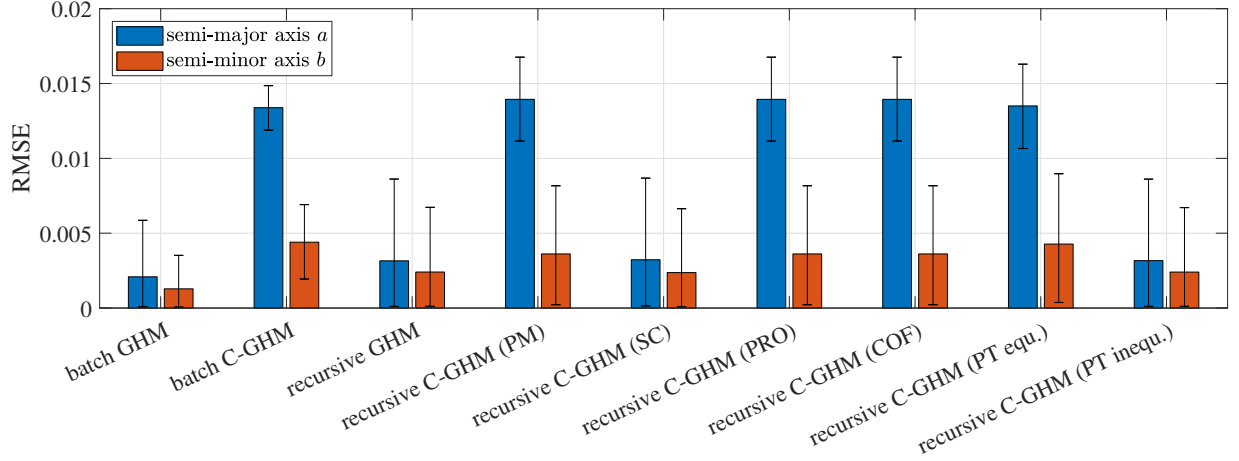
Figure 3.14: *Mean of the RMSE by means of $S = 5000$ replications and related confidence interval with a significance level of $\alpha = 5\,\%$ for the semi-major axis a (blue) and semi-minor axis b (red) for batch processing and different recursive approaches. In case of the recursive approaches, only the results of the last epoch $k = 100$ are taken into consideration. The used prior information with regard to eccentricity is artificially biased by the factor $\epsilon = 0.5\,\%$ according to Equation (3.41).*

consequently unchanged. When using soft and inequality constraints, deviations from the true values can be achieved, which are in the same order of magnitude as the methods without taking constraints into account. These two possibilities to consider constraints do not fail because of the artificially wrong prior information. However, their resistance to wrong information depends on the selected measurement noise $v_{d,k}$ for the SCs and on the limits d_{lower} and d_{upper} for the inequality constraints.

For this reason, the impact of wrong information as well as the respective parameters for its consideration will be varied for both methods in the following. Similar to the percentage factor ϵ for defining the amount of wrong information, the percentage factor δ for the true limits $\bar{d}_{\text{lower}}$ and $\bar{d}_{\text{upper}}$ of the inequalities is defined below

$$d_{\text{lower}} = \bar{d}_{\text{lower}} - \bar{d}_{\text{lower}} \cdot \delta, \tag{3.42a}$$

$$d_{\text{upper}} = \bar{d}_{\text{upper}} + \bar{d}_{\text{upper}} \cdot \delta. \tag{3.42b}$$

Three different gradations of the three relevant influencing factors (ϵ, $v_{d,k}$ and δ) are applied, on the basis of which the state parameters are estimated recursively. The impact of a percentage error $\epsilon = [0\,\%, 0.5\,\%, 1\,\%]$ is investigated. In contrast, the method of SCs with a measurement noise $v_{d,k} = [0, 0.125, 0.25]$ is used. Furthermore, the PDF truncation method uses inequality constraints with a percentage factor $\delta = [0\,\%, 1\,\%, 2\,\%]$. This results in nine different combinations for both methods, which are shown in Figure 3.15 for the application of SCs and in Figure 3.16 for the consideration of inequality constraints. The factor ϵ increases as indicated per column. In the three rows, the consideration of the constrained approaches ($v_{d,k}$ and δ, respectively) increases accordingly as indicated. For all these combinations the estimated states of the two semi-axes a and b are shown. The small blue dots represent the $S = 5000$ individual realisations of the constrained estimation and give information about the distribution. Their mean value is indicated as a green dot. In addition the true value (red dot) and the mean of the recursive solution without the constraint is given (black dot). Additionally, the two-dimensional confidence ellipses with a significance level of $\alpha = 5\,\%$ based on the classical error propagation (blue ellipse) and MC simulation (green ellipse) are given.

As $v_{d,k} = 0$ applies to the complete first row of Figure 3.15, this corresponds directly to the application of PMs. The presence of wrong prior information in this case directly shows the biased estimation of the states. Irrespective of the correctness of the constraint, the consideration of this constraint leads to a linear dependency between the two parameters to be estimated. The disregard of constraints (black dot) is closer to the true value. The confidence ellipses are strongly distorted and extend in a tangential
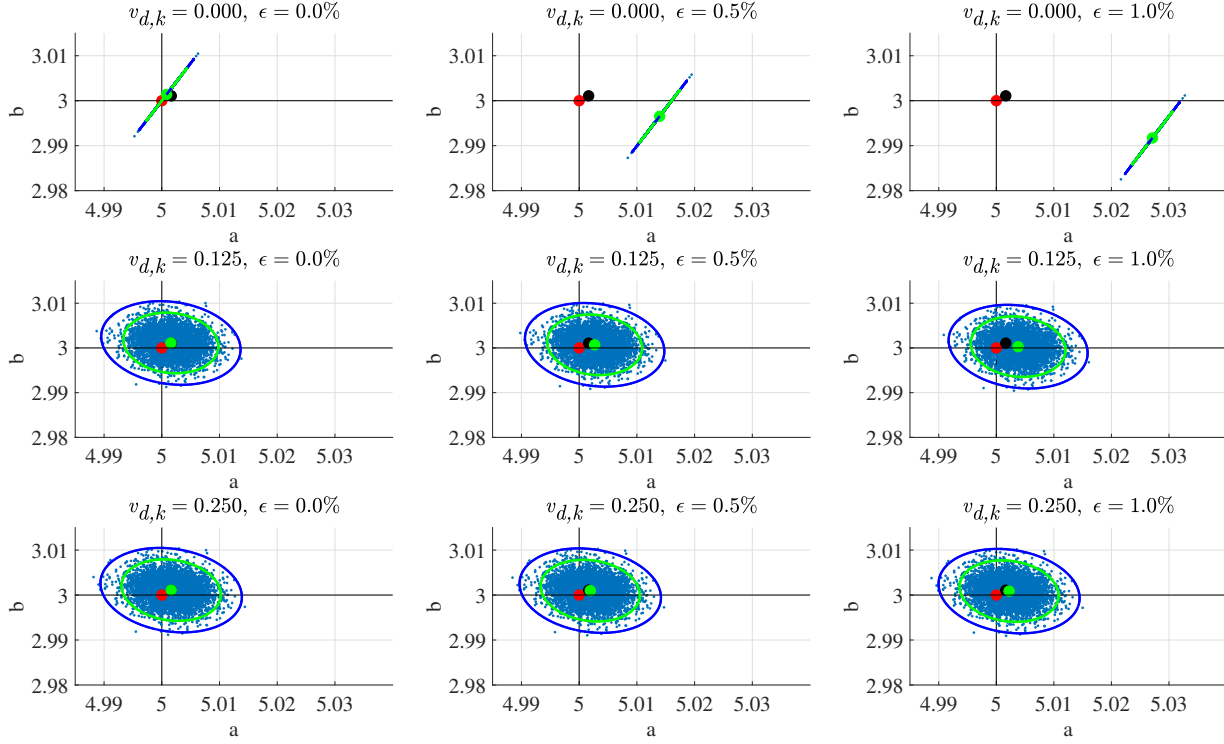
Figure 3.15: *Effect of wrong prior information about the state constraint when using the percentage factor ϵ and applying SCs. The factor ϵ increases per column and the measurement noise $v_{d,k}$ per row. The true value (red dot) and the mean of the constrained approach (green dot) of the two semi-axes a and b is given as well as the mean of the recursive solution without constraints (black dot). The small blue dots represent the $S = 5000$ individual realisations of the constrained estimation. Additionally, the two-dimensional confidence ellipses with a significance level of $\alpha = 5\%$ based on the classical error propagation (blue ellipse) and MC simulation (green ellipse) are given. The axis intervals are identical for all variations.*

direction to the true value. If there is a measurement noise $v_{d,k}$ larger than zero, and thus SCs are present, a more accurate estimation of the states can also be made by using wrong prior information. The extent to which the estimates are closer to the true value than the recursive estimate without any constraints depends on ϵ and $v_{d,k}$. With the factors selected here, recursive estimation without the use of constraints is always at least slightly better as soon as wrong prior information is present. However, if correct prior information is used as a constraint, SCs lead to a more accurate estimation than the complete omission of this additional information. In this case, the use of PMs provides the most accurate estimates. Regardless of the influencing factors varied in Figure 3.15, the pessimistic confidence ellipses based on classical error propagation are noticeable. The distribution of the estimation results based on MC simulation is almost independent of the variations made. Also in Figure 3.16 the first row with $\delta = 0\%$ can be regarded directly as the application of equality constraints with the effects already described. When defining a two-sided interval for the PDF truncation, the wrong prior information can be compensated depending on the selection of δ. In the case described here, δ must be at least twice as large as ϵ in order for the estimate to be at least as accurate as the estimate without constraints. If this is not the case, the estimate becomes more precise (based on the confidence ellipse of the MC simulation) but at the same time less accurate. Simultaneously, an increasing distortion of the estimated values can be observed as the false prior information increases. Overall, the confidence ellipses based on classical error propagation are again too pessimistic, but more circle-shaped compared to the SCs in Figure 3.15. Based on the results, it can be stated that even when using inequality constraints, a more generous selection of δ is reasonable if false prior information is possible. If, on the other hand, these are reliable, no more inaccurate estimates than those obtained by not taking constraints into account are achieved.

Thus, depending on the impact of wrong prior information, the proper selection of $v_{d,k}$ and δ is essential to achieve an accurate and unbiased estimate. At the same time, it should be ensured that an accurate
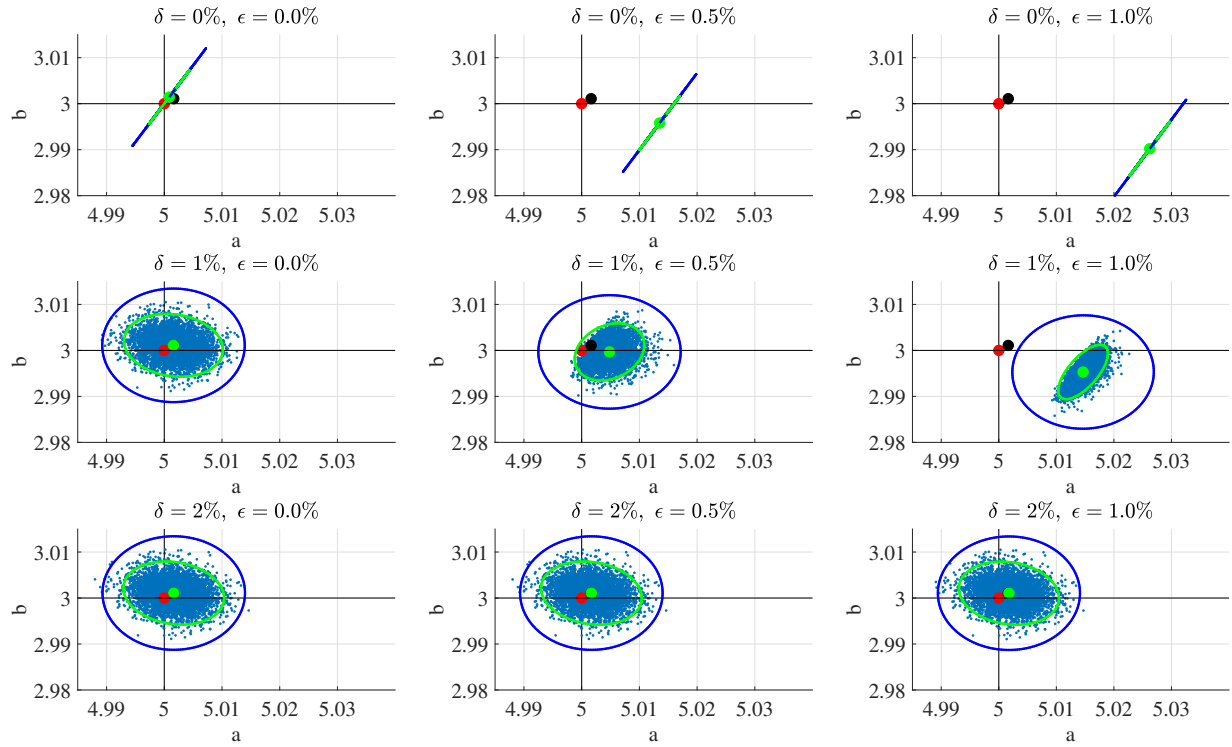
Figure 3.16: *Effect of wrong prior information about the state constraint when using the percentage factor ϵ and applying inequality constraints by means of PDF truncation. The factor ϵ increases per column and the factor δ per row. The true value (red dot) and the mean of the constrained approach (green dot) of the two semi-axes a and b is given as well as the mean of the recursive solution without constraints (black dot). The small blue dots represent the $S = 5000$ individual realisations of the constrained estimation. Additionally, the two-dimensional confidence ellipses with a significance level of $\alpha = 5\%$ based on the classical error propagation (blue ellipse) and MC simulation (green ellipse) are given. The axis intervals are identical for all variations.*

estimate can also be obtained in the case of valid prior information. Thus, Figure 3.17 shows the resulting RMSE for both semi-axes as a function of $v_{d,k}$ (Figure 3.17(a)) and δ (Figure 3.17(b)) for the case when $\epsilon = 0\%$ and thus valid prior information is available. There is a different behaviour for the two semi-axes, but this occurs in both methods. While an increase of the respective influencing factors has only a minor impact on the semi-minor axis b, the RMSE of the semi-major axis a increases significantly. Here, the two methods differ in detail. A threshold of approximately $6 \cdot 10^{-3}$ for a and $4 \cdot 10^{-3}$ for b can be identified when using SCs. Nevertheless, in the case of inequality constraints, there is no clear threshold value in the interval shown. Instead, the RMSE continues to rise monotonously towards the end of the interval shown. In return, the RMSE up to $\delta = 0.3\%$ remains constant for both semi-axes. If valid prior information is available, a measurement noise $v_{d,k}$ greater than zero leads to a larger RMSE. However, this deviation is limited. If inequalities are used, this has no impact up to a value of $\delta = 0.3\%$. Beyond this, the RMSE increases. At this point, it should be mentioned again that these numerical values only apply to this simulation and cannot be directly transferred to other applications.

The findings from Figure 3.17 can also be applied to different realisations of wrong prior information by high-frequency variations of δ. This allows an improved analysis of the effect of all variations on both semi-axes. Thus, the RMSE for the semi-major axis a (Figure 3.18(a)) and the semi-minor axis b (Figure 3.18(b)) are represented as a dependence of $v_{d,k}$ and ϵ when using SCs. The results are averaged over 500 replications. The same is shown in Figure 3.19 depending on δ and ϵ for both semi-axes. Each image is composed of 100×100 pixels, which corresponds to the resolution of each axis. In addition, automatically generated contour lines are specified based on a constant number. The colour representation of the RMSE is limited to the specified interval. In particular for the semi-major axis a the RMSE increases further in the wine-red lower right areas. To ensure comparability, the specified interval is limited.
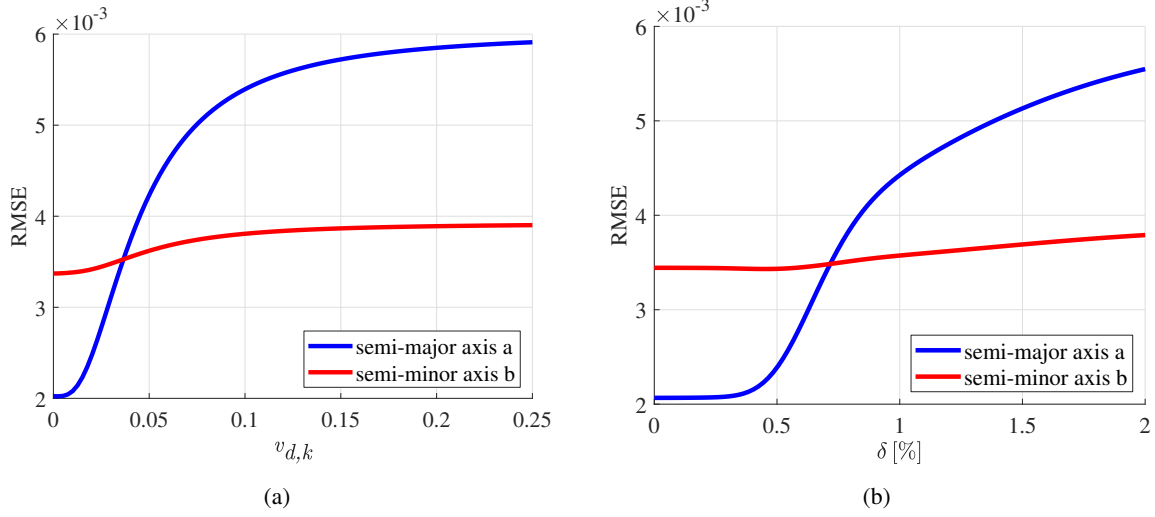
Figure 3.17: *Mean RMSE for both semi-axes a (blue) and b (red) by means of S = 500 replications depending on measurement noise $v_{d,k}$ for SCs (a) and percentage factor δ for inequality constraints (b). Assuming correct prior information when using ε = 0 %.*
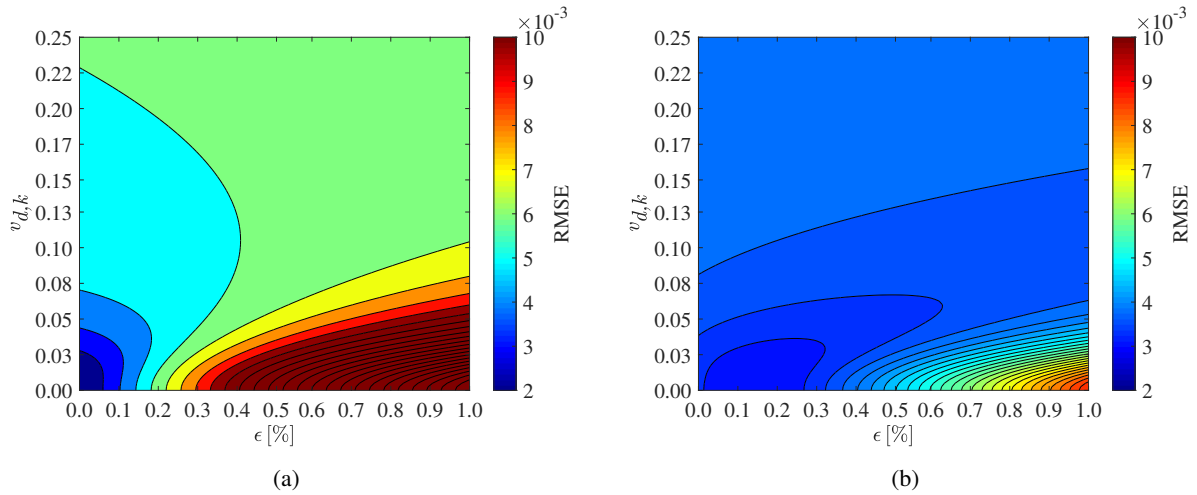
Figure 3.18: *Mean RMSE for various measurement noises $v_{d,k}$ when using SCs and factors ε of wrong prior information by means of 500 replications. The results for the semi-major axis a are given in (a) and for the semi-minor axis b in (b). Automatically generated contour lines are specified based on a constant number. To ensure comparability, the specified interval is limited.*

In principle, both methods show different behaviour depending on the respective semi-axis. The reason for this is the different measuring noise, which is dependent on the respective length of the semi-axis (cf. Equation (3.32)). The semi-major axis a shows a larger RMSE for increasing ε. For the semi-minor axis b, by comparison, an increase of $v_{d,k}$ and δ can lead to a lower RMSE at a lower value. The respective impact on suppressing a wrong prior information in the form of a larger measurement noise $v_{d,k}$ or a larger inequality interval (by means of δ) is thus more noticeable with the semi-minor axis b. In the case of soft constraints, it is also apparent that a small error (ε = 0.02 % to 0.27 %) leads to a lower RMSE compared to ε = 0 %. This can be explained by the strong correlation between the two semi-axes. When using inequality constraints with PDF truncation, the Figure 3.19 shows again that an interval given by δ up to a value of 0.3 % does not affect the RMSE independently of ε. Overall, it can be concluded from the results that the measurement noise $v_{d,k}$ and the inequality interval (by means of δ), should be selected based on the expected degree of error of the prior information (by means of ε).
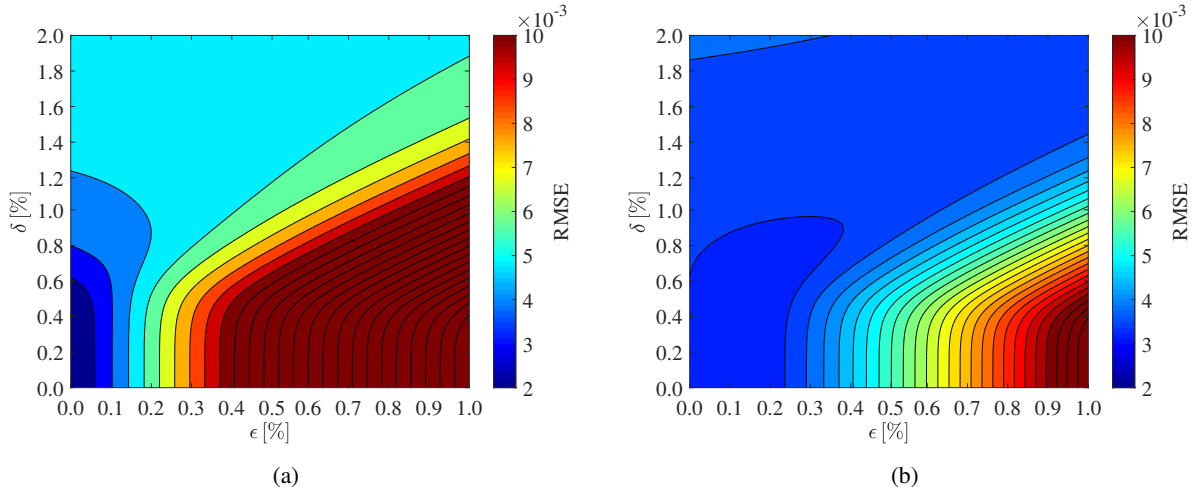
Figure 3.19: *Mean RMSE for various factors δ when using inequality constraints and factors ϵ of wrong prior information by means of* 500 *replications. The results for the semi-major axis a are given in (a) and for the semi-minor axis b in (b). Automatically generated contour lines are specified based on a constant number. To ensure comparability, the specified interval is limited.*

3.4.3 Conclusions

This simulated geometric example was used to validate different approaches for estimating both deterministic parameters (by batch approaches) and probabilistic state parameters (by recursive filter approaches). For this purpose, standard methods from the literature (batch GHM and batch C-GHM) were compared with new adaptations (recursive GHM and recursive C-GHM (PM, SC, PRO, PT equ., PT inequ.)) and own developments (recursive C-GHM (COF)). The used mathematical description of an ellipse (cf. Equation (3.21)) is well suited due to its implicit representation and the possibility to consider the eccentricity as a non-linear constraint of the (state) parameters. Furthermore, the impact of uncertain prior information within the framework of the applied constraints on the respective methods was investigated. The whole investigation represents an innovation both in its individual methods and in its entirety. The combination of an IEKF with implicit measurement equation and the simultaneous consideration of either reliable or uncertain constraints in this form has not yet been investigated. Thus, the newly developed methodology presented in this chapter represents a significant gain when it comes to the recursive solution of implicit problems.

First of all, it should be noted that the fundamental applicability of a recursive GHM could be demonstrated. Furthermore, it has been proven that the recursive methods differ fundamentally from the batch methods with regard to the required computing time. Despite the sequential computations over several epochs, the recursive methods are significantly faster than the batch methods. As mentioned in section 3.4.2, this is due to the different dimensions of the matrices to be inverted.[2] Nevertheless, recursive approaches are more suitable for potential real-time applications. Differences between recursive and batch methods, however, also occur on the basis of the achievable quality measures. The batch methods provide both more accurate (based on the RMSE) and more precise (based on the estimated standard deviations) estimates. At least this applies to the application described here. This is due to the underlying model, where all observations are considered simultaneously. In addition, the estimated standard deviations from the recursive methods are too pessimistic (compared to the MC simulation results). Depending on the application and the respective requirements with regard to maximum run time, accuracy and precision, it is therefore necessary to choose between the different methods. However, if reliable additional prior

---

[2]It should be mentioned that this advantage for recursive methods can be reduced by the integration of matrix calculations on a GPU. This allows more efficient computations compared to the standard execution on a Central Processing Unit (CPU). The calculation on a GPU leads to a significant advantage only for a particular matrix dimension. Below that they are even more inefficient than on a CPU (Ezzatti et al., 2011).

information is available, state constraints always lead to an improvement (in terms of run time, accuracy and precision).

The choice of the method to apply a constraint depends on whether it is to be considered as a hard constraint (as equality or inequality) or SC. This selection, in turn, is strongly related to how certain the prior information is. Soft and inequality constraints lead to accurate estimates, even with uncertain prior information but give slightly inaccurate results for correct prior information. The magnitude depends on the selection of the corresponding parameters $v_{d,k}$ (for SCs) or δ (for inequality constraints). These, in turn, must be carefully selected depending on the application. For all methods used, a final classification is made with regards to three main specifications in Table 3.5. These are the compatibility with certain and uncertain prior information for the use of state constraints, the applicability with regard to big data (rated according to the required run time) and the respective achievable uncertainties of the estimated values.

Table 3.5: *Classification of the methods presented according to possible advantages (+), disadvantages (-) or neutrality (○) with regard to specific prior information, the necessary run time and the uncertainty of the estimated values*

Method	Certain	Uncertain	Run Time	Uncertainty
	prior information			
batch GHM	○	○	-	+
batch C-GHM	+	-	-	+
recursive GHM	○	○	+	○
recursive C-GHM (PM)	+	-	+	○
recursive C-GHM (SC)	○	+	+	○
recursive C-GHM (PRO)	+	-	+	○
recursive C-GHM (COF)	+	-	+	○
recursive C-GHM (PT equ.)	+	-	+	○
recursive C-GHM (PT inequ.)	○	+	+	○

4 Kinematic Multi-sensor Systems and Their Efficient Calibration

In section 3.1 the versatile recursive state-space filter was introduced in its basic idea. This filter is mainly based on the new methods from sections 3.2 and 3.3. In addition to the application example simulated in section 3.4, compatibility with real data is presented in this chapter. For this purpose, the filter is adapted and applied for a calibration task in the context of a kinematic MSS in section 4.2. Apart from the basic applicability, the resulting advantages, as well as possible limitations of this novel innovative recursive approach, will be discussed. A brief introduction to kinematic MSSs and the associated tasks of calibration, georeferencing and processing is given in section 4.1 in advance.

4.1 Kinematic Multi-sensor Systems

An MSS is characterised by the fact that multiple individual sensors are combined in a specific configuration on a common platform. Several sensors of the same type or an arbitrary number of different types can be used. They are connected to each other in a defined, known and consistent spatial and temporal relationship (Schwarz and El-Sheimy, 1996; Lutter and Olson, 2004). In general, any logical aggregation of individual sensors can be referred to as MSS. In the context of this thesis, however, the term is specifically defined and applied to the combination of suitable sensors for solving *georeferencing* tasks. Basically, there are no limitations to the field of application of such an MSS. The concept of georeferencing describes the continuous determination of the position and the orientation of the MSS in an arbitrary superordinate coordinate system at discrete points in time (Gräfe, 2007; Vennegeerts, 2011; Vogel et al., 2016). This information is also referred to as *pose*[1] and describes three translations and three rotations (Borrmann et al., 2008; Vogel et al., 2019). In addition, *localisation* is also referred to as a representative term. Usually, only the 2D position and a single orientation angle are given in this context (Weiss, 2011; Schlichting, 2018). Without the information about the current pose of the MSS with respect to its environment, no further questions (e.g. the combination of laser scanner-based point clouds from two different points in time) can be answered (Elseberg et al., 2013a; Hartmann et al., 2018; Heinz et al., 2020). For the solution of the georeferencing, there are many different methods, which are used depending on the available sensors, the environment and the requested uncertainty requirements. All of them have corresponding advantages and disadvantages (Vogel et al., 2016). An overview of these methods is presented in detail in chapter 5 in direct relation to a specific application.

A basic distinction can be drawn between static and kinematic MSSs. A static MSS remains in a constant pose during the data acquisition by its sensors. A kinematic MSS, by contrast, can change its pose within the environment simultaneously with the acquisition process (Neitzel and Neumann, 2013; Holst et al., 2015). In the following, only kinematic MSSs are considered. In principle, the approaches of this thesis can also be applied to static MSSs. The specific configuration of such a kinematic MSS can vary greatly and depends on the respective application (El-Sheimy, 2005). This applies both to the specific types of sensors and to the applied platform. Any active or passive sensor can be used, which can contribute to the georeferencing task (Vogel et al., 2016). Also, there are no limitations on the type of mobile platform.

---

[1]Also referred to as 6-DoF parameters

An exemplary MSS with several sensors on the roof of a car is shown in Figure 4.1. Without a claim to completeness, the most common sensor types and platform types are listed in the Tables 4.1 and 4.2. This compilation is supplemented by a selection of scientific applications for the respective sensor types and platforms. In addition, there are many other scientific systems as well as a multitude of commercial systems. Their diversity clearly shows the importance and relevance of such kinematic MSSs. The applications cover all areas of georeferencing and environmental perception in the most diverse environments, each with different circumstances and challenges. Thus, they make an important contribution (e.g., in terms of integrity and collaboration) to areas such as mobile mapping, BIM and autonomous driving (Wang et al., 2019).

Even though each kinematic MSS consists of different sensors, there are similarities in the process chain for its application. The necessity of georeferencing has already been mentioned. However, there are also other aspects. Even if different sensors are used (with regard to type and quantity), their spatial and temporal relationship to each other must be known. In order to achieve reliable, accurate and precise results, their correctness, as well as their temporal stability, is essential. Otherwise, their change over time would have to be known and additionally taken into account. However, this is quite a complex challenge, so their temporal stability is usually assumed, and the best possible effort is made to ensure compliance. The temporal relationship between the individual sensors can be realised via a common time base and is referred to as *synchronisation*. Various methods are available for the selection of this time base and its realisation. With current sensors it is easiest to always refer to the Global Positioning System (GPS) time (using the GPS-Pulse Per Second (PPS)) (Hesse, 2007; Toth et al., 2008; Paffenholz, 2012; Schön et al., 2018). The determination of the spatial relations between the individual sensors is referred to as *calibration*. Comparable to the parameters of georeferencing, three translations and three rotations describe the 6-DoF calibration parameters. They can be determined *in advance*[2] with a sensor of superordinate[3] accuracy. These parameters represent the relative dependencies of the individual sensors to each other in an arbitrary homogeneous coordinate system (Strübing and Neumann, 2013). Usually, a so-called Platform Coordinate System (PCS)[4] is defined and used rigidly on the MSS. Furthermore, intrinsic calibration parameters (e.g., biases or scaling parameters) can also be taken into account (Chow et al., 2011; Hartmann et al., 2017), but will not be discussed in the following. Further information on existing calibration approaches and their methodological foundations are addressed in section 4.2.

For each MSS, the acquired heterogeneous observation data of the individual sensors must be stored. State of the art sensors enable continuously increasing sampling rates and resolutions. In addition, previously expensive sensors (e.g. laser scanners) are nowadays much cheaper to purchase. This leads to an increasing amount of data which will be acquired and stored in an MSS and then processed in a later stage. In this
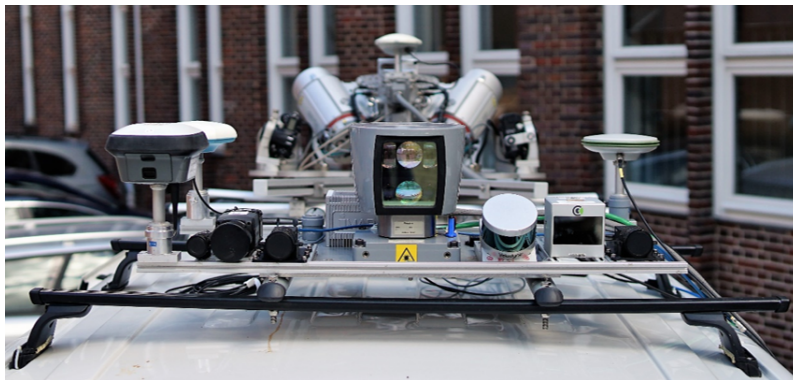
Figure 4.1: *Exemplary MSS on car roof with several sensors fixed to each other on a platform*

---

[2]There are also approaches which estimate the calibration parameters *on-the-fly* during the actual measurement process of the MSS. However, this is rather an exception in the geodetic community and will not be discussed here.

[3]In principle, the reference data can also be acquired with a sensor of comparable accuracy. However, a higher-level accuracy is preferable.

[4]Also referred to as fixed *body coordinate system*

Table 4.1: *Compilation of possible sensor types for kinematic MSSs. In addition, a small selection of applications with a scientific relation is given for the individual types. There is no claim to completeness in this list.*

Sensor	Scientific Application
2D & 3D Laser Scanner	Talaya et al. (2004); Gräfe (2007); Bosse et al. (2012); Keller (2016) Hartmann et al. (2018); Schön et al. (2018); Bureick et al. (2019b); Heinz et al. (2020)
Mono & Stereo Camera	Geiger et al. (2013); Steffen (2013); Schneider et al. (2016); Schön et al. (2018)
GNSS antenna	Sternberg (2000); Talaya et al. (2004); Gräfe (2007); Paffenholz (2012) Schneider et al. (2016); Eling (2016); Schön et al. (2018)
Inertial Measurement Unit	Sternberg (2000); Talaya et al. (2004); Gräfe (2007); Bosse et al. (2012) Schneider et al. (2016); Keller (2016); Schön et al. (2018)

Table 4.2: *Compilation of possible platform types for kinematic MSSs. In addition, a small selection of applications with a scientific relation is given for the individual types. There is no claim to completeness in this list.*

Platform	Scientific Application
Wearable	Bosse et al. (2012); Frei (2013)
Handcart	Vennegeerts (2011); Keller (2016); Hartmann et al. (2018); Heinz et al. (2020)
Unmanned Aerial Vehicle	Nagai et al. (2009); Schneider et al. (2016); Eling (2016); Bureick et al. (2019b)
Motor Car	Gräfe (2007); Jaakkola et al. (2010); Geiger et al. (2013); Hofmann (2017); Schön et al. (2018)

context, *big data* is therefore also referred to. This requires high demands regarding the necessary computing capacities on the one hand and efficient algorithms on the other hand. Especially the use of laser scanners and high-resolution cameras can lead to an enormous amount of observation data (Elseberg et al., 2013b; Schön et al., 2018; Peters and Brenner, 2018). This especially concerns applications in the field of mobile mapping and autonomous driving.

Finally, it can be summarised that for each kinematic MSS identical tasks and challenges regarding calibration, georeferencing and data acquisition, as well as processing, arise. Figure 4.2 visualises this relationship schematically. Parameter estimation is a key factor in each of these three tasks. In all cases, optimal estimated values for different parameters (e.g., 6-DoF calibration parameters or pose parameters of the MSS with respect to a superordinate coordinate system) must be obtained. The following application examples in chapters 4 and 5 show the extent to which the innovations presented in chapter 3 can contribute to improving reliability, uncertainty and efficiency. Moreover, the methods used for this purpose are themselves innovative and novel approaches.

4.2 Calibration of Laser Scanner-based Multi-sensor Systems

4.2.1 Motivation

As already mentioned in section 4.1, reliable and accurate calibration of an MSS is essential. If the exact relative position and orientation of the individual sensors with respect to each other and with respect to a superordinate PCS is unknown, no exact georeferencing of the MSS and accurate subsequent products
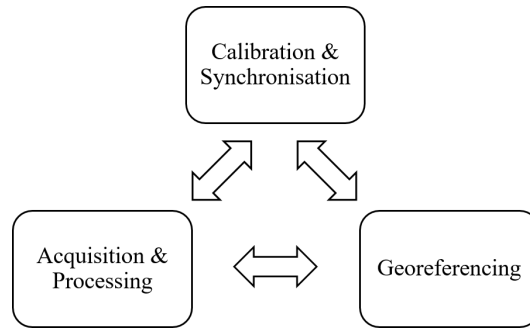
Figure 4.2: *Strongly simplified process chain of a kinematic MSS with its elementary tasks*

(e.g., joint 3D point clouds) will be possible (Elseberg et al., 2013a; Hartmann et al., 2018; Heinz et al., 2020). An insufficient calibration can, therefore, be a limiting factor with regard to the achievable accuracies in such applications since systematic errors are likely (Underwood et al., 2007). For example, an angular deviation of about $0.006°$ already leads to a deviation of $1\,\mathrm{mm}$ on the object at a distance of $10\,\mathrm{m}$. For this reason, there are many methods for the precise and accurate determination of the unknown calibration parameters. However, the method depends strongly on the respective sensor type (cf. Table 4.1) and the equipment available for calibration. The methods described in the following are therefore based on the assumption that a laser tracker with necessary additional equipment (e.g. hand-held probe tip) is available which can be regarded as a referencing sensor with superior accuracy[5]. In principle, other suitable referencing sensors can also be used for the calibration process.

Under these conditions, the calibration parameters of an IMU or GNSS antenna[6] can be obtained relatively straightforward[7]. Specifically, this can be achieved by the respective exterior housing in combination with known construction drawings (in case of an IMU) or defined mounting points (in case of a GNSS antenna) (Schön et al., 2018). For sensors whose local Sensor Own Coordinate System (SOCS) is not exactly specified by the manufacturer — as this is often not technically possible or reasonable —, the calibration parameters must be determined indirectly. The latter applies to cameras and usually also to laser scanners. Where the use of known control points over a resection has proven successful in the case of cameras (Schneider, 2008; Luhmann, 2010, pp. 561 ff.), the use of known reference planes establishes for laser scanners (Gräfe, 2007; Strübing and Neumann, 2013; Strübing, 2015; Heinz et al., 2015; Hartmann et al., 2017; Schön et al., 2018). The continuous further development and improvement of these processes are still ongoing. In particular, there are also methods which directly determine relative extrinsic calibration parameters between a camera and a laser scanner (Zhang and Pless, 2004; Pandey et al., 2012; Zhou et al., 2018; Omidalizarandi et al., 2019). Here the focus lies on the methods that describe the calibration of a laser scanner with respect to a specific PCS. Furthermore, there are also entropy-based approaches to determine the calibration parameters required. These belong to robotics and rely on the minimisation of a cost function that describes the inconsistencies within the point cloud. However, there is a strong dependence on the respective environment. Quality measures are also not directly determined (Maddern et al., 2012; Hillemann et al., 2019; Heinz et al., 2020).

The current state of research on the existing approaches for the calibration of laser scanner-based MSSs is summarised in section 4.2.3. All of them have in common that they determine the estimates within a batch approach (cf. section 2.1). Although this allows an accurate estimate to be made, it also has drawbacks. The high run time required for such an overall adjustment already mentioned in section 3.4 exists, but is not a serious issue. Since the calibration has to be calculated only once in advance, it is not time-critical[8]. Nevertheless, this fact of the high run time remains. Directly related to this run time issue is the associated

---

[5]Accuracy of $\pm 15\,\mathrm{\mu m} + 6\,\mathrm{\mu m/m}$ (as a Maximum Permissible Error (MPE) for the 3D position) (Hexagone Metrology, 2015)

[6]In the context of this thesis, a combination of antenna and receiver is always assumed. However, the geometrically relevant reference point is defined by the antenna phase centre.

[7]Assuming that the respective sensor reference points are already defined in advance by manufacturer's specifications or previous intrinsic sensor calibration

[8]If applications should be attempted to an on-the-fly solution, then the required run time is again important

reduction in the available observation data. With laser scanner-based MSSs, many observation data are acquired which cannot all be included in the adjustment in their entirety. Although this is theoretically feasible, it can lead to numerical instabilities and is therefore not useful. This is because the dimension of the normal equation system to be solved increases with the number of laser scanner points and cannot be solved within a reasonable run time with usual computers. To overcome this problem, an artificial subsampling of the observations is recommended (Hartmann et al., 2017), which can lead to a loss of information. The recursive approach from section 3.3 thus represents a suitable solution for this area of application. With a sequential estimation, all (or at least much more) available observations can be considered. Therefore, the application example in this section also refers to the determination of such a laser scanner-based kinematic MSS, which is introduced in section 4.2.2. The specific realisation for this application is done in sections 4.2.3 (by classical batch methods) and 4.2.4 (by the new recursive methods). A comparison and discussion of both types of methods is given in section 4.2.5.

4.2.2 Experimental Setup

In particular, the SOCS of a *Velodyne Puck VLP-16* laser scanner is to be calibrated with respect to a specific PCS. Furthermore, a *Vectornav VN-200* IMU is mounted on the platform of the MSS, which, however, is neglected in the course of this calibration. As described above, their calibration values can be determined directly and do not represent a difficulty in this context. The platform for mounting the laser scanner has drilling holes that define the PCS (cf. Figure 4.3(a)). By using these drilling holes, the joint adaptation can be applied universally on any other platform. The spatial relationship to the SOCS of the laser scanner can then be established via the drilling holes and the calibration parameters. The platform with the laser scanner is shown in Figure 4.3 together with both PCS and SOCS. The 6-DoF calibration parameters between these two coordinate systems are thus to be determined. The laser scanner used measures with 16 individual scan lines, which are almost perpendicular to its vertical axis and have an angular resolution of around $2°$. The combination of these single scan lines and an internal rotation results in a panoramic 3D point cloud. Altogether, the laser scanner has a field of view of $30° \times 360°$. The manufacturer specifies a range accuracy of typically up to $3\,\mathrm{cm}$ (Velodyne LiDAR, 2018b), without indicating the associated quality parameter. In order to obtain the 6-DoF calibration parameters, the platform is aligned so that the individual scan lines of the laser scanner hit reference planes distributed in the measuring laboratory[9]. It is important to make sure that the planes are properly aligned so that all 6-DoF parameters can be accurately determined. This is ensured by the respective arrangement of the individual planes with respect to the SOCS of the laser scanner (Hartmann et al., 2019; Heinz et al., 2020). There are sensitive tilts for each coordinate axis. In addition, it is also necessary to ensure different distances between the planes and the SOCS. All individual planes are measured with a *Leica Absolute*

(a)   (b)

Figure 4.3: *Laser scanner-based MSS with Velodyne Puck VLP-16 laser scanner and red Vectornav VN-200 IMU on a platform with numbered drilling holes (a) and schematic representation of the MSS with the red PCS and the blue SOCS of the laser scanner (b)*

---

[9]It should be mentioned that due to the measuring distances that arise, not all 16 scan lines necessarily hit all planes. However, it was ensured that at least two scan lines hit each plane.

Tracker AT960, so that high-accurate reference values are known with regard to their plane parameters. This requires only four to five single point measurements per plane. For this purpose, the laser tracker with its specific SOCS defines a superordinate World Coordinate System (WCS). Since the drilling holes on the platform are also measured with the laser tracker, all measured values are located in an identical coordinate system. Additionally, there are only the point cloud observations of the laser scanner, which refer to its SOCS. Several rotations (depending on the rotation rate) of the laser scanner are executed so that there are a multitude of points per scan line and per plane. In the further course, one complete rotation of the laser scanner is referred to as one epoch k. Overall, there are between 500 and 6000 3D points on each plane measured by the laser scanner. The experimental setup itself and the relevant observation variables are shown in Figure 4.4. However, only a part of the complete setup is shown. In total 12 planes were set up in a sub-section of almost $270°$ of the laser scanner's field of view. The complete calibration procedure with regard to the measurement acquisition and the two different adjustment strategies is summarised and shown schematically in Figure 4.5.

4.2.3 Classical Methods

The methodical approach to determine the calibration parameters of a laser scanner-based MSS on the basis of several well distributed reference planes was developed by Strübing and Neumann (2013). They use the restriction that the distances between the observed reference planes and the measured 3D point observations of the laser scanner to be calibrated should be minimal. The corresponding nominal values for the reference geometries are determined on the basis of a sensor of superordinate accuracy. In the application presented here, this is done by a laser tracker. Overall, this method is inspired by the work of Rietdorf (2005) and Gräfe (2007). Both also use reference planes for calibration. While the former only determines intrinsic sensor-specific calibration parameters of a laser scanner, the latter introduces the minimisation condition based on fitting lines. However, a general approach based on a distance function is not described. In addition, the approach by Strübing and Neumann (2013) can also be extended with regard to other geometric primitives such as cylinders or spheres as reference objects to be used. This would only lead to a small adaptation of the functional model and would not have any effects on the calibration process itself. Another approach for the calibration of a laser scanner with respect to a PCS by using a plane and a cylinder is given in Underwood et al. (2007). This also minimises distances. For the cylinder, these are the mean squared perpendicular 2D distances for each laser scanner point (assigned to the cylinder) with respect to the mean value of the total laser scanner points (assigned to the cylinder). The same applies to the plane, where the mean squared 1D distances of each plane point are used for the mean
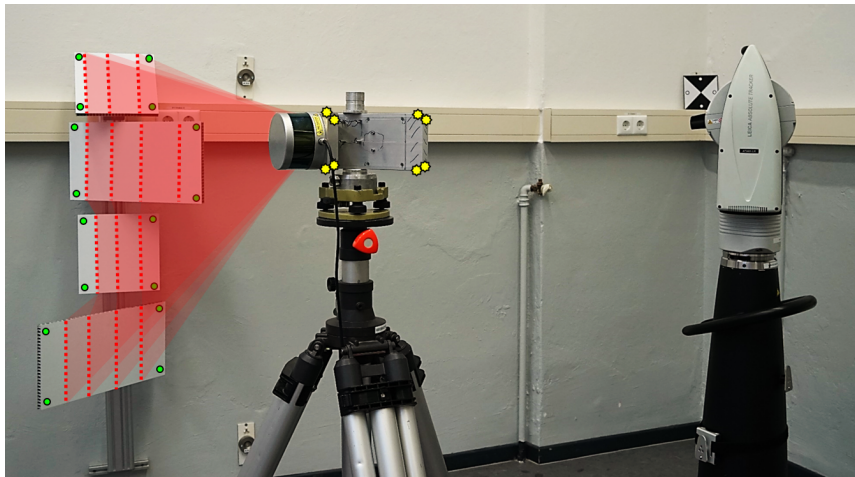
Figure 4.4: *Visualisation of the laser scanner-based MSS (centre) during its calibration. The reference planes (left) are captured by individual scan lines (red dots) and measured (green dots) by the laser tracker (right). In addition, the drilling holes on the platform (yellow stars) are measured with the laser tracker. Further arranged planes are located outside the shown part of the image.*
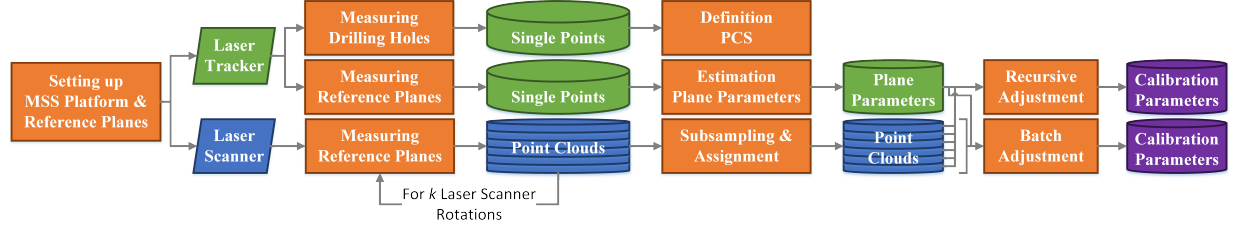
Figure 4.5: *The basic calibration procedure with regard to the measurement execution and the subsequent adjustment strategies. The colours refer to the two sensors (laser scanner (blue) and laser tracker (green)), the required tasks (orange) and the parameters requested (purple).*

value of all plane points. For these reference geometries, in contrast to the method described here, there are no high-accurate reference measurements based on a second sensor of superior accuracy. Instead, only the available observations are used, taking into account the minimisation functions mentioned above. Furthermore, there are also methods where only one single reference plane is used (Wasielewski and Strauss, 1995; Zhang and Pless, 2004; Unnikrishnan and Hebert, 2005; Zhou et al., 2018). This plane is arranged differently one after the other in the calibration process, and thus the necessary geometric configurations can be achieved. However, in these approaches, only the relative extrinsic calibration parameters between a laser scanner and a camera are determined and not the relationship to a superordinate PCS. In addition, these approaches often do not provide complete variance-covariance information.

Further specific applications of the approach from Strübing and Neumann (2013) with regard to the calibration of laser scanner-based MSSs can be found in Heinz et al. (2015) and Hartmann et al. (2017). Independently of the approach used, the 6-DoF calibration parameters requested are composed of the three translations[10] $t_{\text{SOCS-PCS},x}$, $t_{\text{SOCS-PCS},y}$ and $t_{\text{SOCS-PCS},z}$ and the three rotations[11] $\omega_{\text{SOCS-PCS}}$, $\varphi_{\text{SOCS-PCS}}$ and $\kappa_{\text{SOCS-PCS}}$. A scaling parameter is not taken into account as this is negligible due to the sensor mounting. Together, these unknown parameters describe the spatial transformation between the SOCS of the laser scanner and the PCS of the MSS. The alignment of the individual coordinate axes is shown in Figures 4.3(b) and 4.6. The corresponding rotation angles are to be assigned to the individual axes in identical order. For all $j_e = 1, \ldots, J_e$ sets of 3D points $\boldsymbol{P}_{\text{Scanner},e,j_e}$ measured by the laser scanner with respect to its local SOCS and assigned to the $e = \{1, \ldots, 12\}$ individual reference planes, the following applies

$$\underbrace{\begin{bmatrix} x_{\text{MSS},e,j_e} \\ y_{\text{MSS},e,j_e} \\ z_{\text{MSS},e,j_e} \end{bmatrix}}_{\boldsymbol{P}_{\text{MSS},e,j_e}} = \underbrace{\begin{bmatrix} t_{\text{SOCS-PCS},x} \\ t_{\text{SOCS-PCS},y} \\ t_{\text{SOCS-PCS},z} \end{bmatrix}}_{\boldsymbol{t}_{\text{SOCS-PCS}}} + \boldsymbol{R}_{\text{SOCS-PCS}}\left(\boldsymbol{\theta}_{\text{SOCS-PCS}}\right) \cdot \underbrace{\begin{bmatrix} x_{\text{Scanner},e,j_e} \\ y_{\text{Scanner},e,j_e} \\ z_{\text{Scanner},e,j_e} \end{bmatrix}}_{\boldsymbol{P}_{\text{Scanner},e,j_e}}, \tag{4.1}$$

where $\boldsymbol{P}_{\text{MSS},e,j_e}$ are the transformed laser scanner 3D points with respect to the PCS. It should be noted that J_e can be different for each plane e. Furthermore, $\boldsymbol{R}_{\text{SOCS-PCS}}$ describes the 3D rotation matrix[12] composed of the calibration angles $\boldsymbol{\theta}_{\text{SOCS-PCS}} = [\omega_{\text{SOCS-PCS}}, \varphi_{\text{SOCS-PCS}}, \kappa_{\text{SOCS-PCS}}]^T$. The following relationship applies

$$\boldsymbol{R}_{\text{SOCS-PCS}}\left(\boldsymbol{\theta}_{\text{SOCS-PCS}}\right) = \boldsymbol{R}_{x,\text{SOCS-PCS}}\left(\omega_{\text{SOCS-PCS}}\right) \cdot \boldsymbol{R}_{y,\text{SOCS-PCS}}\left(\varphi_{\text{SOCS-PCS}}\right) \cdot \boldsymbol{R}_{z,\text{SOCS-PCS}}\left(\kappa_{\text{SOCS-PCS}}\right), \tag{4.2}$$

which defines the concatenation of the individual rotation angles around the corresponding rotation axes. As additional information, the four to five sets of 3D points $\boldsymbol{P}_{\text{RFG},e}$ measured by the laser tracker on the individual reference plane e as well as the 3D points $\boldsymbol{P}_{\text{PCS}}$ of the drilling holes of the MSS platform are available. Both types of 3D point coordinates are given with respect to the WCS of the laser tracker. Based on the point observations of the reference planes, related plane parameters in the Hesse normal form can be

---

[10]Also referred to as *lever arms*

[11]Also referred to as *bore-sight angles* and indicated here as Euler angles

[12]When generating rotation matrices, the correct sequence of the individual rotations around the corresponding axes must always be taken into account. It is also important to consider that the Euler angles are given with respect to fixed or co-rotating axes.

determined[13]. These are composed of a 3×1 unit normal vector $\boldsymbol{n}_{\mathrm{RFG},e} = [n_{\mathrm{RFG},e,x}, n_{\mathrm{RFG},e,y}, n_{\mathrm{RFG},e,z}]^T$ as well as a distance to the origin $d_{\mathrm{RFG},e}$ for each of the e planes and can be determined according to Drixler (1993), for example. This information is summarised for each plane in the vector $\boldsymbol{a}_{\mathrm{RFG},e}$ according to

$$\boldsymbol{a}_{\mathrm{RFG},e} = [\boldsymbol{n}_{\mathrm{RFG},e}; d_{\mathrm{RFG}e}] \tag{4.3}$$

and the following applies

$$||\boldsymbol{n}_{\mathrm{RFG},e}|| = \sqrt{n_{\mathrm{RFG},e,x}^2 + n_{\mathrm{RFG},e,y}^2 + n_{\mathrm{RFG},e,z}^2} = 1. \tag{4.4}$$

A further transformation is necessary to establish the relationship between the plane parameters $\boldsymbol{a}_{\mathrm{RFG},e}$ measured by the laser tracker and the original laser scanner observations. Therefore, the following applies to the transformation of the laser scanner observations with reference to the PCS of the MSS (already available with Equation (4.1)) into the WCS of the laser tracker

$$\underbrace{\begin{bmatrix} x_{\mathrm{LT},e,j_e} \\ y_{\mathrm{LT},e,j_e} \\ z_{\mathrm{LT},e,j_e} \end{bmatrix}}_{\boldsymbol{P}_{\mathrm{LT},e,j_e}} = \underbrace{\begin{bmatrix} t_{\mathrm{PCS\text{-}WCS},x} \\ t_{\mathrm{PCS\text{-}WCS},y} \\ t_{\mathrm{PCS\text{-}WCS},z} \end{bmatrix}}_{\boldsymbol{t}_{\mathrm{PCS\text{-}WCS}}} + \boldsymbol{R}_{\mathrm{PCS\text{-}WCS}}\left(\boldsymbol{\theta}_{\mathrm{PCS\text{-}WCS}}\right) \cdot \begin{bmatrix} x_{\mathrm{MSS},e,j_e} \\ y_{\mathrm{MSS},e,j_e} \\ z_{\mathrm{MSS},e,j_e} \end{bmatrix}, \tag{4.5}$$

where $\boldsymbol{P}_{\mathrm{LT},e,j_e}$ defines the measurements of the reference planes by the laser scanner which are transformed into the WCS of the laser tracker. The vectors $\boldsymbol{t}_{\mathrm{PCS\text{-}WCS}}$ and $\boldsymbol{\theta}_{\mathrm{PCS\text{-}WCS}} = [\omega_{\mathrm{PCS\text{-}WCS}}, \varphi_{\mathrm{PCS\text{-}WCS}}, \kappa_{\mathrm{PCS\text{-}WCS}}]^T$ contain the corresponding 6-DoF transformation parameters and $\boldsymbol{R}_{\mathrm{PCS\text{-}WCS}}\left(\boldsymbol{\theta}_{\mathrm{PCS\text{-}WCS}}\right)$ is calculated analogously to Equation (4.2). Overall, the approach of Strübing and Neumann (2013) to determine the required calibration parameters is thus based on a two-fold transformation. Their order and corresponding relationships are described in the Equations (4.1) and (4.5) and are schematically summarised in Figure 4.6. The parameters of the second transformation between the PCS and the WCS are directly determined by the laser tracker. As already mentioned, the parameters of the first transformation (from the SOCS of the laser scanner to the PCS of the MSS) have to be determined during the calibration process. In order to obtain these parameters, the approach of Strübing and Neumann (2013) solves the calibration task by restricting the distances d_{j_e} within a GHM (cf. section 2.1.2). The functional relationship between the observations and parameters according to Equation (2.21) is as follows

$$d_{j_e} = 0 = h_{j_e}\left(\boldsymbol{P}_{\mathrm{Scanner},e,j_e}, \boldsymbol{a}_{\mathrm{RFG},e}, \boldsymbol{t}_{\mathrm{SOCS\text{-}PCS}}, \boldsymbol{\theta}_{\mathrm{SOCS\text{-}PCS}}, \boldsymbol{t}_{\mathrm{PCS\text{-}WCS}}, \boldsymbol{\theta}_{\mathrm{PCS\text{-}WCS}}\right) \tag{4.6a}$$

$$= \boldsymbol{n}_{\mathrm{RFG},e}^T \cdot \boldsymbol{P}_{\mathrm{LT},e,j_e} - d_{\mathrm{RFG}e} \tag{4.6b}$$

$$= \begin{bmatrix} n_{\mathrm{RFG},e,x} \\ n_{\mathrm{RFG},e,y} \\ n_{\mathrm{RFG},e,z} \end{bmatrix}^T \cdot \begin{bmatrix} x_{\mathrm{LT},e,j_e} \\ y_{\mathrm{LT},e,j_e} \\ z_{\mathrm{LT},e,j_e} \end{bmatrix} - d_{\mathrm{RFG}e}, \tag{4.6c}$$

where the distances d_{j_e} are to be interpreted as contradictions of the GHM. This is an implicit relationship between the observations and parameters according to Equation (2.21). The observed quantities in this GHM are arranged in the observation vector $\boldsymbol{l}$ as follows

$$\boldsymbol{l} = \left[\boldsymbol{P}_{\mathrm{Scanner},1,1:J_e}^T, \ldots, \boldsymbol{P}_{\mathrm{Scanner},12,1:J_e}^T, \boldsymbol{a}_{\mathrm{RFG},1}^T, \ldots, \boldsymbol{a}_{\mathrm{RFG},12}^T, \boldsymbol{t}_{\mathrm{PCS\text{-}WCS}}^T, \boldsymbol{\theta}_{\mathrm{PCS\text{-}WCS}}^T\right]^T. \tag{4.7}$$

Both the plane parameters $\boldsymbol{a}_{\mathrm{RFG},e}$ as well as the translations $\boldsymbol{t}_{\mathrm{PCS\text{-}WCS}}$ and rotations $\boldsymbol{\theta}_{\mathrm{PCS\text{-}WCS}}$ are considered to be original observations. This leads to a reduced adjustment problem and is recommended due to

---

[13]In principle, the parametrisation of a plane can also be done in other ways. In Unger et al. (2016), for example, two angles and a single shift parameter are suggested for this purpose. Thus, the number of parameters to be estimated can be reduced (if the plane parameters are part of the parameter vector $\boldsymbol{x}$).
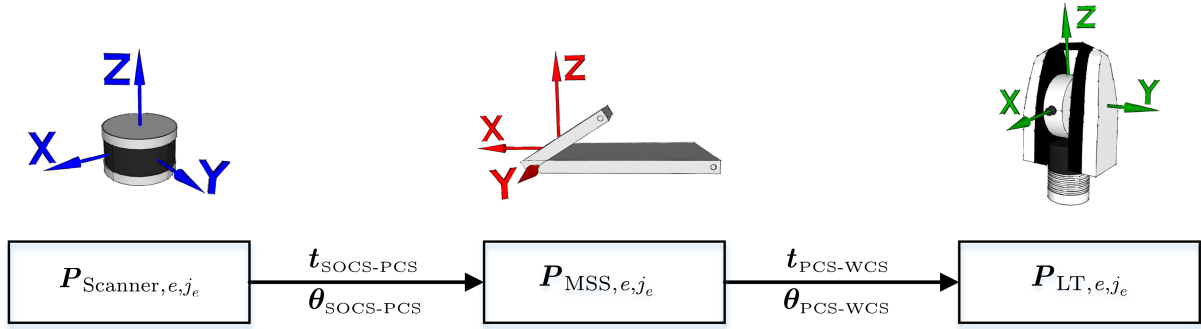
Figure 4.6: *Schematic representation of the transformations to be applied during the calibration. The original 3D point observations of the laser scanner $P_{Scanner,e,j_e}$ are available with respect to its SOCS, are then transformed into the PCS of the MSS (P_{MSS,e,j_e}) and finally transformed into the WCS of the laser tracker (P_{LT,e,j_e}).*

the high information density that already occurs (Strübing and Neumann, 2013). Associated uncertainty information of the individual observation groups is given in the VCM Σ_{ll} with a block structure as follows

$$\Sigma_{ll} = \begin{bmatrix} \Sigma_{ll,P_{Scanner,1,1:J_e}} & \cdots & 0 & 0 & \cdots & 0 & 0 & 0 \\ \vdots & \ddots & \vdots & \vdots & \ddots & \vdots & \vdots & \vdots \\ 0 & \cdots & \Sigma_{ll,P_{Scanner,12,1:J_e}} & 0 & \cdots & 0 & 0 & 0 \\ 0 & \cdots & 0 & \Sigma_{ll,a_{RFG,1}} & \cdots & 0 & 0 & 0 \\ \vdots & \ddots & \vdots & \vdots & \ddots & \vdots & \vdots & \vdots \\ 0 & \cdots & 0 & 0 & \cdots & \Sigma_{ll,a_{RFG,12}} & 0 & 0 \\ 0 & \cdots & 0 & 0 & \cdots & 0 & \Sigma_{ll,t_{PCS-WCS}} & 0 \\ 0 & \cdots & 0 & 0 & \cdots & 0 & 0 & \Sigma_{ll,\theta_{PCS-WCS}} \end{bmatrix}. \quad (4.8)$$

The quantities to be estimated are in turn summarised in the parameter vector x. Since individual elements from the observation vector l are derived quantities, they are also contained in the parameter vector x so that they can be updated as part of the adjustment. The following applies

$$x = \begin{bmatrix} t^T_{SOCS-PCS}, \theta^T_{SOCS-PCS}, a^T_{RFG,1}, \ldots, a^T_{RFG,12}, t^T_{PCS-WCS}, \theta^T_{PCS-WCS} \end{bmatrix}^T. \quad (4.9)$$

As already stated in section 2.1.2, suitable approximate values x_0 are required to solve this GHM. These can be based on rough dimensions and can be updated after a successful adjustment, if necessary. As the functional model is based on the planarity of the individual reference planes, it should be noted that compliance with this model is a prerequisite for obtaining reliable estimates. The parameters requested can then be obtained iteratively by solving the normal equation system according to Equation (2.30) and considering Equation (2.35a).

Although the plane parameters $a_{RFG,e}$ are also contained in the parameter vector x, there is no constraint in Strübing and Neumann (2013) regarding their normalised length (cf. Equation (4.4)). For the shown application with a 2D profile laser scanner this is reasonable, because with this measuring technique precise plane estimation is possible. Hartmann et al. (2017) also omit the introduction of such a constraint, which might also be due to the use of a laser scanner in profile mode. Furthermore, they generally excluded the plane parameters from the observation and parameter vector. This is justified by the superior accuracy of the coordinates observed by the laser tracker. Instead, the plane parameters are thus regarded as quasi error-free quantities which are known and constant. Within the framework of a general approach, an additional constraint of the plane parameters according to Equation (4.4) should be considered. In principle, this calibration approach can also be used for 3D laser scanners where it would make sense to apply such a constraint. The application of such a constraint concerning the plane parameters is also used

in Skaloud and Lichti (2006) for the determination of the bore-sight angles within airborne laser scanning. Therefore, Equation (4.4) must be expressed according to Equation (2.38), from which follows

$$g_e\left(\boldsymbol{x}\right) = \sqrt{n_{\mathrm{RFG},e,x}^2 + n_{\mathrm{RFG},e,y}^2 + n_{\mathrm{RFG},e,z}^2} = 1, \tag{4.10}$$

where $g_e\left(\boldsymbol{x}\right)$ is the non-linear constraint function for the respective plane e. The adjustment problem can then be solved according to Equation (2.46). Its impact on the estimation is shown in section 4.2.5 based on the calibration task introduced in section 4.2.2.

The general ability to solve the resulting normal equation matrix depends strongly on the available computing capacities and the amount of 3D laser scanner observations J assigned to the individual planes e. The *Velodyne Puck VLP-16* laser scanner used in this experiment measures approximately 300 000 points per second (Velodyne LiDAR, 2018b). The rotation rate can be selected between 5 Hz to 20 Hz, resulting in 15 000 to 60 000 single 3D points per 360° rotation[14]. If the dimension of the normal equation system becomes too large with respect to the available computing power, numerical instabilities are likely. For this reason, Hartmann et al. (2017) proposes the artificial reduction of the available laser scanner observational data. This subsampling results in the loss of existing observation data. The level of reduction depends on the existing total number of 3D points, the number of reference planes, as well as the available computing capacities, and is, therefore, application and hardware dependent. However, artificial reduction also has a positive impact since the same number of laser scanner observations are available for each plane. This supports the weighting between the individual planes, which would otherwise depend strongly on the distance and alignment to the laser scanner.

4.2.4 Novel Recursive Calibration Approach

The loss of information occurring in the classical calibration method from section 4.2.3 (due to the necessary subsampling) can be avoided when using the recursive approach for implicit relationships from section 3.3. The necessity of the novel approach presented in this thesis is caused by the implicit relationship according to Equation (4.6). At the same time, the positive impact in terms of equal weighting of the individual reference planes can be maintained. For the application of the recursive GHM, the total number of available laser scanner observations is, therefore, subdivided into $k = 1, \ldots, K$ individual epochs. With regard to the experimental setup described in section 4.2.2, a complete 360° rotation of the laser scanner is suitable for the definition of one single epoch k. During such a certain epoch k, the respective 3D point cloud is assigned to the individual reference planes. Thus, there are for each epoch k in total $n_e = 1, \ldots, N_e$ 3D laser scanner observations on each plane e, where N_e can be different for each of the 12 planes in total and must not be constant for each epoch k. If N_e equals J_e, the recursive calibration approach is identical to the classical batch approach. Thus the following observation vector $\boldsymbol{l}_k$ results in dependence of the respective epoch k

$$\boldsymbol{l}_{k=1} = \left[\boldsymbol{P}_{\mathrm{Scanner},k,1,1:N_e}^T, \ldots, \boldsymbol{P}_{\mathrm{Scanner},k,12,1:N_e}^T, \boldsymbol{a}_{\mathrm{RFG},k,1}^T, \ldots, \boldsymbol{a}_{\mathrm{RFG},k,12}^T, \boldsymbol{t}_{\mathrm{PCS\text{-}WCS},k}^T, \boldsymbol{\theta}_{\mathrm{PCS\text{-}WCS},k}^T\right]^T. \tag{4.11}$$

In general, both the plane parameters $\boldsymbol{a}_{\mathrm{RFG},k,e}$ and the transformation parameters $\boldsymbol{t}_{\mathrm{PCS\text{-}WCS},k}$ and $\boldsymbol{\theta}_{\mathrm{PCS\text{-}WCS},k}$ from the PCS to the WCS can be observed and considered in each epoch k. For practical reasons in the experimental procedure, it is also possible to proceed with a shortened observation vector $\boldsymbol{l}_k$ for epochs $k > 1$

$$\boldsymbol{l}_{k>1} = \left[\boldsymbol{P}_{\mathrm{Scanner},k,1,1:N_e}^T, \ldots, \boldsymbol{P}_{\mathrm{Scanner},k,12,1:N_e}^T\right]^T. \tag{4.12}$$

---

[14]The number of points assigned to the planes is smaller, but in this application it is still about 500 3D points per 360° rotation

As a consequence of the recursive approach, the parameters will be estimated for each individual epoch k and are gathered in the state parameter vector $\boldsymbol{x}_k$ as follows

$$\boldsymbol{x}_k = \left[\boldsymbol{t}^T_{\text{SOCS-PCS},k}, \boldsymbol{\theta}^T_{\text{SOCS-PCS},k}, \boldsymbol{a}^T_{\text{RFG},k,1}, \ldots, \boldsymbol{a}^T_{\text{RFG},k,12}, \boldsymbol{t}^T_{\text{PCS-WCS},k}, \boldsymbol{\theta}^T_{\text{PCS-WCS},k} \right]^T . \tag{4.13}$$

Thus, the only difference to the batch approach from section 4.2.3 is that here the parameters for several consecutive epochs k are determined and that corresponding subsets of observations are available. Since this recursive GHM is based on a filter approach, it is also necessary to specify uncertainties regarding the state parameters by means of the VCM $\boldsymbol{\Sigma}_{\boldsymbol{xx},k}$ for initialisation, resulting in

$$\boldsymbol{\Sigma}_{\boldsymbol{xx},k} = \begin{bmatrix} \boldsymbol{\Sigma}_{\boldsymbol{xx},k,\boldsymbol{t}_{\text{SOCS-PCS}}} & \boldsymbol{0} & \boldsymbol{0} & \ldots & \boldsymbol{0} & \boldsymbol{0} & \boldsymbol{0} \\ \boldsymbol{0} & \boldsymbol{\Sigma}_{\boldsymbol{xx},k,\boldsymbol{\theta}_{\text{SOCS-PCS}}} & \boldsymbol{0} & \ldots & \boldsymbol{0} & \boldsymbol{0} & \boldsymbol{0} \\ \boldsymbol{0} & \boldsymbol{0} & \boldsymbol{\Sigma}_{\boldsymbol{xx},k,\boldsymbol{a}_{\text{RFG},1}} & \ldots & \boldsymbol{0} & \boldsymbol{0} & \boldsymbol{0} \\ \vdots & \vdots & \vdots & \ddots & \vdots & \vdots & \vdots \\ \boldsymbol{0} & \boldsymbol{0} & \boldsymbol{0} & \ldots & \boldsymbol{\Sigma}_{\boldsymbol{xx},k,\boldsymbol{a}_{\text{RFG},12}} & \boldsymbol{0} & \boldsymbol{0} \\ \boldsymbol{0} & \boldsymbol{0} & \boldsymbol{0} & \ldots & \boldsymbol{0} & \boldsymbol{\Sigma}_{\boldsymbol{xx},k,\boldsymbol{t}_{\text{PCS-WCS}}} & \boldsymbol{0} \\ \boldsymbol{0} & \boldsymbol{0} & \boldsymbol{0} & \ldots & \boldsymbol{0} & \boldsymbol{0} & \boldsymbol{\Sigma}_{\boldsymbol{xx},k,\boldsymbol{\theta}_{\text{PCS-WCS}}} \end{bmatrix} . \tag{4.14}$$

The VCM $\boldsymbol{\Sigma}_{\boldsymbol{ww},k}$ of the process noise is also specified with a dimension that corresponds to the state vector. The solution of this recursive GHM is based on section 3.3. As already mentioned in section 4.2.3 for the classical method, it is recommended to consider constraints for the plane parameters according to Equation (4.10) also in this recursive approach. Therefore, these are considered for each individual epoch k. Various methods for considering these constraints in the context of implicit relationships are given in section 3.2. Since Equation (4.10) specifies an equality constraint according to section 2.3.1, only the PRO method (cf. section 3.2.3), the introduction of PMs (cf. section 3.2.1) or the application of the COF method (cf. section 3.2.2) are suitable. However, the results in the following section 4.2.5 are limited to the application of the last two methods, as all methods produce basically similar results.

The data set for the calibration of the laser scanner-based MSS (cf. section 4.2.2) is based on Ernst (2019). In addition, Ernst (2019) also describes the recursive estimation of the calibration parameters requested. However, the simultaneous use of constraints regarding the length of the plane normal vectors (cf. Equation (4.10)) leads to numerical instabilities. For this reason Ernst (2019) uses an extended measurement model compared to Equation (4.6), which causes a normalisation of the plane parameters. This procedure proves to be successful (also with respect to the classical solution of the normal GHM according to section 2.1.2). However, this approach is limited to the use of planes as reference geometries and is not versatile. Furthermore, any other constraints cannot be considered in this way. Therefore, the following solutions are shown, which are completely independent of the type of constraint and can therefore be used in many other applications and situations. In principle, it is also possible to extend the whole adjustment model (both in the batch and recursive approach) with regard to the simultaneous consideration of several individual calibration positions of the MSS. Thus, an excellent coverage of all necessary sensitive geometric arrangements of the planes can be achieved. However, the dimension of the adjustment problem increases steadily and again emphasizes the demand for a recursive method of adjustment. However, this will not be discussed further. Instead, the first realisation of this is presented in Ernst (2019).

4.2.5 Comparison and Discussion

Used Numerical Values

As application-dependent adjustment parameters, initial approximate values $\boldsymbol{x}_0$ as well as information regarding the observation uncertainties $\boldsymbol{\Sigma}_{ll,k}$ are necessary, both for the classical batch and for the novel recursive approach. In the case of the recursive GHM, the process noise $\boldsymbol{\Sigma}_{ww,k}$ as well as the VCM $\boldsymbol{\Sigma}_{\boldsymbol{xx},0}$ of the initial state vector $\boldsymbol{x}_0$ must also be defined. The uncertainty information regarding the initial values

can be provided by means of a simplified pre-adjustment and might also be used in the batch approach based on stochastic prior information. This improves the comparability between the two basic approaches. The initial values themselves thus also result from such a pre-adjustment. Their specific numerical values depend on a random selection of the point observations used. The VCMs correspond to the block structure as given in Equations (4.8) and (4.14). Their individual blocks describe the following uncertainties. The measurement noise for the 3D point observations of the laser scanner $\Sigma_{ll,k,P_{\mathrm{Scanner}}}$ is assumed to be $0.5\,\mathrm{cm}$ for each of the three coordinate directions. This specification differs from the manufacturer's declaration given above and, under the circumstances described, has a more realistic value, which has been determined empirically for this experiment. The uncertainties regarding the plane parameters of the reference geometries are based on the not fully populated VCM $\Sigma_{ll,k,a_{\mathrm{RFG}}}$, which is obtained within the plane estimation according to Drixler (1993). The remaining uncertainty information $\Sigma_{ll,k,t_{\mathrm{PCS\text{-}WCS}}}$ and $\Sigma_{ll,k,\theta_{\mathrm{PCS\text{-}WCS}}}$ regarding the transformation parameters between the PCS and WCS originates directly from the measurement software of the laser tracker. The following applies to the individual blocks of the VCM $\Sigma_{xx,0}$ of the initial state vector

$$\Sigma_{xx,0,a_{\mathrm{RFG}}} = \Sigma_{ll,a_{\mathrm{RFG}}}, \tag{4.15a}$$

$$\Sigma_{xx,0,t_{\mathrm{PCS\text{-}WCS}}} = \Sigma_{ll,t_{\mathrm{PCS\text{-}WCS}}}, \tag{4.15b}$$

$$\Sigma_{xx,0,\theta_{\mathrm{PCS\text{-}WCS}}} = \Sigma_{ll,\theta_{\mathrm{PCS\text{-}WCS}}}, \tag{4.15c}$$

where additionally for the initial pose the corresponding VCMs $\Sigma_{xx,k,t_{\mathrm{SOCS\text{-}PCS}}}$ and $\Sigma_{xx,k,\theta_{\mathrm{SOCS\text{-}PCS}}}$ based on the mentioned pre-adjustment are used.

Although the calibration approach itself remains unchanged in its methodology, the application of the recursive GHM requires minor modifications for this calibration task. Besides the partitioning of the observation data and state parameters, this applies in particular to the consideration of the process noise. In this thesis the process noise $\Sigma_{ww,k}$ is applied with a consistent standard deviation $\sigma_w = 10^{-3}$ for all states, whereas the respective units result from the VCM $\Sigma_{xx,k}$. The selection of this process noise is based on the investigations shown in Appendix A.2. Although it must be considered that the investigations there are based on a different application example (cf. section 3.4), findings can still be used for the experiment described here. Nevertheless, an independent analysis of the results, considering a variation of the process noise, would also be appropriate in this case in the future. Moreover, when considering the following results, it has to be taken into account that the main focus of this thesis lies on the methodological development of the versatile IEKF (cf. chapter 3). For this reason, it is not possible to optimally adjust all influencing parameters or to conclusively examine all effects in detail. Instead, the focus lies on the general applicability of the new recursive approach and the identification of possible advantages and limitations.

Comprehensive Data Base

The evaluated data set consists in total of 54 epochs (each with a complete $360°$ rotation) of the laser scanner. Depending on the distance to the laser scanner, an average of between 18 and 115 single point measurements of the laser scanner are obtained per epoch on each of the 12 reference planes. This corresponds to a total number of about $25\,000$ measured 3D points over all epochs. Since this large number of observations leads to numerical instabilities in the batch methods, a reduction of the data quantity must be performed. In specific terms, the following results relate exclusively to 15 epochs. This still corresponds to about 7000 individual 3D point observations, where an average of 40 point observations per epoch are available on a single reference plane. Based on this comprehensive data base, the calibration parameters $\hat{t}_{\mathrm{SOCS\text{-}PCS}}$ and $\hat{\theta}_{\mathrm{SOCS\text{-}PCS}}$ are estimated once by means of the different batch and recursive methods. Their numerical values are listed in Table 4.3. If no constraints are applied, the recursive GHM and the standard batch method are equal to a few hundredths of a millimetre for the translations. The differences for the rotations are $0.1\,\mathrm{m°}$. The differences are therefore quite small. However, if constraints are taken into account, differences between the two types of estimation will be up to $1.6\,\mathrm{mm}$ and $0.07°$, respectively. Overall, the maximum difference between the consideration and the neglection of constraints is $3\,\mathrm{mm}$ in translation and $0.1°$ in rotation. The corresponding estimated standard deviations $\hat{\sigma}_{t_{\mathrm{SOCS\text{-}PCS}}}$ and $\hat{\sigma}_{\theta_{\mathrm{SOCS\text{-}PCS}}}$ of the individual calibration parameters are given in Table 4.4. These are lower without the use of con-

Table 4.3: *Estimated calibration parameters ($\hat{t}_{SOCS\text{-}PCS}$ and $\hat{\theta}_{SOCS\text{-}PCS}$) for batch processing and different recursive approaches with respect to last epoch $k = 15$ in case of recursive estimation. All available observations are used.*

Method	Translations [m]			Rotations [°]		
	$\hat{t}_{SOCS\text{-}PCS,x}$	$\hat{t}_{SOCS\text{-}PCS,y}$	$\hat{t}_{SOCS\text{-}PCS,z}$	$\hat{\omega}_{SOCS\text{-}PCS}$	$\hat{\varphi}_{SOCS\text{-}PCS}$	$\hat{\kappa}_{SOCS\text{-}PCS}$
batch GHM	0.0149	0.0544	0.0775	0.0302	−34.8577	0.0300
batch C-GHM	0.0151	0.0526	0.0747	0.1254	−34.8538	−0.0789
recursive GHM	0.0149	0.0544	0.0775	0.0301	−34.8578	0.0299
recursive C-GHM (PM)	0.0165	0.0532	0.0763	0.0650	−34.8976	0.0156
recursive C-GHM (COF)	0.0161	0.0529	0.0761	0.0741	−34.8859	−0.0026

Table 4.4: *Standard deviations of the estimated calibration parameters ($\hat{\sigma}_{t_{SOCS\text{-}PCS}}$ and $\hat{\sigma}_{\theta_{SOCS\text{-}PCS}}$) for batch processing and different recursive approaches with respect to last epoch $k = 15$ in case of recursive estimation. All available observations are used.*

Method	Translations [m]			Rotations [°]		
	$\hat{\sigma}_{t_{SOCS\text{-}PCS,x}}$	$\hat{\sigma}_{t_{SOCS\text{-}PCS,y}}$	$\hat{\sigma}_{t_{SOCS\text{-}PCS,z}}$	$\hat{\sigma}_{\omega_{SOCS\text{-}PCS}}$	$\hat{\sigma}_{\varphi_{SOCS\text{-}PCS}}$	$\hat{\sigma}_{\kappa_{SOCS\text{-}PCS}}$
batch GHM	$2.3 \cdot 10^{-4}$	$3.4 \cdot 10^{-4}$	$2.2 \cdot 10^{-4}$	0.0104	0.0037	0.0090
batch C-GHM	$7.5 \cdot 10^{-4}$	0.0011	$7.2 \cdot 10^{-4}$	0.0331	0.0118	0.0287
recursive GHM	$1.1 \cdot 10^{-4}$	$1.6 \cdot 10^{-4}$	$1.1 \cdot 10^{-4}$	0.0049	0.0018	0.0043
recursive C-GHM (PM)	$9.0 \cdot 10^{-4}$	0.0016	$9.6 \cdot 10^{-4}$	0.0747	0.0192	0.1024
recursive C-GHM (COF)	$8.6 \cdot 10^{-4}$	0.0013	$8.1 \cdot 10^{-4}$	0.0371	0.0135	0.0317

straints. For all methods the maximum values are $1.6\,\mathrm{mm}$ and $0.1°$, respectively. Since the estimation parameters are based on a comprehensive observation vector, this is to the expense of the necessary run times. The long run times required in particular for batch procedures are shown in Table 4.5. The recursive approaches are at least 20 times faster. The fastest solution is achieved by using recursive GHM without constraints. In addition, the mentioned different dimensions of the state vector must be taken into account.

It would be useful to evaluate the estimated parameters and their standard deviations with regard to the deviations between the different methods for their significance. However, similar to section 3.4.2, the distribution of the estimated parameters is unknown. Thus, again *bootstrap hypothesis testing* according to Efron and Tibshirani (1993, pp. 220 ff.) and MacKinnon (2007) is referred to here. Furthermore, it should be mentioned that in the batch and recursive methods used, the dimension of the state vector is not identical overall. If no constraints are considered (batch GHM and recursive GHM), the plane parameters (four elements for each of the 12 planes) are not part of the state vector. When constraints are applied, the state vector naturally contains the corresponding plane parameters. This affects the dimension of the design matrix $\boldsymbol{A}$ and thus has a negative impact on the computing time. The batch method without consideration of constraints can be considered as *state of the art* method according to section 4.2.3.

Monte-Carlo Simulation

To ensure comparability between the classical batch approach and the novel recursive calibration method, a comprehensive *MC simulation* is performed similarly to section 3.4.1. Thus, a variety of slightly different realisations can be obtained and a more meaningful assessment based on the central moments is

Table 4.5: *Necessary absolute and relative (with respect to the recursive C-GHM (COF) approach) run times for batch process-ing and different recursive approaches by using 7000 individual 3D point observations for the calibration task. A computer with the performance of a Intel Xeon E5-1650 (6-cores, 3.60 GHz) and 64 GB RAM was used.*

Method	Run Time	
	Absolute [s]	Relative [−]
batch GHM	2244	17.3
batch C-GHM	2666	20.5
recursive GHM	45	0.3
recursive C-GHM (PM)	116	0.9
recursive C-GHM (COF)	130	1.0

possible. A multitude of runs is necessary to obtain reliable results with MC simulation. This requires a further reduction of the observation data to ensure acceptable run times for the individual approaches. Therefore, within the 15 epochs, only five random[15] points are used on a single reference plane per epoch. This reduces the total number of 3D point observations to 900 over the 15 epochs. This means that not all available point observations are used per reference plane, but instead, a subsampling is performed. How-ever, this is still necessary due to the large amount of data. The varying quantities of the MC simulation are then the selection of the 3D laser scanner points used on the individual reference planes. This also causes the initial approximate values x_0 to vary. The sequence of a single realisation of the MC simulation is shown schematically in Figure 4.7. The reduction in the number of observations shows significantly lower absolute run times (cf. Table 4.6) compared to the comprehensive data set before (cf. Table 4.5). In addi-tion, it can be observed that the relative run time does not change linearly with the number of observations. The relative differences in the run time between the batch and recursive procedure are also reduced. The standard deviations σ indicate the variation over the $S = 5000$ replications. These are higher, especially for recursive methods when constraints are taken into account.

The median of the estimated calibration parameters over all $S = 5000$ replications is given for the indivi-dual elements in Table 4.7. The numerical differences between the individual methods (with and without constraints as well as among themselves) are almost identical to the values given above (a few millimetres and a tenth of a degree), taking into account the larger data set. Also, the total deviation with respect to the number of observations used is below these numerical values. A subsampling thus has no negative impact on the estimation parameters in the present application. Only the standard deviations increased by a factor of about 2.6 due to the reduced amount of data (cf. Table 4.8). However, this is in contrast to the significant reduction of the required run time.
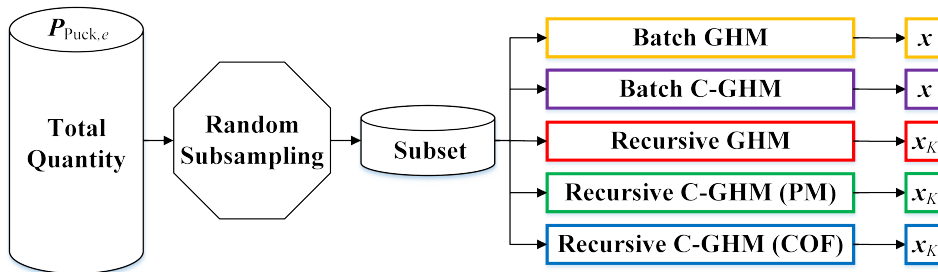
Figure 4.7: *Sequence of one single run during MC simulation for different batch and recursive methods (colour-coded). The random subsampling of the total quantity of the laser scanner data $P_{Scanner,e}$ varies for each run. In case of the recursive approaches, the parameter vector x_K corresponds to the last estimate of epoch K.*

---

[15] As a precaution, geometrically unfavourable constellations are avoided

Table 4.6: *Median of the absolute and relative run times with related standard deviations by means of $S = 5000$ replications of the MC simulation for batch processing and different recursive approaches with respect to recursive C-GHM (COF) approach. A computer with the performance of an Intel Xeon E5-1650 (6-cores, 3.60 GHz) and 64 GB RAM was used for the calculations.*

Method	Run Time		$\sigma[\text{s}]$
	Absolute [s]	Relative [−]	
batch GHM	21.1	6.5	0.8
batch C-GHM	28.1	8.7	1.0
recursive GHM	0.9	0.3	0.6
recursive C-GHM (PM)	4.8	1.5	2.6
recursive C-GHM (COF)	3.2	1.0	1.7

Table 4.7: *Median of the estimated calibration parameters ($\hat{t}_{SOCS\text{-}PCS}$ and $\hat{\theta}_{SOCS\text{-}PCS}$) by means of $S = 5000$ replications of the MC simulation for batch processing and different recursive approaches with respect to last epoch $k = 15$ in case of recursive estimation.*

Method	Translations [m]			Rotations [°]		
	$\hat{t}_{\text{SOCS-PCS},x}$	$\hat{t}_{\text{SOCS-PCS},y}$	$\hat{t}_{\text{SOCS-PCS},z}$	$\hat{\omega}_{\text{SOCS-PCS}}$	$\hat{\varphi}_{\text{SOCS-PCS}}$	$\hat{\kappa}_{\text{SOCS-PCS}}$
batch GHM	0.0157	0.0537	0.0786	0.0054	−34.8797	0.0559
batch C-GHM	0.0159	0.0520	0.0759	0.0928	−34.8789	−0.0536
recursive GHM	0.0157	0.0537	0.0786	0.0053	−34.8797	0.0558
recursive C-GHM (PM)	0.0177	0.0530	0.0791	−0.0444	−35.0196	0.0878
recursive C-GHM (COF)	0.0174	0.0529	0.0788	−0.0321	−34.9941	0.0682

Table 4.8: *Median of the estimated standard deviations of the calibration parameters ($\hat{\sigma}_{t_{SOCS\text{-}PCS}}$ and $\hat{\sigma}_{\theta_{SOCS\text{-}PCS}}$) by means of $S = 5000$ replications of the MC simulation for batch processing and different recursive approaches with respect to last epoch $k = 15$ in case of recursive estimation.*

Method	Translations [m]			Rotations [°]		
	$\hat{\sigma}_{t_{\text{SOCS-PCS},x}}$	$\hat{\sigma}_{t_{\text{SOCS-PCS},y}}$	$\hat{\sigma}_{t_{\text{SOCS-PCS},z}}$	$\hat{\sigma}_{\omega_{\text{SOCS-PCS}}}$	$\hat{\sigma}_{\varphi_{\text{SOCS-PCS}}}$	$\hat{\sigma}_{\kappa_{\text{SOCS-PCS}}}$
batch GHM	$6.8 \cdot 10^{-4}$	$9.3 \cdot 10^{-4}$	$7.5 \cdot 10^{-4}$	0.0295	0.0121	0.0238
batch C-GHM	0.0021	0.0029	0.0023	0.0902	0.0374	0.0732
recursive GHM	$2.9 \cdot 10^{-4}$	$4.0 \cdot 10^{-4}$	$3.2 \cdot 10^{-4}$	0.0127	0.0053	0.0102
recursive C-GHM (PM)	0.0023	0.0031	0.0026	0.1093	0.0425	0.0867
recursive C-GHM (COF)	0.0023	0.0031	0.0024	0.0892	0.0389	0.0727

Figure 4.8 shows the histograms of the $S = 5000$ replications of the MC simulation for all six calibration parameters, represented by the estimated translation in z-direction $t_{\text{SOCS-PCS},z}$ for all batch and recursive methods. The basic appearance is similar for all six calibration parameters for the individual procedures, that is why the others are not shown here. Similar to the median of the estimated standard deviations (cf. Table 4.8), the scattering within the $S = 5000$ replications is higher for those methods that take constraints
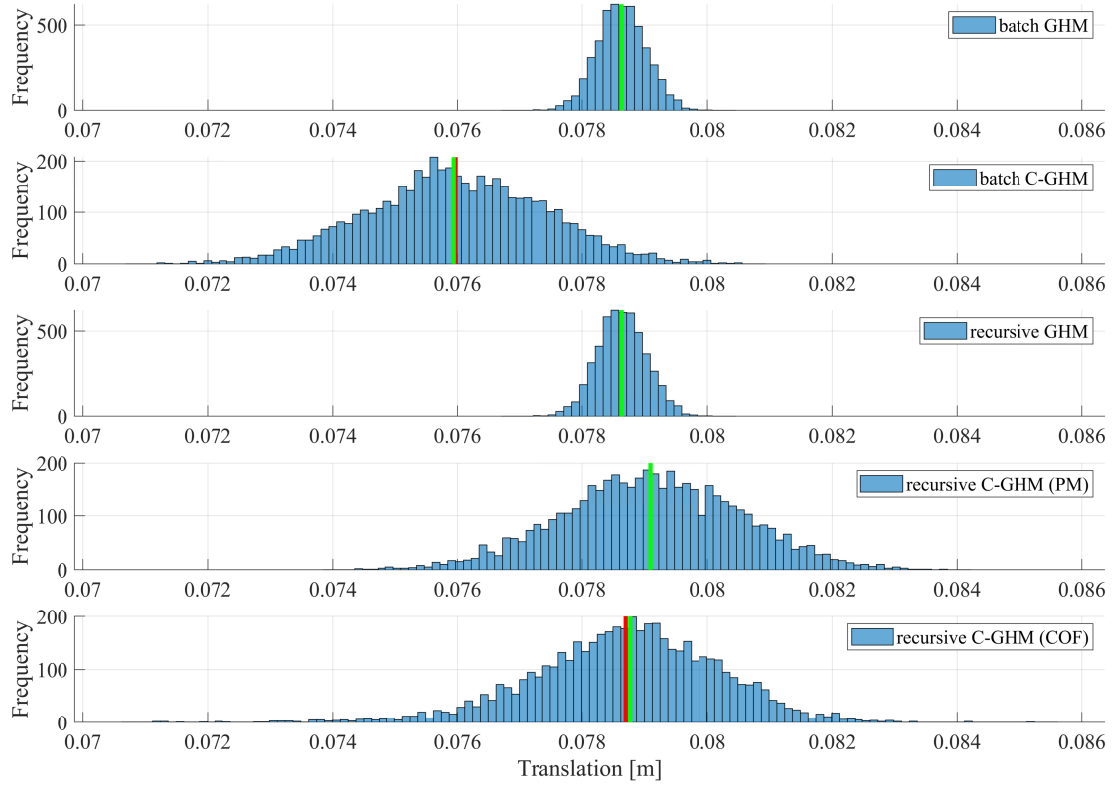
Figure 4.8: *Histograms of the estimated translations $t_{SOCS\text{-}PCS,z}$ by means of $S = 5000$ replications of the MC simulation for different batch and recursive approaches. Respective median is given by a green bar. The mean value (if not approximately identical with the median) is shown with a red bar. The partially different scaling of the vertical axis should be taken into account.*

into account. While the standard deviation of all realisations, when no constraints are considered, is about $0.4\,\mathrm{mm}$ in translation and $0.01°$ in rotation, the standard deviation of the other methods is about $6.5\,\mathrm{mm}$ for translation and $0.2°$ for rotation. The random selection of the corresponding 3D point observations on the individual planes (cf. Figure 4.7) thus has a stronger impact on the methods in which constraints are considered. It should also be mentioned that the edges of the individual distributions are partly truncated for visualisation purposes. This is especially true for the three approaches where constraints are considered. Thus, a few individual runs lead to estimates that are further away from the median, which is already evident from the standard deviations mentioned. In the recursive C-GHM (COF) this behaviour leads to a noticeable difference between the median and the mean value of less than $0.1\,\mathrm{mm}$. For the other methods, this difference is about a factor of 10 smaller.

Cross-validation

In contrast to the simulated example from section 3.4, the true (state) parameter vector $\bar{x}$ is unknown in this real calibration example. Furthermore, it is also not possible to judge which approach best approximates the true values. Thus, only conclusions regarding the precision of the individual approaches can be stated. In order to evaluate to what extent the individual batch and recursive methods provide reasonable results, the concept of so-called *(k-fold) cross-validation* can be applied. According to Efron and Tibshirani (1993, pp. 239 ff.), Efron and Hastie (2016, pp. 208 ff.) and James et al. (2017, pp. 176 ff.), this method is based on the strategy of randomly assigning the available measurement data into k exclusive, of equally sized subsets[16] within a multitude of individual runs. Then $k-1$ subsets are selected and summarised as training data set. The one remaining subset is referred to as the test data set. With the larger training set, the unkown

---

[16] Also referred to as *folds*

calibration parameters are then estimated as before. The smaller test set is used subsequently to verify the results (by means of the contradictions $d_{e,i}$) based on the training set. Thereafter, a new training data set is generated from a new composition of $k-1$ subsets and a single test data set is defined simultaneously. The subsequent estimation and validation is performed as described above. This procedure is applied until k cycles are completed. Within the k realisations the training data set and the test data set are therefore always different. Overall, this procedure is referred to as one single run of the cross-validation. For statistically reliable statements, a multitude of such runs have to be performed, whereby the assignment of the original observation data to the k subsets is always random. Subsequently, all contradictions over all runs can be represented in a histogram and the statistical central moments can be calculated. In the literature, 10 is often suggested for the selection of k, which is also applied to the specific example of the calibration task here. This is a good compromise between the required run time and variation. A simplified schematic overview of the sequence of one single run during the 10-fold cross-validation is shown in Figure 4.9.

The cross validation method differs in detail from the MC simulation described above. The latter varies per run the observation data to be used (3D points measured by the laser scanner). Since only five 3D points of each reference plane are used within one run, compared to a multitude of available observations, the composition of the observation data set has a high variation for each run. Cross-validation, on the other hand, neglects just a low percentage of all available observations. The variation within the observations to be used is, therefore, small for each run. In addition, the excluded observations are used again for validation. In this specific example, the cross-validation also considers essentially more observation data compared to the MC simulation described above. For this reason, cross-validation is carried out exclusively with the recursive approaches due to the large run times of the batch methods in combination with the large number of runs. As part of the validation, all individual 3D point observations from the test set, taking into account the parameters estimated with the training set, are inserted into Equation (4.6) (simultaneously considering Equations (4.1) and (4.5)) and the contradictions are estimated. However, it should be noted that only the estimated state parameters of the last epoch K are considered.

The 10-fold cross-validation method was performed in the course of 500 replications for the described data set. By choosing $k = 10$, this corresponds to 5000 differently and independently realised data sets. The number of all contradictions results from the sum of the 3D point observations, which were defined as the test data set in each realisation. Their distributions for the three recursive methods are shown as histograms in Figure 4.10. In total, the median of all contradictions $\bar{d}$ for the individual methods is $0.370\,\text{mm}$ (recursive GHM), $0.054\,\text{mm}$ (recursive C-GHM (PM)) and $-0.003\,\text{mm}$ (recursive C-GHM (COF)). The corresponding standard deviations σ_d, which give information about the scattering of the contradictions, are $10.5\,\text{mm}$ (recursive GHM), $8.4\,\text{mm}$ (recursive C-GHM) (PM)) and $5.7\,\text{mm}$ (recursive C-GHM (COF)). Based on the results of cross-validation, the recursive C-GHM (COF) thus provides the most reliable results.
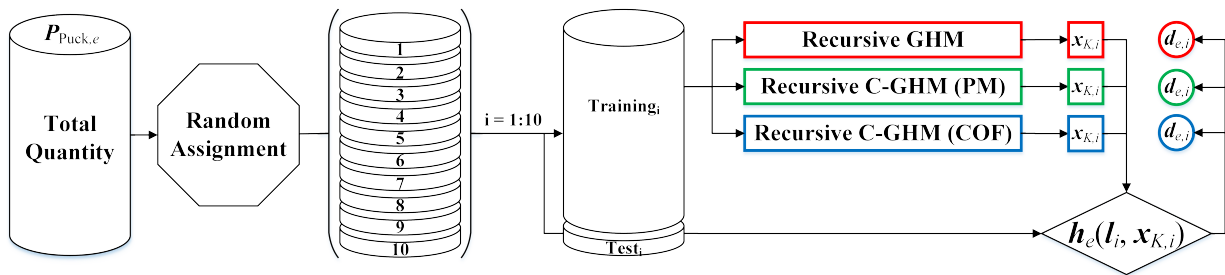
Figure 4.9: *Sequence of one single run during 10-fold cross-validation. The random assignment of the total quantity of the laser scanner data $P_{Scanner,e}$ into $k = 10$ equal-sized subsets varies for each run. These k subsets are systematically divided k times into the specific training and test data set i. Then, for each of the k combinations, the corresponding contradictions must be determined. These distances $d_{e,i}$ (or rather contradictions) from the functional relationship $h_e\,(l, x_K)$ (cf. Equation (4.6)) for each of the e planes are related to the respective methods used for the training data i and are colour-coded. The parameter vector $x_{K,i}$ corresponds to the last estimate of epoch K.*
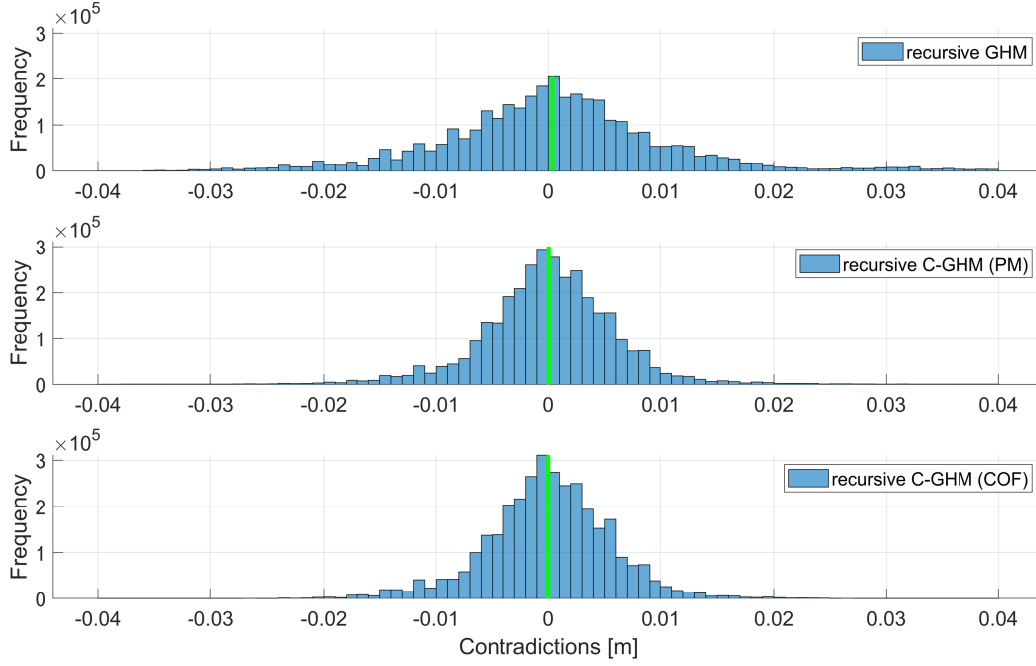
Figure 4.10: *Results of the k-fold cross-validation with k = 10. The individual contradictions $d_{e,i}$ for the three different re-alisations of the recursive GHM are shown in corresponding histograms, taking into account 500 replications. Respective median is given by a green bar.*

For a more detailed investigation, the distribution of the contradictions $d_{e,i}$ should also be established with respect to the individual reference planes. In this way, generally unfavourable or faulty planes could be identified and excluded from the adjustment. Other advanced analyses of the occurring PDFs (e.g. to what extent a normal distribution applies) are not directly related to the objectives of this thesis and are therefore not discussed here.

Conclusions

As expected, an increase of the observation data leads simultaneously to an increase of the necessary computing time. This is independent of the method used. Nevertheless, the recursive methods require shorter run times compared to the batch methods. This factor is non-linear and becomes more significant, the more observations are used. If no additional information in terms of constraints are used, the recursive estimation gives almost identical results compared to the overall adjustment (with a simultaneous reduction of the computing time). This is also independent of the number of observations used. If constraints are used, there will be small deviations in the estimation results among each other and in comparison to not taking them into account. However, statements regarding the accuracy of the individual methods are difficult, as the true values are not known. For this reason, it cannot be verified whether the accuracy of the calibration parameters is improved by taking constraints into account. Furthermore, it is also not possible to conclude to what extent the number of observations affects the accuracy of the estimation parameters. However, the precision of the estimation parameters increases slightly if fewer observations are used. The cross-validation shows that with the recursive C-GHM (COF) method, the most reliable results in this application example can be achieved. The basis for this is a large number of estimated contradictions, which could only be performed for the recursive methods due to the high demands on the computing time (cf. Table 4.6).

Overall, in this specific application example, the translations are determined more precisely than the corresponding rotations. This is independent of the adjustment approach used and can be improved by better geometric coverage and arrangement of the reference geometries. Otherwise, an uncertainty of $0.1°$ in the orientation, at a typical measurement distance of $15\,\mathrm{m}$, leads to a transverse deviation of about $2.6\,\mathrm{cm}$. As

already mentioned in section 4.2.4, the simultaneous integration of several individual calibration positions of the MSS in the adjustment approach can also lead to more precise calibration parameters.

In general, the calibration approach shown can also be extended by further additional constraints with the new methods. If suitable additional information is available, its consideration can have a positive impact on the estimation of the calibration parameters or their uncertainties. Such possible prior information could, for example, be provided by reference points or surfaces signalised by the manufacturer on the sensor in a specific manner. In combination with a defined uncertainty, this can then be considered in the estimation by means of constraints. As already mentioned in section 4.2.3, the parametrisation of a plane can also be done in other ways (e.g. by means of angular relationships). This has the advantage that no constraint regarding the length of the normal unit vector is necessary. However, such an alternative parametrisation is not necessarily possible for all geometric primitives. An example is the use of elliptical cylinders as reference geometries.

The classical method from section 4.2.3 still has its justification and should be used if the run time is not important for the computation. However, this requires that, depending on the number of observations, appropriately dimensioned computing capacities are available, and thus no numerical instabilities occur. If this cannot be guaranteed or if there is a demand for a faster solution (e.g. in the case of an in-situ calibration on-the-fly), the recursive method from section 4.2.4 offers new possibilities.

5

Information-based Georeferencing

This chapter describes another application example with real data, which is also based on the innovations presented in chapter 3. The basic idea and associated challenges of georeferencing a kinematic MSS are motivated in section 5.1. In section 5.2 the underlying experiments are introduced. The current state of research on this topic is presented in section 5.3. By using recursive state estimation in the GHM and the simultaneous combination of state constraints, a novel approach for georeferencing a laser scanner-based kinematic MSS is introduced in section 5.4. For this purpose, additional information from the object space is used, which gives advantages in complex and challenging environments such as highly urbanised areas. The results are discussed in section 5.5, where the advantages and limitations of the new approach are emphasized.

5.1 Motivation

The relevance and usage of kinematic MSSs — as already introduced comprehensively in section 4.1 — has increased steadily over the last decades. This applies both to geodetic measuring systems in particular (Schwarz and El-Sheimy, 1996; El-Sheimy, 2005; Gräfe, 2007; Puente et al., 2013; Nex and Remondino, 2014; Vogel et al., 2016) as well as to various other disciplines (e.g. robotics (Hertzberg et al., 2012)). This increase is clearly visible, for example, in the highly popular topic of autonomous driving. This progression also brings around questions and challenges from various disciplines (Schlichting, 2018). Vehicles are already equipped with a multitude of different sensors which contribute to safe autonomous driving. Furthermore, the use of UAVs is another highly relevant application to be mentioned. The high occurrence and diverse application of these MSSs is also a result of the development of low-cost and lightweight sensors for environmental perception. As for autonomous vehicles, the requirements in terms of pose estimation for such UAVs are becoming increasingly stringent (Kaul et al., 2016; Zwiener, 2019). After all, an (autonomous) vehicle or a UAV with all its sensors is nothing else than a kinematic MSS. Therefore, it is also necessary to provide accurate, precise, and reliable georeferencing solutions for such systems. Ensuring integrity aspects becomes particularly important when such systems are used in close proximity to people. However, it must be taken into account that due to financial reasons, only sensors with a moderate accuracy level are used. This applies in particular to mass-market systems in the automotive industry. Regardless of the specific realisation of a kinematic MSS, there are many different approaches to solve the georeferencing task, each of which depends strongly on the available sensors and the respective environment. These approaches have different advantages and disadvantages, which are presented and discussed in detail in section 5.3.

The most common method for reliable positioning of a kinematic MSS (and especially of a vehicle and a UAV) is the use of GNSS observations. Such observation data are available worldwide and can be obtained in different levels of accuracy (depending on the specific application). By adding IMU measurements to the GNSS solution, all 6-DoF can be determined in combination. Although this is sufficient for a wide range of applications, there are a significant proportion of situations where a reliable and accurate GNSS-based georeferencing solution is whether not always possible or not feasible at all. This is generally the case in indoor environments but also applies to urban areas, where the challenges increase as the

environment becomes more urbanised. Especially in so-called *urban canyons* no reliable georeferencing of a kinematic MSS by GNSS observations is possible due to multipath effects (Gang-jun et al., 2009; Wang et al., 2013; Zhu et al., 2018; Zhang, 2019). The presence of tall buildings leads to distorted GNSS measurements, which are also referred to as *Non-Light-Of-Sight (NLOS)* observations (Hsu, 2018). This can lead to an overall positioning error of several metres (Zhang et al., 2018; Dehbi et al., 2019). Thus, the georeferencing of a kinematic MSS under consideration of integrity aspects is strongly limited.

Because of these weaknesses, there is a high demand for other georeferencing methods that provide more reliable, accurate and precise solutions in such challenging environments. Many approaches already address this issue, with several different strategies being pursued. These approaches comprise an improved use of the affected GNSS observations, the usage of other sensors, the consideration of suitable additional information from object space as well as the use of redundant systems. In general, the interaction of several independent approaches and sensors should always be aimed for due to the resulting flexibility and higher reliability. However, this requires increased additional effort, since several systems must be purchased, operated, calibrated, synchronised and evaluated. For this reason, a new approach is presented in section 5.4, which claims to be more reliable and accurate within challenging narrow urban streets. The achievable accuracies are strongly dependent on the quality of the available sensors. However, this is directly dependent on the associated acquisition costs. In applications such as autonomous driving (where costs play a key role) or UAVs (where weight is a crucial factor), this must be taken into account.

The objective of the new information-based georeferencing approach should be to obtain a pose solution with an accuracy of at least $10\,\mathrm{cm}$ for the position and $0.5°$ for the orientation even in the aforementioned challenging environments. Thus, this approach is intended to provide helpful support for the long-term trend in pose determination. These numerical values are based on the specifications of automotive industries for autonomous driving. In Kwoczek (2015), it is assumed that with a typical vehicle width of $2\,\mathrm{m}$ and a lane width of $3.5\,\mathrm{m}$ for a standard road, there is a distance of $0.75\,\mathrm{m}$ on both sides of the vehicle. In order to ensure positioning with respect to the individual lane, half of this is taken as the necessary accuracy, which is $37.5\,\mathrm{cm}$. To take into account different lane and vehicle widths, an accuracy of $10\,\mathrm{cm}$ is used here to ensure an additional buffer. The selection of the accuracy for orientation is based on the assumption that with an angular error of $0.5°$ at a range of $10\,\mathrm{m}$, a deviation of about $10\,\mathrm{cm}$ can be expected. For this purpose, object space information is used as an independent and complementary source of information. Thus, there is also the claim to contribute to the assurance of the integrity of such MSSs.

5.2 Experimental Setup

To simulate the challenging circumstances of georeferencing kinematic MSSs in urban areas (cf. section 5.1), the following experiments are introduced. They represent typical application scenarios for respective environments. Furthermore, they serve as a suitable reference to introduce the already existing methods for georeferencing in section 5.3 in an application-oriented way and to validate the new approach in section 5.4. There are two independent data sets, which differ in the MSS used and the specific environment. Both data sets were acquired with a kinematic laser scanner-based MSS and are located in an urban environment with larger buildings. The laser scanners each have different degrees of accuracy. Below follows a brief overview of the two MSSs with their respective sensors, information on the two scenarios and the additionally available object space information.

5.2.1 Kinematic Laser Scanner-based Multi-sensor Systems

Research-based Unmanned Aerial Vehicle

UAVs are characterised by a compact design and flexible movement possibilities. Therefore, they are well suited for mapping tasks in challenging environments where ground-based platforms are difficult or impossible to operate, and static terrestrial laser scanning is inefficient. In the course of a project at the Geodetic Institut (GIH) in cooperation with the Institut of Photogrammetry and GeoInformation

(IPI) of Leibniz University Hannover (LUH) a kinematic MSS by means of a research-based[1] UAV was developed. Among other sensors, this includes a 3D laser scanner. In this case it is a *Velodyne Puck VLP-16*, which is also calibrated in section 4.2 with respect to a superior PCS. With its 16 individual scan lines and a field of view of $30° \times 360°$ it provides a highly suitable 3D point cloud of the environment. The manufacturer specifies a typical value of up to $3\,\mathrm{cm}$ for the range accuracy (Velodyne LiDAR, 2018b), without indicating the associated quality parameter. The measured 3D point coordinates are available with respect to the local SOCS of the laser scanner. In the experiment a rotation frequency of $10\,\mathrm{Hz}$ is selected, which corresponds up to $30\,000$ single 3D points per $360°$ rotation. GPS time information is assigned to each of these 3D points through an additional GNSS unit. This enables reliable synchronisation with other sensors of the MSS. Absolute position information based on the GNSS observations is theoretically also available but is inaccurate and unreliable due to the sensor quality. Although an additional *Vectornav VN-200* IMU is mounted, this information will be disregarded in the following due to unavailable calibration parameters. Thus, only laser scanner observations are available and no information regarding the MSS pose. The actual use case of this MSS intends that the UAV should mainly fly just above the eave heights of the buildings, so that information of the roof structures can be captured and used (Bureick et al., 2019a). However, the following data set was acquired at the height of approximately $2\,\mathrm{m}$ above the ground. For better stabilisation and damping, all sensors are mounted on a gimbal. The UAV with the laser scanner is shown in Figure 5.1(a).

Mobile Mapping System *RIEGL VMX-250*

Vehicle-based MMSs are suitable for surveying and mapping of large-scale areas as long as they are accessible by road. There are many different commercial systems (Puente et al., 2013). For the experiment here, measured data from a *RIEGL VMX-250* are used. This MMS consists of two *Riegl VQ-250* laser scanners, a precise *Applanix POS-LV 510* GNSS-IMU positioning unit and an odometer (referred to as Distance Measurement Indicator (DMI)). In addition, several cameras are available, but these are not considered within the context of this thesis. All sensors are already calibrated by the manufacturer with respect to each other. During acquisition, the MMS is mounted on a roof rack of a van. Each laser scanner captures 3000 individual scan points per $360°$ rotation, which is also referred to as a single profile or scan strip. The measuring frequency of such profiles is $100\,\mathrm{Hz}$. The manufacturer specifies an accuracy of $10\,\mathrm{mm}$ and a precision of $5\,\mathrm{mm}$ for the measurement uncertainty[2] of the laser scanners. The accurate georeferencing of the MMS by means of GNSS and IMU observations is done in post-processing and allows the integration of base station data from a GNSS reference station. However, only a filtered trajectory is available, and there is no access to the original measurements. According to the manufacturer, this trajectory has an

(a)   (b)

Figure 5.1: *Overview of the two kinematic laser scanner-based MSSs. The research-based UAV in (a), where the Velodyne Puck VLP-16 is highlighted with a red circle. Modified according to Bureick et al. (2019a). Furthermore, the RIEGL VMX-250 MMS is mounted on a van during the measurement campaign (b).*

---

[1] Also referred to as *prototype*
[2] Both in terms of $1\,\sigma$ at $50\,\mathrm{m}$ range (RIEGL Laser Measurement Systems, 2012b)

absolute accuracy of $2\,\mathrm{cm}$ to $5\,\mathrm{cm}$. The accuracy of the roll[3] and pitch[4] angles is quantified with $0.005°$ and for the heading angle with $0.015°$. All these values refer to a $1\,\sigma$-environment and presuppose the availability of the DMI, base station data and no GNSS outages (RIEGL Laser Measurement Systems, 2012a). However, Schlichting (2018) and Hofmann (2017) state that an accuracy[5] of $10\,\mathrm{cm}$ to $20\,\mathrm{cm}$ for the position is more realistic in urban areas for this MMS.

The measured 3D point coordinates are available with respect to the respective local SOCS of both laser scanners. By using available calibration parameters, these can be transformed into a fixed PCS, which coincides with the SOCS of the IMU[6]. Each individual measured point coordinate is provided with a timestamp. Thus a temporal reference to the pose determined from GNSS and IMU observations (and the information of the DMI) is realised. The GPS time also serves as a uniform time base here. Thus, the local point clouds can be transformed into a superordinate WCS (e.g. Universal Transverse Mercator (UTM) projection with respect to the European Terrestrial Reference System 1989 (ETRS89)).

Furthermore, it should be mentioned that the two laser scanners are aligned slightly inclined to the direction of movement, which is also termed as *butterfly alignment* (Keller and Sternberg, 2013). Thus the two scanning planes intersect, and areas in front of and behind the vehicle are captured. To achieve a high density of the point cloud and to obtain as many individual epochs as possible, the MMS was driven at walking speed during the experiment. Figure 5.1(b) shows the MMS mounted on the van during the measurement campaign.

5.2.2 Scenarios and Measuring Process

The kinematic MSSs described in section 5.2.1 are used in two different environments. This involves firstly an inner courtyard, which is to be mapped. The second scenario was acquired with a MMS within the framework of the RTG *i.c.sens 2159* and additionally includes a highly accurate reference trajectory. This exemplary scenario addresses the challenges of georeferencing laser scanner-based autonomous vehicles in urban canyons. A map-based representation of the areas of both scenarios is provided in Figure 5.2. Their respective characteristics are described in detail below.

         (a)   (b)

Figure 5.2: *Map-based representation of the two application scenarios. A spacious inner courtyard is shown in (a) and a street section within an urban canyon in (b). The irrelevant areas are shaded out. The red dots in both maps represent the locations from where the images in Figures 5.3 and 5.4 were taken. The background map is taken from OpenStreetMap.*

---

[3]Also referred to as the angle of rotation along the coordinate axis in the direction of movement
[4]Also referred to as the angle of rotation along the transverse coordinate axis in the direction of movement
[5]Without indicating the associated quality parameter
[6]The GNSS observations obtained are processed internally, so that their position solution also refers to the PCS

Mapping Within an Inner Courtyard

A spacious inner courtyard within an urban environment offers perfect conditions for the application of the new information-based approach (cf. section 5.4) for georeferencing a kinematic MSS. Although the multitude of buildings from all sides leads to unfavourable GNSS conditions, they provide a valuable source of reference in terms of object space information. Their continuous detection is also supported by the distinct field of view of the 3D laser scanner with its full $360°$. The availability of such additional information is necessary to reliably determine all 6-DoF over time. Nevertheless, the registration of building facades is partly affected by parked cars, containers and items placed outside. In terms of vehicle-based mapping, the inner courtyard is not a typical environment. The paths between the buildings are very narrow, so there is no regular car traffic. For the application of a UAV, which has to be georeferenced reliably and accurately for mapping tasks in environments similar to this one, for example, the setting is quite realistic. Furthermore, due to the aforementioned reasons, it is a convenient scenario for examining the applicability of the proposed method in section 5.4. For this reason, the described research-based UAV in section 5.2.1 is used to perform measurements in this environment. Figure 5.3 gives an overview of the surroundings, especially with regard to the available buildings.

The realisation of an accurate reference pose is generally desirable, but is not present here. As the MSS moves over a relatively long distance through the built-up inner courtyard, no permanent line-of-sight for external tracking can be realised. This makes it difficult to validate the obtained results. The only available observations are the N_k 3D point coordinates $\boldsymbol{P}_{\mathrm{UAV},k}$ of the laser scanner with respect to its SOCS per individual epoch $k = 1, \ldots, K$. Here, K is the total number of epochs and the following applies

$$\boldsymbol{P}_{\mathrm{UAV},k} = \left[x_{\mathrm{UAV},k,1}, y_{\mathrm{UAV},k,1}, z_{\mathrm{UAV},k,1}, \ldots, x_{\mathrm{UAV},k,N_k}, y_{\mathrm{UAV},k,N_k}, z_{\mathrm{UAV},k,N_k} \right]^T . \tag{5.1}$$

Note that N_k can vary per epoch and one single epoch k contains all observations of a complete $360°$ rotation. Since every single measured point has an individual timestamp, the averaged timestamp is used as a time reference for the combination of all point observations in one epoch k. The requested quantities for each epoch k are three translations $t_{\mathrm{UAV},x,k}$, $t_{\mathrm{UAV},y,k}$ and $t_{\mathrm{UAV},z,k}$, three rotations $\omega_{\mathrm{UAV},k}$, $\varphi_{\mathrm{UAV},k}$ and $\kappa_{\mathrm{UAV},k}$, three velocities $v_{\mathrm{UAV},x,k}$, $v_{\mathrm{UAV},y,k}$ and $v_{\mathrm{UAV},z,k}$ as well as three angular velocities $v_{\mathrm{UAV},\omega,k}$, $v_{\mathrm{UAV},\varphi,k}$ and $v_{\mathrm{UAV},\kappa,k}$. They describe the pose and velocity of the MSS with respect to a superordinate coordinate system and must be determined with a suitable georeferencing method.

Georeferencing of an Autonomous Vehicle Within an Urban Canyon

A typical urban canyon is used to investigate the challenges and limitations of accurate and reliable georeferencing in such environments. Although there are much narrower and deeper street canyons in com-
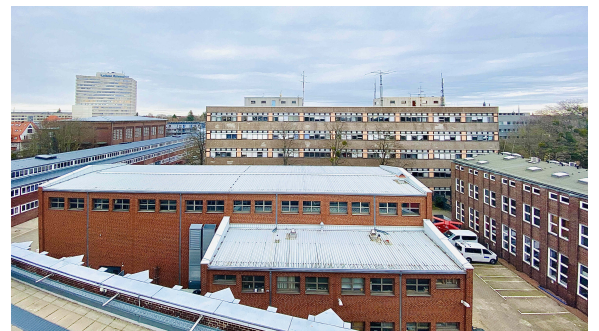
(a)	(b)

Figure 5.3: *Images of the measured area in a spacious inner courtyard. The spatial environment for the initialisation is shown in (a). The narrow inner courtyard with a multitude of buildings is shown in (b). The respective locations where the images were taken are shown in Figure 5.2(a).*

parison, the environment used still represents a realistic application scenario for the georeferencing of an autonomous vehicle. It is characterised by diverse buildings with several large-scale facade elements. In comparison to the inner courtyard, buildings with potential object space information are only available laterally along the street. This imposes special challenges, in particular with regard to positioning along the direction of movement. To counteract this unfavourable geometric configuration, appropriate building structures (e.g. house edges or jutties) are required, which provide information regarding corresponding coordinate axis. In addition, the registration of building facades is partly affected by parked cars. Figure 5.4 gives an impression of the surroundings.

In this environment the vehicle-based MMS *RIEGL VMX-250* is used. With regard to the sensor arrangement and its quality, this kinematic MSS is just partly suitable as an example of an autonomous vehicle. Although the precision of the *Riegl VQ-250* is higher compared to the *Velodyne Puck VLP-16*, the two profile laser scanners provide overall less spatial coverage and density of the 3D point cloud. This disadvantage is counterbalanced by certain advantages. Due to the precise *Applanix POS-LV 510* GNSS-IMU positioning unit an almost referenceable pose is available. Despite the suboptimal GNSS conditions, this solution can be considered as a reliable reference at this point, since the quality of the positioning unit and especially of the IMU used is of the highest standard. The use of such a system is obviously not realistic for georeferencing of an autonomous vehicle. However, by applying an artificial noise to the reference pose, the specific accuracy level for an autonomous vehicle can be simulated in the subsequent investigations. Since the MSS is a commercial system, an independently determined absolute 3D point cloud is also available in a superordinate coordinate system. This can be used, for example, for validation purposes by a point cloud comparison.

The elongated road segment offers suitable possibilities to realise a further reference trajectory by external tracking. This enables an alternative independent validation option and is realised by the high-accurate[7] *Leica Absolute Tracker AT960* (cf. Figure 5.5(a)), which is also used for the calibration task in section 4.2. To be able to determine the position of the MMS, a Corner Cube Reflector (CCR) is rigidly adapted to the system (cf. Figure 5.5(b)). The CCR is mounted so that it can be observed while the vehicle is in motion. Its position with respect to the PCS from the MMS must be known as part of an accurate calibration. With a measuring frequency of $50\,\mathrm{Hz}$, the laser tracker provides 3D point coordinates with respect to its internal SOCS. This allows relative comparisons between the obtained trajectories. For an absolute comparison, the observations of the laser tracker must be transformed into a superordinate WCS (e.g. UTM projection with respect to the ETRS89) by using known control points. It should be noted that some uncertainties arise from the use of the control points and the subsequent transformation. Furthermore, it must be taken into account that the accuracy specifications for the laser tracker from the

(a)   (b)

Figure 5.4: *Images of the measured area in an urban canyon. Besides the MMS RIEGL VMX-250 used, the building facades on both sides of the street are also shown in (a) and (b). The respective locations where the images were taken are shown in Figure 5.2(b).*

---

[7]Accuracy of $\pm 15\,\mu\mathrm{m} + 6\,\mu\mathrm{m/m}$ (as a MPE for the 3D position) (Hexagone Metrology, 2015)

(a)   (b)
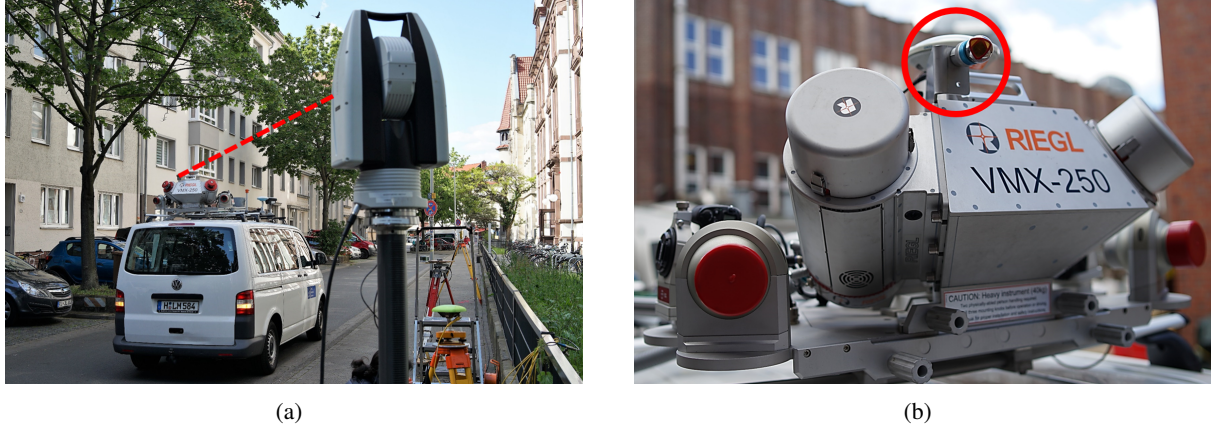
Figure 5.5: *Measurement configuration to provide a highly accurate reference trajectory. A Leica Absolute Tracker AT960 observes the moving MMS during data acquisition (a). In advance, a CCR is rigidly mounted on the MMS and calibrated with respect to the PCS (b).*

manufacturer are only valid under laboratory conditions and within certain measuring distances. Due to outdoor applications, atmospheric influences affect the quality of the reference trajectory. Nevertheless, an accuracy in the sub-millimetre range can be assumed here. These values are only valid if the relative trajectory is used with respect to the SOCS of the laser tracker. Specific empirical values are not known for this tracking task and should be determined and considered in the future.

It should also be noted that in the context of this thesis, the scale factor with regard to the underlying UTM projection is not considered. Influences arising from this can be neglected in relation to the inaccuracies mentioned above. For the measurement area given here, the scale factor is about 0.9996297, which leads to an error of about $6\,\text{mm}$ at a typical measurement distance of $15\,\text{m}$. For larger measurement areas, this should be taken into account in future. Regardless of this, time synchronisation between the observation variables of the MMS and the laser tracker must be ensured. Here, this is realised by an external GNSS receiver, which stores GPS timestamps with the same frequency of $50\,\text{Hz}$ for each 3D coordinate of the laser tracker. Due to the external tracking, the trajectory is limited to the maximum measuring range of the laser tracker. According to the manufacturer, this is theoretically $80\,\text{m}$ under laboratory conditions (Hexagone Metrology, 2015), but practically in outdoor areas, it is about $50\,\text{m}$. The acquisition of a reference pose with respect to the complete 6-DoF is theoretically possible but requires a different target instead of the CCR. In addition, the measurable range would be further reduced significantly.

To obtain a 3D point cloud, the $M_{I,k}$ coordinates $\boldsymbol{P}_{\text{Riegl,I},k}$ and $M_{II,k}$ coordinates $\boldsymbol{P}_{\text{Riegl,II},k}$ of the two laser scanners with regard to their respective SOCS are combined for epoch $k = 1, \ldots, K$ in a joint point cloud $\boldsymbol{P}_{\text{Riegl},k}$ according to

$$\boldsymbol{P}_{\text{Riegl,I},k} = \left[x_{\text{Riegl,I},k,1}, y_{\text{Riegl,I},k,1}, z_{\text{Riegl,I},k,1}, \ldots, x_{\text{Riegl,I},k,M_{I,k}}, y_{\text{Riegl,I},k,M_{I,k}}, z_{\text{Riegl,I},k,M_{I,k}} \right]^T, \tag{5.2a}$$

$$\boldsymbol{P}_{\text{Riegl,II},k} = \left[x_{\text{Riegl,II},k,1}, y_{\text{Riegl,II},k,1}, z_{\text{Riegl,II},k,1}, \ldots, x_{\text{Riegl,II},k,M_{II,k}}, y_{\text{Riegl,II},k,M_{II,k}}, z_{\text{Riegl,II},k,M_{II,k}} \right]^T, \tag{5.2b}$$

$$\boldsymbol{P}_{\text{Riegl},k} = \left[\boldsymbol{P}_{\text{Riegl,I},k}^T, \boldsymbol{P}_{\text{Riegl,II},k}^T \right]^T. \tag{5.2c}$$

Note that $M_{I,k}$ and $M_{II,k}$ can vary per epoch and that for each individual scan point it is known by which of the two laser scanners it was acquired. Furthermore, one single epoch k contains all observations of a complete $360°$ rotation of the laser scanners. Since every single measured point has an individual timestamp, the averaged timestamp is used as a time reference for the combination of all point observations in one epoch k. Thus, to a certain extent, a spatial point cloud can be derived as with a 3D laser scanner. For this purpose, a transformation of all observations with reference to their respective SOCS into a common coordinate system is required. This is realised in the PCS, which coincides with the SOCS of the IMU. The necessary transformation parameters are known from the manufacturer.

In addition, the pose parameters $[\boldsymbol{t}_{\mathrm{MMS},k}, \boldsymbol{\theta}_{\mathrm{MMS},k}]^T$ per epoch k based on the GNSS-IMU positioning unit are available as further information. These refer directly to the WCS and represented an already filtered solution

$$\boldsymbol{t}_{\mathrm{MMS},k} = [t_{\mathrm{MMS,x},k}, t_{\mathrm{MMS,y},k}, t_{\mathrm{MMS,z},k}]^T , \tag{5.3a}$$

$$\boldsymbol{\theta}_{\mathrm{MMS},k} = [\omega_{\mathrm{MMS},k}, \varphi_{\mathrm{MMS},k}, \kappa_{\mathrm{MMS},k}]^T . \tag{5.3b}$$

Within the context of this scenario, it is therefore investigated to what extent the use of complementary object space information can contribute to an improved georeferencing solution. The independence of this pose information for ensuring integrity aspects is analysed and possible deviations in accuracy, precision and reliability are determined. The unfavourable point cloud geometry due to the present laser scanner arrangement as well as the elongated street canyon have to be considered as special challenges. The observations of a laser tracker are used for validation purposes. This reference includes the 3D positions $\boldsymbol{t}_{\mathrm{LT},k}$ which refer to the corresponding SOCS and can be transformed into the superordinate WCS for each epoch k

$$\boldsymbol{t}_{\mathrm{LT},k} = [t_{\mathrm{LT,x},k}, t_{\mathrm{LT,y},k}, t_{\mathrm{LT,z},k}]^T . \tag{5.4}$$

Furthermore, the requested quantities are the three translations $t_{\mathrm{Riegl},x,k}$, $t_{\mathrm{Riegl},y,k}$ and $t_{\mathrm{Riegl},z,k}$, three rotations $\omega_{\mathrm{Riegl},k}$, $\varphi_{\mathrm{Riegl},k}$ and $\kappa_{\mathrm{Riegl},k}$, three velocities $v_{\mathrm{Riegl},x,k}$, $v_{\mathrm{Riegl},y,k}$ and $v_{\mathrm{Riegl},z,k}$ as well as three angular velocities $v_{\mathrm{Riegl},\omega,k}$, $v_{\mathrm{Riegl},\varphi,k}$ and $v_{\mathrm{Riegl},\kappa,k}$ per epoch k. As with the UAV, these describe the pose and velocity of the MMS with respect to a superordinate coordinate system and must be determined with a suitable georeferencing method.

5.2.3 Additional Object Space Information

Digital Terrain Model

The use of absolute height information is a helpful additional information for georeferencing. A Digital Terrain Model (DTM) describes the surface of the Earth without considering any objects (e.g. buildings, plants) (Doyle, Frederick, J., 1978). Nowadays, its realisation is mainly based on airbone laser scanning, so that a wide availability can be provided. Thus, within the framework of a uniform grid, absolute height information can be specified with regard to an arbitrary reference system. The DTM used in this application example has a grid width of $1\,\mathrm{m}$ and refers to the Deutsches Haupthöhennetz 2016 (DHHN2016) (Landeshauptstadt Hannover, 2017b). The accuracy of this height information is less than $0.3\,\mathrm{m}$, whereas the associated quality parameter is not indicated. Figure 5.6 shows the height values for the urban areas to which the measurements in this experiment refer (cf. section 5.2.2). Even if these are exclusively terrain heights, urban structures are clearly visible. The area of the inner courtyard appears slightly higher with respect to its surroundings. Overall, the heights in both measuring areas are fairly constant or vary within the range of the specified accuracy.

Three-dimensional Building Model

Digital city models exist for a variety of international cities which represent the outer shell of buildings in three dimensions. In general, they are based on building surveys for the cadastre, DTMs for the height allocation (cf. section 5.2.3) and 3D point clouds from airbone laser scanning (Vosselman and Dijkman, 2001). A distinction is made between different Level of Details (LoDs) according to the standardised CityGML format (Gröger et al., 2012). While LoD-1 approximates buildings in the form of cubes, LoD-2 contains standardised roof shapes. In addition, there are also more detailed generalisations, but these are less widely available (Biljecki et al., 2016). Throughout Germany, 53 million buildings with LoD-1 and 45 million buildings with LoD-2 have been modelled. There the update is annual (AdV, 2020). The available accuracy in position depends on the data in the official real estate map and may theoretically be a

few centimetres. However, since the modelling is a highly simplified generalisation of the actual building, a much more pessimistic value of a few centimetres to a few decimetres must be assumed. The resulting deviations from reality must be taken into account in the further course of this thesis. The resulting deviations from reality must be taken into account in the further course of this thesis. The accuracy in the height component is $5\,\mathrm{m}$ for the LoD-1 and $1\,\mathrm{m}$ for the LoD-2, whereas the associated quality parameter is not indicated (Landeshauptstadt Hannover, 2017a).

Each building is modelled in three dimensions based on its outline. The coordinates of the respective vertices are available in a superordinate coordinate system (e.g. UTM projection with respect to the ETRS89) (Landeshauptstadt Hannover, 2017a). Thus absolute information is available, and the building model can be interpreted as a network in which each node is assigned a three-dimensional coordinate. The topology of the individual nodes is known, so that individual planes in the form of arbitrary planar polygons are defined by at least three nodes (vertices). Figure 5.7 shows the building models used for the two measurement areas.

(a)   (b)
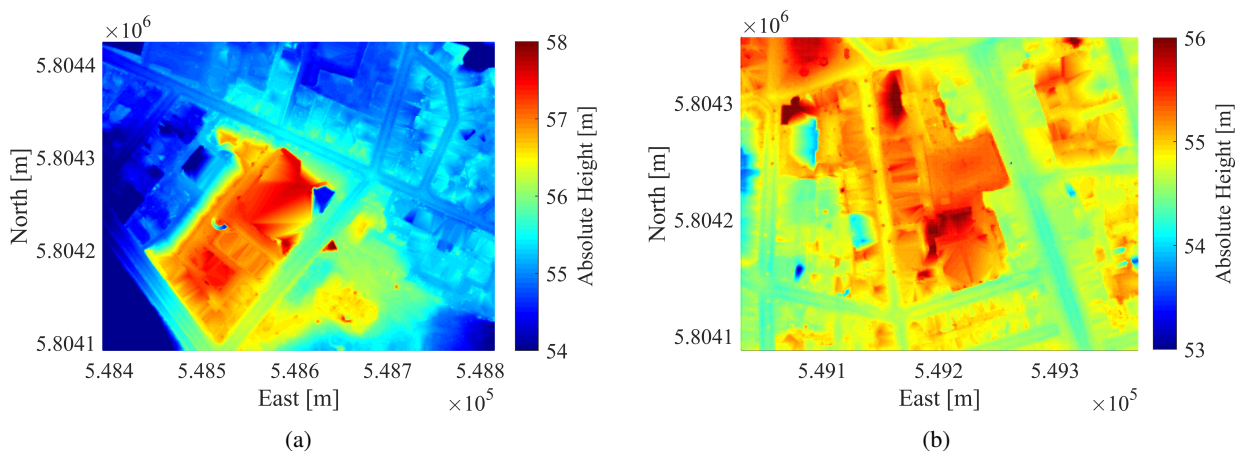
Figure 5.6: *Part of the DTM for the two different measurement areas. For the inner courtyard (mainly red/yellow area in the left half of the map) in (a) and the urban canyon (yellow road in north-south direction with several red spots in the left half of the map) in (b). Note the different scaling of the colour bar with respect to the absolute height shown in both figures.*

(a)   (b)   (c)
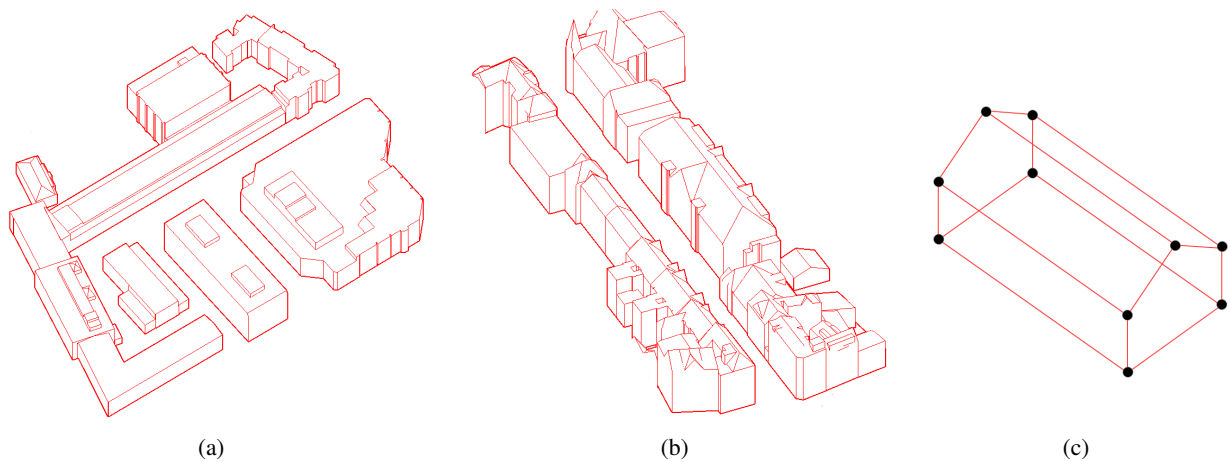
Figure 5.7: *Illustration of the three-dimensional building model with LoD-2. The part of the inner courtyard (a) and the urban canyon (b) is shown as well as the detailed representation of a single building (c) with respective nodes/vertices (black circles) and the topology (red lines).*

5.3 State of the Art Methods

In section 5.2.1 two laser scanner-based MSSs are presented, which shall be georeferenced accurately, precisely, reliably and continuously in two different environments (cf. section 5.2.2)[8]. However, the respective environment holds challenges with regard to these georeferencing requirements. For this reason, a general overview of current possibilities for georeferencing an arbitrary MSS is given below. This enables a better classification of the own new approach compared to the existing methods.

The basic concept and definition of georeferencing is already given in section 4.1. Generally, all individual sensors of an arbitrary MSS acquire their measurement data with respect to their unique local SOCS. With a suitable strategy for calibration, the relationship between the individual local SOCSs and one common superordinate PCS can be realised (cf. section 4.2). However, if the spatial reference to a global WCS[9] is also required, georeferencing is necessary. This enables a unique determination of the pose of an arbitrary MSS with respect to its spatial environment. Especially with kinematic MSSs, the temporal changes of the pose are of special interest. The accurate, precise, reliable and also efficient solution of this task depends strongly on the available sensors and hardware, the environment and the respective requirements. Consequently, there are a multitude of approaches that depend on the mentioned influencing factors. All of these methods can basically be divided into the three categories *direct*, *indirect* and *data-driven* georeferencing (Schuhmacher and Böhm, 2005; Paffenholz, 2012; Neitzel and Neumann, 2013; Holst et al., 2015; Vogel et al., 2016). Generally, these techniques can be applied to both static and kinematic MSSs. However, kinematic systems are in the main focus of this thesis. The three categories are briefly introduced below and discussed in terms of their respective disadvantages and suitability for application. Specific examples of the individual techniques are directly related to the compilation of different kinematic MSSs in Table 4.1. Subsequently, a selection of currently relevant approaches is given in connection with the experiment described in section 5.2 and the associated objectives. Furthermore, Kuutti et al. (2018) provides a comprehensive compilation of localisation techniques and their respective potentials, especially for autonomous vehicle applications. This includes the use of onboard sensors as well as cooperative localisation methods.

Direct[10] *georeferencing* is characterised by the fact that all 6-DoF of the MSS are determined directly by sensors, which are part of the system and therefore rigidly attached to it. In most cases these are GNSS antennas, IMUs or odometers. Furthermore, reflectors can also be mounted on the MSS, which are tracked by an external sensor (e.g. a total station or laser tracker). In general, the combined use of GNSS and IMU measurements is highly recommended. Thus all 6-DoF can be determined. An advantage is that GNSS observations allow absolute positioning, which is not directly possible with other sensors. To achieve highest accuracies[11] (up to $1\,cm$ to $2\,cm$), methods like differential GNSS or real-time kinematic are required (Gleason and Gebre-Egziabher, 2009, pp. 349). However, as already mentioned in section 5.1, no reliable and accurate positioning can be guaranteed in urban areas. This is in contrast to important integrity aspects of autonomous driving or UAVs, for example (Wörner et al., 2016; Reid et al., 2019). IMUs are affected by temporal bias drifts due to integration errors with increased measuring time. This depends on the respective accuracy class and is additionally superposed by a significant noise characteristic (Grejner-Brzezinska et al., 2005; Hesch et al., 2010; Glennie, 2007). Thus, IMUs cannot compensate for the disadvantages of GNSS observations in urban areas (Zhang, 2019). Nevertheless, in the short term for individual epochs IMUs show a locally helpful inner accuracy. The external tracking of a reflector means that the flexibility of direct georeferencing is lost and the mobility of the kinematic MSS is limited depending on the constant line of sight. In addition, the applicability depends on the environment and is, therefore, not a practical solution. This method can be reasonable only for validation purposes with a sensor of higher accuracy (e.g. laser tracker).

---

[8]Although the MMS *RIEGL VMX-250* provides pose information in the second scenario, those are only used here for validation purposes

[9]The WCS is characterised by the fact that it is a unique and earth-fixed coordinate system and thus represents a relationship to its environment. In general, it is signalised by physical or artificial control points. Its spatial dimensions can be arbitrary.

[10]Also referred to as *sensor-driven*

[11]Indicated as $95\,\%$ confidence interval

For *indirect*[12] *georeferencing*, the sensors used are also part of the MSS, but require known targets in a superordinate earth-fixed coordinate system to determine the pose parameters. These are mainly laser scanners and stereo or mono cameras. The targets can be signalised control points or geometric primitives and require a prior alignment in terms of global position and orientation. The pose estimation is then based on a combination of the locally measured observations of the sensors and the targets in the super-ordinate coordinate system. This procedure requires certain effort in the realisation and pre-acquisition of the targets. Depending on the complexity of the environment (e.g. full visibility) and requested flexi-bility and reliability, the effort can be immense. Therefore, for large-scale areas, which extend over more than one road section, this is not economically feasible. Consequently, this procedure is mainly used for georeferencing of static MSSs (Paffenholz, 2012).

Data-driven georeferencing has similarities to the aforementioned indirect georeferencing. The difference is that instead of signalised targets, already existing reference data are used. These can be already georef-erenced point clouds, digital building models as well as digital terrain or surface models. The assignment between the measured observations of the MSS and the available data is based on various matching tech-niques. The quality of this type of georeferencing depends directly on the quality and up-to-dateness of the preliminary information. The most popular assignment method is the so-called Iterative Closest Point (ICP) algorithm from Besl and McKay (1992), which has numerous variations today. The class of data-driven approaches for georeferencing an MSS comprises a broad range. In particular, methods based on the Simultaneous Localisation and Mapping (SLAM) approach could be mentioned here. This approach was initially developed by Smith and Cheeseman (1986) and comprises various adaptations and further developments today. The special feature of such an approach is that no prior information is re-quired. Instead, the georeferencing is solved, and a map of the environment is generated simultaneously. Many of these SLAM approaches can be assigned to the robotics field (Thrun et al., 2005; Nüchter et al., 2007; Siciliano et al., 2009). However, quality parameters are not always fully taken into account and dis-closed. This is a major difference to methods in geodesy. In addition, SLAM approaches usually provide only relative pose information. This leads to a precise solution, while at the same time, the accuracy is poor compared to reality. Therefore, it is not compatible with integrity requirements for accurate georef-erencing during autonomous driving. Nevertheless, it is a method that can be used independently of its environment and without any prior information. The only prerequisite is that suitable features (e.g. poles, edges) are consistently available in sufficient quantity. For SLAM approaches mainly laser scanners are used. The application of cameras is also possible, which is referred to as *visual* SLAM (Davison, 2003; Konolige and Agrawal, 2008; Steffen, 2013). However, an unambiguous texture is necessary here. Fur-thermore, only relatively low frequencies can be achieved compared to the use of a laser scanner. However, in comparison to laser scanning, the measurements from cameras (images) take place simultaneously.

It can be concluded that each of the three categories has its advantages and disadvantages. In order to provide suitable solutions for the challenges in urban areas (cf. section 5.1), it is important to apply the described approaches appropriately. Basically, the use of GNSS observations and data from an IMU is indispensable. However, it is necessary to identify insufficient situations and to provide alternative solutions. From the perspective of the GNSS community, two basic approaches, among others, are pursued to counteract this drawback (Zhang et al., 2018). On the one hand, there are approaches which identify the NLOS observations with the aid of 3D building models and thus can be excluded from the position estimation. On the other, the availability of such 3D city models can also be used to create a so-called *predictive GNSS positioning error map*. This can then be used to classify the available GNSS observations with respect to their quality. This information can be considered for an improved estimation. The basis in each case is the consideration of 3D building models of the respective environment. Such models are available at least for a variety of urban areas worldwide and are already used as important additional information for various applications (Biljecki et al., 2015). As in Zhang et al. (2018) it is also here to a large extent about visibility analyses (Wang et al., 2013).

The information from 3D building models can also be used directly to estimate the pose of a kinematic MSS. In Hebel et al. (2009) this is applied on airborne laser scanning. Their goal is to improve the inaccurate pose based on GNSS and IMU observations. For this purpose, planes are detected in the point

---

[12]Also referred to as *target-based*

cloud of a laser scanner and assigned to known planes of a building model. A similar approach is applied in Bureick et al. (2019b), where 3D point observations of a laser scanner are assigned to planes of a known building model with LoD-2 to improve the pose of a UAV in a simulated environment. The basis is the IEKF for explicit and implicit measurement equations from Vogel et al. (2018, 2019), as also given in section 3.1. In Bureick et al. (2019a), the approach is validated with real data and also extended by additional assignments to a DTM. A detailed description and further extension of this approach is given in section 5.4. Dehbi et al. (2019) are using an approach that is also intended to improve GNSS trajectories within urban environments. No filter approach is used here, but the captured point cloud is matched to a city model with LoD-1by using a point-to-plane ICP. Therefore a Support Vector Machine (SVM) is used to distinguish between facade elements and remaining points. A building model with LoD-2 is also used in Garcia-Fernandez and Schön (2019). Here the known planes serve as landmarks and are used as Vehicle-to-Infrastructure (V2I) measurements for pose estimation in collaborative positioning.

Besides a building model, other information from the object space can be used to support the pose estimation, which already happens frequently. Using laser scanner observations, the pose of a vehicle is improved in Weiss (2011) with regard to driver assistance systems. For this purpose, an initial solution is improved by means of a highly accurate digital map. However, this only refers to the 2D position and the heading angle[13]. An estimation and improvement of all 6-DoF is not made. For some applications, this might be sufficient, but if, for example, accurate 3D point clouds are to be generated based on the pose information, additional degrees of freedom are missing. Also Soloviev et al. (2007) show that extracted object space information from laser scanner measurements, e.g. in the form of line segments, can be used to estimate pose parameters. Vennegeerts (2011) also uses information from object space for pose estimation of a laser scanner-based MMS. Line segments are detected over several epochs and serve for high-frequency stabilisation of the roll angle. Fixed landmarks such as lanterns, traffic lights or traffic signs are used for localisation tasks in Brenner and Hofmann (2012); Hofmann (2017); Schlichting (2018).

Object space information can also be considered by constraints. In terms of georeferencing a kinematic MSS, Vogel et al. (2018, 2019) introduces geometric conditions regarding the angular relationships between different walls. Further restrictions, which contribute to an improved estimation, may be present, e.g. in the form of road boundaries (Brembeck, 2019) or planar surface assumptions (Nüchter et al., 2015). Brembeck formulates these as inequalities by using MHE. In Zwiener (2019), a robust simplex-KF for explicit measurement equations is presented, which considers inequalities and conditional equations for an improved estimation by limiting the solution space. This approach is applied to the navigation solution of a UAV, but does not explicitly refer to challenging environments like urban canyons.

Constraints can also be considered in SLAM approaches. In Jung et al. (2015), line features are extracted from a laser scanner point cloud, and geometric constraints regarding perpendicularity and parallelism are established. This contributes to improved localisation within an indoor environment. Nguyen et al. (2006) also uses lines for localisation purposes that are exclusively parallel or perpendicular to each other. SLAM methods for pose determination are used much more frequently, which do not explicitly consider additional constraints. The simultaneous localisation and acquisition of the environment is solved in Bosse et al. (2012) exclusively on the basis of a spring-mounted 2D laser scanner and an IMU. For this purpose, the trajectory is partitioned into individual sub-scans, and for each, a separate rigid transformation is calculated by using ICP. This approach is refined by a non-rigid registration in Kaul et al. (2016) for georeferencing of a UAV by using a continuous-time SLAM approach. A time-discrete approach is not possible there because no high-frequency sensors are used, and the UAV is constantly in motion. In Elseberg et al. (2013a) a semi-rigid registration of single scan strips of a laser scanner based MSS is applied. A SLAM approach for urban environments is presented in Nüchter et al. (2007). They used a stop-and-go procedure, whereby the individual scans are assigned to each other via ICP.

Although there are several different SLAM approaches, they exist exclusively in the context of explicit relationships. Besides the disadvantages mentioned above, there is also a lack of long-term support. Small errors can accumulate over time. Therefore, independent and complementary information from a building model is recommended. Therefore, considering the scenarios described in section 5.2, many of the approaches presented here are not applicable. Only laser scanner observations and object space information

---

[13]Also referred to as *azimut* or *yaw*

regarding the ground and surrounding buildings are available. Thus, the application of a method which belongs to the class of data-driven approaches is appropriate. This is applied in the following section 5.4.

5.4 Novel Information-based Georeferencing Approach

As shown in section 5.3, there are many methods for georeferencing a kinematic MSS. However, for complex and challenging environments, such as urban areas, there is still potential for improvement. For georeferencing of the specific kinematic MSSs introduced in section 5.2.1, it is necessary to find the optimal solution under the given conditions. A new approach is introduced in Bureick et al. (2019b), which is mainly based on the combination of 3D laser scanner observations and their assignment to building facades. The facade elements are regarded as planes, which are allocated in a digital city model with global coordinate information (cf. section 5.2.3). The first application with real data in an outdoor environment has already been performed in Bureick et al. (2019a). This approach is based on the versatile recursive state-space filter for explicit and implicit measurement equations from section 3.1. The main idea has already been presented in Vogel et al. (2019) in parts and was used to georeference a kinematic MSS within an indoor environment. The innovations in this thesis include the consideration of geometric constraints when they are applied on two real data sets, which were introduced in section 5.2.2. Furthermore, for the first time, a highly accurate reference solution is realised in an outdoor environment and is used for validation purposes. The basic idea of the novel approach is explained below.

5.4.1 Basic Idea

To ensure the integrity of a kinematic MSS regardless of the environment, georeferencing is achieved by using two independent and complementary information sources. If there are appropriate conditions for georeferencing on the basis of GNSS observations (cf. Figure 5.8(a)), this is the method of choice in combination with an IMU. Several established methods already exist for this use case (Petovello, 2004), and therefore they are not further discussed here. The opposite is true in urban environments (cf. Figure 5.8(c)), where GNSS and IMU observations alone are insufficient. Here, information from a 3D building model must be used additionally. Moreover, even if the building model is partly not available in such challenging environments[14], helpful additional information can be used by geometric constraints. For the application of such geometric restrictions (e.g. facades are generally perpendicular to the ground), the independent segmentation of facade elements by using a suitable method[15] is required. A justification and specific definition of such a geometric condition can be based on standards from the civil engineering industry (DIN 18202:2019-07, 2019). In addition to the common solution when using GNSS and IMU observations, the integration of information from the building model enables a long-term stabilisation of the pose. This can be useful even if appropriate GNSS conditions exist (cf. Figure 5.8(b)). This is because both information sources can be used independently of each other to verify the integrity of the kinematic MSS. The use of additional independent observations from a DTM (cf. section 5.2.3) can be realised regardless of the environment and is generally reasonable.

The realisation of the approach itself is based on three central elements. Within each epoch $k = 1, \ldots, K$ it is first to *transform* the measured laser scanner point cloud P_k^{SOCS} into the superordinate WCS. The transformation parameters required for this are based on sufficiently accurate approximate values in the first epoch. For the following epochs, the predicted poses of the MSS are used. Then the point cloud P_k^{WCS} is aligned with respect to the WCS and the *assignment* with regard to captured buildings and the terrain surface can be applied. The absolute vertices contained in the building model, as well as the absolute height information from the DTM, are used for this purpose. The assignment results in a classified point cloud C_k^{WCS}, in which the relationship to corresponding surfaces of the building model or grid cells of the DTM are stored. Subsequently, this connection with the available object space information enables an estimation in the *versatile IEKF* for explicit and implicit measurement equations (cf. section

---

[14] A possible reason for this absence would be, for example, an outdated model
[15] For example, the use of a SVM according to (Dehbi et al., 2019) can be mentioned here

3.1). Additional constraints regarding the states are taken into account by using an arbitrarily suitable method according to section 3.2. Here, there is the possibility of hard constraints (cf. section 2.3.1) or the permission of minimal deviations when using SC (cf. section 2.3.2).

The general procedure of the information-based georeferencing approach is summarised in Figure 5.9. Besides the three central elements, spatial subsampling is also mentioned there. This enables an optional reduction of the available observation data. Therefore, several 3D point observations within a certain
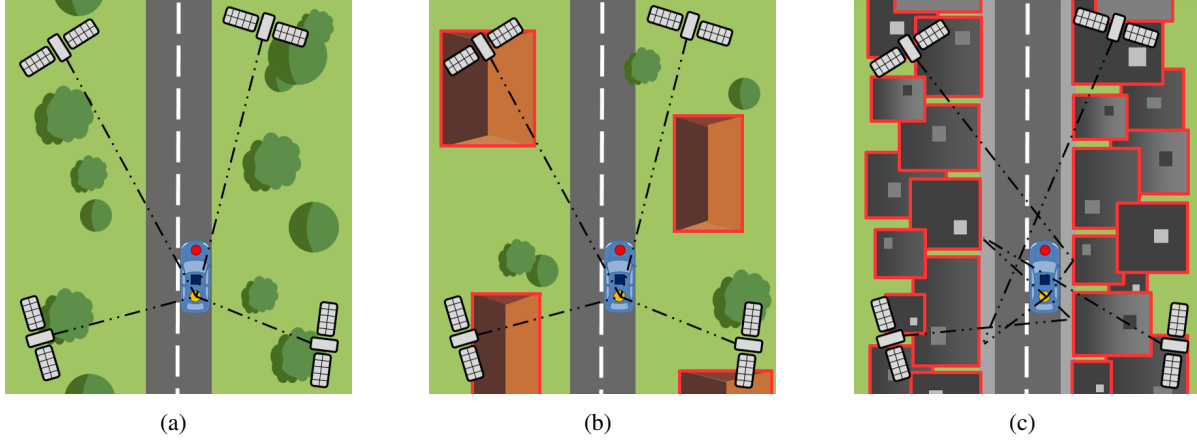
Figure 5.8: *Simplified overview of three typical environments in which a kinematic MSS operates. The example shows a vehicle with a laser scanner (red circle), a GNSS antenna (yellow heptagon) and an IMU (blue square). Shown is a country road without buildings (a), a sparsely populated suburban road (b) and an urban canyon (c). Exemplary GNSS observations are shown with black dashed lines. Information from a building model are symbolised with red outlines.*
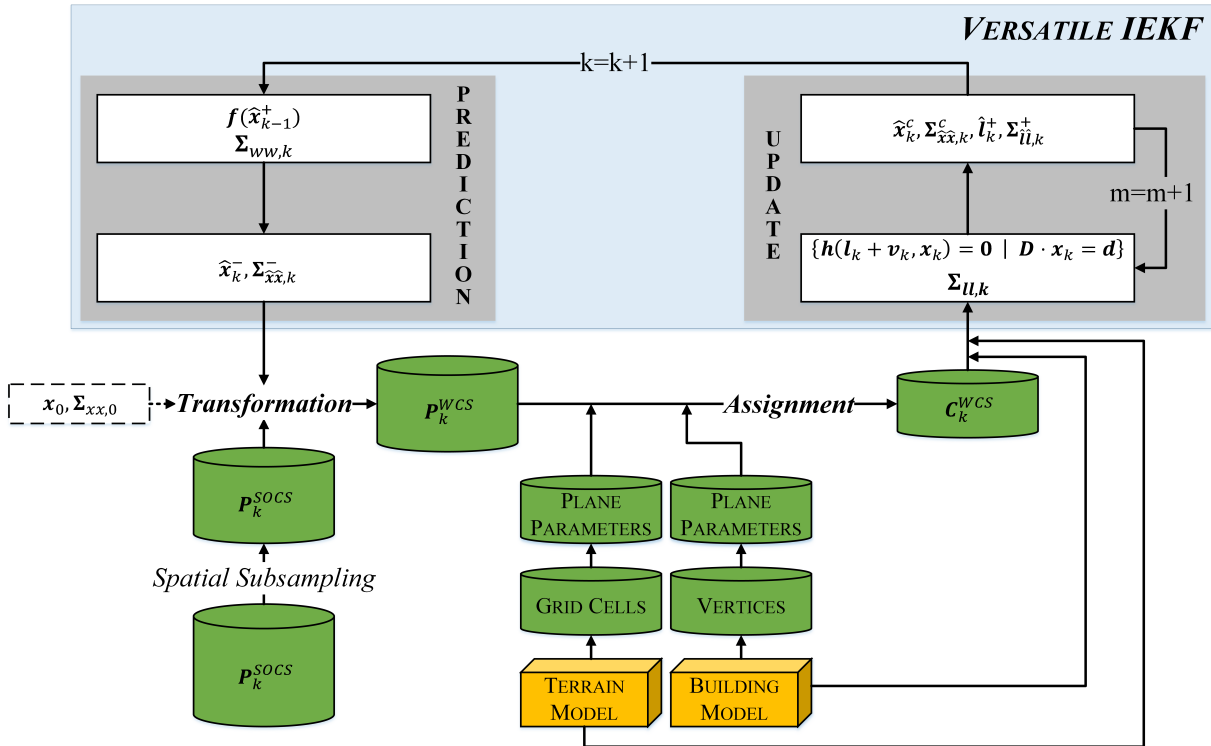
Figure 5.9: *Simplified process of the information-based approach for georeferencing a laser scanner-based MSS in urban areas. Central elements represent the transformation, assignment and application in the versatile IEKF of the 3D point clouds within each epoch k. The variable m specifies the iterations within the update step. The start of the flowchart is the acquisition of a 3D point cloud with respect to a SOCS for the first epoch $k = 1$ (lower left corner).*

three-dimensional area are reduced to one single mean observation. The side length $d_{\text{Subsampling}}$ of this voxel can be freely chosen. Although this allows faster run times, important information may be lost. Even if no entire areas are neglected by the spatial scanning, this leads to additional weakening of areas with less information at all. Later, it becomes apparent that this can have negative consequences for the assignment as well as the subsequent state estimation. However, spatial subsampling results in a better homogeneity of the point cloud and denser areas tend to have a less strong influence. This addresses the problem already mentioned in section 3.3. It is usually not mandatory to use all available observations for the estimation. However, the selection of the observations to be used is essential. Considering the spatial distribution is a valid concept, but it would make more sense to use the current information content and contribution of a single observation. However, this is not within the scope of this thesis. Nevertheless, it must be noted that this spatial subsampling method results in observations that have never actually been measured. Further details of the three central elements of the approach presented here are explained subsequently.

5.4.2 Transformation of the Laser Scanner Observations

An essential requirement for the following steps is the transformation of the measured laser scanner observations P_k^{SOCS} from their local SOCS to a superordinate WCS (in which the models of the object-space are also located). Thus, point clouds of several epochs can be connected with each other and the subsequent assignment to the models can be realised. In the context of the MSSs and measurement environments from section 5.2 the point clouds P_k^{SOCS} corresponds to $P_{\text{UAV},k}$ (cf. Equation (5.1)) or $P_{\text{Riegl},k}$ (cf. Equation (5.2c)), respectively. The transformed point clouds P_k^{WCS} result from

$$P_k^{\text{WCS}} = t_{\text{SOCS-WCS},k} + R_{\text{SOCS-WCS},k} \left(\boldsymbol{\theta}_{\text{SOCS-WCS},k} \right) \cdot P_k^{\text{SOCS}}, \tag{5.5}$$

where $t_{\text{SOCS-WCS},k}$ compose the three translations $\left[t_{\text{SOCS-WCS},x,k}, t_{\text{SOCS-WCS},y,k}, t_{\text{SOCS-WCS},z,k} \right]^T$ and $R_{\text{SOCS-WCS},k}$ is the 3D rotation matrix containing the three orientation angles $\boldsymbol{\theta}_{\text{SOCS-WCS},k} = \left[\omega_{\text{SOCS-WCS},k}, \varphi_{\text{SOCS-WCS},k}, \kappa_{\text{SOCS-WCS},k} \right]^T$. The following relationship applies to this rotation matrix

$$\begin{aligned} R_{\text{SOCS-WCS},k} \left(\boldsymbol{\theta}_{\text{SOCS-WCS},k} \right) = R_{x,\text{SOCS-WCS},k} \left(\omega_{\text{SOCS-WCS},k} \right) \cdot R_{y,\text{SOCS-WCS},k} \left(\varphi_{\text{SOCS-WCS},k} \right) \\ \cdot R_{z,\text{SOCS-WCS},k} \left(\kappa_{\text{SOCS-WCS},k} \right), \end{aligned} \tag{5.6}$$

which defines the concatenation of the individual rotation angles around the corresponding rotation axes. Together the three translations and three rotations form the corresponding transformation parameters, which must be renewed for each epoch $k = 1, \dots, K$. Their numerical values are initially expressed by the predicted state (or via sufficiently accurate approximate values for the first epoch $k = 1$). These six time-dependent transformation parameters provide the requested pose of the respective kinematic MSS. To ensure the most accurate georeferencing possible, the predicted states must be corrected for each epoch $k = 1, \dots, K$ by available observations and additional information. For this purpose, the assignment of the point observations to the corresponding digital models of the object space is necessary as an essential intermediate step.

It should also be noted that the transformation from SOCS to WCS can be subdivided by an unlimited amount of intermediate transformations. This concerns for example the observation data from the MMS *RIEGL VMX-250* in Equation (5.2c), where the initial observations are transformed from their SOCS to PCS and then to WCS. Here, all necessary transformations are simplified and summarised as one single transformation.

5.4.3 Assignment of the Laser Scanner Observations

The absolute information contained in the building model and in the DTM must be linked to the acquired laser scanner observations of the kinematic MSS in order to be used appropriately. The acquired 3D point cloud represents a reconstruction of the spatial environment and thus contains a variety of measurements from all objects located therein. This also includes measurements regarding the building facades and

the ground, which in turn are approximated in the corresponding models. If the measured 3D point coordinates are assigned to these objects, a direct relationship between the sensor of the MSS and the available object space information can be established. However, a reliable assignment in terms of accuracy, precision, correctness and completeness depends strongly on the quality of the laser scanner and the models themselves. In addition, the laser scanner and the associated MSS must be in the same reference system as the models, so that a suitable assignment can be achieved. The latter is already done by the previously transformed point cloud P_k^{WCS}.

In principle, there are four possibilities for each 3D point observation to be assigned. Point observations that belong to the ground are assigned to the corresponding grid cell of the DTM. Observations that are assigned to a plane of the building model are related to this model and provide an absolute coordinate reference. In addition, there are 3D points that belong to a building facade, but this plane itself is not present in the building model. Therefore no global reference can be established for these observations, but a geometric constraint can be applied. The last possibility includes all observations of any object (e.g. cars, persons, vegetation), which do not contribute to the georeferencing and are not considered further. For the other three options, the corresponding assignment principle and resulting possibilities are described below in detail.

Assignment to Planes from the Building Model

As described in section 5.2.3, the generalised building model contains the vertices of all buildings with absolute coordinates and their respective topology. From this information, individual geometric planes can be derived, which describe each facade. The individual elements of the acquired and transformed point cloud P_k^{WCS} need to be assigned to these geometrical primitives. However, the identification and assignment of such laser scanner observations to geometrical primitives is not the main focus of this thesis but represents a crucial processing step. For this reason, the approach used here is only briefly described and instead further references are referred to. The building model contains $j = 1, \ldots, J$ vertices V_j in total, with

$$V_j = [V_{x,j}, V_{y,j}, V_{z,j}]^T . \tag{5.7}$$

This 3D coordinates are absolute and refer to the WCS. Based on these J vertices, all $e = 1, \ldots, E$ facades can be defined as planes in the Hesse normal form. This includes the 3×1 unit normal vector $n_e = [n_{x,e}, n_{y,e}, n_{z,e}]^T$ as well as the distance parameter to the origin d_e for each plane. The resulting relationship is shown in simplified form in Figure 5.10. Basically, the assignment is performed by using the Euclidean distance of each measured point to each plane of the building model (Unger et al., 2016, 2017)[16]. The individual points are assigned to the nearest plane if a certain maximum distance $d_{\max}$ is
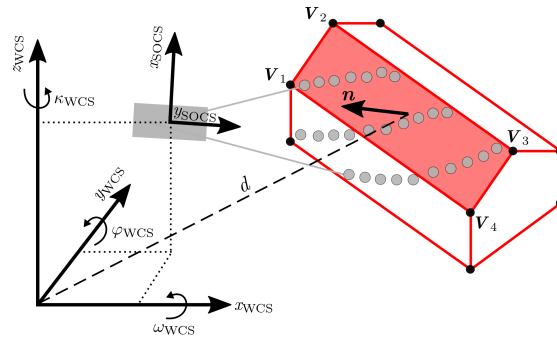
Figure 5.10: *Schematic illustration of the general principle for assigning laser scanner points (grey dots) to a building model (red). In addition, the corresponding coordinate systems are shown. Modified according to Bureick et al. (2019a).*

---

[16]Depending on the measurement area, the building model can contain several thousand or even more planes. To avoid the need to consider all these planes when assigning each individual observation, it is recommended to limit the search space. This can be done by using the predicted pose, and the maximum measuring range of the laser scanner applied.

not exceeded. This threshold is freely selectable and depends on the uncertainty of the laser scanner and building model used. In this thesis $d_{\mathrm{max}} = 0.5\,\mathrm{m}$ is used for both scenarios. Observations that are not assigned to any plane are ignored and do not contribute to the georeferencing task. As a result, the assigned laser scanner point cloud $\boldsymbol{C}_k^{\mathrm{WCS}}$ includes the information to which plane $e = 1, \ldots, E$ each point belongs. Thus, this point cloud consists of E subsets for each plane with $j_e = 1, \ldots, J_e$ assigned 3D coordinates. These subsets are also referred to as $\boldsymbol{C}_{k,e}^{\mathrm{WCS}}$.

Misalignment at intersections of two planes cannot be completely excluded. To counteract this issue, the assignment can subsequently be refined, or outliers can be eliminated. For example, a plane estimation in a Random Sample Consensus (RANSAC) procedure is suitable for this purpose (Fischler and Bolles, 1981). A lower threshold value d_{RANSAC} is selected for this compared to the original assignment. Furthermore, a minimum number of assigned points per plane can also be defined and applied. This further reduces the use of wrong assignments. In this thesis $d_{\mathrm{RANSAC}} = 0.15\,\mathrm{m}$ and a minimum of five 3D points per plane is used for both scenarios. Selecting a too low threshold value d_{RANSAC} or specifying a too large minimum number of assigned points can also lead to the loss of important information.

Assignment to Grid Cells from the Digital Terrain Model

The assignment of the point cloud with regard to the DTM is basically analogous to the building model. Individual planes can also be applied to the various cells of the DTM which is available in a grid structure (cf. section 5.2.3). Here the procedure is simplified, as the assignment is performed to an uniform two-dimensional grid. The individual points are also assigned and stored in $\boldsymbol{C}_k^{\mathrm{WCS}}$ by using the distance to the nearest plane. As with the E planes of the building model, the point observations assigned to each grid cell can also be specified as $\boldsymbol{C}_{k,e}^{\mathrm{WCS}}$. Therefore, the set $e = \{1, \ldots, E\}$ is extended by the $g = \{1, \ldots, G\}$ grid cells to $e = \{1, \ldots, E + G\}$.

However, a special aspect should be mentioned here. Of all laser scanner observations which are assigned to the same grid cell, only that observation with the lowest altitude component is used. All the other observations in the grid cell are neglected. This leads to a reduced overall influence in the estimation but avoids wrong height information. With an edge length of one metre, the grid can contain many different height values of the point cloud. This is the case, for example, if a parked vehicle is partially in the corresponding grid and was captured by the laser scanner.

Assignment to Facades That Are Not Included in the Building Model

The core of the information-based georeferencing approach is based on the assignment of laser scanner observations to digital models and their subsequent use. Therefore, it is assumed that such models are not only available, but also represent reality as accurately as possible within the specifications. This ensures an independent and complementary georeferencing under consideration of integrity aspects in urban areas. However, if the building model is not up-to-date in parts and thus does not correspond to reality, information from the object space should still be used in this approach. There could be a case that a building exists in reality but is not stored in the building model. Consequently, observations of the laser scanner on corresponding facade elements are available, but cannot be assigned without a model. However, the information-based approach does not reject these observations but rather takes them into account when estimating the pose. Even if there is no absolute information regarding the facade, having the knowledge that there is a facade and that it is perpendicular to the ground (according to standards from the civil engineering industry (DIN 18202:2019-07, 2019)) can be used. This information is introduced by means of a constraint. The only requirement for the realisation of this method is identifying the respective facades in the point cloud $\boldsymbol{P}_k^{\mathrm{WCS}}$. For this purpose, various methods exist, for example Schindler et al. (2011); Nurunnabi et al. (2015); Brenner (2016); Dehbi et al. (2019). However, in the context of this thesis, the assignment is solved by using the building model, but the absolute information is not used afterwards. This allows direct comparison regarding the impact of such a geometric constraint on the pose estimation.

The general procedure for the assignment of all laser scanner observations with regard to the different categories is shown in a simplified form in Figure 5.11. For the assignment to an unknown facade — which is therefore not stored in the building model — it is assumed that this facade can be identified by using a suitable additional method. For this category, constraints concerning the identified plane parameters are applied subsequently.

5.4.4 Application of the Versatile Recursive State-space Filter

Once the point cloud observations within each epoch $k = 1, \ldots, K$ are assigned to the building model, to the DTM or to a facade without absolute coordinates, this information is used within the framework of the versatile IEKF to estimate the pose of the kinematic MSS. The theoretical background of this filter approach is given in section 3.1. The state and observation vector, the system and observation model, as well as the non-linear state constraints, are introduced below.

State Parameters and System Equation

The state vector $\boldsymbol{x}_k$ comprises mainly the position $\boldsymbol{t}_{\text{SOCS-WCS},k}$ and the orientation $\boldsymbol{\theta}_{\text{SOCS-WCS},k}$ of the kinematic MSS in all three spatial directions at epoch $k = 1, \ldots, K$. Other states that are also included are the speed $\boldsymbol{v}_{\text{SOCS-WCS},\boldsymbol{t},k} = \left[v_{\text{SOCS-WCS},x,k}, v_{\text{SOCS-WCS},y,k}, v_{\text{SOCS-WCS},z,k} \right]^T$ and the angular velocity $\boldsymbol{v}_{\text{SOCS-WCS},\boldsymbol{\theta},k} = \left[v_{\text{SOCS-WCS},\omega,k}, v_{\text{SOCS-WCS},\varphi,k}, v_{\text{SOCS-WCS},\kappa,k} \right]^T$. Thus, in total 12 states are to be determined and are part of the state vector

$$\boldsymbol{x}_k = \left[\boldsymbol{t}_{\text{SOCS-WCS},k}^T, \boldsymbol{\theta}_{\text{SOCS-WCS},k}^T, \boldsymbol{v}_{\text{SOCS-WCS},\boldsymbol{t},k}^T, \boldsymbol{v}_{\text{SOCS-WCS},\boldsymbol{\theta},k}^T \right]^T . \tag{5.8}$$
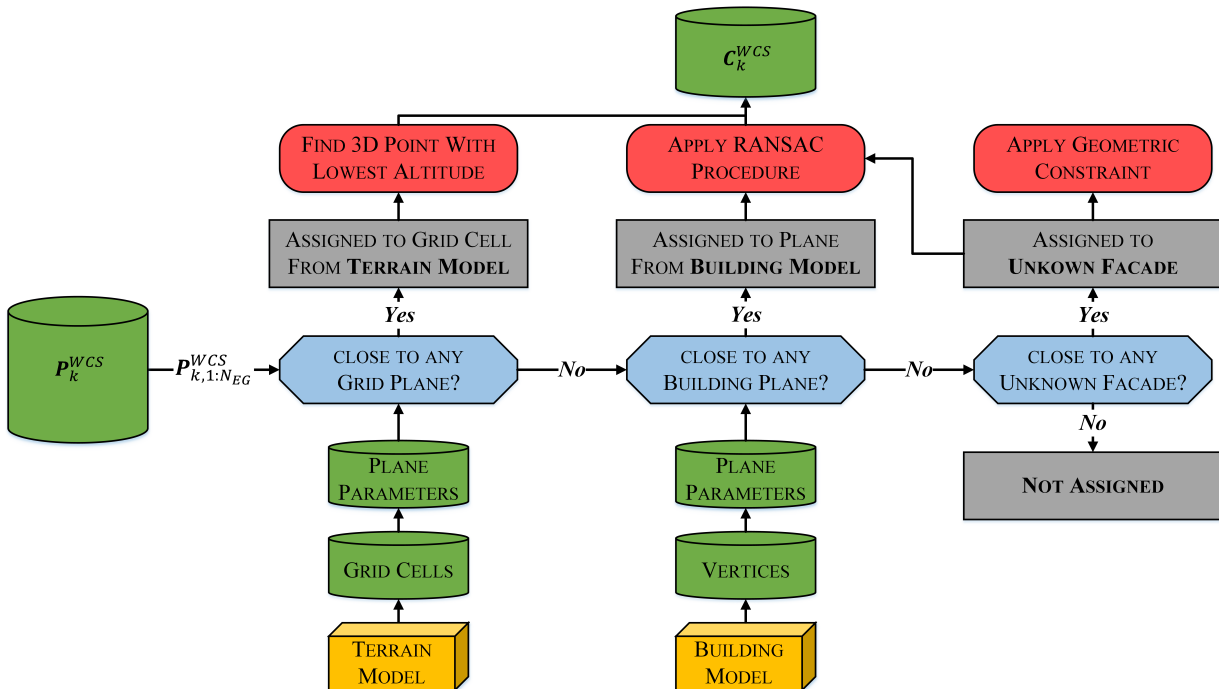
Figure 5.11: *Process of assigning laser scanner observations. Within an epoch k, all N_{EG} 3D point observations $\boldsymbol{P}_{k,1:N_{EG}}^{WCS}$ are assigned to the four categories (grey boxes). For each epoch, further procedures (red boxes) have to be considered for the observations assigned to the different categories. The assigned observations are stored in $\boldsymbol{C}_k^{WCS}$. The start of the flowchart is the availability of a 3D point cloud with respect to the WCS at any given epoch k (left side).*

The initial state vector x_0 can be defined based on a known pose (this applies to the Riegl MMS used in the urban canyon scenario) or it should be specified by using a sufficiently accurate assumption. For the initial VCM $\Sigma_{xx,0}$ of the state vector the following applies

$$\Sigma_{xx,0} = \begin{bmatrix} \mathbf{I}_3 \cdot \sigma_{x,t}^2 & \mathbf{0} & \mathbf{0} & \mathbf{0} \\ \mathbf{0} & \mathbf{I}_3 \cdot \sigma_{x,\theta}^2 & \mathbf{0} & \mathbf{0} \\ \mathbf{0} & \mathbf{0} & \mathbf{I}_3 \cdot \sigma_{x,v_t}^2 & \mathbf{0} \\ \mathbf{0} & \mathbf{0} & \mathbf{0} & \mathbf{I}_3 \cdot \sigma_{x,v_\theta}^2 \end{bmatrix}, \tag{5.9}$$

where $\sigma_{x,t}$, $\sigma_{x,\theta}$, σ_{x,v_t} and σ_{x,v_θ} are the corresponding initial standard deviations for the four individual groups of the state vector. No correlations between the individual elements are assumed for simplification. The system model $f(\cdot)$ used is kept quite simple, in which the predicted pose x_k^- is propagated by the last filtered pose x_{k-1}^+. Speed and angular velocity are assumed to be constant in this model (Bar-Shalom et al., 2001, pp. 268 ff.). Taking into account the time period between two consecutive epochs $\Delta\tau$, the system equations $f\left(x_{k-1}^+, u_{k-1}, 0\right)$ are

$$t_{\text{SOCS-WCS},k}^- = t_{\text{SOCS-WCS},k-1}^+ + v_{\text{SOCS-WCS},t,k-1}^+ \cdot \Delta\tau, \tag{5.10a}$$

$$\theta_{\text{SOCS-WCS},k}^- = \theta_{\text{SOCS-WCS},k-1}^+ + v_{\text{SOCS-WCS},\theta,k-1}^+ \cdot \Delta\tau, \tag{5.10b}$$

$$v_{\text{SOCS-WCS},t,k}^- = v_{\text{SOCS-WCS},t,k-1}^+, \tag{5.10c}$$

$$v_{\text{SOCS-WCS},\theta,k}^- = v_{\text{SOCS-WCS},\theta,k-1}^+. \tag{5.10d}$$

The predicated state estimate x_k^- can then be determined according to Equation (2.71). Here, the control vector u_{k-1} is assumed to be 0. This linear system model could be improved. However, this is not essential within the framework of the approach used and is not the focus of this thesis. The process noise w_k is defined separately within the VCM $\Sigma_{ww,k}$ for the four state groups, where the following applies

$$\Sigma_{ww,k} = \begin{bmatrix} \mathbf{I}_3 \cdot \sigma_{w,t}^2 & \mathbf{0} & \mathbf{0} & \mathbf{0} \\ \mathbf{0} & \mathbf{I}_3 \cdot \sigma_{w,\theta}^2 & \mathbf{0} & \mathbf{0} \\ \mathbf{0} & \mathbf{0} & \mathbf{I}_3 \cdot \sigma_{w,v_t}^2 & \mathbf{0} \\ \mathbf{0} & \mathbf{0} & \mathbf{0} & \mathbf{I}_3 \cdot \sigma_{w,v_\theta}^2 \end{bmatrix}. \tag{5.11}$$

Here, $\sigma_{w,t}$, $\sigma_{w,\theta}$, σ_{w,v_t} and σ_{w,v_θ} are the individual standard deviations for the components of the state vector. It should be mentioned that the process noise applied here is a simplified model which should be refined in the future. For this purpose, different models are particularly suitable, which can be derived directly from the system model on the basis of the differential equations (e.g. Bar-Shalom et al. (2001, pp. 270 ff.) and Grewal and Andrews (2015, pp. 145 ff.)). Finally, the VCM $\Sigma_{xx,k}^-$ of the predicted state results from Equation (2.72).

Observation and Measurement Equation

The observation vector l_k is defined by the laser scanner observations assigned to the individual planes of the building model or the grid cells per epoch with respect to their SOCS. This also includes observations of facades that are not stored with absolute information in the building model. The total number of observations thus varies per epoch. This depends on the total number of assigned building planes E and grid cells G, as well as on the contained individual 3D points J_e. The total number of observations within each epoch k is defined as N_{EG}. Furthermore, the pose $\left[t_{\text{GNSS},k}^T, \theta_{\text{IMU},k}^T\right]^T$ of the GNSS-IMU positioning unit can be considered as additional observations[17]. The following therefore applies

$$l_k = \left[\left(C_k^{\text{SOCS}}\right)^T, t_{\text{GNSS},k}^T, \theta_{\text{IMU},k}^T\right]. \tag{5.12}$$

---

[17] At least this is applicable to the scenario within the urban canyon where such information is constantly available

In detail, the assigned point cloud information C_k^{SOCS} for each plane in the observation vector l_k is composed as follows

$$l_k = \left[\left(C_{k,1}^{\text{SOCS}} \right)^T , \ldots , \left(C_{k,E+G}^{\text{SOCS}} \right)^T , t_{\text{GNSS},k}^T , \theta_{\text{IMU},k}^T \right] \tag{5.13a}$$

$$= \left[\left(C_{k,1,1_1}^{\text{SOCS}} \right)^T , \ldots , \left(C_{k,E+G,J_{E+G}}^{\text{SOCS}} \right)^T , t_{\text{GNSS},k}^T , \theta_{\text{IMU},k}^T \right] \tag{5.13b}$$

$$= \left[x_{k,1,1_1}^{\text{SOCS}} , y_{k,1,1_1}^{\text{SOCS}} , z_{k,1,1_1}^{\text{SOCS}} , \ldots , x_{k,E+G,J_{E+G}}^{\text{SOCS}} , y_{k,E+G,J_{E+G}}^{\text{SOCS}} , z_{k,E+G,J_{E+G}}^{\text{SOCS}} , t_{\text{GNSS},k}^T , \theta_{\text{IMU},k}^T \right] . \tag{5.13c}$$

The associated standard deviations of the individual observation groups are summarised in the VCM $\Sigma_{ll,k}$ according to

$$\Sigma_{ll,k} = \begin{bmatrix} \mathbf{I}_{N_{EG}} \cdot \sigma_{l,\text{LS}}^2 & \mathbf{0} & \mathbf{0} \\ \mathbf{0} & \mathbf{I}_3 \cdot \sigma_{l,\text{Position}}^2 & \mathbf{0} \\ \mathbf{0} & \mathbf{0} & \mathbf{I}_3 \cdot \sigma_{l,\text{Orientation}}^2 \end{bmatrix} . \tag{5.14}$$

The measurement equation $h_{\text{I}}(\cdot)$ follows the transformation of the point observations from the SOCS into the WCS according to Equation (5.5) while fulfilling the corresponding plane equation. This is an implicit equation and must be applied to each individual assigned 3D point. The following applies

$$0 = h_{\text{I},e,j_e} \left(l_k , x_k \right) \tag{5.15a}$$

$$= n_e^T \cdot C_{k,e,j_e}^{\text{WCS}} - d_e \tag{5.15b}$$

$$= n_e^T \cdot \left(t_{\text{SOCS-WCS},k} + R_{\text{SOCS-WCS},k} \left(\theta_{\text{SOCS-WCS},k} \right) \cdot C_{k,e,j_e}^{\text{SOCS}} \right) - d_e \tag{5.15c}$$

$$= \begin{bmatrix} n_{x,e} & n_{y,e} & n_{z,e} \end{bmatrix} \cdot \left(\begin{bmatrix} t_{\text{SOCS-WCS},x,k} \\ t_{\text{SOCS-WCS},y,k} \\ t_{\text{SOCS-WCS},z,k} \end{bmatrix} + R_{\text{SOCS-WCS},k} \left(\theta_{\text{SOCS-WCS},k} \right) \cdot \begin{bmatrix} x_{k,e,j_e}^{\text{SOCS}} \\ y_{k,e,j_e}^{\text{SOCS}} \\ z_{k,e,j_e}^{\text{SOCS}} \end{bmatrix} \right) - d_e . \tag{5.15d}$$

Here the plane parameters n_e and d_e are deterministic quantities and can be derived from the building model. It should be noted that in this way, no uncertainty information is taken into account, and the existing generalisation effects can have a negative impact on the estimation result. Alternatively, their consideration could also be done as additional observations with stochastic prior information or as additional parameters. However, both lead to the disadvantage that the dimension of the estimation problem would increase considerably. Furthermore, if they are introduced as parameters, the underlying vertices of the building model should also be included, and their topology should also be considered. If the corresponding plane is not stored with absolute coordinate information in the building model, the respective four plane variables are automatically considered as parameters to be estimated and have to be included in the state vector (cf. Equation 5.8). Further details on this case will follow separately.

Additional observations in terms of $t_{\text{GNSS},k}$ and $\theta_{\text{IMU},k}$ are considered by the explicit measurement equation $h_{\text{II}}(\cdot)$, whereby the following applies

$$0 = l_k + v_k - h_{\text{II}} \left(x_k \right) \tag{5.16a}$$

$$= \begin{bmatrix} t_{\text{SOCS-WCS},k} \\ \theta_{\text{SOCS-WCS},k} \end{bmatrix} - \begin{bmatrix} t_{\text{GNSS},k} \\ \theta_{\text{IMU},k} \end{bmatrix} \tag{5.16b}$$

$$= \begin{bmatrix} t_{\text{SOCS-WCS},x,k} & t_{\text{SOCS-WCS},y,k} & t_{\text{SOCS-WCS},z,k} & \omega_{\text{SOCS-WCS},k} & \varphi_{\text{SOCS-WCS},k} & \kappa_{\text{SOCS-WCS},k} \end{bmatrix}^T$$
$$- \begin{bmatrix} t_{\text{GNSS},x,k} & t_{\text{GNSS},y,k} & t_{\text{GNSS},z,k} & \omega_{\text{IMU},k} & \varphi_{\text{IMU},k} & \kappa_{\text{IMU},k} \end{bmatrix}^T . \tag{5.16c}$$

Non-linear State Constraints

For all the observed facades that are not stored in the building model, geometric constraints regarding their plane parameters have to be considered. For this, the corresponding elements $\boldsymbol{n}_e = [n_{x,e}, n_{y,e}, n_{z,e}]^T$ must be included in the state vector $\boldsymbol{x}_k$ (cf. Equation (5.8)) as well. Consequently, the measurement equation $\boldsymbol{h}_{\mathrm{I}}(\cdot)$ (cf. Equation (5.15)) remains valid for the corresponding laser scanner observations. However, the deterministic plane parameters contained in this equation are replaced by the previously extended elements (plane parameters) of the state vector. This, in turn, requires the availability of corresponding approximate values. For this purpose a plane estimation can be accomplished by the assigned point observations, for example according to Drixler (1993). Thus, initial uncertainty information $\mathbf{I}_3 \cdot \sigma_{\boldsymbol{x,n}}$ and $\sigma_{\boldsymbol{x,d}}$ is also available for the extended VCM $\boldsymbol{\Sigma}_{\boldsymbol{xx},k}$ of the state vector. The process noise in Equation (5.11) is also extended accordingly by $\mathbf{I}_3 \cdot \sigma^2_{\boldsymbol{w,n}}$ and $\sigma^2_{\boldsymbol{w,d}}$. These corresponding noise values must be defined in advance. Furthermore, the system model in Equation (5.10a) is enlarged by

$$\boldsymbol{n}^-_{\text{SOCS-WCS},k} = \boldsymbol{n}^+_{\text{SOCS-WCS},k-1}. \tag{5.17}$$

Afterwards, the geometric constraints can be applied with regard to these states. In this thesis, this is accomplished by two non-linear equations. The function $g_{I,e}(\boldsymbol{x})$ ensures that the normal vector of the plane has the unit length 1 according to

$$g_{I,e}(\boldsymbol{x}) = ||\boldsymbol{n}_e|| \tag{5.18a}$$

$$= \sqrt{n^2_{x,e} + n^2_{y,e} + n^2_{z,e}} \tag{5.18b}$$

$$= b_I = 1. \tag{5.18c}$$

Furthermore, an intersection angle of 90° between the facade plane and the X-Y coordinate plane is defined and applied with function $g_{II,e}(\boldsymbol{x})$. The following applies

$$g_{II,e}(\boldsymbol{x}_k) = cos^{-1}\left(\frac{|\boldsymbol{n}_e \cdot \boldsymbol{n}_{\text{X-Y}}|}{|\boldsymbol{n}_e| \cdot |\boldsymbol{n}_{\text{X-Y}}|}\right) \tag{5.19a}$$

$$= cos^{-1}\left(\frac{|n_{x,e}n_{\text{X-Y}_x} + n_{y,e}n_{\text{X-Y}_y} + n_{z,e}n_{\text{X-Y}_z}|}{\sqrt{n^2_{x,e} + n^2_{y,e} + n^2_{z,e}} \cdot \sqrt{n^2_{\text{X-Y}_x} + n^2_{\text{X-Y}_y} + n^2_{\text{X-Y}_z}}}\right) \tag{5.19b}$$

$$= b_{II} = 90°. \tag{5.19c}$$

While $g_{I,e}(\boldsymbol{x})$ is a hard equality constraint, $g_{II,e}(\boldsymbol{x})$ should be considered as a soft constraint. The latter allows minor deviations from perpendicularity to be taken into account. Standards from the civil engineering industry serve as a basis for these deviations. There, thresholds are defined with regard to angular deviations for vertical surfaces, which depend on the respective length. With a typical building height between 6 m and 15 m, a maximum deviation of 0.15° or 0.06° can be assumed (DIN 18202:2019-07, 2019). The higher the building, the lower the permissible angular deviation. A conversion of these thresholds to a standard deviation σ_d for the application of soft constraints is not directly possible. This problem has already been addressed in section 3.4.2.

Instead of the intersection angle (cf. Equation (5.19)), the perpendicularity of a plane e can also be forced via the normal vector $\boldsymbol{n}_e$ of it, if the following is applied

$$n_{z,e} = 0. \tag{5.20}$$

This can be considered instead of the intersection angle without linearisation. However, if the dependence between two planes is relevant (e.g. if they should be parallel), Equation (5.19) is preferred. Moreover, a minimum deviation from the requested value in terms of the standard deviation σ_d (for the consideration as a soft constraint) cannot be derived directly here either.

5.5 Comparison and Discussion

The novel information-based georeferencing approach presented in section 5.4 is to be validated on the basis of the two kinematic MSS in their respective urban environments from section 5.2. First, an overview of the achieved results is given and subsequently, depending on the scenario, more detailed studies are discussed. Depending on the respective circumstances, different validation procedures are applied. The scenario for georeferencing an autonomous vehicle within a city canyon provides both an independent pose information as well as a highly accurate reference of the positioning solution. However, neither of these are available for the scenario of mapping within an inner courtyard. Furthermore, the following results focus on the estimated translations and, with some limitations, on the orientations. The speed and angular velocity in the three spatial axes, which are also contained in the state vector, have a minor relevance for georeferencing and therefore will not be considered below.

When considering the results achieved, it should be noted that the main focus of this thesis lies on the methodological development of the versatile IEKF in its application-independent definition (cf. chapter 3). The practical application of this methodology is intended to show the general application possibilities, but in particular, it cannot conclusively address all the questions that arise in this context. This refers mainly to the careful selection of appropriate uncertainty information for the VCMs to be considered. A reasonable adaptation must be performed separately for each specific application and cannot be provided here in detail. Instead, the aim is to present both the new possibilities in comparison to existing approaches and the limitations of the own methodological contribution. This advice has already been mentioned in the context of the novel recursive calibration approach in section 4.2, and is even more valid for this information-based georeferencing approach. The required transformations, point assignments and geometric constraints represent a complex relationship and cannot be fully regarded within the scope of this thesis. Therefore, the optimal adjustment of all influencing parameters must be determined in subsequent investigations and is highly dependent on the application.

The estimated state parameters by the versatile IEKF approach (cf. section 5.4) are shown in Figure 5.12 for the 2D position together with the building model used for both scenarios. There is a significant difference in the respective length of both trajectories. In addition, the trajectory in the courtyard is highly non-linear, while in the street canyon it is almost linear. These differences are due to the realisation of a high-accurate reference solution by external tracking in the urban canyon. This considerably limits the possible range and movement of the kinematic MSS. If the reference solution can be omitted, longer and non-linear trajectories are also possible with this specific MSS. Since validation of the trajectory in Figure

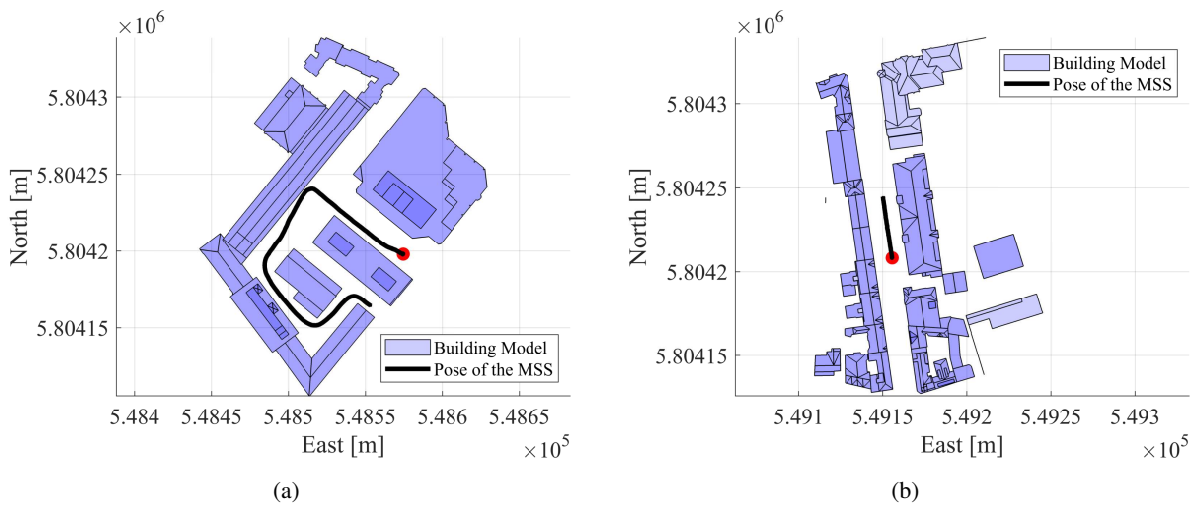|	
(a)	(b)

Figure 5.12: *Representation of the estimated trajectories (black) over all epochs with respect to the building model (blue). For clarity, the DTM is not shown. The results for the scenario in the inner courtyard are shown in (a) and for the scenario in the urban canyon in (b). The starting positions are each highlighted with a red circle.*

5.12(a) is not possible due to a missing reference, section 5.5.1 provides other possibilities for evaluating these results. Moreover, since the basic feasibility for longer and more complex scenarios can already be proven with the first scenario, the general validation of the trajectory is the focus of the second scenario in section 5.5.2.

General key information on both scenarios are summarised in Table 5.1. This indicates, for example, the different measuring frequencies of the two MSS depending on the number of available epochs and the corresponding temporal expansion. In addition, the different number of 3D laser scanner point observations captured and actually used per epoch is also noticeable. This difference is based on the individual laser scanners and their respective arrangement with respect to the environment. While a comparable homogeneous spatial distribution is guaranteed by the spatial subsampling (cf. section 5.4.1), this may also have consequences for the application of the IEKF. The difference in the number of assigned facades can be explained by the different environments and their respective representation in the building model.

In section 5.4.4 the uncertainty information regarding the initial system state $\Sigma_{xx,0}$, the process noise Σ_{ww} and the measurement noise Σ_{ll} have already been introduced in general. Depending on the individual scenarios, the applied standard deviations are summarised in Table 5.2. Therefore, the urban canyon scenario additionally distinguishes between two versions. On the one hand, there is the independent pose information of the manufacturer (referred to as *Riegl Pose*) and on the other hand an artificially worsened version of it (referred to as *Artifical Pose*). This is due to the generation of a more realistic additional pose information regarding the originally described scenario. Further details are given in section 5.5.2. The standard deviations of the initial system state x_0 are identical for the two scenarios. Using a different MSS (e.g. with regard to the type of motion and sensor arrangement) requires a suitable modification of the process noise. Although the *Riegl VQ-250* laser scanners used in the urban canyon scenario are more precise than the *Velodyne Puck VLP-16*, larger standard deviations $\sigma_{l,\mathrm{LS}}$ for the measurement noise have to be considered in the urban canyon scenario. Regardless of this, the laser scanner observations are distinguished whether they are assigned to a plane of the building model or to the DTM. Since the latter object space information generally is less accurate, it is down-weighted at this point by using an increased standard deviation.

Table 5.1: *Summary of the specific circumstances and key information for the two described scenarios. The number of assigned facades does not include multiple assignments over several epochs. The geometrical length of the trajectory is based on the summed Euclidean 3D distances between two successive epochs. The respective number of captured, subsampled and assigned 3D point observations of the laser scanners are rounded values and refer to the median value over all epochs.*

	Inner Courtyard	**Urban Canyon**
Applied Platform	Unmanned Aerial Vehicle	Motor Car
Laser Scanner	1× moderate *Velodyne Puck VLP-16* (3D)	2× precise *Riegl VQ-250* (2D)
Trajectory Length	∼288.3 m within 190.2 s	∼44.1 m within 24.8 s
# Available Epochs	1902	2482
# Captured 3D Points	∼19 000	∼5000
# Subsampled 3D Points	∼5000	∼800
# Assigned 3D Points	∼2000	∼350
# Assigned Facades	98	41
Grid Size for Subsampling	$d_{\mathrm{Subsampling}} = 25\,\mathrm{cm}$	$d_{\mathrm{Subsampling}} = 25\,\mathrm{cm}$
Reference Pose	-	GNSS/IMU (6-DoF) Laser Tracker (3-DoF)

Table 5.2: *Overview of the standard deviations used for the VCM $\Sigma_{xx,0}$ of the initial state vector x_0, the process noise $\Sigma_{ww,k}$ and the measurement noise $\Sigma_{ll,k}$. Shown for each of the two scenarios, whereby two different versions exist for the urban canyon. The process noise is given in dependence of $\Delta\tau = 10\,\text{Hz}$ (inner courtyard) and $\Delta\tau = 100\,\text{Hz}$ (urban canyon) according to Equation* (5.11).

		Inner Courtyard	Urban Canyon Riegl Pose	Urban Canyon Artificial Pose
$\Sigma_{xx,0}$	Position $\sigma_{x,t}$	0.5 m	0.5 m	0.5 m
	Orientation $\sigma_{x,\theta}$	0.2°	0.2°	0.2°
	Speed σ_{x,v_t}	1.0 m/s	1.0 m/s	1.0 m/s
	Angular Velocity σ_{x,v_θ}	1.0 °/s	1.0 °/s	1.0 °/s
$\Sigma_{ww,k}$	Position $\sigma_{w,t}$	0.3 m	0.2 cm	0.2 cm
	Orientation $\sigma_{w,\theta}$	0.3°	2.0 m°	2.0 m°
	Speed σ_{w,v_t}	0.5 m/s	0.5 cm/s	0.5 cm/s
	Angular Velocity σ_{w,v_θ}	0.5 °/s	5.0 m°/s	5.0 m°/s
	Plane $\sigma_{w,n}$, $\sigma_{w,d}$	-	$10^{-5}\,[-]$	$10^{-5}\,[-]$
$\Sigma_{ll,k}$	Assigned to Building Model $\sigma_{l,\text{LS}}$	1.7 cm	20.0 cm	20.0 cm
	Assigned to DTM $\sigma_{l,\text{LS}}$	17.0 cm	30.0 cm	30.0 cm
	Position $\sigma_{l,\text{Position}}$	-	7.5 cm	100.0 cm
	Orientation $\sigma_{l,\text{Orientation}}$	-	0.5°	5.0°

In general, it should be noted that the selected standard deviations are not necessarily realistic and do not correspond to the manufacturer's specifications. This applies in particular to the process and measurement noise, which must be selected in a KF in direct dependence of each other. Several uncertainty measures are specified by the manufacturer without indication of the respective uncertainty parameter, which makes this issue even more difficult. Thus, the standard deviations listed in Table 5.2 are based on assumed values and may have to be replaced by more realistic values in further investigations. While the process noise $\Sigma_{ww,k}$ tends to be too large for the inner courtyard scenario, the measurement noise $\Sigma_{ll,k}$ is actually too small to take into account the existing generalisation effects in the LoD-2 building model. A comprehensive investigation of the sensitivity of the individual standard deviations cannot be carried out since this thesis aims to prove the basic applicability of the own approach. The selected influencing parameters are sufficient for this purpose.

5.5.1 Mapping Within an Inner Courtyard

The results in this application scenario are based exclusively on the use of absolute object space information. Additional information for the continuous georeferencing solution by means of other poses (e.g., by an IMU) is not considered since this information is not available. Furthermore, only facades that can be assigned to the building model are identified. Other facades without absolute information are neglected. The use of geometric constraints according to the principle of the section 5.4.3 can therefore not be used in this application.

The trajectory in Figure 5.12(a) is a visualisation of the route actually taken. However, as no reference solution exists, this cannot be assessed numerically and quantified more accurately. Nevertheless, it can be stated that there are no major outliers, and at the same time, a continuous solution is realised. Besides the trajectory, the resulting point cloud can also be roughly verified for validity. Therefore, Figure 5.13 shows the point clouds obtained for the inner courtyard scenario. Note that in Figure 5.13(a) the original 3D point information is represented. In contrast, Figure 5.13(b) shows the filtered observations l_k^+, which contain only the laser scanner information assigned to the planes of the two object space models. If the estimated
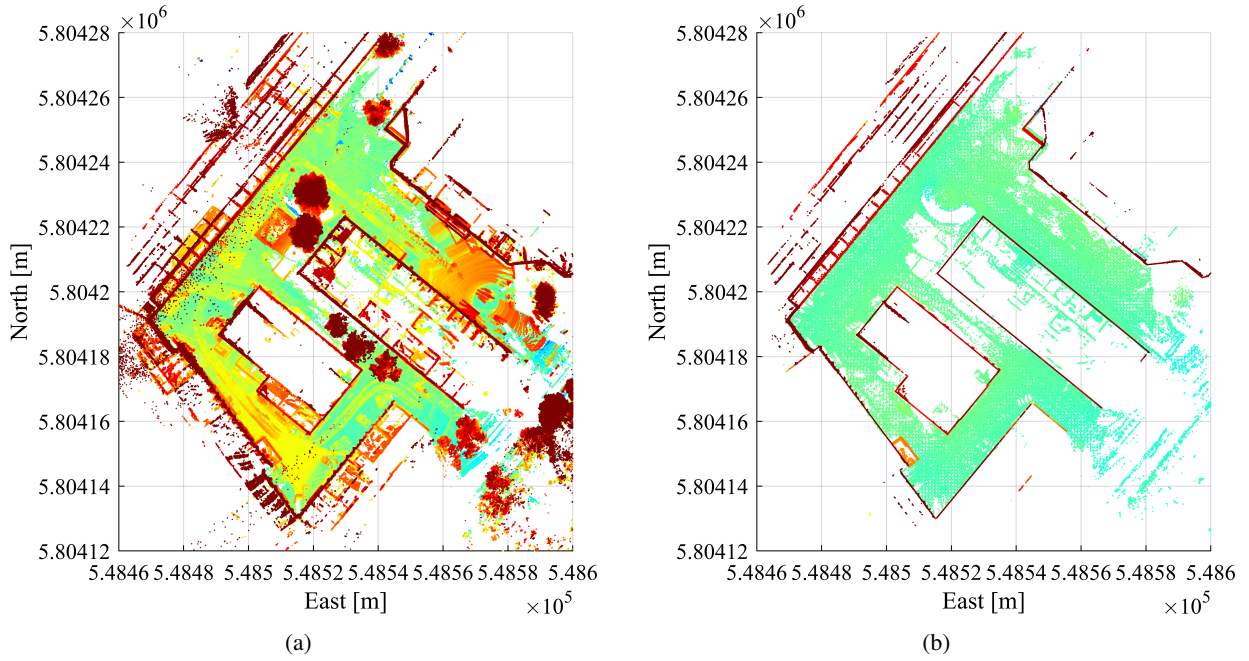
Figure 5.13: *Transformed point clouds for the scenario in the inner courtyard based on the estimated poses. The transformed original point observations are shown in (a) and the transformed filtered observations l_k^+ in (b). The colours represent the respective altitude values. Blue is low and red is high.*

pose is used as transformation parameters within each epoch k, these joint 3D point clouds result. The comparison between these two realisations indicates that many of the available laser scanner observations were assigned to planes and thus contribute to the georeferencing task. This successful assignment applies to both the building facades and the ground. Even some roofs have been observed (cf. upper left area in Figure 5.13(b)). Interfering objects in the point cloud (such as parked cars, containers and stored material) are not assigned to the models and therefore do not affect the georeferencing. The mapping of the reality by the captured and georeferenced point clouds is consistent overall. However, this cannot be verified numerically here either. This would require, for example, the availability of a suitable reference point cloud created by an independent procedure. Statically captured point clouds would be particularly suitable since these usually have a better accuracy compared to this kinematically captured point clouds. With an ICP approach, for example, both statically and kinematically acquired point clouds could be compared and possible contradictions could be identified. However, depending on the respective ICP algorithm, a similar point density is required for this purpose. Furthermore, there are other possibilities to validate the georeferencing results on the basis of the resulting point cloud. For example, the planarity of individual facade segments could be investigated. Thus, it could be verified whether a facade which is planar in reality also has this property in the point cloud.

In the context of this thesis, the evaluation of the pose is performed exclusively on the basis of the estimated standard deviations. Together with the relative changes of the pose (compared to the first epoch $k = 1$) the standard deviations are shown in Figure 5.14. Here, the specified values refer to the superordinate WCS. The position changes are mainly in the east and north component. In comparison, the changes in the altitude component are relatively constant. This is also evident for the three orientation angles. While ω (roll) and φ (pitch) show mostly small changes, κ (yaw) varies most due to the movement pattern (cf. Figure 5.14(a)). The standard deviations of the pose show that they are smaller for those components in which changes are present over time. While for the east and north component they are almost consistently between $1\,\mathrm{mm}$ to $2\,\mathrm{mm}$, for the height components they are averaged at $4\,\mathrm{mm}$. In addition, there is a higher level of noise in the height component, so that maximum values between $1\,\mathrm{cm}$ to $3\,\mathrm{cm}$ occur (cf. Figure 5.14(b)). This can be explained by the less accurate height information in the DTM compared to the 2D location. It is also noticeable that from about the 180-th second onward, the number of assigned planes steadily decreases and the standard deviations for the east and north component slightly increase.
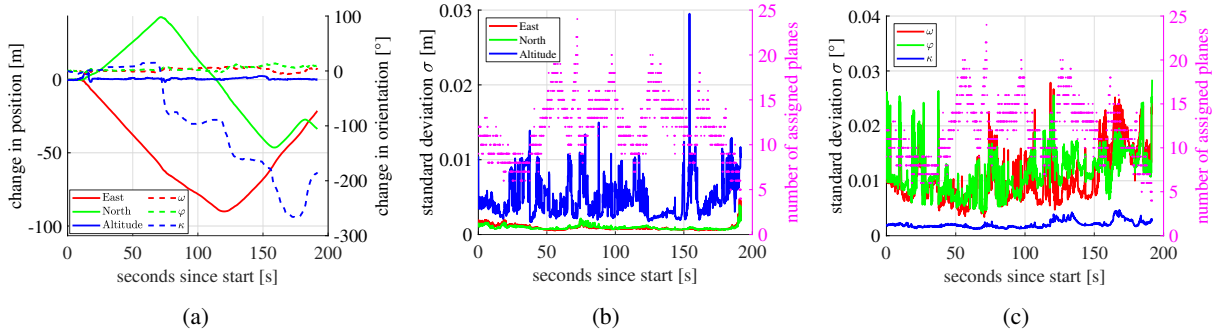
Figure 5.14: *Time variation of the estimated pose and their estimated standard deviations. The change in position and orientation is shown in (a) with regard to two vertical axes, whereas the standard deviations for the position are shown in (b) and for the orientation in (c). As additional information, the respective number of assigned planes per epoch is given for the standard deviations with reference to a second vertical axis (magenta).*

This is due to the fact that at the end of the trajectory, only planes along the direction of movement are available (cf. Figure 5.12(a)).

The standard deviation of the yaw angle κ is between $0.001°$ to $0.004°$. The other two angles have a significantly higher noise and are between $0.004°$ to $0.03°$ (cf. Figure 5.14(c)). For both position and orientation, a correlation between the number of assigned planes and the noisy components of the pose can be identified. If more than 15 planes are assigned, the corresponding standard deviations tend to be smaller. This is due to the higher availability of the planes, which causes a better geometric distribution of object space information. Moreover, it should be mentioned that the investigations in section 3.4 have shown that the estimated standard deviations are too pessimistic. To what extent this also applies to the present application cannot be assessed. However, the precisions given here are obviously not too pessimistic but too optimistic. This applies in particular to the north and east components and the yaw angle. Due to the generalisation effects in the building model and the resulting plane misalignments, such consistently small standard deviations cannot be expected.

Despite the limited evaluation possibilities for this application scenario, it can be stated that the novel information-based georeferencing approach from section 5.4 basically works in urban environments. Furthermore, no additional pose information is required within the estimation. However, the prerequisite for this is the continuous availability of suitable object space information in appropriate quantity and quality. A detailed numerical validation is still pending. The extent to which a lack of absolute object space information can be compensated for by geometric restrictions according to the principle of section 5.4.3 is also not determined. These two issues are examined in the following section in the context of the application scenario within an urban canyon.

5.5.2 Georeferencing of an Autonomous Vehicle Within an Urban Canyon

The considered part of the urban canyon in this scenario provides additional challenges in terms of reliable georeferencing compared to the extensive inner courtyard from section 5.5.1. Due to the structural conditions and the MMS used in this scenario, those building facades are captured in the urban canyon that is almost exclusively parallel to the street. This circumstance is typical for such environments. Only the building on the eastern side of the street offers a few individual facades which are transverse to the direction of driving due to its structural house edges and jutties (cf. Figure 5.12(b)). This challenge is additionally affected by the MSS used. The two profile laser scanners in the present arrangement provide a 3D point information for each epoch that is only partly suitable for georeferencing purposes. However, even if their individual point clouds are sparse as a result, they are precise due to the available sensor quality. In combination with a sufficiently accurate initial pose, there is still potential for improved georeferencing by taking object space information into account. Moreover, there are many observations of the ground.

Since the spatial distribution of the object space information in this scenario is inhomogeneous, it is necessary to consider additional information regarding the pose. Otherwise, a reliable estimation of all 6-DoF of the kinematic MSS in this part of the urban canyon cannot be ensured. A suitable source of information is the pose of the *Applanix POS-LV 510* GNSS-IMU positioning unit. This filtered solution is available in post-processing. However, in reality, a potential mass-market autonomous vehicle will never have such high-precision and high-priced referencing sensors. For this reason, the results of this subsection are determined both on the basis of the actual *Riegl pose* of the positioning unit and on the basis of an *artificial noise-containing pose*. The latter simulates the less precise information that would be available in a potential autonomous vehicle. In the following, the realisation of the artificial solution is briefly described, and then the respective results for both versions are presented. The results are also different depending on whether the geometric constraints (according to section 5.4.3) are neglected or taken into account with regard to specially assigned facades.

Realisation of a More Realistic Pose Information Through Artificial Noise

To generate a more realistic pose ($t_{\text{r-MMS},k}$ and $\theta_{\text{r-MMS},k}$) for this application scenario, specific random Gaussian noise $v_{\text{r-Position}}$ and $v_{\text{r-Orientation}}$ are applied to the original Riegl solution $t_{\text{MMS},k}$ and $\theta_{\text{MMS},k}$ (cf. Equation (5.3)) in each epoch k. The term *more realistic* is to be interpreted as a simulated solution and does not represent a claim to actual real conditions. The following applies

$$t_{\text{r-MMS},k} = t_{\text{MMS},k} + v_{\text{r-Position}}, \qquad v_{\text{r-Position}} \sim N\left(\mathbf{0}, \Sigma_{\text{r-Position}}\right), \tag{5.21a}$$

$$\theta_{\text{r-MMS},k} = \theta_{\text{MMS},k} + v_{\text{r-Orientation}}, \quad v_{\text{r-Orientation}} \sim N\left(\mathbf{0}, \Sigma_{\text{r-Orientation}}\right) \tag{5.21b}$$

where the corresponding standard deviations $\sigma_{\text{r-Position}}$ and $\sigma_{\text{r-Orientation}}$ (diagonal elements of $\Sigma_{\text{r-Position}}$ and $\Sigma_{\text{r-Orientation}}$) are related to the following expected orders of magnitude[18]

$$\sigma_{\text{r-Position}} = 1.0\,\text{m}, \tag{5.22a}$$

$$\sigma_{\text{r-Orientation}} = 5.0°. \tag{5.22b}$$

To additionally reproduce the bad GNSS conditions within an urban canyon, the standard deviation $\sigma_{\text{r-Position}}$ is tripled for $85\,\%$ of all epochs. For this purpose, the value of $\sigma_{\text{r-Position}}$ is set to $3.0\,\text{m}$ for corresponding epochs in Equation (5.21a). Thus, for example, multipath effects are to be simulated. The selection of these epochs is random and the additionally increased noise is limited exclusively to the 3D position. Since this noisy pose is considered as additional information in the IEKF, the standard deviations $\sigma_{l,\text{Position}}$ and $\sigma_{l,\text{Orientation}}$ of measurement noise $\Sigma_{ll,k}$ must be modified (cf. Table 5.2). However, this has no influence on the process noise $\Sigma_{ww,k}$ or the initial system state x_0 and its VCM $\Sigma_{xx,0}$.

For an improved comparability, a Linear Kalman Filter (LKF) according to Simon (2006, pp. 124 ff.) is additionally realised exclusively on the basis of the artificially noise-containing pose data $t_{\text{r-MMS},k}$ and $\theta_{\text{r-MMS},k}$. Thus, the possible benefit of using object space information within the framework of the IEKF can be proven. The LKF describes the identical state vector x_k according to Equation (5.8) and thus also has the same initialisation as well as the corresponding initial VCM $\Sigma_{xx,0}$. The system model according to Equation (5.10a) also remains valid and the unchanged standard deviations for the process noise $\Sigma_{ww,k}$ are assumed. The same applies to the measurement noise, whereby only $\sigma_{l,\text{Position}}$ and $\sigma_{l,\text{Orientation}}$ are considered here. The underlying measurement model basically follows the explicit Equation (5.16) which is linear.

The initially available pose of the Riegl MMS is depicted in Figure 5.15(a) with regard to the relative temporal changes compared to the first epoch $k = 1$. The almost linear movement is evident, which is mainly in the north direction. The change in the eastern direction is due to the orientation of the road with respect to the WCS. All three orientation angles show only minor changes. The deviations of the absolute pose compared to the available high-accurate reference solution of the laser tracker is given in Figure 5.15(b) with regard to the 3D position. In all three coordinate directions, there is a significant

---

[18]These values are still optimistic with regard to the values given in section 5.1, but should represent a first reasonable approximation in the context of this thesis. Furthermore, the occurrence of uncertain GNSS observations may vary depending on the environment and satellite configuration.
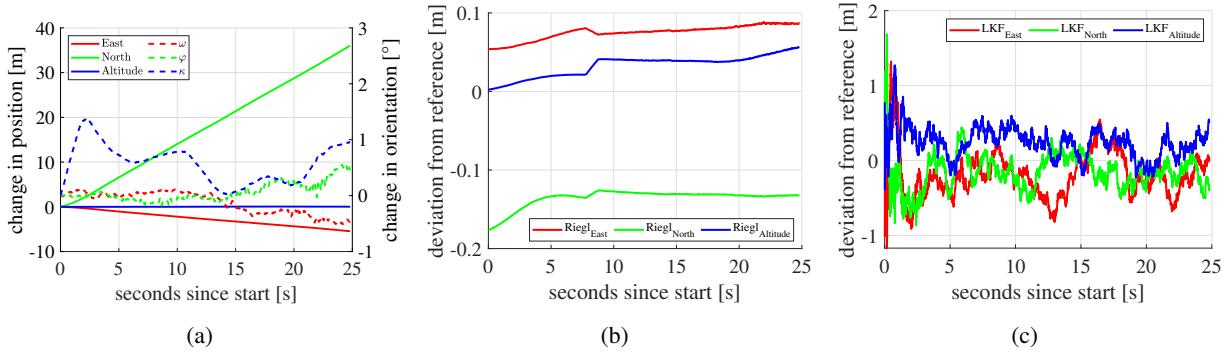
Figure 5.15: *Time variation of different pose and position information. The change in position and orientation of the Riegl pose is shown in (a) with regard to two vertical axes. The deviations from the laser tracker reference are shown in (b) for the Riegl trajectory and in (c) for the artificial trajectory (when using a LKF).*

absolute difference between the position solution filtered by the software of the manufacturer and the one measured by the laser tracker. Except for the northern component[19] (which corresponds approximately to the direction of driving) these deviations tend to increase over time and can reach up to $17\,\text{cm}$. Only for the altitude component, the deviations are virtually zero at the beginning, but then they increase steadily. In addition, between the eighth and ninth second a sudden increase (north and altitude component) or decrease (east component) by $1\,\text{cm}$ to $2\,\text{cm}$ can be identified, which could be due to a bump. The reasons for the global deviations in the higher centimetre range cannot be fully clarified. The alignment of the laser tracker into the WCS, the influence of the urban canyon on the pose of Riegl MMS and all necessary transformations could be mentioned as potential influencing factors at this point. In addition, the stated uncertainty specifications for the laser tracker are only valid under laboratory conditions. Thus, in outdoor areas, worsened uncertainties should be expected. The calibration of the CCR with respect to the PCS also contains uncertainties. Nevertheless, these device-specific influences should be neglected with respect to the other influencing factors mentioned above. Therefore, the position solution of the laser tracker is assumed as a reference in the following. Additionally, Figure 5.15(c) shows the deviation of the additional pose information compared to the laser tracker reference after considering Equation (5.21) with corresponding standard deviations $\sigma_{\text{r-Position}}$ and $\sigma_{\text{r-Orientation}}$. This indicates the applied noise level, resulting in higher deviations compared to the reference.

After applying the georeferencing approach from section 5.4.4, the resulting 2D trajectory[20] is shown in Figure 5.12(b). Visually, it corresponds to the actual driven route. The track is quite linear and comprises almost $44\,\text{m}$ metres in total. The individual georeferenced 3D point information per epoch k is depicted as joint point clouds in Figure 5.16. Identical to the inner courtyard scenario, both the transformed original observations (cf. Figure 5.16(a)) and the transformed filtered observations l_k^+ (cf. Figure 5.16(b)) are presented. The transformation parameters are each based on the application of the versatile IEKF considering the actual Riegl pose as additional information. A visual difference when using the artificially noise-containing pose information would not be noticeable in this representation. Irrelevant objects in the point cloud are neglected by the assignment algorithm and are therefore missing in the representation when the filtered observations are used. There, in turn, the facades on both sides of the street are continuously integrated as observation variables into the georeferencing process. The visible grid structure of the observations assigned to the DTM results from the assignment algorithm and corresponds to the present grid width of $1\,\text{m}$ (cf. section 5.2.3). Additionally, the butterfly alignment of the two 2D laser scanners is visible. The individual scan profiles are rotated by $120°$ to each other. A more detailed investigation of the estimated results with respect to the high-accurate reference solution of the laser tracker is given below.

---

[19]The small deviation in altitude results from the deliberate addition of an altitude offset of $1.75\,\text{m}$. The consideration of this offset is indispensable for the basic applicability of the data set and results from the temporal drift of the Riegl MMS during the whole experiment within the height component.

[20]This trajectory actually refers to the *Riegl* solution, although differences to the *Artificial* solution would not be recognisable due to the scale
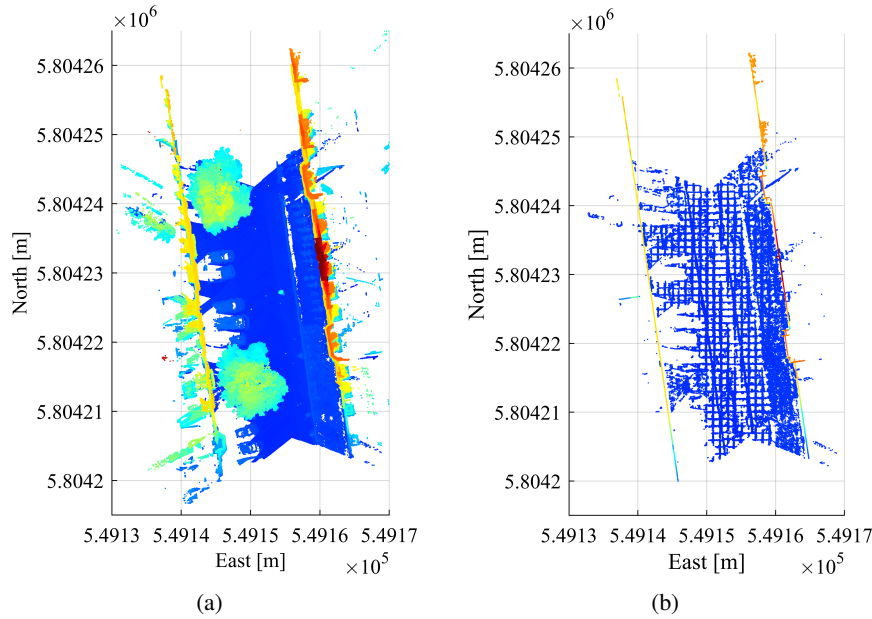
Figure 5.16: *Transformed point clouds for the scenario in the urban canyon based on the estimated poses. The transformed original point observations are shown in (a) and the transformed filtered observations l_k^+ in (b). The colours represent the respective altitude values. Blue is low and red is high.*

Use of Actual Riegl Pose Information

Since the Riegl pose of the MMS used is based on high-quality and precise sensors, an improvement of this solution is not expected neither by the introduction of object space information nor by the application of geometric constraints. At least this applies in terms of improving precision. The situation is different with absolute accuracy, where an improvement is possible at least in the altitude component. After all, this component cannot be determined precisely by means of GNSS observations and also IMU data do not provide long-term support. Thus, due to the environmental conditions in the urban canyon, it is recommended to include additional pose information in the IEKF. In contrast to the inner courtyard scenario in section 5.5.1, the exclusive use of object space information is only possible here to a limited extent. Therefore, it is investigated in advance which results could be achieved by using the original pose in order to create a basis of comparison for a more realistic prior information of the pose. The different results are subsequently assessed by using the RMSE. This uncertainty measure is determined with respect to the laser tracker reference over all epochs $k = 1, \dots, K$.

Figure 5.17 summarises the results for this scenario if, in addition to the additional pose information, only laser scanning points assigned to the two basic models (DTM and building model) are considered. A distinction is made with regard to the use of geometric constraints. In Figure 5.17(a), the corresponding absolute information from the building model exists for each facade to which laser scanner observations are assigned. A constraint regarding the plane parameters should therefore not be applied. The situation is different in Figure 5.17(b). Here one single plane of the building model is selected, which is still used for the assignment of the 3D point observations, but whose absolute coordinate information is subsequently assumed not to exist. Thus, the two geometric constraints according to Equations (5.18) and (5.20) are applied and are intended to improve the georeferencing results. The one selected plane in this application corresponds to a house facade on the western side of the street, is parallel to the street, and it is observed continuously for the first 19 seconds. The results are presented separately for the three coordinate axes.

Within the first epochs, there is always a typical start-up phase of the filter, with a rapid increase of the RMSE values. As expected, Figure 5.17(a) shows that the Riegl pose generally provides a more accurate solution. It should be noted that this is not the case for all coordinate components. In the driving direction (north direction), the IEKF provides a more accurate estimation compared to the Riegl solution. The difference between the two solutions is about 10 cm for the first 8 seconds and then decreases to about
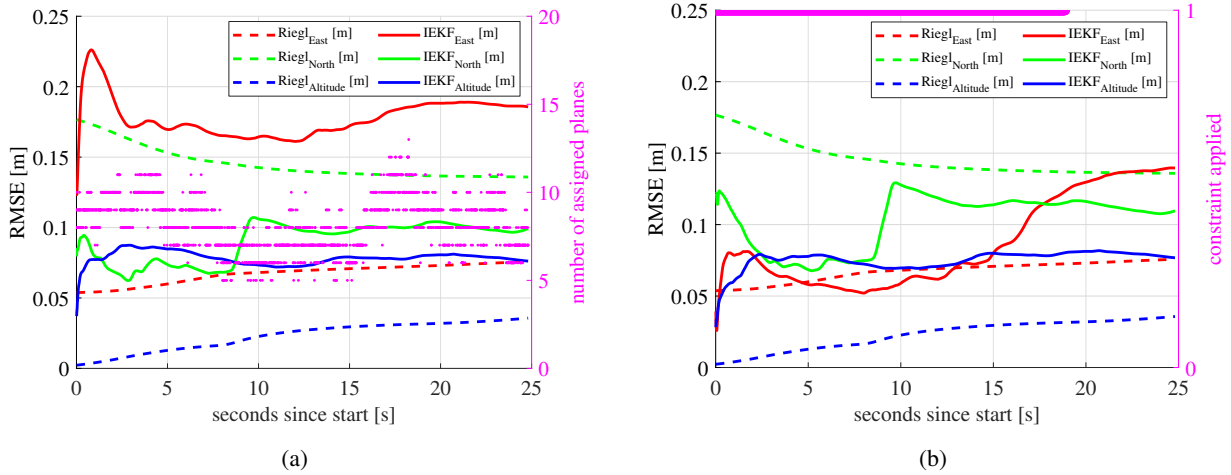
Figure 5.17: *Visualisation of the RMSE over all epochs by considering the original Riegl pose as additional information as well as the assigned object space information. Firstly, absolute coordinate information is available for all assigned facades (a) and secondly, the geometric constraints according to Equations (5.18) and (5.20) are applied to a single facade (b). The results refer to the original Riegl pose (dashed line) and to the filtered position of the IEKF (solid line). In addition, the number of assigned planes per epoch is shown in (a) on a second vertical axis (magenta). In (b), the second vertical axis (magenta) in binary form shows when the geometric constraint is applied.*

$4\,\mathrm{cm}$. Additionally, there is an increase in the IEKF solution of about $3\,\mathrm{cm}$ between the eighth and ninth second, identical to the situation in Figure 5.15(b). The solution of the IEKF transverse to the direction of motion (east direction) is most inaccurate with an RMSE of about $16\,\mathrm{cm}$ to $23\,\mathrm{cm}$. The expected improvement regarding the altitude component is not apparent in the results. A dependence of the RMSE with the number of assigned planes cannot be clearly identified for all components. Although the building model tends to provide limited information in the direction of driving, the Riegl solution can still be improved with respect to the reference by using the IEKF estimates. This improvement can be even higher if geometric constraints regarding the selected facade plane are taken into account (cf. Figure 5.17(b)). While this additional information has no significant effect on the altitude component, an improvement of the RMSE is achieved transverse to the direction of motion (east direction). For this component, the RMSE is less than $10\,\mathrm{cm}$ for the first 17 seconds and has a minimum of $5.2\,\mathrm{cm}$. At the same time, the RMSE in northern direction receives an almost constant offset of about $1\,\mathrm{cm}$ to $2\,\mathrm{cm}$ while the constraint is applied. Taking into account the geometric restriction, an improvement transverse to the direction of motion is thus achieved, which is due to the spatial conditions. Thus, it can be stated that additional geometric information, in combination with the use of absolute position information from the building model, makes a beneficial contribution to high-quality (i.e. accurate) georeferencing. For this case, the combination is especially important, since absolute information is indispensable for the estimation. In the specific situation, this absolute information is already available through the precise Riegl pose. It is, therefore, necessary to investigate to what extent this behaviour also applies to less precise additional pose information, which is by far more realistic for an autonomous vehicle.

Use of Artificial but More Realistic Pose Information

To represent the conditions of an autonomous vehicle more realistically, less accurate pose information must be applied. For this purpose, the realisation of an artificial pose information is already described in advance. Thus a pose is continuously available, but its uncertainty level is more realistic (less accurate and precise) than the pre-filtered Riegl solution. The assessment of the resulting findings is also based on the RMSE and is shown in Figure 5.18. Again, a distinction is made between not taking into account (cf. Figure 5.18(a)) and considering (cf. Figure 5.18(b)) geometric constraints with regard to the mentioned specific facade plane. Additionally, the solution of the LKF is included based on the noisy artificial pose. Neither the building model and the DTM nor the geometric constraints have any influence on the results of this LKF. The typical start-up phase can also be observed for the LKF. In all coordinate components
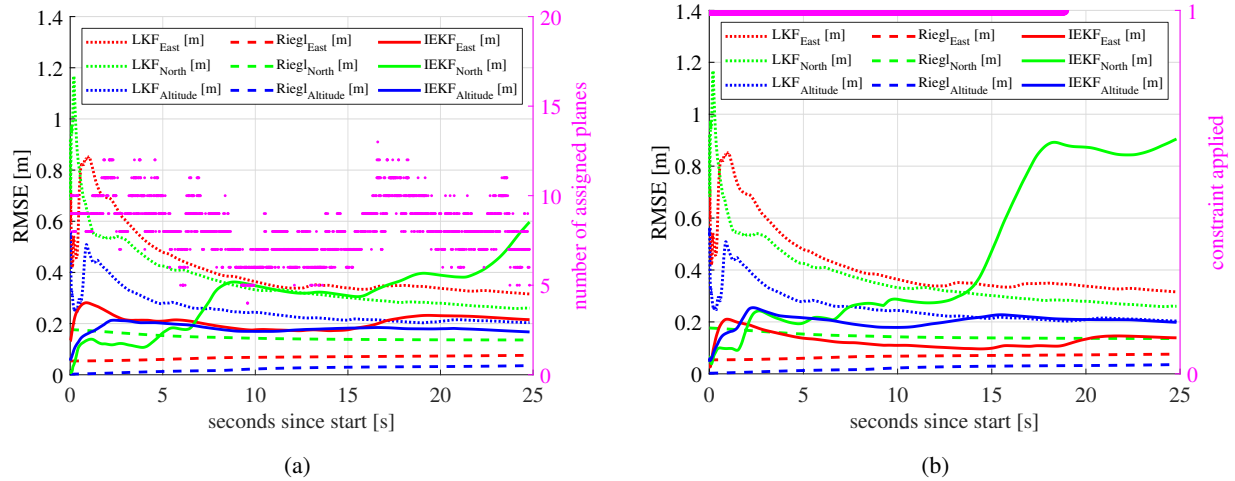
Figure 5.18: *Visualisation of the RMSE over all epochs by considering the artificial pose as additional information as well as the assigned object space information. Firstly, absolute coordinate information is available for all assigned facades (a) and secondly, the geometric constraints according to Equations (5.18) and (5.20) are applied to a single facade (b). The results refer to the original Riegl pose (dashed line), the filtered position of the IEKF (solid line) and to the filtered position of the LKF (dotted line). In addition, the number of assigned planes per epoch is shown in (a) on a second vertical axis (magenta). In (b), the second vertical axis (magenta) in binary form shows when the geometric constraint is applied.*

the RMSE values initially rise up to $0.5\,\text{m}$ (altitude), $0.85\,\text{m}$ (east) and $1.2\,\text{m}$ (north). These values then decrease to about $0.2\,\text{m}$ to $0.35\,\text{m}$. Therefore, the positioning solution is always less accurate than the original Riegl solution. This is expected due to the artificial noise.

For the IEKF, within the first epochs, the typical start-up phase of the filter appears again. Furthermore, the following findings can be derived especially from Figure 5.18(a). Within the first four seconds its position solution in the northern component is more accurate than the Riegl solution, but then the IEKF solution increases and is at the last epoch with $0.6\,\text{m}$ less accurate than the corresponding solution of the LKF. Based on the IEKF, the other two components are less accurate than the Riegl solution, but with about $0.17\,\text{m}$ to $0.23\,\text{m}$ more accurate compared to the LKF. Thus, the largest impact of taking into account object space information is on the component which is transverse to the driving direction (east direction). If geometric constraints are considered for this plane instead of the absolute information of a single facade, the accuracy of the east component is additionally improved by about $8\,\text{cm}$ (cf. Figure 5.18(b)). However, the other two components become slightly (altitude component) or strongly (north component) less accurate. In the direction of driving, the RMSE becomes stable again at about $0.9\,\text{m}$ as soon as the restriction no longer applies. Despite the less accurate position estimates, no fundamental change in the number of planes assigned per epoch can be observed.

Overall, using the realistic pose as additional observations according to Equation (5.16) leads to a less accurate georeferencing than using the original Riegl pose (cf. Figure 5.17). This is generally expected and is caused by the different accuracy of the respective information. The exclusive use of the object space information (as in the inner courtyard scenario in section 5.5.1) leads to highly inaccurate results in the urban canyon and is not further described within this thesis. Therefore, a completely independent georeferencing based on the object space information cannot be guaranteed continuously. For this purpose, facades in the surrounding area must be constantly available and these, in turn, must be captured by the laser scanner and assigned to the digital models. Nevertheless, the consideration of this absolute information results in an improved accuracy compared to the exclusive use of GNSS and IMU observations. This applies to the altitude component as well as the component which is transverse to the driving direction (east) over all epochs. Only in the direction of driving (north), no continuous improvement can be achieved unless appropriately aligned facades are available in the environment. Individual geometric constraints can have an additional positive effect, which in this scenario is advantageous to the component that is transverse to driving direction.

5.5.3 Conclusions

In general, the information-based georeferencing approach for laser scanner-based MSSs is applicable within challenging environments. The approach itself is introduced in section 5.4 and can improve existing positioning solutions with respect to their accuracy. Therefore, the consideration of independent object space information within a versatile IEKF is essential. By including such additional information, the redundancy of the adjustment problem is increased, which in turn has a positive impact on the reliability. This complementary information enables a relation in terms of absolute coordinates with respect to the superordinate WCS and can be additionally supported by suitable geometric constraints. If sufficient appropriate object space information is available, a completely independent pose estimation can also be performed continuously, depending on the MSS used. It should be ensured that appropriately aligned building facades are always present so that accurate positioning with respect to all three spatial axes is possible. However, in straight urban canyons, continuous georeferencing along the road cannot be guaranteed. Moreover, the presented approach cannot be used to provide a completely independent solution in such complex situations. The usage of additional pose information is indispensable if sparse point clouds are available due to the given sensor configuration. Therefore, the use of a 3D laser scanner with a field of view in all spatial directions to ensure spatially distributed point clouds is recommended for such challenging environments.

Accuracies of $10\,\text{cm}$ in position and $0.5°$ in orientation mentioned in section 5.1 cannot be consistently guaranteed for all coordinate directions. Due to the lack of a reference, only corresponding standard deviations of the filtered state parameters can be specified for the inner courtyard scenario. These are usually in the lower millimetre range for the position and less than $0.03°$ for the orientation. For the urban canyon, there exists a reference which, based on the RMSE, indicates an accuracy between $5\,\text{cm}$ to $20\,\text{cm}$ (if the Riegl pose is used) or between $17\,\text{cm}$ to $90\,\text{cm}$ (if the artificial pose is used). Temporarily and for individual components, such targeted orders of magnitude can be achieved. Therefore, the assurance of integrity aspects is only possible to a limited extent. If poor object space information is available, an independent solution is not possible. However, if corresponding complementary observations are available, existing georeferencing approaches can be supplemented or independently validated. Nevertheless, the presented approach is suitable for supporting the long-term trend with regard to the pose. Locally, for a few epochs, the inner uncertainty can already be ensured by observations of a sufficiently accurate IMU. Globally, this information is then supported by the absolute information from the DTM as well as the building model and supplemented by geometric constraints.

The use of geometric constraints proves to be beneficial within urban canyons. However, it is necessary to investigate to what extent geometric properties (e.g. such as perpendicularity or parallelism) should be applied as hard or soft constraints and how corresponding thresholds should be applied. The latter refers to aspects as they were also analysed in section 3.4.2 regarding the selection of the measurement noise $v_{d,k}$ in the application of SCs as well as the selection of the percentage factor δ in the consideration as inequalities. Also, it should be examined to what extent these geometric constraints should be applied even if the corresponding planes are stored with absolute information within the building model. In principle, an estimation of all the plane parameters and vertices of the building model would also be possible. However, this procedure requires the inclusion of the topology between all available vertices. Furthermore, this would significantly increase the dimensions of the corresponding matrices within the filtering algorithm. This, in turn, affects the run time. In addition, the building model could also be checked for consistency and updated or extended as necessary. For this purpose, other reliable pose information should be available.

It is also advisable to investigate the selection of the process and measurement noise, according to Table 5.2. The investigations in the context of the application example in section 3.4 already demonstrates the complex relationship between these noise parameters (cf. Appendix A.2). This is further intensified by the complexity of the information-based georeferencing task in this chapter. There are a multitude of transformations (e.g. SOCS to WCS, registration of the laser tracker in the WCS) and the resulting uncertainties that have to be considered. Thus, a different weighting offers further potential for improvement and might be adjusted depending on the environment and MSS. This is a general challenge when filtering approaches are used.

The application of the information-based georeferencing approach should be extended to further experiments regarding various environments and different MSSs. Longer trajectories and also junctions within urban canyons would be of particular interest. Thus, a more comprehensive assessment of the approach with regard to its applicability and the assurance of integrity aspects can be achieved. If validation of the results based on a point cloud comparison against a more accurate reference can be performed, much longer trajectories can be realised. In this case, the limitation by observing with the laser tracker is not mandatory. Nevertheless, this highly accurate sensor offers excellent possibilities for a highly accurate comparison of the estimated pose parameters. However, in the context of the investigations presented, only for the position and not for the orientation.

Furthermore, it is not investigated to what extent the selection of $d_{\mathrm{Subsampling}}$ for the spatial subsampling affects the estimation results. However, the most time-consuming part of the described approach requires the assignment of the laser scanner observations to the building model. This is not the focus of this thesis, and thus still offers potential for a more efficient implementation. This, in turn, could lead to the consideration of more observations in total. In general, this is not strictly necessary, but it could also allow to consider facade structures that would otherwise be lost due to too extensive subsampling. Irrespective of this, the applied spatial subsampling generates observations by averaging, which in reality have never been measured. However, in the context of this thesis, it is assumed that the generation of these artificial observations is permissible because of the already generalised and approximated building model and the related uncertainties. Positive aspects are the homogeneous spatial distribution and better comparability. Nevertheless, more suitable possibilities for subsampling should be investigated in the future.

The extent to different accuracy levels of the laser scanner measurements and their effects on the final estimations was not in the scope of this thesis. Therefore both MSSs should be used in the same environment. Furthermore, a more comparable spatial distribution of the individual point clouds would be advantageous. In addition to a laser scanner, additional observations in the form of features from a suitable camera system could be used. Thus, corresponding object space information can also be assigned and used for independent georeferencing. The possibility for a future real-time application is basically given by the IEKF. However, as already mentioned, the assignment to the building model should be made more efficient for this purpose. Furthermore, it is necessary to investigate how many and which point observations are strictly necessary.

6

Conclusions

6.1 Summary

In this thesis, the development of a versatile recursive state-space filter has been presented. This approach is characterised by its flexibility in using both explicit and implicit mathematical relationships between the available observations and the states to be estimated. The specific realisation takes place within an IEKF. To benefit additionally from the consideration of any suitable linear and non-linear state constraints, their compatibility with implicit functions within the IEKF is investigated for the first time in this thesis. Thus, various existing methods for using hard or soft constraints on explicit relations are adapted accordingly. As this is only possible for individual methods under special consideration of arising contradictions, a completely new approach is presented. This COF approach considers hard constraints directly during the solution of the normal equation system as part of the update step and is therefore efficient. For this purpose, the objective function is extended by corresponding constraints and then minimised. However, the approach is limited to equality constraints.

The versatile IEKF can also be modified to provide recursive parameter estimation in the Gauss-Helmert model for the first time. Such recursive methods have so far been limited to Gauss-Markov models in which only explicit measurement equations can be considered. By omitting the system model within the prediction step of the IEKF and thus, the parameters depend only on the available observations, this can now also be realised for implicit relationships. This innovation enables new possibilities for adjustment tasks, which were previously limited to comprehensive batch adjustments. Even if the parameters to be estimated are constant over time and all observations are available at once, the recursive estimation shows a gain in the required computing time for large datasets. By artificial partitioning of the observation data into individual epochs and sequential estimation of the parameters, an otherwise necessary reduction of information can be avoided. A consideration of arbitrary constraints is also flexibly possible for explicit as well as implicit relationships by the methods mentioned above.

The general applicability of the newly introduced methodology is shown in a comprehensive MC simulation for a simple geometric example. The application of batch and recursive methods for implicit relationships as well as the consideration of constraints by different approaches are investigated. Further analysis also indicates that the appropriate selection of process and measurement noise has an impact on the estimation results. The advantage of recursive methods is clearly evident in the required run times, whereas the accuracy and precision of the estimated parameters are still better in batch processing. However, further investigations show that the standard deviations estimated in the IEKF are too pessimistic. The test for consistency of the recursively estimated parameters indicates anomalies. Nevertheless, it should be noted that this statistical test is strictly speaking neither intended for implicit and non-linear equations nor for the combination with constraints. The recursive methods also have advantages when considering prior information in the context of constraints that have a certain degree of uncertainty. Then especially soft or inequality constraints are recommended, which estimate accurate parameters, even if the prior information is slightly wrong. In this case, a careful selection of the corresponding measurement noise $v_{d,k}$ (in case of soft constraints) or threshold values d_{lower} and d_{upper} (in case of inequality constraints) is necessary. The selection of these parameters always depends on the respective application. In principle,

inequality constraints can also be used for batch processing. However, their use increases the complexity of the adjustment, as this leads to a quadratic programming problem.

The necessity of the new methodological contributions from this thesis can be emphasised with reference to current research topics. Today, many applications require reliable and accurate point clouds of the environment to model the reality in three dimensions. This can be the case, for example, when realising accurate and precise 3D city models or when using spatial information within constantly updated BIM processes. Kinematic MSSs are used to acquire and provide such spatial data. However, to ensure that the resulting point clouds are of appropriate quality, the accurate, precise and complete georeferencing of such systems must be continuously guaranteed. This is possible in a variety of environments with state of the art approaches. Urban areas with many tall buildings, however, cause problems. Within urban canyons, the GNSS observations that are usually used for georeferencing are inaccurate and not reliable. This issue is not limited to applications for mapping the environment. The field of autonomous driving is also affected by this. Such vehicles are also kinematic MSSs, which act autonomously in the direct surroundings of humans. Their reliable, accurate and precise pose estimation must also be guaranteed at all times, regardless of the environment. Due to the security risks involved, integrity aspects are essential here. With the current developments in this area, the demand for reliable methods will continue to increase in the future. Therefore, in the context of this thesis, the methodology is given, with whose assistance an independent and complementary georeferencing can be achieved in challenging environments. Beyond that, the approach is completely flexible in its use and can also be transferred for other application purposes. This is proven by different examples. The most important investigations and findings are summarised below.

The applicability of the versatile IEKF is demonstrated for two practical application examples which are directly related to kinematic MSSs. There are several tasks in this field of application where efficient parameter estimation is crucial. With the use of current MSSs there is an increasing amount of data to be processed when using the latest sensors. *Big data* is a common term and is directly related to recurring tasks of data acquisition, system calibration and georeferencing. In this context, the potential of the recursive GHM in the calibration of a laser scanner-based MSS is investigated. For this purpose, a state of the art approach is adapted to the extent that the calibration parameters are not determined in a batch procedure but recursively over several epochs. The underlying mathematical model, therefore, remains unchanged, and only the observations and parameters are divided into individual epochs. Non-linear constraints are also included. Since the batch method cannot be solved when using all available 3D point information due to numerical instabilities, subsampling must be performed in advance. Again, the required run times of the recursive methods always show strong advantages. Independent of this, a comprehensive MC simulation indicates that a use of all observations is not necessary, but that even a subset can be sufficient. To what extent the batch or recursive methods are more accurate cannot be evaluated due to the lack of a reliable reference. This also applies to the impact of the constraints. Therefore, cross-validation is performed instead. The results show that with the recursive GHM, when using the COF method for constraints, the most reliable calibration parameters can be obtained.

As a second practical application, the versatile IEKF is applied for georeferencing two different laser scanner-based MSSs. This results in the novel information-based georeferencing approach based on independent and complementary object space information. The approach is specifically developed for challenging urban environments where existing georeferencing methods are inaccurate or unreliable. For this reason, there is a high demand for solutions that include integrity aspects. Especially with regard to autonomous driving, this will become increasingly important in the future. Nevertheless, also other application areas such as efficient mapping and three-dimensional modelling of urban areas can benefit from it. The application, therefore, takes place both within an inner courtyard (which has to be mapped) and within an urban canyon (in which a potential autonomous vehicle is to be georeferenced). In both cases, absolute coordinate information from a digital building model as well as from a DTM is available. Within the information-based approach, the captured laser scanner observations are assigned to these models, and thus a global reference to the environment is established. If individual facades are captured by the laser scanner but are not stored in the building model, geometric constraints can be applied instead. Specifically, this involves assumed perpendicularities, which in turn are based on defined standards from the civil engineering industry. The resulting findings show that the method can be used to support the

long-term trend in georeferencing. This is partially validated with a high-accurate reference solution of a laser tracker. In principle, the availability of additional pose information is recommended. This can be based on IMU observations, for example, and thus locally improve the inner accuracy. A completely independent georeferencing can only be achieved with the new approach if a sufficient number of appropriately aligned building facades are available in the environment. The spatial field of view of the laser scanner used also has a significant influence. Here, especially in narrow urban canyons, the use of a 3D laser scanner is recommended, even if this sensor has a moderate level of uncertainty. In general, the approach thus offers helpful possibilities to ensure the georeferencing of a corresponding MSS, even in such challenging environments while maintaining integrity aspects. This advantage applies to the extent that the solution by means of object space information is basically independent of other solutions and thus represents complementary information.

In conclusion, the versatile recursive state-space filter is a flexible framework for a variety of problems in geodesy as well as for general adjustment tasks in various fields of application. The new approach allows for the first time to consider both explicit and implicit mathematical measurement equations in a uniform framework. This flexibility is further supplemented by the possibility of applying arbitrary suitable state constraints. The approach also enables recursive parameter estimation in the GHM.

6.2 Outlook

The versatile recursive state-space filter allows the flexible application of explicit and implicit measurement equations and also provides for the first time validated methods for the consideration of arbitrary state constraints. Nevertheless, there are still several open questions that offer the potential for further investigation. This applies both to the methodology itself and to the specific application in the context of kinematic MSSs. A selection of relevant topics is therefore indicated below.

For the application of the IEKF it is currently assumed that the available observation data are free of outliers. However, this does not correspond to reality, especially with regard to the applications shown in relation to laser scanner point clouds. In general, the existence of individual distorted measurements and wrongly assigned observations cannot be excluded. Therefore, this requires a robustification of the filter approach. In this context, it is necessary to investigate to what extent robust estimators are consistent with the implicit measurement equations and the simultaneous consideration of state constraints.

The risk of numerical instabilities increases when additional pseudo observations are taken into account. This is especially the case if constraints are integrated into the filter approach by means of PMs or as SCs. Therefore, regularisation methods should be evaluated to counteract ill-conditioned matrices.

Potential advancements of the IEKF are also proposed with regard to two aspects:

- The transfer of the implicit filter approach with regard to a PF would eliminate the necessity of linearisation of the non-linear measurement equations. Especially for highly non-linear relationships, this is of relevance. This requires the use of PDFs and enables the consideration of constraints by means of bounded densities as well.

- For a more efficient solution, the adaptation of a Dual State Kalman Filter (DSKF) is recommended. In such an approach, the quantities to be estimated are subdivided into system states (e.g. the pose of a vehicle) and model parameters (e.g. plane parameters of a building facade) and determined iteratively. Due to the division, the corresponding dimensions are reduced, which has a positive effect on the necessary computing time. Further details can be found in Wenzel et al. (2006), for example.

As part of further applications, it should generally be investigated to what extent is it necessary to consider all available observations in the case of mass data. In this context, the question also arises how a reasonable selection of redundant information can be realised so that only observations are considered that have the strongest possible influence on an accurate, precise and reliable estimation. The availability of an appropriate reference is essential with regard to validation aspects. However, this should not lead to practical limitations in application.

A

<div style="text-align: right">Appendix</div>

A.1 Pseudocode of the Versatile Recursive State-space Filter

Taking into account the research of Dang (2007), the methodological extensions from section 3.1 result in the versatile recursive state-space filter. With this approach, arbitrary non-linear measurement equations can be applied, which can be formulated explicitly or implicitly. If the mathematical relationship is explicit, it can be transformed considering Equation (3.4). In general, Algorithm 1 applies.

Algorithm 1: Versatile recursive state-space filter based on an IEKF. Arbitrary linear and non-linear state constraints can be applied in dependence of the respective method (cf. section 3.2).

---

1   System model $\boldsymbol{x}_k = \boldsymbol{f}\left(\boldsymbol{x}_{k-1}, \boldsymbol{u}_{k-1}, \boldsymbol{w}_{k-1}\right), \quad \boldsymbol{w}_{k-1} \sim N\left(\boldsymbol{0}, \boldsymbol{\Sigma}_{ww,k}\right)$

2   Observation model $\boldsymbol{h}\left(\boldsymbol{l}_k + \boldsymbol{v}_k, \boldsymbol{x}_k\right) = \boldsymbol{0}, \quad \boldsymbol{v}_k \sim N\left(\boldsymbol{0}, \boldsymbol{\Sigma}_{ll,k}\right)$

3   Initial state vector and its VCM: $\hat{\boldsymbol{x}}_0^+ = \boldsymbol{x}_0, \quad \boldsymbol{\Sigma}_{\hat{x}\hat{x},0}^+ = \boldsymbol{\Sigma}_{xx,0}, \quad k = 1$

4   **while** $k < \mathrm{K}$ **do**

5   *Prediction Step*

6      $\boldsymbol{\Phi}_{k-1} = \nabla_x \boldsymbol{f}\left(\boldsymbol{x}\right)\Big|_{\hat{\boldsymbol{x}}_{k-1}^+, \boldsymbol{u}_{k-1}, \boldsymbol{w}_{k-1}}$

7      $\boldsymbol{G}_{k-1} = \nabla_w \boldsymbol{f}\left(\boldsymbol{x}\right)\Big|_{\hat{\boldsymbol{x}}_{k-1}^+, \boldsymbol{u}_{k-1}, \boldsymbol{w}_{k-1}}$

8      $\hat{\boldsymbol{x}}_k^- = \boldsymbol{f}\left(\hat{\boldsymbol{x}}_{k-1}^+, \boldsymbol{u}_{k-1}, \boldsymbol{0}\right)$

9      $\boldsymbol{\Sigma}_{\hat{x}\hat{x},k}^- = \boldsymbol{\Phi}_{k-1} \cdot \boldsymbol{\Sigma}_{\hat{x}\hat{x},k-1}^+ \cdot \boldsymbol{\Phi}_{k-1}^T + \boldsymbol{G}_{k-1} \cdot \boldsymbol{\Sigma}_{ww,k-1} \cdot \boldsymbol{G}_{k-1}^T$

10   *Update Step*

11      $\check{\boldsymbol{l}}_{k,m=0} = \boldsymbol{l}_k, \quad \check{\boldsymbol{x}}_{k,m=0} = \hat{\boldsymbol{x}}_k^-$

12   **for** $m = 0 \dots M-1$ **do**

13          $\mathbf{A}_{k,m} = -\nabla_x \boldsymbol{h}\left(\check{\boldsymbol{l}}_{k,m}, \check{\boldsymbol{x}}_{k,m}\right)\Big|_{\check{\boldsymbol{x}}_{k,m}, \check{\boldsymbol{l}}_{k,m}, \boldsymbol{v}_{k,m}}, \quad \mathbf{B}_{k,m} = \nabla_l \boldsymbol{h}\left(\check{\boldsymbol{l}}_{k,m}, \check{\boldsymbol{x}}_{k,m}\right)\Big|_{\check{\boldsymbol{x}}_{k,m}, \check{\boldsymbol{l}}_{k,m}, \boldsymbol{v}_{k,m}}$

14          $\boldsymbol{K}_{k,m} = \boldsymbol{\Sigma}_{\hat{x}\hat{x},k}^- \cdot \boldsymbol{A}_{k,m}^T \cdot \left(\left(\boldsymbol{A}_{k,m} \cdot \boldsymbol{\Sigma}_{\hat{x}\hat{x},k}^- \cdot \boldsymbol{A}_{k,m}^T\right) + \left(\boldsymbol{B}_{k,m} \cdot \boldsymbol{\Sigma}_{ll,k} \cdot \boldsymbol{B}_{k,m}^T\right)\right)^{-1}$

15          $\check{\boldsymbol{x}}_{k,m+1} = \hat{\boldsymbol{x}}_k^- - \boldsymbol{K}_{k,m} \cdot \left(\boldsymbol{h}\left(\check{\boldsymbol{l}}_{k,m}, \check{\boldsymbol{x}}_{k,m}\right) + \boldsymbol{B}_{k,m} \cdot \left(\boldsymbol{l}_k - \check{\boldsymbol{l}}_{k,m}\right) + \boldsymbol{A}_{k,m} \cdot \left(\hat{\boldsymbol{x}}_k^- - \check{\boldsymbol{x}}_{k,m}\right)\right)$

16          $\boldsymbol{F}_{k,m} = \boldsymbol{\Sigma}_{ll,k} \cdot \boldsymbol{B}_{k,m}^T \cdot \left(\left(\boldsymbol{A}_{k,m} \cdot \boldsymbol{\Sigma}_{\hat{x}\hat{x},k}^- \cdot \boldsymbol{A}_{k,m}^T\right) + \left(\boldsymbol{B}_{k,m} \cdot \boldsymbol{\Sigma}_{ll,k} \cdot \boldsymbol{B}_{k,m}^T\right)\right)^{-1}$

17          $\check{\boldsymbol{l}}_{k,m+1} = \boldsymbol{l}_k - \boldsymbol{F}_{k,m} \cdot \left(\boldsymbol{h}\left(\check{\boldsymbol{l}}_{k,m}, \check{\boldsymbol{x}}_{k,m}\right) + \boldsymbol{B}_{k,m} \cdot \left(\boldsymbol{l}_k - \check{\boldsymbol{l}}_{k,m}\right) + \boldsymbol{A}_{k,m} \cdot \left(\hat{\boldsymbol{x}}_k^- - \check{\boldsymbol{x}}_{k,m}\right)\right)$

18      $\hat{\boldsymbol{x}}_k^+ = \check{\boldsymbol{x}}_{k,M}$

19      $\hat{\boldsymbol{l}}_k^+ = \check{\boldsymbol{l}}_{k,M}$

20      $\boldsymbol{\Sigma}_{\hat{x}\hat{x},k}^+ = \left(\mathbf{I} - \boldsymbol{K}_{k,M-1} \cdot \boldsymbol{A}_{k,M-1}\right) \cdot \boldsymbol{\Sigma}_{\hat{x}\hat{x},k}^- \cdot \left(\mathbf{I} - \boldsymbol{K}_{k,M-1} \cdot \boldsymbol{A}_{k,M-1}\right)^T + \boldsymbol{K}_{k,M-1} \cdot \left(\boldsymbol{B}_{k,M-1} \cdot \boldsymbol{\Sigma}_{ll,k} \cdot \boldsymbol{B}_{k,M-1}^T\right) \cdot \boldsymbol{K}_{k,M-1}^T$

21      $\boldsymbol{H}_k = \boldsymbol{F}_{k,M-1} \cdot \boldsymbol{A}_{k,M-1}$

22      $\boldsymbol{\Sigma}_{\hat{l}\hat{l},k}^+ = \boldsymbol{\Sigma}_{ll,k} + \boldsymbol{F}_{k,M-1} \cdot \boldsymbol{B}_{k,M-1} \cdot \boldsymbol{\Sigma}_{ll,k} \cdot \boldsymbol{B}_{k,M-1}^T \cdot \boldsymbol{F}_{k,M-1}^T - \boldsymbol{H}_k \cdot \boldsymbol{\Sigma}_{\hat{x}\hat{x},k}^- \cdot \boldsymbol{H}_k^T$

A.2 Analysis for the Selection of a Suitable Measurement and Process Noise

The investigations in section 3.4, when using a comprehensive MC simulation, are based on the use of a constant process noise $\sigma_w = 1 \cdot 10^{-3}$ and a specific factor $\eta = 1.5\,\%$ for the measurement noise. The parameter η represents the percentage of influence based on the length of the respective semi-axis. The measurement noise is then obtained according to Equation (3.32). Besides the initial state vector and its VCM, these noise values are the main factors influencing recursive state-space filtering. For the investigation of their influence on the estimates, a variety of different combinations of σ_w and η were established and applied on two independent filter approaches. The recursive GHM without consideration of constraints (cf. Figure A.1) and the recursive C-GHM when using the COF method (cf. Figure A.2) were used as representative approaches. The assessment is based on the mean RMSE for the semi-major axis a and the semi-minor axis b over 500 individual replications.

Regardless of the approach and the semi-axis, it is evident that η has a minor influence, as long as $\eta > 0.02\,\%$ applies. Much more relevant is the magnitude of the process noise σ_w. If this is less than approximately 10^{-4}, there is also almost no influence. The contour lines show a negative exponential curve throughout. However, a variation of the resulting RMSE values is concentrated in a range between approximately 10^{-4} to 10^{-1} regarding process noise σ_w. The RMSE increases with larger process noise. The numerical values differ depending on the semi-axis and method. If no constraints are applied (cf. Figure A.1), the RMSE is between approximately 0.006 to 0.025 units (semi-major axis a) and approximately 0.003 to 0.016 units (semi-minor axis b). The consideration of constraints by means of the COF method (cf. Figure A.2) leads to a variation of the RMSE between approximately 0.002 to 0.008 units (semi-major axis a) between approximately 0.003 to 0.013 units (semi-minor axis b) as a consequence of the selection of the parameters. The overall influence is therefore lower. For comparison, the incorporation of biased prior information in section 3.4.2 resulted in a maximum RMSE of approximately 0.015 across all approaches. Finally, the selection of $\sigma_w = 1 \cdot 10^{-3}$ and $\eta = 1.5\,\%$ represents a trade-off. In the context of these investigations, this corresponds in each case to the lowest classification of the RMSE, and the values chosen are not overoptimistic. Nevertheless, the values are chosen to be as realistic as possible and still have some influence. Furthermore, not taking into account the process noise can lead to numerical instabilities.
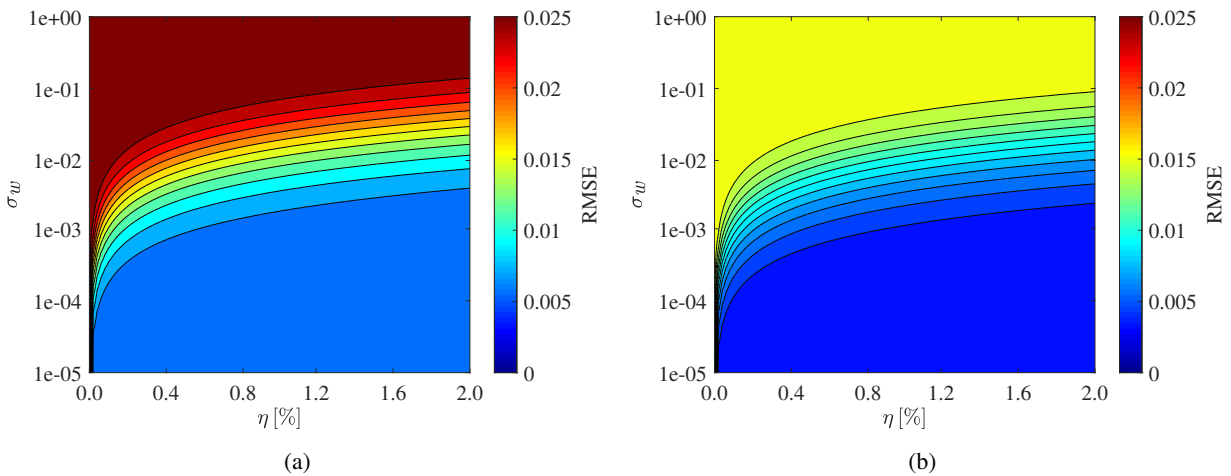

(a)   (b)

Figure A.1: *Mean RMSE for various factors η and σ_w when using recursive GHM without constraints by means of 500 replications. The results for the semi-major axis a are given in (a) and for the semi-minor axis b in (b). Automatically generated contour lines are specified based on a constant number. To ensure comparability, the specified interval is limited. The logarithmic scaling of the vertical axis should be taken into account.*

Figure A.2: *Mean RMSE for various factors η and σ_w when using recursive C-GHM (COF) by means of 500 replications. The results for the semi-major axis a are given in (a) and for the semi-minor axis b in (b). Automatically generated contour lines are specified based on a constant number. To ensure comparability, the specified interval is limited. The logarithmic scaling of the vertical axis should be taken into account.*
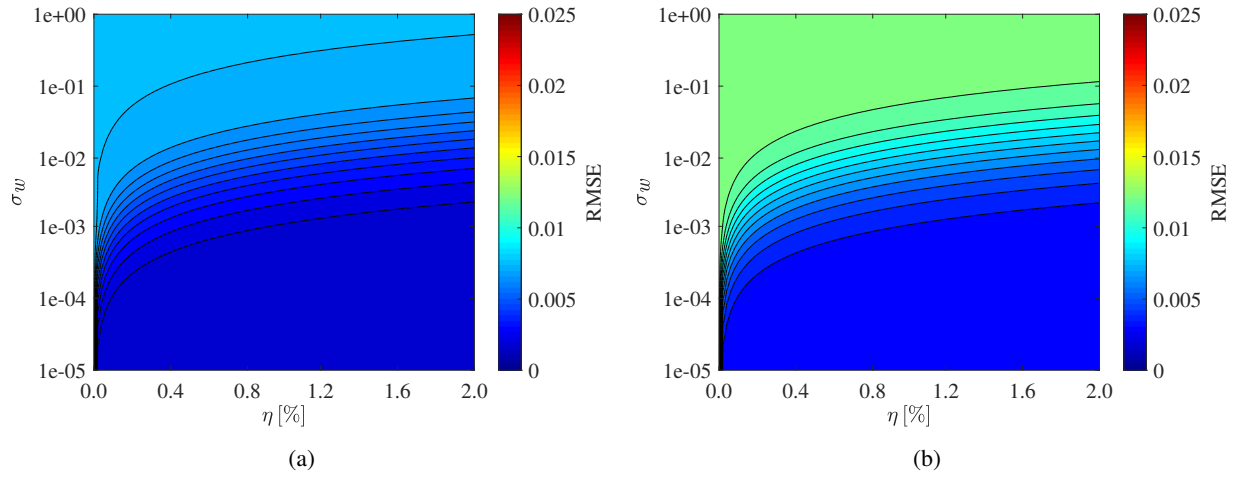
Bibliography

AdV. Die amtlichen 3D-Gebäudemodelle in den Ausprägungen LOD1 und LOD2. URL: `http://www.adv-online.de/AdV-Produkte/Weitere-Produkte/3D-Gebaeudemodelle-LoD/`, Accessed: 2020-02-17.

Alkhatib, H., Omidalizarandi, M., and Kargoll, B. (2019). A Bootstrap Approach to Testing for Time-Variability of AR Process Coefficients in Regression Time Series with t-Distributed White Noise Components. In: *International Association of Geodesy Symposia*. Springer, Berlin, Heidelberg. DOI: `https://doi.org/10.1007/1345_2019_78`.

Bar-Shalom, Y., Li, X.-R., and Kirubarajan, T. (2001). *Estimation with Applications to Tracking and Navigation: Theory, Algorithms and Software*. Wiley, New York, NY. DOI: `https://doi.org/10.1002/0471221279`.

Besl, P. J. and McKay, H. D. (1992). A Method for Registration of 3-D Shapes. In: *IEEE Transactions on Pattern Analysis and Machine Intelligence*, 14(2), pp. 239–256. DOI: `https://doi.org/10.1109/34.121791`.

Biljecki, F., Ledoux, H., and Stoter, J. (2016). An Improved LOD Specification for 3D Building Models. In: *Computers, Environment and Urban Systems*, 59, pp.25–37. DOI: `https://doi.org/10.1016/j.compenvurbsys.2016.04.005`.

Biljecki, F., Stoter, J., Ledoux, H., Zlatanova, S., and Çöltekin, A. (2015). Applications of 3D City Models: State of the Art Review. In: *ISPRS International Journal of Geo-Information*, 4(4), pp. 2842–2889. DOI: `https://doi.org/10.3390/ijgi4042842`.

Björck, A. (1996). *Numerical Methods for Least Squares Problems*. Society for Industrial and Applied Mathematics (SIAM), Philadelphia, Pa. DOI: `https://doi.org/10.1137/1.9781611971484`.

Bogue, R. (2017). Domestic Robots: Has Their Time Finally Come? In: *Industrial Robot: An International Journal*, 44(2), pp. 129–136. DOI: `https://doi.org/10.1108/IR-01-2017-0018`.

Borrmann, A., König, M., Koch, C., and Beetz, J. (2018). Building Information Modeling: Why? What? How?. In: Borrmann, A., König, M., Koch, C., and Beetz, J., Editors, *Building Information Modeling*, Volume 145, pp. 1–24. Springer, Cham. DOI: `https://doi.org/10.1007/978-3-319-92862-3_1`.

Borrmann, D., Elseberg, J., Lingemann, K., Nüchter, A., and Hertzberg, J. (2008). Globally Consistent 3D Mapping with Scan Matching. In: *Robotics and Autonomous Systems*, 56(2), pp. 130–142. DOI: `https://doi.org/10.1016/j.robot.2007.07.002`.

Bosse, M., Zlot, R., and Flick, P. (2012). Zebedee: Design of a Spring-Mounted 3-D Range Sensor with Application to Mobile Mapping. In: *IEEE Transactions on Robotics*, 28(5), pp. 1104–1119. DOI: `https://doi.org/10.1109/TRO.2012.2200990`.

Boudette, N. E. (2019). Despite High Hopes, Self-Driving Cars Are 'Way in the Future'. In: *The New York Times*. URL: `https://www.nytimes.com/2019/07/17/business/self-driving-autonomous-cars.html`, Accessed: 2020-02-05.

Brembeck, J. (2019). Nonlinear Constrained Moving Horizon Estimation Applied to Vehicle Position Estimation. In: *Sensors (Basel, Switzerland)*, 19(10), 2276, pp. 1–26. DOI: `https://doi.org/10.3390/s19102276`.

Brenner, C. (2016). Scalable Estimation of Precision Maps in a Mapreduce Framework. In: *Proceedings of the 24th ACM SIGSPATIAL International Conference on Advances in Geographic Information Systems - GIS '16*, New York, NY, USA, pp. 1–10. DOI: `https://doi.org/10.1145/2996913.2996990`.

Brenner, C. and Hofmann, S. (2012). Evaluation of Automatically Extracted Landmarks for Future Driver Assistance Systems. In: Yeh, A. G., Shi, W., Leung, Y., and Zhou, C. H., Editors, *Advances in Spatial Data Handling and GIS*, Lecture Notes in Geoinformation and Cartography, pp. 169–181. Springer, Berlin, Heidelberg. DOI: `https://doi.org/10.1007/978-3-642-25926-5_13`.

Bureick, J., Vogel, S., Neumann, I., Diener, D., and Alkhatib, H. (2019a). Geo-Referenzierung von Unmanned Aerial Systems über Laserscannermessungen und 3D-Gebäudemodelle. In: DVW e.V., Editor, *Terrestrisches Laserscanning 2019 (TLS 2019)*, *Schriftenreihe des DVW*, Volume 96, pp. 63–74. Wißner-Verlag, Augsburg.

Bureick, J., Vogel, S., Neumann, I., Unger, J., and Alkhatib, H. (2019b). Georeferencing of an Unmanned Aerial System by Means of an Iterated Extended Kalman Filter Using a 3D City Model. In: *Journal of Photogrammetry, Remote Sensing and Geoinformation Science (PFG)*, 87(5-6), pp. 229–247. DOI: `https://doi.org/10.1007/s41064-019-00084-x`.

Candy, J. V. (2016). *Bayesian Signal Processing: Classical, Modern, and Particle Filtering Methods*. Wiley, Hoboken, New Jersey, Second Edition. DOI: `https://doi.org/10.1002/9781119125495`.

Chiang, Y.-T., Wang, L.-S., and Chang, F.-R. (2002). Filtering Method for Nonlinear Systems with Constraints. In: *IEE Proceedings - Control Theory and Applications*, 149(6), pp. 525–531. DOI: `https://doi.org/10.1049/ip-cta:20020799`.

Chow, J., Lichti, D. D., and Glennie, C. (2011). Point-Based versus Plane-Based Self-Calibration of Static Terrestrial Laser Scanners. In: *ISPRS International Archives of the Photogrammetry, Remote Sensing and Spatial Information Science*, XXXVIII-5/W12, pp. 121–126. DOI: `https://doi.org/10.5194/isprsarchives-XXXVIII-5-W12-121-2011`.

Colomina, I. and Molina, P. (2014). Unmanned Aerial Systems for Photogrammetry and Remote Sensing: A Review. In: *ISPRS Journal of Photogrammetry and Remote Sensing*, 92, pp. 79–97. DOI: `https://doi.org/10.1016/j.isprsjprs.2014.02.013`.

Dang, T. (2007). Kontinuierliche Selbstkalibrierung von Stereokameras, PhD Thesis. In: *Schriftenreihe / Institut für Mess- und Regelungstechnik, Universität Karlsruhe (TH)*. Univ.-Verl. Karlsruhe, Karlsruhe. DOI: `https://doi.org/10.5445/KSP/1000006635`.

Dang, T. (2008). An Iterative Parameter Estimation Method for Observation Models with Nonlinear Constraints. In: *Metrology and Measurement Systems*, 15(4), pp. 421–432.

Davison, A. J. (2003). Real-Time Simultaneous Localisation and Mapping with a Single Camera. In: *IEEE International Conference on Computer Vision*, Nice, France, pp. 1403–1410. DOI: `https://doi.org/10.1109/ICCV.2003.1238654`.

de Geeter, J., van Brussel, H., de Schutter, J., and Decreton, M. (1997). A Smoothly Constrained Kalman Filter. In: *IEEE Transactions on Pattern Analysis and Machine Intelligence*, 19(10), pp. 1171–1177. DOI: `https://doi.org/10.1109/34.625129`.

Dehbi, Y., Lucks, L., Behmann, J., Klingbeil, L., and Plümer, L. (2019). Improving GPS Trajectories Using 3D City Models and Kinematic Point Clouds. In: *ISPRS Annals of Photogrammetry, Remote Sensing and Spatial Information Sciences*, IV-4/W9, pp. 35–42. DOI: `https://doi.org/10.5194/isprs-annals-IV-4-W9-35-2019`.

Denham, W. F. and Pines, S. (1966). Sequential Estimation when Measurement Function Nonlinearity is Comparable to Measurement Error. In: *AIAA Journal*, 4(6), pp. 1071–1076. DOI: `https://doi.org/10.2514/3.3606`.

DIN 18202:2019-07. Toleranzen im Hochbau - Bauwerke. DOI: `https://dx.doi.org/10.31030/3061349`.

Doyle, F., J. (1978). Digital Terrain Models: An Overview. In: *Photogrammetric Engineering and Remote Sensing*, 44(12), pp. 1481–1485. URL: `https://www.asprs.org/wp-content/uploads/pers/1978journal/dec/1978_dec_1481-1485.pdf`, Accessed: 2020-02-17.

Drixler, E. (1993). Analyse der Form und Lage von Objekten im Raum, PhD Thesis. In: *DGK*, Reihe C, 409. Munich.

Ebinger, B., Bouaynaya, N., Polikar, R., and Shterenberg, R. (2015). Constrained State Estimation in Particle Filters. In: *IEEE International Conference on Acoustics, Speech and Signal Processing (ICASSP)*, Brisbane, QLD, pp. 4050–4054. DOI: `https://doi.org/10.1109/ICASSP.2015.7178732`.

Efron, B. and Hastie, T. (2016). *Computer Age Statistical Inference: Algorithms, Evidence, and Data Science (Institute of Mathematical Statistics Monographs)*. Cambridge University Press, New York. DOI: `https://doi.org/10.1017/CBO9781316576533`.

Efron, B. and Tibshirani, R. (1993). *An Introduction to the Bootstrap (Monographs on Statistics and Applied Probability)*. Chapman & Hall, New York.

El-Sheimy, N. (2005). An Overview of Mobile Mapping Systems. In: *Proceedings of FIG Working Week and GSDI-8*, Cairo, Egypt, pp. 1–24.

Eling, C. (2016). Entwicklung einer direkten Georeferenzierungseinheit zur Positions- und Orientierungsbestimmungleichter UAVs in Echtzeit, PhD Thesis. In: *DGK*, Reihe C, 788. Munich.

Elseberg, J., Borrmann, D., and Nüchter, A. (2013a). Algorithmic Solutions for Computing Precise Maximum Likelihood 3D Point Clouds from Mobile Laser Scanning Platforms. In: *Remote Sensing*, 5(11), pp. 5871–5906. DOI: `https://doi.org/10.3390/rs5115871`.

Elseberg, J., Borrmann, D., and Nüchter, A. (2013b). One Billion Points in the Cloud – an Octree for Efficient Processing of 3D Laser Scans. In: *ISPRS Journal of Photogrammetry and Remote Sensing*, 76, pp. 76–88. DOI: `https://doi.org/10.1016/j.isprsjprs.2012.10.004`.

Ernst, D. (2019). *Objektraumbasierte Kalibrierung und Georeferenzierung eines Unmanned Aerial Systems*. Bachelor Thesis (unpublished), Leibniz Universität Hannover, Hanover.

Ettlinger, A., Neuner, H., and Burgess, T. (2018). Development of a Kalman Filter in the Gauss-Helmert Model for Reliability Analysis in Orientation Determination with Smartphone Sensors. In: *Sensors (Basel, Switzerland)*, 18(2), 414, pp. 1–21   DOI: https://doi.org/10.3390/s18020414.

Ezzatti, P., Quintana-Ortí, E. S., and Remón, A. (2011). Using Graphics Processors to Accelerate the Computation of the Matrix Inverse. In: *The Journal of Supercomputing*, 58(3), pp. 429–437. DOI: https://doi.org/10.1007/s11227-011-0606-4.

Fagnant, D. J. and Kockelman, K. (2015). Preparing a Nation for Autonomous Vehicles: Opportunities, Barriers and Policy Recommendations. In: *Transportation Research Part A: Policy and Practice*, 77, pp. 167–181. DOI: https://doi.org/10.1016/j.tra.2015.04.003.

Fischler, M. A. and Bolles, R. C. (1981). Random Sample Consensus: A Paradigm for Model Fitting with Applications to Image Analysis and Automated Cartography. In: *Communications of the ACM*, 24(6), pp. 381–395. DOI: https://doi.org/10.1145/358669.358692.

Fletcher, R. (2008). *Practical Methods of Optimization*. Wiley, Chichester, 2nd Editon. DOI: https://doi.org/10.1002/9781118723203.

Förstner, W. and Wrobel, B. P. (2016). *Photogrammetric Computer Vision*. Springer, Cham. DOI: https://doi.org/10.1007/978-3-319-11550-4.

Frei, E. A. (2013). Kinematische Scanlösungen von P3D Systems. In: DVW e.V., Editor, *Terrestrisches Laserscanning 2013 (TLS 2013)*, *Schriftenreihe des DVW*, Volume 72, pp. 107–124. Wißner-Verlag, Augsburg.

Gang-jun, L., Kefei, Z., Falin, W., Liam, D., and Retscher, G. (2009). Characterisation of Current and Future GNSS Performance in Urban Canyons using a High Quality 3-D Urban Model of Melbourne, Australia. In: *Journal of Applied Geodesy*, 3(1), pp. 15–24. DOI: https://doi.org/10.1515/JAG.2009.002.

Garcia-Fernandez, N., Alkhatib, H., and Schön, S. (2019). Collaborative Navigation Simulation Tool using Kalman Filter with Implicit Constraints. In: *ISPRS Annals of Photogrammetry, Remote Sensing and Spatial Information Sciences*, IV-2/W5, pp. 559–566. DOI: https://doi.org/10.5194/isprs-annals-IV-2-W5-559-2019.

Garcia-Fernandez, N. and Schön, S. (2019). Optimizing Sensor Combinations and Processing Parameters in Dynamic Sensor Networks. In: *Proceedings of the 32nd International Technical Meeting of the Satellite Division of The Institute of Navigation (ION GNSS+ 2019)*, Miami, Florida, pp. 2048–2062. DOI: https://doi.org/10.33012/2019.16885.

Geiger, A., Lenz, P., Stiller, C., and Urtasun, R. (2013). Vision meets Robotics: The KITTI Dataset. In: *The International Journal of Robotics Research*, 32(11), pp. 1231–1237. DOI: https://doi.org/10.1177/0278364913491297.

Gelb, A. (1974). *Applied Optimal Estimation*. MIT Press, Cambridge.

Gleason, S. and Gebre-Egziabher, D. (2009). *GNSS Applications and Methods*. GNSS Technology and Applications Series. Artech House, Boston, Massachusetts.

Glennie, C. (2007). Rigorous 3D Error Analysis of Kinematic Scanning Lidar Systems. In: *Journal of Applied Geodesy*, 1(3), pp. 147–157. DOI: https://doi.org/10.1515/jag.2007.017.

Gräfe, G. (2007). Kinematische Anwendungen von Laserscannern im Straßenraum, PhD Thesis. In: *Universität der Bundeswehr München, Fakultät für Bauingenieur- und Vermessungswesen*, Issue 84, Neubiberg.

Grejner-Brzezinska, D., Toth, C., and Yi, Y. (2005). On Improving Navigation Accuracy of GPS/INS Systems. In: *Photogrammetric Engineering & Remote Sensing*, 71(4), pp. 377–389. DOI: https://doi.org/10.14358/PERS.71.4.377.

Grewal, M. S. and Andrews, A. P. (2015). *Kalman Filtering: Theory and Practice using MATLAB*. Wiley, Hoboken, NJ. DOI: https://doi.org/10.1002/9781118984987.

Gröger, G., Kolbe, T. H., Nagel, C., and Häfele, K.-H. (2012). OGC City Geography Markup Language (CityGML) Encoding Standard: OGC Document No. 12-019. Version 2.0.0 URL: https://portal.opengeospatial.org/files/?artifact_id=47842, Accessed: 2020-02-17.

Gupta, N. and Hauser, R. (2007). Kalman Filtering with Equality and Inequality State Constraints. URL: https://arxiv.org/abs/0709.2791, Accessed: 2019-10-05.

Hansen, P. C. (2007). Regularization Tools Version 4.0 for Matlab 7.3. In: *Numerical Algorithms*, 46(2), pp. 189–194. DOI: https://doi.org/10.1007/s11075-007-9136-9.

Hartmann, J., Paffenholz, J.-A., Strübing, T., and Neumann, I. (2017). Determination of Position and Orientation of Lidar Sensors on Multisensor Platforms. In: *Journal of Surveying Engineering*, 143(4), pp. 1–11. DOI: https://doi.org/10.1061/(ASCE)SU.1943-5428.0000226.

Hartmann, J., Trusheim, P., Alkhatib, H., Paffenholz, J.-A., Diener, D., and Neumann, I. (2018). High Accurate Pointwise (Geo-)Referencing of a k-TLS Based Multi-Sensor-System. In: *ISPRS Annals of Photogrammetry, Remote Sensing and Spatial Information Sciences*, IV-4, pp. 81–88. DOI: https://doi.org/10.5194/isprs-annals-IV-4-81-2018.

Hartmann, J., von Gösseln, I., Schild, N., Dorndorf, A., Paffenholz, J.-A., and Neumann, I. (2019). Optimisation of the Calibration Process of a k-TLS Based Multi-Sensor-System by Genetic Algorithms. In: *ISPRS International Archives of the Photogrammetry, Remote Sensing and Spatial Information Sciences*, XLII-2/W13, pp. 1655–1662. DOI: `https://doi.org/10.5194/isprs-archives-XLII-2-W13-1655-2019`.

Hebel, M., Arens, M., and Stilla, U. (2009). Utilization of 3D City Models and Airborne Laser Scanning for Terrain-Based Navigation of Helicopters and UAV. In: *ISPRS International Archives of Photogrammetry, Remote Sensing and Spatial Information Sciences*, 38(3/W4), pp. 187–192.

Hegarty, C., Leva, J., Dyke, K. V., and Walter, T. (2017). Performance of Stand-Alone GNSS. In: Kaplan, E. D. and Hegarty, C., Editors, *Understanding GPS/GNSS*, Chapter 7, Artech House, Norwood, MA.

Heiker, A. (2013). Mutual Validation of Earth Qrientation Parameters, Geophysical Excitation Functions and Second Degree Gravity Field Coefficients, PhD Thesis. In: *DGK*, Reihe C, 697. Munich.

Heinz, E., Eling, C., Wieland, M., Klingbeil, L., and Kuhlmann, H. (2015). Development, Calibration and Evaluation of a Portable and Direct Georeferenced Laser Scanning System for Kinematic 3D Mapping. In: *Journal of Applied Geodesy*, 9(4), pp. 227–243. DOI: `https://doi.org/10.1515/jag-2015-0011`.

Heinz, E., Eling, C., Wieland, M., Klingbeil, L., and Kuhlmann, H. (2017). Analysis of Different Reference Plane Setups for the Calibration of a Mobile Laser Scanning System. In: Lienhart, W., Editor, *Ingenieurvermessung 17. Beiträge zum 18. Internationalen Ingenieurvermessungskurs, Graz, Austria*, pp. 131–145. Wichmann, Berlin. URL: `http://hdl.handle.net/20.500.11811/1352`.

Heinz, E., Holst, C., Kuhlmann, H., and Klingbeil, L. (2020). Design and Evaluation of a Permanently Installed Plane-Based Calibration Field for Mobile Laser Scanning Systems. In: *Remote Sensing*, 12(3), 555, pp. 1–29. DOI: `https://doi.org/10.3390/rs12030555`.

Hertzberg, J., Lingemann, K., and Nüchter, A. (2012). *Mobile Roboter: Eine Einführung aus Sicht der Informatik*. Springer, Berlin. DOI: `https://doi.org/10.1007/978-3-642-01726-1`.

Hesch, J. A., Mirzaei, F. M., Mariottini, G. L., and Roumeliotis, S. I. (2010). A Laser-Aided Inertial Navigation System (L-INS) for Human Localization in Unknown Indoor Environments. In: *IEEE International Conference on Robotics and Automation (ICRA)*, Anchorage, AK, pp. 5376–5382. DOI: `https://doi.org/10.1109/ROBOT.2010.5509693`.

Hesse, C. (2007). Hochauflösende kinematische Objekterfassung mit terrestrischen Laserscannern, PhD Thesis. In: *DGK*, Reihe C, 608. Munich.

Heuel, S. (2001). Points, Lines, and Planes and Their Optimal Estimation. In: Goos, G., Hartmanis, J., van Leeuwen, J., Radig, B., and Florczyk, S. H., Editors, *Pattern Recognition, Lecture Notes in Computer Science*, Volume 2191, pp. 92–99. Springer, Berlin. DOI: `https://doi.org/10.1007/3-540-45404-7_13`.

Hexagone Metrology (2015). Leica Absolute Tracker AT960 (Product Brochure): Absolute Portability. Absolute Speed. Absolute Accuracy. URL: `https://w3.leica-geosystems.com/downloads123/m1/metrology/general/brochures/leica%20at960%20brochure_en.pdf`, Accessed: 2020-02-05.

Hillemann, M., Meidow, J., and Jutzi, B. (2019). Impact of Different Trajectories on Extrinsic Self-Calibration for Vehicle-Based Mobile Laser Scanning Systems. In: *ISPRS International Archives of the Photogrammetry, Remote Sensing and Spatial Information Sciences*, XLII-2/W16, pp. 119–125. DOI: `https://doi.org/10.5194/isprs-archives-XLII-2-W16-119-2019`.

Hofmann, S. (2017). Potential von LiDAR Mobile Mapping für hochgenaue Karten, PhD Thesis. In: *DGK*, Reihe C, 801. Munich.

Holst, C., Kuhlmann, H., Paffenholz, J.-A., and Neumann, I. (2015). TLS im Statischen, Stop & Go sowie Kinematischen Einsatz. In: DVW e.V., Editor, *Terrestrisches Laserscanning 2015 (TLS 2015), Schriftenreihe des DVW*, Volume 81, pp. 9–26. Wißner-Verlag, Augsburg.

Hsu, L.-T. (2018). Analysis and Modeling GPS NLOS Effect in Highly Urbanized Area. *GPS Solutions*, 22(1), pp. 1–12. DOI: `https://doi.org/10.1007/s10291-017-0667-9`.

Ibeo Automotive Systems (2020). ibeoNEXT Generic 4D Solid State LiDAR: Die Zukunft des autonomen Fahrens! URL: `https://www.ibeo-as.com/de/produkte/sensoren/ibeoNEXTgeneric`, Accessed: 2020-02-06.

Jaakkola, A., Hyyppä, J., Kukko, A., Yu, X., Kaartinen, H., Lehtomäki, M., and Lin, Y. (2010). A Low-cost Multi-sensoral Mobile Mapping System and Its Feasibility for Tree Measurements. In: *ISPRS Journal of Photogrammetry and Remote Sensing*, 65(6), pp. 514–522. DOI: `https://doi.org/10.1016/j.isprsjprs.2010.08.002`.

Jäger, R., Müller, T., Saler, H., and Schwäble, R. (2005). *Klassische und Robuste Ausgleichsverfahren: Ein Leitfaden für Ausbildung und Praxis von Geodäten und Geoinformatikern*. Wichmann, Heidelberg.

James, G., Witten, D., Hastie, T., and Tibshirani, R. (2017). *An Introduction to Statistical Learning: With Applications in R*. Springer, New York, Heidelberg,

Dordrecht, London. DOI: `https://doi.org/10.1007/978-1-4614-7138-7`.

Jazwinski, A. H. (1970). *Stochastic Processes and Filtering Theory*. Acad. Press, New York, NY.

Jung, J., Yoon, S., Ju, S., and Heo, J. (2015). Development of Kinematic 3D Laser Scanning System for Indoor Mapping and As-Built BIM Using Constrained SLAM. In: *Sensors (Basel, Switzerland)*, 15(10), pp. 26430–26456. DOI: `https://doi.org/10.3390/s151026430`.

Kalman, R. E. (1960). A New Approach to Linear Filtering and Prediction Problems. In: *Journal of Basic Engineering*, 82(1), pp. 35–45.

Kalman, R. E. and Bucy, R. S. (1961). New Results in Linear Filtering and Prediction Theory. In: *Journal of Basic Engineering*, 83(1), pp. 95–108. DOI: `https://doi.org/10.1115/1.3658902`.

Kaul, L., Zlot, R., and Bosse, M. (2016). Continuous-Time Three-Dimensional Mapping for Micro Aerial Vehicles with a Passively Actuated Rotating Laser Scanner. In: *Journal of Field Robotics*, 33(1), pp. 103–132. DOI: `https://doi.org/10.1002/rob.21614`.

Keller, F. (2016). Entwicklung eines forschungsorientierten Multi-Sensor-Systems zum kinematischen Laserscanning innerhalb von Gebäuden, PhD Thesis. *HafenCity Universität Hamburg*, Shaker Verlag.

Keller, F. and Sternberg, H. (2013). Multi-Sensor Platform for Indoor Mobile Mapping: System Calibration and Using a Total Station for Indoor Applications. In: *Remote Sensing*, 5(11), pp. 5805–5824. DOI: `https://doi.org/10.3390/rs5115805`.

Koch, K.-R. (1999). *Parameter Estimation and Hypothesis Testing in Linear Models*. Springer, Berlin, Heidelberg. DOI: `https://doi.org/10.1007/978-3-662-03976-2`.

Koch, K.-R. (2000). *Einführung in die Bayes-Statistik*. Springer, Berlin, Heidelberg. DOI: `https://doi.org/10.1007/978-3-642-56970-8`.

Konolige, K. and Agrawal, M. (2008). FrameSLAM: From Bundle Adjustment to Real-Time Visual Mapping. In: *IEEE Transactions on Robotics*, 24(5), pp. 1066–1077. DOI: `https://doi.org/10.1109/TRO.2008.2004832`.

Krebs, V. (1980). *Nichtlineare Filterung*. Methoden der Regelungstechnik. Oldenbourg, München.

Kuutti, S., Fallah, S., Katsaros, K., Dianati, M., Mccullough, F., and Mouzakitis, A. (2018). A Survey of the State-of-the-Art Localization Techniques and Their Potentials for Autonomous Vehicle Applications. In: *IEEE Internet of Things Journal*, 5(2), pp. 829–846. DOI: `https://doi.org/10.1109/JIOT.2018.2812300`.

Kwoczek, A. et al. (2015). 5G Automotive Vision. White Paper. URL: `https://5g-ppp.eu/wp-content/uploads/2014/02/5G-PPP-White-Paper-on-Automotive-Vertical-Sectors.pdf`, Accessed: 2020-03-15.

Landeshauptstadt Hannover (2017a). Produktinformation: Digitales 3D-Stadtmodell. FB Planen und Stadtentwicklung, Bereich Geoinformation. URL: `https://www.hannover.de/content/download/641402/15208189/file/Produktblatt_DGM.pdf`, Accessed: 2020-02-18.

Landeshauptstadt Hannover (2017b). Produktinformation: Digitales Geländemodell (DGM1). FB Planen und Stadtentwicklung, Bereich Geoinformation. URL: `https://www.hannover.de/content/download/641518/15209724/file/Produktblatt_3DStadtmodell.pdf`, Accessed: 2020-02-18.

Lenzmann, L. and Lenzmann, E. (2004). Strenge Auswertung des nichtlinearen Gauß-Helmert-Modells. In: *AVN (Allgemeine Vermessungs-Nachrichten)*, 111(2), pp. 68–73.

Lösler, M. and Nitschke, M. (2010). Bestimmung der Parameter einer Regressionsellipse in Allgemeiner Raumlage. In: *AVN (Allgemeine Vermessungs-Nachrichten)*, 117(3), pp. 113–117. DOI: `https://doi.org/10.5445/IR/1000014897`.

Luhmann, T. (2010). *Nahbereichsphotogrammetrie: Grundlagen, Methoden und Anwendungen*. Wichmann, Berlin.

Lutter, R. P. and Olson, T. (2004). Multi-Sensor System. US 6771208 B2. URL: `https://patents.google.com/patent/US6771208`, Accessed: 2020-02-06.

MacKinnon, J. (2007). Bootstrap Hypothesis Testing. In: *Handbook of Computational Econometrics*, pp. 183–213. DOI: `https://doi.org/10.1002/9780470748916.ch6`.

Maddern, W., Harrison, A., and Newman, P. (2012). Lost in Translation (and Rotation): Rapid Extrinsic Calibration for 2D and 3D Lidars. In: *IEEE International Conference on Robotics and Automation (ICRA)*, Piscataway, NJ, pp. 3096–3102. DOI: `https://doi.org/10.1109/ICRA.2012.6224607`.

Mallozzi, P., Pelliccione, P., Knauss, A., Berger, C., and Mohammadiha, N. (2019). Autonomous Vehicles: State of the Art, Future Trends, and Challenges. In: Dajsuren, Y. and van den Brand, M., Editors, *Automotive Systems and Software Engineering*, pp. 347–367. Springer, Cham. DOI: `https://doi.org/10.1007/978-3-030-12157-0_16`.

Moftizadeh, R. (2019). *Kalman Filtering with State Constraints for Georeferencing of Multi-Sensor-Systems*. Master Thesis (unpublished), Leibniz Universität Hannover, Hanover.

Mulquiney, J. E., Norton, J. P., Jakeman, A. J., and Taylor, J. A. (1995). Random Walks in the Kalman Filter: Implications for Greenhouse Gas Flux Deductions. *Environmetrics*, 6(5):pp. 473–478. DOI: `https://doi.org/10.1002/env.3170060509`.

Nagai, M., Chen, T., Shibasaki, R., Kumagai, H., and Ahmed, A. (2009). UAV-Borne 3-D Mapping System by Multisensor Integration. *IEEE Transactions on Geoscience and Remote Sensing*, 47(3), pp. 701–708. DOI: `https://doi.org/10.1109/TGRS.2008.2010314`.

Neitzel, F. and Neumann, I. (2013). Scanning in Motion - Kinematisches TLS mittels mobiler Plattformen. In: DVW e.V., Editor, *Terrestrisches Laserscanning 2013 (TLS 2013)*, *Schriftenreihe des DVW*, Volume 72, pp. 89–106. Wißner-Verlag, Augsburg.

Nex, F. and Remondino, F. (2014). UAV for 3D Mapping Applications: A Review. In: *Applied Geomatics*, 6(1), pp. 1–15. DOI: `https://doi.org/10.1007/s12518-013-0120-x`.

Nguyen, V., Harati, A., Martinelli, A., Siegwart, R., and Tomatis, N. (2006). Orthogonal SLAM: A Step Toward Lightweight Indoor Autonomous Navigation. In: *IEEE/RSJ International Conference on Intelligent Robots and Systems*, pp. 5007–5012. DOI: `https://doi.org/10.1109/IROS.2006.282527`.

Niemeier, W. (2008). *Ausgleichungsrechnung: Statistische Auswertemethoden*. De Gruyter. Berlin.

Ning, X., Wang, F., and Fang, J. (2017). An Implicit UKF for Satellite Stellar Refraction Navigation System. In: *IEEE Transactions on Aerospace and Electronic Systems*, 53(3), pp. 1489–1503. DOI: `https://doi.org/10.1109/TAES.2017.2671684`.

Nüchter, A., Borrmann, D., Koch, P., Kühn, M., and May, S. (2015). A man-portable, IMU-free Mobile Mapping System. In: *ISPRS Annals of Photogrammetry, Remote Sensing and Spatial Information Sciences*, II-3/W5, pp. 17–23. DOI: `https://doi.org/10.5194/isprsannals-II-3-W5-17-2015`.

Nüchter, A., Lingemann, K., Hertzberg, J., and Surmann, H. (2007). 6D SLAM—3D Mapping Outdoor Environments. In: *Journal of Field Robotics*, 24(8-9), pp. 699–722. DOI: `https://doi.org/10.1002/rob.20209`.

Nurunnabi, A., West, G., and Belton, D. (2015). Outlier Detection and Robust Normal-Curvature Estimation in Mobile Laser Scanning 3D Point Cloud Data. In: *Pattern Recognition*, 48(4), pp. 1404–1419. DOI: `https://doi.org/10.1016/j.patcog.2014.10.014`.

Omidalizarandi, M., Kargoll, B., Paffenholz, J.-A., and Neumann, I. (2019). Robust External Calibration of Terrestrial Laser Scanner and Digital Camera for Structural Monitoring. In: *Journal of Applied Geodesy*, 13(2), pp. 105–134. DOI: `https://doi.org/10.1515/jag-2018-0038`.

Paffenholz, J.-A. (2012). Direct Geo-Referencing of 3D Point Clouds with 3D Positioning Sensors, PhD Thesis. In: *DGK*, Reihe C, 689. Munich.

Pandey, G., Mcbride, J. R., Savarese, S., and Eustice, R. M. (2012). Automatic Targetless Extrinsic Calibration of a 3D Lidar and Camera by Maximizing Mutual Information. In: *Proceedings of the AAAI National Conference on Artificial Intelligence*, Toronto, Canada, pp. 2053–2059.

Perwass, C., Gebken, C., and Sommer, G. (2005). Estimation of Geometric Entities and Operators from Uncertain Data. In: Kropatsch, W. G., Editor, *Pattern Recognition*, *Lecture Notes in Computer Science*, Volume 3663, pp. 459–467. Springer, Berlin. DOI: `https://doi.org/10.1007/11550518_57`.

Peters, T. and Brenner, C. (2018). Conditional Adversarial Networks for Multimodal Photo-Realistic Point Cloud Rendering. In: Raubal, M., Wang, S., Guo, M., Jonietz, D., and Kiefer, P., Editors, *Spatial Big Data and Machine Learning in GIScience, GIScience Workshop 2018*, Melbourne, Australia, pp. 48–53.

Petersen, A. and Koch, R. (2010). Statistical Analysis of Kalman Filters by Conversion to Gauss-Helmert Models with Applications to Process Noise Estimation. In: *20th International Conference on Pattern Recognition*, Istanbul, Turkey, pp. 2386–2389. DOI: `https://doi.org/10.1109/ICPR.2010.584`.

Petovello, M. G. (2004). Real-Time Integration of a Tactical-Grade IMU and GPS for High-Accuracy Positioning and Navigation, PhD Thesis. In: Department of Geomatics Engineering, University of Calgary, Canada.

Plackett, R. L. (1950). Some Theorems in Least Squares. In: *Biometrika*, 37(1/2), pp. 149–157. DOI: `https://doi.org/10.2307/2332158`.

Porrill, J. (1988). Optimal Combination and Constraints for Geometrical Sensor Data. In: *The International Journal of Robotics Research*, 7(6), pp. 66–77. DOI: `https://doi.org/10.1177/027836498800700606`.

Prakash, J., Patwardhan, S. C., and Shah, S. L. (2008). Constrained State Estimation Using Particle Filters. In: *IFAC Proceedings Volumes*, 41(2), pp. 6472–6477. DOI: `https://doi.org/10.3182/20080706-5-KR-1001.01091`.

Puente, I., González-Jorge, H., Martínez-Sánchez, J., and Arias, P. (2013). Review of Mobile Mapping and Surveying Technologies. In: *Measurement*, 46(7), pp. 2127–2145. DOI: `https://doi.org/10.1016/j.measurement.2013.03.006`.

Randall, T. (2019). Waymo Starts Selling Sensors to Lower Cost of Self-Driving Cars. In: *Bloomberg*. URL: `https://www.bloomberg.com/news/articles/2019-03-06/waymo-starts-selling-sensors-to-lower-cost-of-self-driving-cars`, Accessed: 2020-02-06.

Reid, T. G., Houts, S. E., Cammarata, R., Mills, G., Agarwal, S., Vora, A., and Pandey, G. (2019). Localization Requirements for Autonomous Vehicles. In: *SAE International Journal of Connected and Automated Vehicles*, 2(3), pp. 173–190. DOI: `https://doi.org/10.4271/12-02-03-0012`.

RIEGL Laser Measurement Systems (2012a). Datasheet: Riegl VMX-250. URL: `http://www.riegl.com/uploads/tx_pxpriegldownloads/10_DataSheet_VMX-250_20-09-2012.pdf`, Accessed: 2020-02-19.

RIEGL Laser Measurement Systems (2012b). Datasheet: Riegl VQ-250. URL: `http://www.riegl.com/uploads/tx_pxpriegldownloads/10_DataSheet_VQ-250_rund_25-09-2012.pdf`, Accessed: 2020-02-19.

Rietdorf, A. (2005). Automatisierte Auswertung und Kalibrierung von scannenden Messsystemen mit tachymetrischem Messprinzip, PhD Thesis. In: *DGK*, Reihe C, 582. Munich.

Robertson, D. G., Lee, J. H., and Rawlings, J. B. (1996). A Moving Horizon-Based Approach for Least-Squares Estimation. In: *AIChE Journal*, 42(8), pp. 2209–2224. DOI: `https://doi.org/10.1002/aic.690420811`.

Robosense (2020). Datasheet: RS-Lidar-32. URL: `https://www.robosense.ai/rslidar/rs-lidar-32`, Accessed: 2020-02-06.

Roese-Koerner, L. R. (2015). Convex Optimization for Inequality Constrained Adjustment Problems, PhD Thesis. In: *DGK*, Reihe C, 759. Munich.

Schindler, F., Förstner, W., and Frahm, J.-M. (2011). Classification and Reconstruction of Surfaces from Point Clouds of man-made Pbjects. In: *IEEE International Conference on Computer Vision Workshops (ICCV Workshops)*, pp. 257–263. DOI: `https://doi.org/10.1109/ICCVW.2011.6130251`.

Schlichting, A. (2018). Fahrzeuglokalisierung durch Automotive Laserscanner unter Verwendung statischer Merkmale, PhD Thesis. In: *DGK*, Reihe C, 826. Munich.

Schneider, D. (2008). Geometrische und stochastische Modelle für die integrierte Auswertung terrestrischer Laserscannerdaten und photogrammetrischer Bilddaten, PhD Thesis. In: *DGK*, Reihe C, 642. Munich.

Schneider, J., Eling, C., Klingbeil, L., Kuhlmann, H., Forstner, W., and Stachniss, C. (2016). Fast and Effective Online Pose Estimation and Mapping for UAVs. In: Okamura, A. and Menciassi, A., Editors, *2016 IEEE International Conference on Robotics and Automation, Stockholm, Sweden*, pp. 4784–4791, Piscataway, NJ. DOI: `https://doi.org/10.1109/ICRA.2016.7487682`.

Schön, S., Brenner, C., Alkhatib, H., Coenen, M., Dbouk, H., Garcia-Fernandez, N., Fischer, C., Heipke, C., Lohmann, K., Neumann, I., Nguyen, U., Paffenholz, J.-A., Peters, T., Rottensteiner, F., Schachtschneider, J., Sester, M., Sun, L., Vogel, S., Voges, R., and Wagner, B. (2018). Integrity and Collaboration in Dynamic Sensor Networks. In: *Sensors (Basel, Switzerland)*, 18(7), pp. 21. DOI: `https://doi.org/10.3390/s18072400`.

Schuhmacher, S. and Böhm, J. (2005). Georeferencing of Terrestrial Laserscanner Data for Applications in Architectural Modeling. In: El-Hakim, S., Remondino, F., and Gonzo, L., Editors, *3D-ARCH 2005: Virtual Reconstruction and Visualization of Complex Architectures* Mestre-Venice, Italy, pp. 1–7. DOI: `https://doi.org/10.18419/OPUS-3749`.

Schwarz, K. P. and El-Sheimy, N. (1996). Kinematic Multi-Sensor Systems for Close Range Digital Imaging. In: *ISPRS International Archives of the Photogrammetry, Remote Sensing and Spatial Information Sciences*, XXXI-5/W3, pp. 774–784.

Shimada, N., Shirai, Y., Kuno, Y., and Miura, J. (1998). Hand Gesture Estimation and Model Refinement Using Monocular Camera-Ambiguity Limitation by Inequality Constraints. In: *Third IEEE International Conference on Automatic Face and Gesture Recognition*, Los Alamitos, California, pp. 268–273. DOI: `https://doi.org/10.1109/AFGR.1998.670960`.

Siciliano, B., Khatib, O., Groen, F., and Stachniss, C. (2009). *Robotic Mapping and Exploration*, volume 55. Springer, Berlin, Heidelberg. DOI: `https://doi.org/10.1007/978-3-642-01097-2`.

Simon, D. (2006). *Optimal State Estimation*. John Wiley & Sons, New Jersey.

Simon, D. (2010). Kalman Filtering with State Constraints: A Survey of Linear and Nonlinear Algorithms. In: *IET Control Theory & Applications*, 4(8), pp. 1303–1318. DOI: `https://doi.org/10.1049/iet-cta.2009.0032`.

Simon, D. and Chia, T. L. (2002). Kalman Filtering with State Equality Constraints. In: *IEEE Transactions on Aerospace and Electronic Systems*, 38(1), pp. 128–136. DOI: `https://doi.org/10.1109/7.993234`.

Simon, D. and Simon, D. L. (2006). Kalman Filtering with Inequality Constraints for Turbofan Engine Health Estimation. In: *IEE Proceedings - Control Theory and Applications*, 153(3), pp. 371–378. DOI: `https://doi.org/10.1049/ip-cta:20050074`.

Simon, D. and Simon, D. L. (2010). Constrained Kalman Filtering via Density Function Truncation for Turbofan Engine Health Estimation. In: *International Journal of Systems Science*, 41(2), pp. 159–171. DOI: `https://doi.org/10.1080/00207720903042970`.

Sircoulomb, V., Hoblos, G., Chafouk, H., and Ragot, J. (2008). State Estimation under Nonlinear State Inequality Constraints. A Tracking Application. In: *16th Mediterranean Conference on Control and Automation, 2008*, Piscataway, NJ, pp. 1669–1674. DOI: `https://doi.org/10.1109/MED.2008.4602024`.

Skaloud, J. and Lichti, D. (2006). Rigorous Approach to Bore-Sight Self-Calibration in Airborne Laser Scanning. In: *ISPRS Journal of Photogrammetry and Remote Sensing*, 61(1), pp. 47–59. DOI: `https://doi.org/10.1016/j.isprsjprs.2006.07.003`.

Smith, R. C. and Cheeseman, P. (1986). On the Representation and Estimation of Spatial Uncertainty. In: *The International Journal of Robotics Research*, 5(4), pp. 56–68. DOI: `https://doi.org/10.1177/027836498600500404`.

Soatto, S., Frezza, R., and Perona, P. (1994). Motion Estimation on the Essential Manifold. In: Eklundh, J.-O., Editor, *Computer Vision - ECCV '94*, *Lecture Notes in Computer Science*, Volume 801, pp. 60–72. Springer, Berlin. DOI: `https://doi.org/10.1007/BFb0028335`.

Soloviev, A., Bates, D., and van GRAAS, F. (2007). Tight Coupling of Laser Scanner and Inertial Measurements for a Fully Autonomous Relative Navigation Solution. In: *Navigation*, 54(3), pp. 189–205. DOI: `https://doi.org/10.1002/j.2161-4296.2007.tb00404.x`.

Steffen, R. (2013). Visual SLAM from Image Sequences Acquired by Unmanned Aerial Vehicles, PhD Thesis. In: *DGK*, Reihe C, 709. Munich.

Steffen, R. and Beder, C. (2007). Recursive Estimation with Implicit Constraints. In: Hamprecht, F. A., Schnörr, C., and Jähne, B., Editors, *Pattern Recognition*, *Lecture Notes in Computer Science*, Volume 4713, pp. 194–203. Springer, Berlin. DOI: `https://doi.org/10.1007/978-3-540-74936-3_20`.

Sternberg, H. (2000). Zur Bestimmung der Trajektorie von Landfahrzeugen mit einem hybriden Meßsystem, PhD Thesis. In: *Schriftenreihe des Studienganges Geodäsie und Geoinformation der Universität der Bundeswehr München*, Neubiberg.

Strassen, V. (1969). Gaussian Elimination is not Optimal. In: *Numerische Mathematik*, 13(4), pp. 354–356. DOI: `https://doi.org/10.1007/BF02165411`.

Strübing, T. (2015). Kalibrierung und Auswertung von lasertriangulationsbasierten Multisensorsystemen am Beispiel des Gleisvermessungssystems RACER II, Ph.D. Thesis. In: *Schriftenreihe des Studienganges Geodäsie und Geoinformation der Universität der Bundeswehr München*, Neubiberg.

Strübing, T. and Neumann, I. (2013). Positions- und Orientierungsschätzung von Lidar-Sensoren auf Multisensorplattformen. In: *Zeitschrift für Geodäsie, Geoinformation und Landmanagement*, 138(3), pp. 210–221.

Talaya, J., Alamus, R., Bosch, E., Serra, A., Kornus, W., and Baron, A. (2004). Integration of a Terrestrial Laser Scanner with GPS/IMU Orientation Sensors. In: *ISPRS International Archives of the Photogrammetry, Remote Sensing and Spatial Information Science*, XX-5, pp. 121–126.

Teixeira, B. O. S., Torres, L. A. B., Aguirre, L. A., and Bernstein, D. S. (2008). Unscented Filtering for Interval-Constrained Nonlinear Systems. In: *47th IEEE Conference on Decision and Control, 2008*, Piscataway, NJ, pp. 5116–5121. DOI: `https://doi.org/10.1109/CDC.2008.4739141`.

Thrun, S., Burgard, W., and Fox, D. (2005). *Probabilistic Robotics*. MIT Press, Cambridge and Mass.

Tikhonov, A. N. and Arsenin, V. Y. (1977). *Solutions of Ill-Posed Problems*. Scripta Series in Mathematics. Winston, Washington, D.C.

Toth, C., Shin, S. W., Grejner-Brzezinska, D. A., and Kwon, J. H. (2008). On Accurate Time Synchronization of Multi-Sensor Mobile Mapping Systems. In: *Journal of Applied Geodesy*, 2(3), pp. 159–166. DOI: `https://doi.org/10.1515/JAG.2008.018`.

Underwood, J., Hill, A., and Scheding, S. (2007). Calibration of Range Sensor Pose on Mobile Platforms. In: *IEEE/RSJ International Conference on Intelligent Robots and Systems, 2007*, Piscataway, NJ, pp. 3866–3871. DOI: `https://doi.org/10.1109/IROS.2007.4398971`.

Ungarala, S., Dolence, E., and Li, K. (2007). Constrained Extended Kalman Filter for Nonlinear State Estimation. In: *IFAC Proceedings*, 40(5), pp. 63–68. DOI: `https://doi.org/10.3182/20070606-3-MX-2915.00058`.

Unger, J., Rottensteiner, F., and Heipke, C. (2016). Integration of a Generalised Building Model into the Pose Estimation of UAS Images. In: *ISPRS International Archives of the Photogrammetry, Remote Sensing and Spatial Information Sciences*, XLI-B1, pp. 1057–1064. DOI: `https://doi.org/10.5194/isprsarchives-XLI-B1-1057-2016`.

Unger, J., Rottensteiner, F., and Heipke, C. (2017). Assigning Tie Points to a Generalised Building Model for UAS Image Orientation. In: *ISPRS International Archives of the Photogrammetry, Remote Sensing and Spatial Information Sciences*, XLII-2/W6, pp. 385–392. DOI: `https://doi.org/10.5194/isprs-archives-XLII-2-W6-385-2017`.

Unnikrishnan, R. and Hebert, M. (2005). Fast Extrinsic Calibration of a Laser Rangefinder to a Camera. Technical Report, CMU-RI-TR-05-09. In: *Robotics Institute*, Pittsburgh, PA.

Velodyne LiDAR (2018a). Datasheet: HDL-64E: High Definition Real-Iime 3D LiDAR. URL: `https://velodynelidar.com/products/hdl-64e/`, Accessed: 2020-02-06.

Velodyne LiDAR (2018b). Datasheet: Velodyne LiDAR Puck: Real-Time 3D LiDAR Sensor. URL: https://velodynelidar.com/vlp-16.html, Accessed: 2019-12-12.

Vennegeerts, H. (2011). Objektraumgestützte kinematische Georeferenzierung für Mobile-Mapping-Systeme, PhD Thesis. In: *DGK*, Reihe C, 657. Munich.

Vogel, S., Alkhatib, H., Bureick, J., Moftizadeh, R., and Neumann, I. (2019). Georeferencing of Laser Scanner-Based Kinematic Multi-Sensor Systems in the Context of Iterated Extended Kalman Filters Using Geometrical Constraints. In: *Sensors (Basel, Switzerland)*, 19(10), pp. 2–22. DOI: https://doi.org/10.3390/s19102280.

Vogel, S., Alkhatib, H., and Neumann, I. (2016). Accurate Indoor Georeferencing with Kinematic Multi Sensor Systems. In: *International Conference on Indoor Positioning and Indoor Navigation (IPIN)*, Alcala de Henares, Spain, pp. 1–8. DOI: https://doi.org/10.1109/IPIN.2016.7743601.

Vogel, S., Alkhatib, H., and Neumann, I. (2018). Iterated Extended Kalman Filter with Implicit Measurement Equation and Nonlinear Constraints for Information-Based Georeferencing. In: *21st International Conference on Information Fusion (FUSION)*, Cambridge, United Kingdom, pp. 1209–1216. DOI: https://doi.org/10.23919/ICIF.2018.8455258.

Vosselman, G. and Dijkman, S. (2001). 3D Building Model Reconstruction from Point Clouds and Ground Plans. In: *ISPRS International Archives of Photogrammetry, Remote Sensing and Spatial Information Sciences*, 34(3/W4), pp. 37–43. URL: http://www.isprs.org/proceedings/XXXIV/3-W4/pdf/Vosselman.pdf.

Wang, Chen, Zhu, Liu, Li, and Zheng (2019). A Survey of Mobile Laser Scanning Applications and Key Techniques over Urban Areas. In: *Remote Sensing*, 11(13), pp. 1–20. DOI: https://doi.org/10.3390/rs11131540.

Wang, L., Groves, P. D., and Ziebart, M. K. (2013). GNSS Shadow Matching: Improving Urban Positioning Accuracy Using a 3D City Model with Optimized Visibility Scoring Scheme. In: *Navigation*, 60(3), pp. 195–207. DOI: https://doi.org/10.1002/navi.38.

Wasielewski, S. and Strauss, O. (1995). Calibration of a Multi-Sensor System Laser Rangefinder/Camera. In: *Intelligent Vehicles '95. Symposium*, pp. 472–477.

Weiss, T.-T. (2011). Hochgenaue Positionierung und Kartographie mit Laserscannern für Fahrerassistenzsysteme, PhD Thesis. In: *Schriftenreihe des Instituts für Mess-, Regel- und Mikrotechnik*. Univ., [Fak. für Ingenieurwiss. und Informatik], Ulm.

Wenzel, T. A., Burnham, K. J., Blundell, M. V., and Williams, R. A. (2006). Dual Extended Kalman Filter for Vehicle State and Parameter Estimation. In: *Vehicle System Dynamics*, 44(2),

pp. 153–171. DOI: https://doi.org/10.1080/00423110500385949.

Wichmann, K. (2007). Auswertung von Messdaten: Statistische Methoden für Geo- und Ingenieurwissenschaften. De Gruyter. München. DOI: https://doi.org/10.1524/9783486844184.

Wörner, M., Schuster, F., Dolitzscher, F., Keller, C. G., Haueis, M., and Dietmayer, K. (2016). Integrity for Autonomous Driving: A Survey. In: *Proceedings of the 2016 IEEE/ION Position, Location and Navigation Symposium*, Piscataway, NJ, pp. 666–671. DOI: https://doi.org/10.1109/PLANS.2016.7479759.

Yang, C. and Blasch, E. (2009). Kalman Filtering with Nonlinear State Constraints. In: *IEEE Transactions on Aerospace and Electronic Systems*, 45(1), pp. 70–84. DOI: https://doi.org/10.1109/TAES.2009.4805264.

Zhang, G. (2019). 3D Mapping Aided GNSS-Based Cooperative Positioning Using Factor Graph Optimization. In: *Proceedings of the 32nd International Technical Meeting of the Satellite Division of The Institute of Navigation (ION GNSS+ 2019)*, Miami, Florida, pp. 2269–2284. DOI: https://doi.org/10.33012/2019.16957.

Zhang, G., Wen, W., and Hsu, L.-T. (2018). Collaborative GNSS Positioning with the Aids of 3D City Models. In: *Proceedings of the 31st International Technical Meeting of The Satellite Division of the Institute of Navigation (ION GNSS+ 2018)*, Miami, Florida, pp. 143–149. DOI: https://doi.org/10.33012/2018.15830.

Zhang, Q. and Pless, R. (2004). Extrinsic Calibration of a Camera and Laser Range Finder (Improves Camera Calibration). In: *Proceedings of 2004 IEEE/RSJ International Conference on Intelligent Robots and Systems*, Sendai, Japan, pp. 2301–2306. DOI: https://doi.org/10.1109/IROS.2004.1389752.

Zhou, L., Li, Z., and Kaess, M. (2018). Automatic Extrinsic Calibration of a Camera and a 3D Lidar Using Line and Plane Correspondences. In: *2018 IEEE/RSJ International Conference on Intelligent Robots and Systems (IROS)*, Madrid, Spain, pp. 5562–5569. DOI: https://doi.org/10.1109/IROS.2018.8593660.

Zhu, N., Marais, J., Betaille, D., and Berbineau, M. (2018). GNSS Position Integrity in Urban Environments: A Review of Literature. In: *IEEE Transactions on Intelligent Transportation Systems*, 19(9), pp. 2762–2778. DOI: https://doi.org/10.1109/TITS.2017.2766768.

Zwiener, J. (2019). Robuste Zustandsschätzung zur Navigation und Regelung autonomer und bemannter Multikopter mit verteilten Sensoren, PhD Thesis. *Universitäts- und Landesbibliothek Darmstadt*, Darmstadt.

Acknowledgments

Curriculum Vitae

Personal Information

Name	Sören Vogel
Date of Birth	April 07, 1988
Place of Birth	Leimen, Germany

Work Experience

since 12/2014	Geodetic Institute Leibniz Universität Hannover *Research Assistant*
01/2010 – 07/2012	Geodetic Institute, Institut of Geodesy Leibniz Universität Hannover *Student Assistant*

Education

12/2016 – 11/2019	DFG Research Training Group i.c.sens (RTG 2159) Leibniz Universität Hannover *PhD Student*
04/2014 – 10/2014	Volkswagen AG, Wolfsburg Development Department *Master Thesis*
10/2009 – 11/2014	Study of Geodesy and Geoinformatics Leibniz Universität Hannover *Bachelor of Science* (2012), *Master of Science* (2014)
10/2008 – 09/2009	Study of Physics Leibniz Universität Hannover
07/2007 – 03/2008	Civil Service
07/2000 – 06/2007	High school